SWINBURNE UNIVERSITY OF TECHNOLOGY

Faculty of Science, Engineering and Technology

Centre for Astrophysics and Supercomputing

Structure and Scaling Relations in Disc Galaxies: Bars, Peanuts and Black Holes

Constantin Bogdan Ciambur

Presented in fulfilment of the requirements

of the degree of Doctor of Philosophy

August 10, 2017

Abstract

The structure of a galaxy is one of its fundamental characteristics, as it carries the imprint of key evolutionary properties, such as age, stellar and gas content, merger history, environment, dynamics, star formation history, and central black hole mass. This thesis has developed different methods to probe and quantify galaxy structure, and applied them to study primarily late-type galaxies, their discs, their non-axisymmetric structures, such as bars or X/peanut–shaped (X/P) features, their bulges, and the massive black holes they harbour at their cores. The focus has been to analyse bar-related dynamical processes, measure the size and orientation of the Milky Way's bar and X-shaped "bulge", and constrain galaxy–(black hole) co-evolution in the unexplored regime of "intermediate-mass" black holes.

I first developed a new software package, ISOFIT, to accurately model isophotal structure in morphologically complex galaxies. With an improved formulation of the mathematical description of galaxy isophotes, ISOFIT can model galaxies with strong deviations from pure ellipticity, capturing features with unprecedented accuracy, and enabling new science on a broad range of topics.

Further, I isolated and studied the isophotal imprint of X/peanut "bulges". Although these distinctive features are common in barred galaxies across a wide range of morphological type, robust, quantitative techniques to study them have been lacking in the field. Based on their characteristic signature in the isophotes of their host galaxies, I developed a framework to quantify the radius, vertical extent above the disc plane, and "strength" of the X/P instability. Applied to near-infrared imaging of twelve nearby galaxies with X/P bulges, this method revealed new structural scaling relations among the peanut spatial parameters, including correlations with the host galaxy dynamics, and a link between peanuts and the stellar disc in which they are embedded. Thanks to ISOFIT, I also discovered previously unknown double peanuts – in a "nested" arrangement – in two galaxies which additionally showed the signatures of nested bars in their surface brightness profiles, further consolidating the association between bars and peanut–shaped structures.

This approach was subsequently applied to quantify the closest X/P structure to the Sun, that in the "bulge" of our own Milky Way galaxy. The size and geometry of the Galaxy's X/P–shaped "bulge" and "long bar" are still uncertain and disputed in the literature, due primarily to our restricted perspective of these two components, which we observe through, and from within, the Galactic disc. By analysing near-infrared imaging of the Milky Way taken with the Wide–field Infrared Survey Explorer, we brought new

constraints to the intrinsic sizes of both the X/P structure and long bar, as well as their inclination relative to our line-of-sight to the Galactic Centre. We further compared the X/P diagnostics of the Milky Way with those in nearby galaxies, finding typical values for the size parameters, but a peanut strength marginally higher than expected.

To characterise the properties of each structural constituent of a galaxy, as they contribute to its one-dimensional light profile, I developed a new and comprehensive program, PROFILER, which was released into the public domain. PROFILER was designed to perform multi-component decompositions of structurally complex galaxies, offering a variety of analytical models for discs, spheroidals, stellar bars, rings, and resolved or point-like nuclear sources.

The algorithms and techniques developed throughout are expected to be useful for studying a plethora of issues in extragalactic astronomy. In this thesis they were central to investigate challenges to, and unexplored regimes in, well-known scaling relations between central black hole mass ($M_\bullet$) and the luminosity, concentration, and stellar mass of the host galaxy's spheroidal component. We addressed the claim of an "over-massive" black hole in a discy elliptical galaxy, which we explained had originated from a previously incorrect modelling of this galaxy's large-scale spheroid and embedded disc. Further, we focussed on the low–mass regime occupied by rare "intermediate-mass" black holes (IMBH), hypothesized to link stellar mass ($< 10^2 M_\odot$), and super-massive ($> 10^5 M_\odot$), black holes, but lacking conclusive, direct detection due to the limitations of current instruments. We modelled the structure of an interesting edge-on disc galaxy hosting an off-centre (~ 3.7 kiloparsecs), strong IMBH candidate. We further revealed the barred nature of a dwarf spiral galaxy with a *central* IMBH candidate, and placed it for the first time on the near-quadratic (black hole mass - spheroid stellar mass) scaling relation. In six additional spiral galaxies reported to host probable IMBHs, we determined the concentration ($n_{\rm sph}$) and luminosity ($L_{\rm sph}$) of their spheroidal components and predicted their black hole mass via the most recent ($M_\bullet - n_{\rm sph}$) and ($M_\bullet - L_{\rm sph}$) scaling relations. We combined these results with independent estimators, to place strong constraints on the expected black hole masses in these objects, and provide a robust, indirect, approach to further probe the intermediate mass black hole population.

Declaration

The work presented in this thesis has been carried out in the Centre for Astrophysics & Supercomputing at Swinburne University of Technology between 2015 and 2017. This thesis contains no material that has been accepted for the award of any other degree or diploma. To the best of my knowledge, this thesis contains no material previously published or written by another author, except where due reference is made in the text of the thesis. The content of the chapters listed below has appeared, or will appear, in refereed journals.

- Chapter 2 has been published as *"Beyond Ellipse(s): Accurately Modelling the Isophotal Structure of Galaxies with* ISOFIT *and* CMODEL*"*, by B. C. Ciambur, in the Astrophysical Journal, Vol. 810, No. 2, ID 120 (2015)

- Chapter 3 has been published as *"Quantifying the (X/Peanut)–Shaped Structure in Edge-on Disc Galaxies: Length, Strength, and Nested Peanuts"*, by B. C. Ciambur and A. W. Graham, in Monthly Notices of the Royal Astronomical Society, Vol. 459, pp. 1276–1292 (2016)

- Chapter 4 has been submitted to the Monthly Notices of the Royal Astronomical Society, and is intended for publication as *"Quantifying the (X/Peanut)–Shaped Structure of the Milky Way – New Constraints on the Bar Geometry"*, B. C. Ciambur, A. W. Graham and J. Bland-Hawthorn

- Chapter 5 has been published as *"*PROFILER*– A Fast and Versatile New Program for Decomposing Galaxy Light Profiles"*, by B. C. Ciambur, in Publications of the Astronomical Society of Australia, Vol. 33, Ed. 62 (2016)

- Parts of Chapter 6 have been published in four articles to which I have extensively contributed, namely:

    1. *"Disky Elliptical Galaxies and the Allegedly Over-massive Black Hole in the Compact Massive 'ES' Galaxy NGC 1271"*, by A. W. Graham, **B. C. Ciambur** and G. A. D. Savorgnan, The Astrophysical Journal, Vol. 831, ID. 132 (2016)

    2. *"Understanding the Environment Around the Intermediate Mass Black Hole Candidate ESO 243-49 HLX-1"*, by N. A. Webb, A. Guérou, **B. C. Ciambur**,

A. Detoeuf, M. Coriat, O. Godet, D. Barret, F. Combes, T. Contini, A. W. Graham, T. J. Maccarone, M. Mrkalj, M. Servillat, I. Schroetter, and K. Wiersema, Astronomy & Astrophysics, in press (2017)

3. *"Does the Intermediate-Mass Black Hole in LEDA 87300 (RGG 118) Follow the Near-quadratic $M_{BH} - M_{Spheroid}$ Relation?"*, by A. W. Graham, **B. C. Ciambur** and R. Soria, The Astrophysical Journal, Vol. 818, ID. 172 (2016)

4. *"Searching for Intermediate-Mass Black Holes in Galaxies With Low-Luminosity AGN: a Multiple-Method Approach"*, by F. Koliopanos, **B. C. Ciambur**, A. W. Graham, N. A. Webb, M. Coriat, B. Mutlu-Pakdil, B. L. Davis, O. Godet, D. Barret, M. S. Seigar, Astronomy & Astrophysics, Vol. 601, ID. A20 (2017)

My contribution to the papers presented in Chapters 2, 3, 4 and 5 is detailed in the appended authorship indication forms (Appendix A). My contribution to the papers in Chapter 6 was as follows.

In Graham et al. (2016a) I acquired and processed the archival HST imaging data, and modelled the galaxy's surface photometry and 1D light profile, obtaining the parameters of the galaxy's constituent components (listed in Table 1 in the paper). Of principal interest in this work were the spheroid component's major axis Sérsic index and total luminosity, which I obtained from the 1D fits. I generated Figures 2 and 3 in this paper, and provided text describing my contribution.

My contribution to Webb et al. (2017) was to acquire and process archival HST imaging data, and to model the galaxy surface photometry and 1D light profile, revealing the barred nature of the galaxy, and obtaining the best-fit parameters of its constituent photometric components. I provided two estimates for the mass of the central black hole in this galaxy, based on the spheroid parameters I obtained from the 1D models, and the black hole scaling relations reported in Savorgnan et al. (2016) and Savorgnan (2016). Further, I processed and modelled proprietary MUSE data, to constrain the astrometry of HLX-1, the object of interest. I generated Figure 3 in this paper, and provided text describing my contribution.
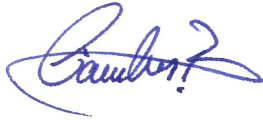
My contribution to Graham et al. (2016b) was to acquire and process archival SDSS data, and model the galaxy's 1D light profile, obtaining the best-fit parameters of its constituent components, which are listed in Table 1 of the paper. Of particular interest

were the Sérsic index, magnitude and colour of the bulge component, which I obtained from the 1D fits. I generated Figures 2, 3, 4, 5 and 6 in the paper.

My contribution to Koliopanos et al. (2017) was to acquire and process archival HST and *Spitzer* data, and model the surface photometry and 1D light profiles of the six galaxies in the sample. I obtained the major axis Sérsic indices, and total luminosities, of their bulge components, and provided two predictions for the black hole mass in each galaxy, as listed in Table 2 of the paper. I also computed the stellar mass of the bulge components, and generated Figures 2 and 4 in the paper.

I warrant that I have obtained, where necessary, permission from the copyright owners to use any third party copyright material reproduced in the thesis (such as artwork, images, unpublished documents), or to use any of my own published work (such as journal articles) in which the copyright is held by another party (such as publisher, co-author).

Constantin Bogdan Ciambur

Contents

1

Introduction

In his X$^{\text{th}}$ century *Book of Fixed Stars*, the Persian astronomer Abd al-Rahman Al-Sufi noted the presence of the Large Magellanic Cloud and of the Andromeda galaxy, which he referred to as a "little cloud" (Schjellerup 1874) . However, it would take until the first decades of the XX$^{\text{th}}$ century before it became firmly rooted in our cosmological paradigm that the Universe is populated with myriads of galaxies, vast stellar systems like the Milky Way, existing and evolving outside of our Galaxy.

By the XVIII$^{\text{th}}$ century, several hazy, "nebulous stars" were known, most notably the "unresolvable star" in the "girdle of Andromeda" (Marius 1614; Hodierna 1654; Hevelius & von Schmieden 1690), now known as the Andromeda galaxy, and astronomers were beginning to seek, and catalogue, these objects. Some of the most important early efforts was Charles Messier's catalogue of 103 such nebulae (Messier 1784), most of which still being referred to by their M (for Messier) number. In a series of publications, William Herschel and his sister, Caroline, compiled catalogues of some few thousand nebulae (Herschel 1786, 1802). These were later systematised and enlarged by William's son, John Herschel (Herschel 1864), and would form the basis of the *New General Catalogue* (NGC), and *Index Catalogue* (IC), *of Nebulae and Clusters of Stars* (Dreyer 1888, 1895, Dreyer 1910). As more and more such objects were being discovered, William Henry Parsons notably revealed, through a 1845 drawing of the "Whirlpool galaxy", M51a (or NGC 5194), that some nebulae possessed spiral structure.

Influenced by Newton's theory of gravity, Immanuel Kant was first to make the conceptual link between these fuzzy objects and our Galaxy. The notion that the Milky Way consists of a large number of small stars, grouped closely together, goes as far back as Anexagoras and Democritus, in the the V$^{\text{th}}$ century B.C., according to Aristotle's treatise

Meteorologica. Galileo Galilei later confirmed this view, noting that the density of stars increases when pointing a telescope towards the patches of the sky crossed by the band of the Milky Way (Galilei 1610). More than a century later, in his book *An Original Theory or New Hypothesis of the Universe*, Thomas Wright introduced a number of important concepts about the Milky Way. He argued that the appearance of the Galaxy is due to the fact that the Sun is located within a "flat layer" of stars (Wright 1750). He imagined this as a vast flattened ring of stars, in orbit about an unknown, hidden body at its centre (an "*incognitum*"). Wright also imagined the Milky Way as a great whirlpool ("*Vortex Magnus*"). Kant (1755) built upon Wright's work, and conjectured that the Sun is embedded in a rotating *disc* of stars held together by gravity, which formed, much like the Solar system, from a spinning nebula (the well known "nebular hypothesis"). Kant went further to suggest that the faint nebulous bodies known at the time are distant stellar systems, arranged, like the Milky Way, in discs – an argument which he based on their regular, oval appearance. It was later that von Humboldt (1850) would coin the concept of "*Weltinsel*", meaning "island world" or "island universe", a term attributed to Kant, which would stick until the 1930's.

The advent of photography made it possible to study the features of these "spiral nebulae" in much more detail, and early classification systems soon appeared (Wolf 1908; Curtis 1918; Jeans 1919). The understanding of our own Galaxy too was evolving away from a heliocentric picture (e.g., the "Kapteyn Universe" – Kapteyn & van Rhijn 1920 Kapteyn 1922). By studying the distribution of, and distances to, globular clusters in the Milky Way, Harlow Shapley concluded, correctly, that the Sun is located in the outer parts of the Milky Way's disc, while the centre of the Galaxy is in the direction of the *Sagittarius* constellation (Shapley & Swope 1924; Shapley 1928). However, the question of whether the "nebulae" were part of our own Galaxy, or indeed extra-galactic, was still unresolved.

The American astronomer Vesto Melvin Slipher measured radial velocities of nearby spiral nebulae, and found that most were receding from us, with much larger relative velocities than those of nearby stars (Slipher 1913, 1917). Using the relationship between the pulsation period and absolute luminosity of Cepheid variable stars (Leavitt 1908; see also Shapley 1914), Edwin Hubble later measured distances to M31 and M33[1] (Hubble 1925). These studies would consolidate the hypothesis that some of the "nebulae" were indeed

---

[1]Hubble's measured distance of ≈ 285 kpc (to both galaxies) was actually an underestimate by a factor of $\sim$ 2-3.

extragalactic stellar systems. The notion of other galaxies, external to the Milky Way, and receding from us in all directions in proportion to their distance (Hubble 1929), lent support to the emerging theories of a dynamic (as opposed to previously-thought steady-state), expanding Universe (de Sitter 1917; Friedmann 1922; Lundmark 1924; Lemaître 1927; Robertson 1929). The implications were profound: the Universe, and galaxies within it, would have had to form at a distant time in the past, and *evolve* to the present epoch. Much of modern extragalactic astrophysics has since focussed on understanding how this happens, and a powerful method to characterise many aspects of a galaxy's evolutionary processes is the study of its *structure*.

Galaxy Structure

The structural composition of a galaxy is one of its fundamental characteristics, as it carries the imprints of its merger history, dynamics, age, stellar and gas content, environment, star formation history, and central black hole mass.

The modern galaxy structural classification systems are broadly based on the early schemes outlined by James Jeans (Jeans 1919, 1929) and elaborated by Hubble (Hubble 1926, 1936), in which galaxies were arranged, based on their apparent morphology, along a sequence shaped like a tuning fork. Elliptical, or "early-type" galaxies occupy the handle, and are grouped in order of increasing ellipticity towards the bifurcation point, which is marked by the transition class of lenticular, or S0 galaxies. From this juncture, the spiral, or "late-type" galaxies branch into two parallel sub-sequences (the prongs of the tuning fork) – normal and barred spirals – arranged in order of decreasing bulge-to-disc ratio and/or increasing spiral arm pitch angle (these concepts will become clearer in §1.1.2).

The Hubble-Jeans sequence has been revised, expanded and refined over the years (Sandage 1961; de Vaucouleurs 1959; de Vaucouleurs et al. 1991; Sandage & Bedke 1994; Buta et al. 2015), to include dwarf and irregular galaxies as well as additional morphological features, and sub-divisions according to their "stage" along the sequence, their "family" (e.g., non-barred – SA, intermediate – SAB, or barred – SB, disc galaxies), and their nuclear, or outer, "variety" (given by specific morphological features, such as rings, lenses, bar-lenses, etc. – see §1.1.2), as detailed in Buta et al. (2015). Although not intended to represent an *evolutionary* sequence (indeed, it has been since established that this is not the case), this classification system remains in use today, as a popular means

of representation of the immense structural diversity observed in the galaxy population. The notation and terminology of the modern classification systems (Buta et al. 2015) will be employed throughout the text.

Early-type Galaxies

The category of galaxies collectively referred to as "early-types" includes elliptical (E) and lenticular (S0) galaxies.

Elliptical Galaxies

Elliptical galaxies are among the most massive and luminous known stellar systems. They generally have red colours, old stars (typically K giants), and little star formation, cold gas ($\sim 1\%$, Knapp et al. 1985), and dust. They are characterised by a smooth light distribution with a radially declining profile very well described by the Sérsic (1963) function (Caon et al. 1993; D'Onofrio et al. 1994), which is given by:

$$I(R) = I_e \exp\left\{-b_n\left[\left(\frac{R}{R_e}\right)^{\frac{1}{n}} - 1\right]\right\},\tag{1.1}$$

where R_e is the effective, or "half-light", radius (as its name suggests, the isophotal radius enclosing 50% of the light), I_e is the intensity at the half-light radius, and n is the Sérsic index, which encapsulates how centrally concentrated the light becomes as $R \to 0$, and how gradually it declines at $R \to \infty$. The parameter b_n is not free but a function of n (a more detailed description of the analytical functions used to model galaxy light profiles is given in Chapter 5). As elliptical galaxies appear to lack an actual "edge"[2], it is common practice to use the half-light radius as their characteristic scale. Ellipticals display a range in Sérsic indices (roughly between 1 and $\sim7 - 8$) which correlate with their luminosity, such that the more luminous galaxies are also more concentrated (Caon et al. 1993; Young & Currie 1994; Prugniel & Simien 1997; Graham & Guzmán 2003; Ferrarese et al. 2006; Savorgnan 2016). These galaxies in fact obey a host of scaling relations between their structural parameters (I_e, R_e, n) and luminosity, as reviewed in Graham (2013).

From a dynamical point of view, the more luminous ellipticals are typically supported

---

[2]In Equation 1.1, the intensity declines asymptotically with radius, to infinity, so the light profile has no "edge".

by stellar velocity dispersion, and are believed to have a triaxial structure and sometimes "boxy" isophotes (Bender & Moellenhoff 1987), whereas their less luminous couterparts show increased levels of ordered motion of stars, specifically rotation, and hence have a more oblate structure with "discy" isophotes (Davies et al. 1983; Kormendy & Bender 1996). The velocity dispersion (σ) is therefore believed to be a fundamental global parameter of elliptical galaxies, which correlates with their dynamical mass, and thus luminosity, as $L \propto \sigma^{\alpha}$. The early form of this relation is the popular Faber–Jackson (Faber & Jackson 1976) relation, where α equals 4. However, several studies have shown strong evidence for variation in α, from ~ 2 for dwarf ellipticals (Davies et al. 1983), to ~ 5 for giant ellipticals (Schechter 1980; Malumuth & Kirshner 1981; see also Graham 2013). As we have seen above, the structural (I_e, R_e, n), and dynamical (σ), parameters of ellipticals correlate with the total luminosity. It is therefore natural that there exists a tight relation in the three-dimensional space defined by R_e, I_e[3] and σ, in the form of a so-called "fundamental plane" (Dressler et al. 1987; Djorgovski & Davis 1987; Faber et al. 1987). Recent measurements define this plane as $R_e \propto \sigma^{1.3} \, I_e^{-0.76}$ (Bernardi et al. 2007).

Lenticular Galaxies

Lenticular galaxies are systems with colours, sizes, gas content and star formation properties very similar to ellipticals (Caldwell et al. 1993). However, unlike the latter, S0s are dominated by a large-scale, rotationally-supported disc (lacking a spiral pattern), often with a sharply truncated surface brightness profile that thus defines an outer "edge" for these systems. S0 galaxies are structurally more complex than other early-type galaxies, having, in addition to the disc, a central spheroidal component, or "bulge", which typically accounts for $10 - 75\%$ of the galaxy light (Laurikainen et al. 2005, 2010). Other common components (in disc galaxies in general, as we shall expand on in §1.1.2) are stellar bars (present in $\sim 2/3$ of *all* disc galaxies; de Vaucouleurs 1963; Eskridge et al. 2000; Whyte et al. 2002; Barazza et al. 2008; Masters et al. 2011) and "ovals" or "lenses" (see Kormendy & Kennicutt 2004).

The presence or absence of a significant rotational component in E and S0 galaxies have led Emsellem et al. (2007), and the ATLAS[3D] team[4], to argue for a purely kinematic classification criterion of the early-type sequence. They advocate to divide this sequence

---

[3] As shown by Prugniel & Simien (1997), the third Sérsic parameter – the concentration (or Sérsic index) – also enters in this picture, as it correlates well with the residuals in the "fundamental plane".

[4] http://www-astro.physics.ox.ac.uk/atlas3d/

into slow and fast rotators, based on a quantitative parameter, λ_R, which encapsulates the relative (projected) stellar angular momentum per unit mass (see also Bertola & Capaccioli 1978; Bender & Nieto 1990). Thus, early-type galaxies can be classified as slow or fast rotators based on their λ_R value, with the transition line between the two classes being adopted as $0.31\sqrt{\epsilon}$, where ϵ is the ellipticity at the half-light radius. However, characterising a galaxy by a unique number (chosen as the value of the λ_R profile at R_e) may overly–simplify matters. A galaxy may be rotation-dominated at some scales and dispersion-dominated at others. The apparent continuum in kinematically measured disc sizes (Romanowsky & Fall 2012; Arnold et al. 2014), enforced by an observed photometric continuum of intermediate-scale discs, in "discy elliptical" (ES) galaxies (Liller 1966; Nieto et al. 1988; Simien & Michard 1990), is believed to account for a smooth transition across the early-type galaxy sequence, between E and S0 galaxies. Recognising the presence of intermediate-scale discs embedded in large-scale spheroidal components is important for the understanding of such early-type galaxies, having significant implications for the interpretation of black hole scaling relations (§1.2.3), as will be later shown in Chapter 6 via a study of the ES galaxy NGC 1271 (Walsh et al. 2015; Graham et al. 2016a).

Late-type Galaxies

The "late-type" sequence is comprised of disc galaxies with a recognisable spiral pattern, and is traditionally separated into non-barred, and barred, spirals (Hubble 1936; Sandage 1961; de Vaucouleurs et al. 1991). In contrast to early-type galaxies, spirals are much more gas-rich (e.g., $\sim 10 - 20\%$ of the baryonic mass of luminous spirals is in the form of neutral hydrogen; Blanton & Moustakas 2009), and hence actively star-forming and metal-rich. The bulk of star formation occurs in the disc, often resulting in significant levels of interstellar dust (Draine 2003), centrally concentrated and mainly distributed in the disc plane (noted as early as Curtis 1918). Dust can cause significant obscuration, by absorbing ultraviolet and optical light (especially when the disc is oriented close to edge-on), with re-emission in the infrared (Obrić et al. 2006). In addition to their discs, late-type galaxies exhibit a rich diversity and complex structures ranging from spheroid components, bars, X/Peanut–shaped features, ansae, rings, etc. The spiral galaxy (S) sequence is arranged according to the galaxy's stage, which is denoted as a, b, c, d, and m, with intermediary stages also defined (ab, bc, etc.). The stage of a late-type galaxy along the sequence is given by the appearance and pitch angle of the spiral arms, as well as by the relative prominence of the spheroidal component (the latter two are in fact physically

related quantities; Lin & Shu 1966; Davis et al. 2015).

Discs

The radial light distribution in discs is well approximated by an exponential model (Patterson 1940; de Vaucouleurs 1957; Freeman 1970) of the form:

$$I(R) = I_0 \exp\left(-\frac{R}{h}\right), \tag{1.2}$$

where $I_0 \equiv I(0)$ is the central intensity, and h is the exponential scale length of the disc. Galactic discs usually extend out to roughly 3 to 5 times h (van der Kruit 1987, 2001), where it had initially been thought that their surface brightness profile truncates, rather sharply. A number of recent studies, however, have shown that only $\sim 56\%$ of discs display a truncation, which can be more or less sharp (Pohlen et al. 2004; Pohlen & Trujillo 2006), while $\sim 24\%$ of discs have an up-turn (or anti-truncation), with a shallower slope (Erwin et al. 2005). From the remainder, $\sim 10\%$ of discs show no break at all (some extending up to 10 times h, e.g. Bland-Hawthorn et al. 2005; see also Barton & Thompson 1997; Weiner et al. 2001), while the rest have more complicated surface brightness profiles (Pohlen & Trujillo 2006). The gas component usually extends beyond the stellar component, up to twice the break radius (Swaters et al. 2002), and star formation may also occur in these outer parts (Gil de Paz et al. 2005; Thilker et al. 2007; Christlein & Zaritsky 2008).

Galaxy discs are dynamically supported by rotation. The stars and gas have approximately circular orbits, and rotate differentially with increasing radius from the centre. The rotation curve, expressed as the circular velocity[5] as a function of radius, $v_c(R)$, can be probed beyond the stellar disc via emission at 21 cm due to the HI hyperfine transition. Empirically, rotation curves do not display a Keplerian decline, but rather reach a peak value and flatten in the outskirts, indicating that galaxies have larger dynamical masses than their baryonic content[6]. The maximum circular speed is famously known to correlate with the galaxy's total luminosity via the Tully–Fisher (Tully & Fisher 1977) relation, which is expressed as $v_{c,\mathrm{max}} \propto L^\alpha$, with the most recent measurements (differing due to various systematics, see Strauss & Willick 1995) in the range $\alpha \sim 0.27 - 0.35 \pm 0.15 - 0.4$

---

[5]The circular velocity, $v_c(R)$, is the velocity that a test particle in a galaxy's potential would have if it were on a circular orbit of radius R.

[6]This was among the first lines of evidence for what is now known as *dark matter* (e.g., Bosma 1978; Rubin et al. 1980).

mag (Verheijen 2001; Kannappan et al. 2002; Masters et al. 2006; Courteau et al. 2007).

Spiral arms are characteristic features of late-type galaxy discs. They distort the exponential profile of the disc by inducing "bumps" and/or "troughs" (Erwin 2005). The winding strength, or pitch angle ($\phi_{\rm spir}$), of the spiral arms is one criterion for defining their morphological type, such that Sa – Sab spirals have tightly-wound spiral arms, while the most late-type spirals (Sd, Sm) have very loosely wound spiral arms (high pitch angles). More luminous spirals tend to have more obvious and well-defined spiral arms across the entire azimuthal range of the disc (these are the so-called "grand-design" spirals), while in less luminous discs the spiral pattern is less-well defined and it is hard to discern the number of spiral arms (these are known as "flocculent" spirals).

Bulges

Although pure discs are known to exist (see Kautsch 2009, and references within), most spiral galaxies have additional structural components, most commonly a central "bulge". Bulges become apparent as excess light above the exponential disc extrapolation to the centre of the galaxy. A "classical bulge", or "spheroid", is a red, smooth, Sérsic component, dynamically dominated by stellar velocity dispersion, and believed to be the product of the galaxy's merger history (see §1.2.2). Spheroids are thus similar in many ways to the more massive elliptical galaxies. The relative prominence of the bulge in a spiral galaxy is one of the criteria for determining its morphological class. Spirals have a continuum of spheroid structural properties along the late-type sequence, with spheroid-to-total flux ratios (ranging from $\sim$75% to 0), and Sérsic indices (Graham 2001; Graham & Worley 2008; Gadotti 2009), decreasing from early-type spirals (Sa, Sb) to later-type spirals (Sd, Sm). Many authors identify a separate class of bulges known as "pseudobulges" (see the review by Kormendy & Kennicutt 2004 and references therein), also termed "disc-like" bulges, (Athanassoula 2005). Unlike the classical spheroids, pseudobulges tend to be more oblate, have approximately exponential light profiles, and their dynamics show significant rotation (Kormendy & Illingworth 1982; Kormendy & Kennicutt 2004). Pseudobulges are more likely to occur in later-type spirals and have a separate formation channel than classical bulges, resulting from the secular evolution of the host disc (§1.2.2). Many galaxy bulges may be a combination between a merger-assembled component (classical bulge) and a younger, secular component (pseudobulge) (Norman et al. 1996; Ganda et al. 2006; Seidel et al. 2015).

Bars

A galactic bar is an elongated, triaxial stellar structure which crosses the galaxy centre and rotates roughly as a solid body within the disc (Sellwood & Wilkinson 1993; Buta 1996; Knapen 2010). Bars are ubiquitous structures, occuring in more than two thirds of disc galaxies (de Vaucouleurs 1963; Eskridge et al. 2000; Whyte et al. 2002; Barazza et al. 2008; Masters et al. 2011). Numerical simulations (Hohl 1971; Combes et al. 1990) have shown that differentially rotating discs are unstable to forming bars (a mechanism elucidated theoretically by Toomre 1981 – see §1.2.2), which can appear spontaneously in N-body discs but develop even more efficiently if the galaxy interacts gravitationally with a nearby companion (Berentzen et al. 2004; Athanassoula 2005). When present, bars can accout for $2 - 20\%$ of a galaxy's total flux (Elmegreen & Elmegreen 1985; Gadotti 2009). As shown by Barazza et al. (2008), bars are more likely to occur in bluer (later type) spirals (Sb, Sbc, etc.), but are stronger and more extended in redder lenticular galaxies and earlier type spirals (Sa, Sab) (Erwin 2005; Erwin et al. 2005). The "strength" of a bar is typically quantified from the shape of its isophotes, and is proportional to their axis ratio, or ellipticity (ϵ). As pointed out by Athanassoula et al. (1990), bars are not purely elliptical, but show a rather obround shape, which is additionally taken into account in most photometric bar strength estimators (e.g., Athanassoula 1992; Martin 1995; Aguerri et al. 1998). Other studies have also used gravitational torque as a measure of bar strength (Combes & Sanders 1981; Buta & Block 2001; Laurikainen & Salo 2002).

When viewed in an edge-on disc orientation, and side-on bar orientation, many barred galaxies display a characteristic bi-lobed structure within roughly the inner half of the bar. First noted by Burbidge & Burbidge (1959), these structures are referred to as "boxy", or "peanut", or "X-shaped" bulges (Figure 1.1 displays an example), although extensive studies based on numerical simulations (Combes et al. 1990; Raha et al. 1991; Merritt & Sellwood 1994) and observations (Shaw 1987; Kuijken & Merrifield 1995; Bureau & Freeman 1999; Erwin & Debattista 2016) have shown that unlike bulges, these are not distinct structural components, but rather the inner regions of bars[7]. To avoid any confusion with galaxy spheroids or boxy elliptical galaxies, these features are referred throughout this text as X/Peanut (X/P) structures. They are believed develop as a result of a buckling

---

[7]Note, however, that it is theoretically possible to have peanut-looking structures in galaxies *without* a bar, as pointed out by Patsis et al. (2002).
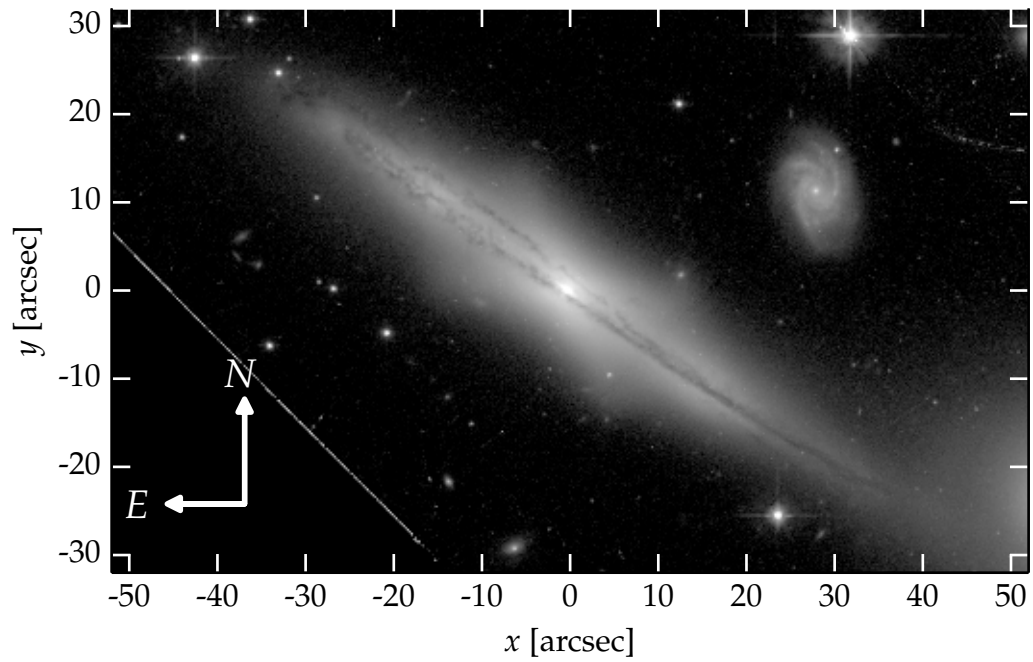
Figure 1.1 – A *Hubble* Space Telecope image of the edge-on galaxy *ESO 597-G036*, taken with the $WFPC2$ camera ($F814W$ filter). The disc is viewed close to edge-on, and shows clear dust lanes, while the central region shows a prominent X-shaped structure.

(bending) instability of the bar in the vertical direction (perpendicular to the plane of the disc), which leads to the X/peanut shape when viewed edge-on. In face-on orientation, X/P structures have the appearance of a "barlens" (Laurikainen et al. 2014; Athanassoula et al. 2015), which is a lens-like structure embedded in a bar (Laurikainen et al. 2011). A significant amount of this thesis is devoted to the quantitative study of X/P structures. Chapter 3 introduces a method for the identification and characterisation of X/P structures from photometric data alone, applying the principle to a sample of twelve nearby galaxies known to host peanut structures. In Chapter 4, this framework is employed to examine the X/P–shaped structure in the Milky Way, comparing its properties with those in other galaxies, and also constraining the size and orientation of the Galactic bar which, as we shall see in the following Section, is currently the object of conflicting interpretations in the literature.

The Milky Way Galaxy

The Milky Way, or the Galaxy, is believed to be a typical spiral galaxy in terms of its mass, size and morphology. It is classified as a barred, intermediate stage (Sb or Sbc), galaxy (Hodge 1983; Kennicutt 2001), with a total stellar mass of $M_\star = 5 \pm 1 \times 10^{10} M_\odot$ (see the review by Bland-Hawthorn & Gerhard 2016).

The majority of its stars, including the Sun, are distributed in a flat disc, and rotate about the Galactic Centre in roughly circular orbits. The Sun is located at a distance $R_0 = 8.2 \pm 0.1$ kpc from the Galactic Centre (Bland-Hawthorn & Gerhard, 2016), and has a small vertical offset from the disc mid-plane ($z_0 = 25 \pm 5$ pc; Jurić et al. 2008). At the solar radius the circular speed is $\sim 220 - 240$ km s^{-1}, which roughly equals the peak value of the Galaxy's rotation curve (Schönrich 2012; Bland-Hawthorn & Gerhard 2016). Observations of the vertical distribution of stars in the disc have revealed the presence of a distinct, and more vertically extended (roughly 4 times in scale height), "thick" disc component superposed on the main "thin" disc (Gilmore & Reid 1983). The thick disc is chemically distinct from, and comprised of older stellar populations than, the thin couterpart (e.g., Bensby 2014; Hawkins et al. 2015). Yoachim & Dalcanton (2006) have found many similar examples in nearby edge-on galaxies, and Comerón et al. (2012) report that the thin and thick components have comparable radial scale *lengths*, based on near-infrared studies of S^{4}G (*Spitzer* Survey of Stellar Structure in Galaxies[8], Sheth et al.

---

[8] http://irsa.ipac.caltech.edu/data/SPITZER/S4G/

2010) galaxies. For the Milky Way, the scale length(s) are difficult to measure due to our location inside the disc, but the literature estimates appear to converge on $h \approx 2.5 - 2.7$ kpc, in the infrared and optical (Licquia & Newman 2016). The more extended gas disc is discussed in Kalberla & Dedes (2008).

Although the disc properties have been constrained to a reasonable degree of accuracy, it is a different matter altogether in the case of the dominant structural components in the Galaxy's inner $\sim 4 - 5$ kpc, namely the bar and "bulge". From the Sun's vantage point, this complex central region, roughly in the direction of the *Sagittarius* constellation, is discernible in Figure 1.2 (at the centre) as the reddish component bulging outside of the bluer disc plane. The nature, intrinsic size, and relative orientation, of the bulge and bar are still subject to conflicting interpretations and debate.

Figure 1.2 – A composite infrared image of the Milky Way from 2MASS (Two-Micron All-Sky Survey), showing the blueish stellar disc, which contains copious amounts of dust (orange), mainly in the mid-plane. Towards the centre of the image, the X/peanut-shaped structure becomes apparent as a reddish feature bulging outside the disc plane. Image credit: 2MASS/J. Carpenter, T. H. Jarrett & R. Hurt

It has long been recognised that the Galaxy hosts a bar, traditionally believed to be roughly 3 kpc in radius and oriented at an angle $\alpha \approx 20 - 30°$ (though values vary considerably in the literature) with respect to our line-of-sight to the Galactic Centre (see the review articles by Gerhard 2002 and Merrifield 2004). This picture changed somewhat after the discovery of a longer bar ($\sim 4 - 5$ kpc), vertically thinner than the "bulge", and oriented at $\alpha \sim 40 - 45°$ (Hammersley et al. 1994). This structure was subsequently confirmed and studied in a series of papers (Hammersley et al. 2000; López-Corredoira et al. 2001, 2007; Cabrera-Lavers et al. 2007, 2008), leading to the hypothesis that the long bar is distinct from, and misaligned with, the triaxial "bulge" of the Galaxy.

To complicate matters, the nature of the "bulge" itself is also unclear, and it is disputed whether it is a classical bulge, a pseudobulge or neither. However, the COBE (COsmic

Background Explorer) satellite revealed for the first time, trough the Diffuse InfraRed Background Experiment (DIRBE), that the "bulge" region is distincly X/peanut–shaped (Weiland et al. 1994; Dwek et al. 1995). The X/P structure was later confirmed in 2MASS (Two-Micron All-Sky Survey; Skrutskie et al. 2006), and follow-up star count and stellar population studies (McWilliam & Zoccali 2010; Ness et al. 2012; Di Matteo 2016) have shown that most stars in the "bulge" region are associated with the X/P structure, and originate from the stellar disc (though a classical, merger-built component to the "bulge" is not ruled out). In a recent study, Wegg et al. 2015 have sought to reconcile the apparent mis-alignment between the long bar and the (X/P) "bulge", arguing (as we have discussed in §1.1.2), that the two are parts of the same structure (see also Gerhard & Martinez-Valpuesta 2012). Nevertheless, a convincing resolution to this problem has yet to be presented. Chapter 4 of this thesis is devoted to investigating the (bar+"bulge") geometry, from the X/P structure perspective.

In addition to the structural components discussed above, the Milky Way also hosts small-scale nuclear structures. The Galaxy displays a nuclear disc, detected in star counts and COBE data, with a break radius of ≈ 90 pc, beyond which its light declines steeply until its edge, at ~ 230 pc (Launhardt et al. 2002; Nishiyama et al. 2013). Also present in the Milky Way is a nuclear star cluster with effective radius (in the *Spitzer*/IRAC 4.5 μm filter) of $R_e = 4.2 \pm 0.4$ pc (Schödel et al. 2014). The centre region of the Galaxy harbours a supermassive black hole, with a dynamically measured mass based on gas cloud motions in the infrared, stellar proper motions in the nuclear star cluster region, adaptive optics astrometry and orbit fitting of the black hole's closest orbiting stars (Lacy et al. 1980; Eckart & Genzel 1997; Ghez et al. 1998; Ghez et al. 2008; Gillessen et al. 2009). The most recent measurements provide a black hole mass of $M_\bullet = 4.2 - 4.3 \times 10^6 M_\odot$.

Measures of Structure

Several techniques have been developed throughout the years to extract quantitative structural information from galaxy imaging and spectroscopic data. Among these there are global non-parametric methods such as CAS (concentration, asymmetry, smoothness – Conselice 2003), and Gini/M_{20} (Abraham et al. 2003; Lotz et al. 2004, 2008), indices. These quantities are efficient for automated, broad classification (for example, Gini indices are quite adept at detecting galaxy mergers or interactions), and are particularly useful for high redshift galaxies (see Conselice 2014). A more detailed insight into the

inner structure and dynamics of a galaxy is provided by analysing stellar and gas kine-matics, traditionally measured via long-slit spectroscopy, and, more recently, through two-dimensional (2D) spatially-resolved kinematic maps (e.g., Bacon et al. 2001, 2010; Croom et al. 2012; Sánchez et al. 2012; Bundy et al. 2015). Perhaps the most com-mon and detailed quantitative technique for galaxy structural analysis is the modelling of its surface brightness distribution. Several methods fall under this category, including isophote–fitting and photometric decomposition. The former method is sensitive to radial gradients in a galaxy's light distribution (and can measure, e.g., triaxiality, bar strength), while the latter method models in detail each structural constituent in a parametric way, through empirically-determined analytical functions (e.g., Sérsic, exponential, Gaussian), and quantifies their spatial extent and integrated luminosity.

Global Indices

The CAS parameters (concentration, asymmetry, smoothness), discussed in Conselice (2003), are designed to capture various global (structural) characteristics of a galaxy in a non-parametric way. The concentration (C) parameter is typically expressed as a ratio of two isophotal radii which enclose different fractions of the galaxy total light (for ex-ample 80% and 20% of the total light: R_{80}/R_{20}). As its name suggests, C measures how centrally concentrated the light is in a galaxy, and is, unsurprisingly, strongly correlated with the Sérsic index n. The asymmetry (A) parameter is computed from the residual image resulting from subtracting a galaxy image rotated by 180° about the photocentre from the original image. A therefore measures the fraction of light within a galaxy's non-(azimuthally symmetric) components. Finally, the smoothness parameter (S) is an indicator of how smooth or clumpy a galaxy's light is. One computes S by smoothing a galaxy image, and subtracting the result from the original image[9]. The residual map is a measure of the level of clumpiness, of a spatial scale defined by the smoothing kernel. Taken together, the CAS indices provide a set of criteria for morphological differentiation between elliptical and spiral galaxies, and provide clues about, e.g., their environment, level of star formation, colour (Rix & Zaritsky 1995; Conselice et al. 2000).

A related set of global coefficients are the Gini/M_{20} indices. The Gini coefficient (G) quantifies the flux distribution among the pixels in an image, and it is a number in the range $0 \leq G \leq 1$, where for G = 0 the flux is equally distributed, while if G =1 the entire

---

[9]The technique is similar to unsharp masking (e.g., Malin & Zealey 1979; Malin et al. 1983; Erwin & Sparke 2003; Laurikainen et al. 2005)

flux is concentrated in a single pixel. The M_{20} parameter (Lotz et al. 2004) is the normalised, second order moment (relative to the photocentre) of the brightest pixels which together amount to 20% of a galaxy's total flux. This coefficient is akin to a concentration parameter, but does not require a *central* concentration (i.e., it is sensitive to bright on- or off-centre nuclei, spiral arms, bars, star clusters, etc.).

Kinematics

Spectroscopic data can provide a wealth of information pertaining to galaxy structure, complementing and relieving some of the biases which act in surface photometry (e.g., the degeneracy between inclination and intrinsic ellipticity in early-type galaxies – Rix & White 1990; Gerhard & Binney 1996). The line-of-sight velocity distribution acquired through long-slit spectroscopy has been extensively used to build rotation curves and velocity dispersion profiles in early-type galaxies (e.g. Davies et al. 1983; Franx et al. 1989; Graham et al. 1998). This type of data has helped to establish large-scale structural and dynamical properties, and scaling relations like the Faber-Jackson relation or the Fundamental Plane (§1.1.1). The line-of-sight velocity distribution allows one to identify rotationally-supported sub-structures such as embedded discs, or counter-rotating kinematically decoupled cores (Efstathiou et al. 1982; Bender 1988a; Franx & Illingworth 1988). In disc galaxies, Kuijken & Merrifield 1995 (see also Bureau & Freeman 1999) have shown that bars leave a characteristic signature in position-velocity diagrams, along the major axis of an edge-on galaxy. They further went on to show that edge-on galaxies with X/P structures, seen in the shapes of their isophotes, also host kinematically–identified bars, thus consolidating the link between the two non-axisymmetric structures. Another kinematical characteristic of X/P structures is cylindrical rotation (Kormendy & Illingworth 1982), i.e., a roughly constant rotation profile with increasing vertical distance from the disc plane.

The advent of integral field unit (IFU) spectrographs has made possible the acquisition of spatially resolved, 2D maps of stellar and gas kinematics across the faces of individual galaxies. To extract quantitative information from such kinematic maps, Krajnović et al. 2006 developed "kinemetry", a formalism designed to study the moments of line-of-sight velocity distributions, analogous to studying the harmonics of isophotes in surface photometry with galaxy images (this will become clearer below). Techniques such as kinemetry and measurements of specific angular momentum within the effective radius (λ_R, as de-

fined in Emsellem et al. 2007), applied to the ATLAS[3D] survey (Cappellari et al. 2011), have confirmed the duality (see §1.1.2) between luminous, boxy, triaxial early-types, and the fainter, discy, axisymmetric (oblate) early-types (Krajnović et al. 2011, 2013), and introduced a dynamical differentiation of early-type galaxies into slow and fast rotators (Cappellari et al. 2011). Furthermore, the continuum in disc sizes across the early-type galaxy sequence has motivated Cappellari et al. (2011) to propose a revision of the Hubble-Jeans "tuning fork" diagram, advocating the "ATLAS[3D] comb". It is worth noting that 2D line-of-sight velocity distribution maps also allow for the identification of X/P structures in barred disc galaxies viewed *face-on* (when the characteristic peanut shape may not be as obvious as in edge-on orientation), as shown in Debattista et al. (2005). This provides a complementary X/P identification criterion to the method presented in this thesis, in Chapter 3.

Surface Photometry and Galaxy Decomposition

A powerful method for characterising the stellar structure of a galaxy involves modelling the shape of its isophotes. The standard practice (Carter 1978; Jedrzejewski 1987a) is to fit (quasi-) ellipses, of incrementing semi-major axis from the photocentre, to the isophotes. Any deviations from pure ellipticity are expressed via a Fourier harmonic expansion, of the form:

$$I(\phi) = I_{\mathrm{ell}} + \sum_n \left[A_n \sin(n\phi) + B_n \cos(n\phi) \right], \qquad (1.3)$$

where I_{ell} is the average intensity of the pure ellipse fit to the isophote, and ϕ is the azimuthal canonical[10] co-ordinate. In this formalism, the geometric parameters of the isophotes are captured via the various Fourier moments in Equation 1.3. The most important are the centre position ($n = 1$), position angle and ellipticity ($n = 2$), and boxyness or discyness (both captured by the $B_4 \cos(4\phi)$ term, where boxy isophotes correspond to $B_4 < 0$ and discy to $B_4 > 0$. The fourth moment has been known for a long time to correlate with physical properties of elliptical galaxies (Carter 1987; Lauer 1985; Bender 1988b; Peletier et al. 1990; Nieto et al. 1991), while Aguerri et al. (1998) have shown how bars in disc galaxies can be quantified through the $n = 2$ mode.

This theory has been implemented in the popular IRAF[11] algorithm ELLIPSE (Jedrze-

---

[10]Measured from the centre of the ellipse, rather than from one of its foci.
[11]Image Reduction and Analysis Facility (`http://iraf.noao.edu`).

jewski 1987a) which, however, fails in the regime where deviations are greater than a few per cent, and/or in systems with high axis ratios, such as edge-on disc galaxies. This problem, which has impacted many studies over the past decades, by producing biased major axis light profiles and residual images marked by prominent artificial (usually cross-shaped) features, originates in the mathematical formulation, and is addressed in detail, solved, and tested in Chapter 2.

In multi-component systems, the gradients in the radial profiles of isophote parameters (ellipticity, position angle, B_4 coefficient, etc.), as well as the shape of the surface brightness profile (SBP), allow for the differentiation between the various constituent structural components, each dominating at different radial scales. In the one-dimensional (1D) photometric decomposition technique, the SBP is modelled as a sum of analytical functions, each corresponding to a single component (e.g., Andredakis et al. 1995; Moriondo et al. 1998; Prieto et al. 2001; Balcells et al. 2003; Graham & Worley 2008). This is a parametric approach: every function, empirically found to represent the component's radial light distribution, is defined by parameters (such as the Sérsic index n, or the exponential scale length h) which are adjusted on a case-by-case basis. Galaxy decomposition is thus a quantitative structural analysis technique which allows one to separate out and study in detail each component (size, individual luminosity, and fractional contribution to the galaxy's total flux), and determine structural scaling relations and correlations with the galaxy's physical properties (see Graham 2013 for a review).

A similar, and recently popular, approach involves modelling the galaxy image directly. In this technique, each component is modelled with the same parametric functions mentioned above, but expressed as a 2D surface brightness distribution, which is the two-dimensional analogue of the SBP. In addition, each component is additionally defined by a fixed minor-to-major axis ratio, position angle, and higher order Fourier terms. A number of software packages have been developed through the years for this purpose, e.g., GIM2D (Simard et al. 2002), BUDDA (de Souza et al. 2004), GALFIT (Peng et al. 2002, 2010), IMFIT (Erwin 2015), providing ever more flexibility in terms of computational time, and number and type of components. The image-fitting approach uses every pixel in the image in the minimsation process, and can easily handle misaligned, non-axisymmetric and off-centre components, all problematic aspects in the 1D approach. However, the image-fitting method typically fails to capture radial gradients in isophote parameters (which can occur even in single-component systems, where they are an important indication of

triaxiality – Mihalas & Binney 1981) due to having fixed geometric parameters for each component. In the latter respect, the 1D isophote-modelling approach is more appropriate. In practice, both 1D and 2D techniques present advantages as well as drawbacks, and some authors opt to use (elements of) both methods in their analyses (e.g., Laurikainen et al. 2005, 2011; Krajnović et al. 2013; Savorgnan & Graham 2016c). To address the lack of a publicly available program dedicated to the 1D decomposition technique and comparable in robustness and sophistication with the latest 2D codes, one such software package was developed and is presented in Chapter 5, along with an in-depth review of the decomposition of 1D galaxy light profiles.

The choice of what structural components one needs to include in a galaxy model is often a non-trivial exercise. Laurikainen et al. (2005) have convincingly demonstrated how the failure to model each structural component in a galaxy can lead to important biases. By accounting for the bar component in their decompositions of disc galaxies, they showed that previous studies which had ignored the bars led to significantly over-estimated bulge-to-total flux ratios in such galaxies. As shown in, e.g., Laurikainen et al. (2005, 2011), Savorgnan & Graham (2016c), it is important to use all available information in the data (these authors examined radial profiles of ellipticity, position angle, Fourier modes, as well as unsharp masks of the images) to identify, where possible, each structural component of a galaxy, before the decomposition process. One must obviously avoid increasing the number of free parameters of a model by adding unjustified components to it, with the sole purpose of reducing the residuals.

Galaxy Evolution

Galaxy formation and evolution is at present understood as a hierarchical process. In our current paradigm, galaxies grow their mass principally by merging with each other, while in the intervening time they undergo slow processes like quiescent star formation, stellar and gas accretion, and re-distribution of their matter and angular momentum, processes collectively termed "secular evolution".

Galaxy Mergers

Galaxy mergers are rapid and violent processes through which two, or more, progenitor galaxies collide and coalesce. Depending on the gas content of the progenitors, mergers

can be "wet" (gas-rich), "dry" (gas-poor), or mixed[12].

Dry mergers are in essence a collisionless (dissipationless) processes, in which the stellar mass of the remnant equals the sum of the stellar masses of the progenitors. Dynamically, the system undergoes violent relaxation (Lynden-Bell 1967; van Albada 1982), a process through which stars lose "memory" of their initial orbits due to the rapid variation of the gravitational potential as the merger unfolds, and settles into a dispersion-dominated spheroid, such as an elliptical galaxy or the classical bulge of a disc galaxy. Some ellipticals show low surface brightness ripples, shells and tidal streams disturbing their smooth light distribution, which are indicative of past mergers or interactions (Malin & Carter 1983; Malin et al. 1983; Athanassoula & Bosma 1985; Del Burgo et al. 2008).

In a wet merger, the gas in the system is compressed and driven to the centre, often leading to a burst in star formation, or "starburst" (Mihos et al. 1992; Cox et al. 2006). The remnant assumes again a spheroidal stellar distribution. In the early Universe, where galaxies were more gas-rich and dusty, wet mergers were more common, and are seen in infrared bands as luminous, and ultraluminous, infrared galaxies (Sanders & Mirabel 1996). Galaxy mergers are classed as major if the mass ratio of the progenitors is between 1:1 and ($\sim 3 - 4$):1, and minor if higher. Minor mergers are less violent, but more common (Bundy et al. 2009), processes in which the less massive progenitor typically becomes disrupted and eventually absorbed by the more massive companion.

Secular Evolution

Galaxy "secular" evolution is defined, in a general sense, as any internally and/or environmentally driven process that occurs gradually in a galaxy over long dynamical time scales, i.e., much longer than the system crossing time $t_{\mathrm{cross}} = r/v$, where r is the system's radial scale, and v is the characteristic orbital velocity. These processes include the steady accretion of gas and stars, *in situ* star formation, recurring spiral structure and radial mixing in discs, the formation, growth and buckling – via dynamical instabilities – of bars, and (pseudo)bulge formation and growth. From a dynamical point of view, secular evolution is summarised as the re-structuring of a galaxy through re-distribution of (externally acquired) angular momentum, in order to reach the lowest attainable en-

---

[12]A special case of a mixed merger type is a "damp" merger, where the system contains sufficient gas for star formation to be triggered, but insufficient to form globular clusters (Forbes et al. 2007).

ergy state (Kormendy 2013; Sellwood 2014). As such, secular processes are particularly relevant in disc systems.

Many galaxy discs display spectacular spiral patterns across their faces. Spiral arms are believed to be gravitationally-induced density waves in stellar discs, as first advanced by Lin & Shu (1964) and later supported observationally by numerous studies (e.g., Schweizer 1976; Visser 1980; Gnedin et al. 1995; Grosbøl et al. 2004; Chemin et al. 2006; Shetty et al. 2007; Zibetti et al. 2009). Simulations indicate that they are transient features, only persisting for a few disc rotations (Sellwood 2011). The increased gas density in spiral arms triggers star formation, observed through blue stars and dust lanes tracing these features. Spiral arms act to increase the velocity dispersion of stars in discs (a process often referred to as dynamical "heating"), and facilitate radial mixing within the disc (Sellwood 2014).

As noted in numerical simulations (Hohl 1971; Ostriker & Peebles 1973; Sparke & Sellwood 1987; Bournaud & Combes 2002), rotation-supported thin discs quickly become dynamically unstable, and develop symmetric two-arm spirals, which can form a straight and persistent bar in the inner regions, while the outer arms wind up and eventually dissolve in the disc. According to Toomre (1981), the bar is a "swing-amplified" mode, akin to a standing wave reflecting off the walls of a "cavity", which is defined by a harmonic-like (i.e., with a rising rotation curve) potential. Once formed, bars slow their rotation and grow in length via dynamical friction (e.g., Athanassoula & Misiriotis 2002). Bar formation and growth is accelerated by the presence of gas in the system (Sellwood 2014) and gravitational interactions with nearby companions (Berentzen et al. 2004; Athanassoula 2005). Observational studies indicate that bars may drive spiral density waves, though probably only in their growth phase (Buta et al. 2009).

After a bar has formed, it usually experiences a different instability which causes it to thicken vertically (outside the plane of the disc) in its central region, and assume a characteristic X/peanut shape when observed in an edge-on orientation of the disc and nearly side-on alignment of the bar (Figure 1.1). This process, believed to occur in a high fraction of barred galaxies (up to $\sim 87\%$ for S0–Sb types; Erwin & Debattista 2013), has been ascribed to orbital resonances between bar and disc stars, specifically at the inner Lindblad resonance radius (Combes & Sanders 1981; Pfenniger & Friedli 1991), and/or a vertical buckling instability of the bar (Raha et al. 1991; Martinez-Valpuesta & Shlosman 2004; Erwin & Debattista 2016). The secular evolution of peanuts mirrors that of

the bars from which they arise: as the bar grows in radius and slows down, the X/P structure follows suit (Athanassoula & Misiriotis 2002). This behaviour is consistent with the resonance point migrating outwards as the bar slows down, as pointed out by Quillen et al. (2014). If bars grow considerably in length, they may undergo a second buckling phase (Martinez-Valpuesta et al. 2006). As noted, the thickening does not occur across the entire length of the bar (Lütticke et al. 2000; Athanassoula 2005; Gadotti et al. 2007), but appears to be confined to roughly the inner half of the bar radius, as recent studies have shown (e.g., Laurikainen & Salo 2017; Erwin & Debattista 2017). This also seems to be the case for the Milky Way, which displays an X/P structure and a long, thin bar extending beyond it (§1.1.3). As is the case for bars, X/P structures may have their strength enhanced through interactions with nearby galaxies, specifically through "cannibalism" of small satellites (Binney & Petrou 1985).

Black Holes

An important breakthrough in our understanding of galaxy evolution has been the realisation that the majority of galaxies harbour supermassive black holes at their cores. The theoretical argument that high-redshift quasar demographics must map onto to the present-epoch black hole distribution (i.e., "dead quasars"; Soltan 1982; see also Rees 1984), implies that most present-day galaxies should host a supermassive black hole. Several key observations confirmed the existence of such black holes in external galaxies (through gravitational broadening of emission lines – Tanaka et al. 1995; and nuclear accretion disc dynamics – Miyoshi et al. 1995; Greenhill et al. 2003), and at the centre of the Milky Way (see §1.1.3), such that presently it is widely accepted that these astrophysical objects exist, in a more or less quiescent state, at the centres of most galaxies (Kormendy & Richstone 1995; Magorrian et al. 1998).

Despite their small (typically sub-parsec scale) gravitational sphere of influence (Peebles 1972), black holes are believed to play an important role in a galaxy's global evolution, through the active galactic nucleus (AGN) phenomenon, observed in many galaxies from radio wavelengths to X-rays, and often invoked in galaxy evolution models as a regulator of star formation (e.g., Croton et al. 2006). That black holes correlate with galaxy properties of spatial scales many orders of magnitude beyond their sphere of influence, has been firmly established through multiple scaling relations between black hole mass ($M_\bullet$) and large-scale galaxy structure (Graham 2016). In particular, strong correlations have

been found between $M_\bullet$ and various properties of the host spheroid (i.e., elliptical galaxy or the bulge of a disc galaxy), such as spheroid luminosity (e.g., Marconi & Hunt 2003; Savorgnan & Graham 2016c), stellar and dynamical mass (Magorrian et al. 1998; Häring & Rix 2004), stellar velocity dispersion (Ferrarese & Merritt 2000; Gültekin et al. 2009), or light concentration (Graham et al. 2001; Graham & Driver 2007; Savorgnan 2016). The more massive/luminous/centrally concentrated spheroids host more massive black holes. A somewhat related black hole scaling relation has been shown to occur in spiral galaxies, and couples black hole mass with the pitch angle of the spiral arms (Seigar et al. 2008; Berrier et al. 2013). As we have seen in §1.1.2, the prominence of the spheroid varies in tandem with the spiral arm pitch angle across the late-type galaxy sequence. As such, galaxies with more massive/luminous/centrally concentrated spheroids also tend to have more tightly–wound spiral arms and more massive black holes at their cores.

The nearly log-linear behaviour of the scaling relation between black hole mass and spheroid luminosity (L_{sph}), at least at the high-mass end, has been interpreted as evidence for co-evolution between black hole and host spheroid, i.e., a common growth mechanism. However, in a recent paper Graham & Scott (2013) notably pointed out that this relation, log-linear for giant elliptical galaxies, steepens and becomes nearly log-quadratic in less luminous systems (see also Savorgnan & Graham 2016c). Graham & Scott (2013) have argued that in the low-mass regime black holes grow faster than the spheroid due to (secular) gas-rich processes. At the high-mass end, both balck holes and bulges grow as a result of dry mergers (§1.2.1), which are additive processes for both the stellar masses and black hole masses of the progenitors, and the log-linear relation is recovered.

The low-mass end of these relations is currently a puzzling area, since there appears to be a dearth in black holes below a mass of $\approx 10^5 M_\odot$. Such objects are termed "intermediate-mass" black holes (IMBH), since they would bridge the "gap" between stellar-mass ($\lesssim 10^2 M_\odot$), and supermassive ($\gtrsim 10^5 M_\odot$), black holes. Despite their apparent scarcity, largely due to the inability of current instruments to resolve their gravitational sphere of influence (and thus obtain direct mass measurements), with only a handful of strong IMBH candidates to date (e.g., Farrell et al. 2009), there is mounting theoretical, and observational (indirect) support for their existence (Quinlan & Shapiro 1990; Madau & Rees 2001; Miller & Hamilton 2002; Gill et al. 2008; Reines et al. 2013; Graham & Scott 2013; Lemons et al. 2015; Ryu et al. 2016). IMBHs are important for galaxy–(black hole) co-evolution theory, as they may constitute the seeds of supermassive black holes

(Mezcua 2017). The formation of the latter is, presently, rather poorly understood, and theories invoke either a Population III star origin, direct collapse of pristine gas clouds in the early Universe, or nuclear star cluster core collapse (see Volonteri & Bellovary 2012), all forming roughly $10^3 - 10^5 M_\odot$ black hole seeds. Whether galaxies can harbour IMBHs at their cores is currently unclear, and this topic is approached in Chapter 6.

Thesis Outline

The aim of this thesis is to bring scientific contributions to several aspects pertaining to the secular evolution, and black hole co-evolution, of disc galaxies, through the quantitative characterisation of their stellar structure, at optical and near-infrared wavelengths. After developing two robust algorithms designed to analyse imaging data, a new framework is introduced to quantify X/peanut–shaped (X/P) structures in barred disc galaxies. X/P features are the product of buckling instabilities that occur throughout the lifetime of stellar bars in galaxies. They are common features, observed in a high fraction of disc galaxies of all morphological types – including our Milky Way – yet, to date, most studies of these distinctive structures have remained predominantly qualitative. The new framework developed here is demonstrated on a sample of twelve nearby galaxies, revealing structural scaling relations and discovering previously unknown, nested, X/P structures. The approach is further applied to the Milky Way, constraining the size and orientation of its bar and peanut structure. Finally, black hole scaling relations are explored, with a particular emphasis on intermediate-mass black holes. The latter are rare astrophysical objects which may be the precursors of supermassive black holes (SMBH). Confirming the existence, and characterising the environment, of intermediate-mass black holes, is important towards elucidating and constraining the formation of SMBH, which is at present still an open question. The thesis is further organised as follows.

In Chapter 2 (Ciambur 2015) I introduce a revised mathematical description of galaxy isophotes, which enables accurate modelling of galaxies with distinctly non-elliptical shapes. I implement this scheme as a new IRAF isophote fitting algorithm (ISOFIT), which I further test on a number of case-study galaxies that highlight its applicability, namely galaxies with edge-on discs, X/P structures, and highly complex isophotal structure (e.g., barlens galaxies viewed face-on). The formulation overcomes the often significant systematics occurring in the standard algorithm ELLIPSE (Jedrzejewski 1987a), and additionally allows the measurement of higher-order Fourier terms (Equation 1.3), i.e. beyond boxy-

ness/discyness. This provides the potential to study complex galaxy structures quantitatively, directly from photometric data.

In Chapter 3 (Ciambur & Graham 2016) I develop a quantitative framework for analysing X/peanut–shaped structures in edge-on disc galaxies, based on their isophotal structure. As previously suggested in Ciambur (2015), the higher[13] order $B_6 \cos(6\phi)$ term in the Fourier expansion of the isophotes (Equation 1.3), is employed as a tracer of X/P features. I define various structural parameters of peanuts, including their physical size in- and off-plane, and the *strength* of the X/P instability. The technique is demonstrated on a sample of twelve X/P galaxies, including the "archetypal" peanut in NGC 128 (Burbidge & Burbidge 1959). Finally, I explore structural scaling relations between various X/P parameters and their correlation with the host galaxy dynamics and disc size.

Chapter 4 (Ciambur et al. 2017) tackles the controversial topic of the nature, and geometry, of the Milky Way's dominant structures in the inner $\sim 4 - 5$ kpc, namely the "bulge" and "long bar". In contrast to the standard approach in the literature – which probes the three-dimensional stellar distribution, as traced by "red clump" giant stars (e.g., López-Corredoira et al. 2007; Wegg et al. 2015) – I instead quantify the properties of the Galaxy's X/peanut structure, and use this information to infer the size and orientation of the long bar. I use infrared imaging of the Milky Way, taken with the Wide-field Infrared Survey Explorer (Wise – Wright et al. 2010; Ness & Lang 2016), at 3.4 μm and 4.6 μm, a wavelength regime best suited to minimise dust obscuration effects in the Galactic mid-plane. In addition to constraining the (bar+peanut) geometry, I also gauge how the Milky Way's X/P structure fits into the scaling relations defined by external galaxies, as presented previously in Ciambur & Graham (2016).

Chapter 5 (Ciambur 2016) focuses on the 1D galaxy decomposition technique, and introduces a new software package (Profiler) developed to model surface brightness profiles of a broad range of galaxy morphological types. This chapter details the available parametric functions routinely used to model various structural components, such as spheroids, discs (at any inclination, and with possible breaks), bars, rings, resolved or unresolved nuclear components, etc., and provides an in-depth treatment of the convolution procedure with the instrumental point-spread-function[14]. I demonstrate the applicability

---

[13]The standard terms range from $n = 1$ to $n = 4$ (Equation 1.3) – see §1.1.4

[14]Every instrument has a diffraction limit to how well it can resolve point sources, and ground-based instruments suffer from additional blurring caused by atmospheric "seeing". The point-spread function

of this algorithm with three examples, namely a cored elliptical galaxy (NGC 3348), a nucleated dwarf galaxy (Pox 52) and an edge-on disc galaxy with nested bars and a truncated outer disc (NGC 2549).

Chapter 6 presents a collection of work that I have contributed to four articles, in the general theme of black hole scaling relations with galaxy structure. Specifically, in Graham et al. (2016a) we revisit the structural composition of the discy elliptical galaxy NGC 1271, addressing the purported "over-massive" black hole issue raised by Walsh et al. (2015). I extract and model this galaxy's light profile, revealing an intermediate-scale disc embedded within a luminous, and concentrated, large-scale spheroid, a model which relieves the claim that this galaxy is an outlier from black hole scaling relations. In Graham et al. (2016b) we reveal the barred nature of LEDA 87300, a dwarf spiral galaxy reported to host an intermediate-mass black hole (§1.2.3) at its core (Baldassare et al. 2015). I model this galaxy's structure and extract its bulge properties, placing it for the first time on the near-quadratic (black hole mass) – (spheroid stellar mass) diagram (Graham & Scott 2013). In Koliopanos et al. (2017), I quantify the structure of six additional late-type galaxies with suspected central black holes in the intermediate-mass range, and use the latest scaling relations between black hole mass and bulge luminosity, and concentration, to predict the masses of their black holes. Finally, in Webb et al. 2017, I investigate the structural properties of the host galaxy of ESO 243-49 HLX-1 (Farrell et al. 2009), an off-centre hyperluminous X–ray source that is one of the best intermediate-mass black hole candidates detected to date.

The thesis concludes with Chapter 7, where the main findings are summarised, and some final remarks are presented, together with an overview of the possible avenues this research may follow in the future.

(PSF) describes the blurring specific to each instrument, which is replicated in the model through a convolution operation.

2

Isophotal Structure

The quantitative analysis of a galaxy's two-dimensional light distribution – as it appears projected onto the plane of the sky – through surface photometry (§1.1.4), involves extracting structural information from the shape and brightness of galaxy isophotes. The first to formulate a mathematical description of realistic isophote shapes, in order to study (relatively simple) elliptical galaxies, was Carter (1978). In his scheme, a pure ellipse was initially fit to an isophote, which was subsequently "rectified" (circularised) and examined for deviations from perfect circularity, by performing a Fourier series expansion as a function of azimuthal angle (ϕ) along the isophote circumference (Equation 1.3). In this rather elegant description, the lower-order harmonics ($n \leq 4$) capture deviations from the initial isophote fit which correspond to geometric corrections to its centre (the $n = 1$ terms), the minor-to-major axis ratio (or ellipticity, ϵ) and position angle (the $n = 2$ cosine and sine terms, respectively), as well as how boxy or discy the isophote appears (a property captured by the $n = 4$ cosine term). As we have seen in Chapter 1, the amplitude of the latter harmonic, namely B_4 in Equation 1.3, correlates with (and can therefore quantify) structural and dynamical properties in early-type galaxies, such as whether they are oblate or triaxial, or whether they are dispersion- or rotation-dominated, etc. (Davies et al. 1983; Bender & Moellenhoff 1987; Kormendy & Bender 1996). Fitting such isophotes at progressively increasing radii from the photometric centre yields the galaxy's radial surface brightness profile (discussed in more detail in Chapter 5), and can reveal isophote twists, or ellipticity gradients, which are further indicators of triaxiality (Mihalas & Binney 1981), and possibly of additional structures which are not otherwise apparent, such as embedded discs, or bars.

This formalism has been implemented in the popular isophote-fitting algorithm called

Ellipse (Jedrzejewski 1987b), part of the STSDAS[1] software package. As its name suggests, Ellipse was designed to model chiefly elliptical galaxies, and has proved to be a powerful tool to perform surface photometry of objects with relatively low ellipticity ($\epsilon \lesssim 0.5$) and/or low-level deviations from purely elliptical isophotes (of the order of $\sim 1\%$). However, for galaxies with more complex isophotal structure than the above, Ellipse has been known to fail, often producing significant, and purely artificial, substructure in residual maps, as well as biased surface brightness profiles.

In this Chapter, the failure of Ellipse is identified to be caused by a major problem, overlooked for decades, in the isophote co-ordinate system employed by this algorithm. This problem is overcome here by re-formulating the mathematical description in Ellipse to allow for the correct and accurate modelling of any isophotal structure, extending the applicability of this program to multi-component, structurally complex, disc galaxies. In the revised scheme, the harmonic terms of quasi-elliptical isophotes are expressed as a function of the eccentric anomaly (rather than the previously used, but incorrect, polar angle), a natural angular co-ordinate for ellipses which is also frequently used in celestial dynamics. The formalism is implemented in a new software tool, based on Ellipse, and named Isofit. Finally, the solution is tested on multiple case-study galaxies, chosen to illustrate the potential for new science with Isofit, which include include disc galaxies viewed in edge-on projection, galaxies with bars, barlenses (Laurikainen et al. 2011), or X/Peanut–shaped structures (§1.1.2). In addition to generating unbiased surface brightness profiles, and capturing complex galaxy features with unprecedented accuracy, Isofit now provides harmonic coefficients beyond boxyness/discyness, and with this, the ability to study quantitatively the isophotal imprint of complicated stellar structures, as we shall expand on here, and in Chapters 3 and 4.

The remainder of this Chapter consists of the article *"Beyond Ellipse(s): Accurately Modelling the Isophotal Structure of Galaxies with* Isofit *and* Cmodel*"*, by B. C. Ciambur, as it appears in the Astrophysical Journal, Vol. 810, No. 2, ID. 120 (2015).

---

[1]The Space Telescope Science Data Analysis System (STSDAS) is a data reduction and analysis package included in the broader Image Reduction and Analysis Facility (IRAF), an extended astronomical software collection written and supported by the National Optical Astronomy Observatories in Tucson, Arizona (United States).

BEYOND ELLIPSE(S): ACCURATELY MODELING THE ISOPHOTAL STRUCTURE OF GALAXIES WITH *ISOFIT* AND *CMODEL*

B. C. Ciambur

Centre for Astrophysics and Supercomputing, Swinburne University of Technology, Hawthorn, VIC 3122, Australia; bciambur@swin.edu.au

ABSTRACT

This work introduces a new fitting formalism for isophotes that enables more accurate modeling of galaxies with non-elliptical shapes, such as disk galaxies viewed edge-on or galaxies with X-shaped/peanut bulges. Within this scheme, the angular parameter that defines quasi-elliptical isophotes is transformed from the commonly used, but inappropriate, polar coordinate to the "eccentric anomaly." This provides a superior description of deviations from ellipticity, better capturing the true isophotal shape. Furthermore, this makes it possible to accurately recover both the surface brightness profile, using the correct azimuthally averaged isophote, and the two-dimensional model of any galaxy: the hitherto ubiquitous, but artificial, cross-like features in residual images are completely removed. The formalism has been implemented into the Image Reduction and Analysis Facility tasks ELLIPSE and BMODEL to create the new tasks "ISOFIT," and "CMODEL." The new tools are demonstrated here with application to five galaxies, chosen to be representative case-studies for several areas where this technique makes it possible to gain new scientific insight. Specifically: properly quantifying boxy/disky isophotes via the fourth harmonic order in edge-on galaxies, quantifying X-shaped/peanut bulges, higher-order Fourier moments for modeling bars in disks, and complex isophote shapes. Higher order ($n > 4$) harmonics now become meaningful and may correlate with structural properties, as boxyness/diskyness is known to do. This work also illustrates how the accurate construction, and subtraction, of a model from a galaxy image facilitates the identification and recovery of overlapping sources such as globular clusters and the optical counterparts of X-ray sources.

Key words: galaxies: fundamental parameters – galaxies: photometry – galaxies: structure – techniques: image processing

1. INTRODUCTION

Galaxies come in a wide variety of shapes and sizes. Among the numerous efforts throughout the years to impose some order among their ever growing numbers, one particular classification scheme remains persistent to this day: grouping galaxies by their shape as it is seen at optical and infrared wavelengths. This is essentially a structural classification—while some galaxies, known as "late-type" on the Hubble/Jeans sequence (Jeans 1919, 1928; Hubble 1926), display disks, spiral arms, bars, and bulges, others are more relaxed systems, and are commonly referred to as "early-type," elliptical or lenticular galaxies. However, even "elliptical" galaxies are rarely truly elliptical. Their isophote shapes often deviate from pure ellipses, in a characteristic way. These deviations, the most common being referred to as "boxyness" or "diskyness," originate from the structure of the stellar orbits that make up the galaxy. Because of the physical link between isophote shape and galaxy (structural) properties, quantifying these deviations provides a valuable tool to study galaxies. Numerous works have revealed correlations between boxyness/diskyness and physical properties such as kinematics (Carter 1978, 1987; Davies et al. 1983; Lauer 1985; Bender 1988; Peletier et al. 1990; Jaffe et al. 1994), brightness profiles (Nieto et al. 1991), and even global radio and X-ray properties (Bender et al. 1989).

However, the formalism used in the past (and to this day) to describe boxyness/diskyness in isophotes has limited applicability. In particular, it is only efficient when applied to galaxy isophotes that are relatively well described by pure ellipses and the deviations from ellipticity are small (a few percent). This has limited isophotal structure studies to only a subsample of the whole galaxy population which met the above conditions, specifically elliptical or early-type galaxies. Even in such objects, the presence of, e.g., embedded disks caused the models to fail and produce residual maps marked by ubiquitous crosses or artificial features. The literature is literally full of such examples (e.g., Reda et al. 2004, 2005; Rothberg & Joseph 2004; Janowiecki et al. 2010; Chies-Santos et al. 2011; Peng et al. 2011; Alamo-Martínez et al. 2013; Capaccioli et al. 2015; Guérou et al. 2015, etc.). Moreover, some of the correlations (or lack thereof) have been affected by the use of a formalism that fails to adequately capture the true isophotal shapes.

In this work, a new isophote fitting formalism is introduced, which is capable of modeling galaxies with significantly more complex or exotic isophote structures, with a particular focus on disk galaxies viewed edge-on. The paper is structured as follows. Section 2 provides a short description of how deviations from perfect ellipticity are commonly expressed and modeled in the popular isophote analysis tool ELLIPSE. In Section 3, a new angular metric is introduced, which better expresses isophote shapes in general and is particularly powerful in modeling disk galaxies viewed edge-on, as well as galaxies with X-shaped/peanut bulges. The formalism is implemented and further demonstrated on a representative galaxy. Section 4 demonstrates the applicability of this formalism to any isophote shape, and explores scientific case-studies where this new technique can provide insight. In this section, four additional galaxies are modeled and the possibility of quantifying the peanut/X-shape bulge of some galaxies from their photometric structure is briefly explored. Finally, in Section 5, the paper reiterates its main conclusions and proposes further potential scientific applications of the method.
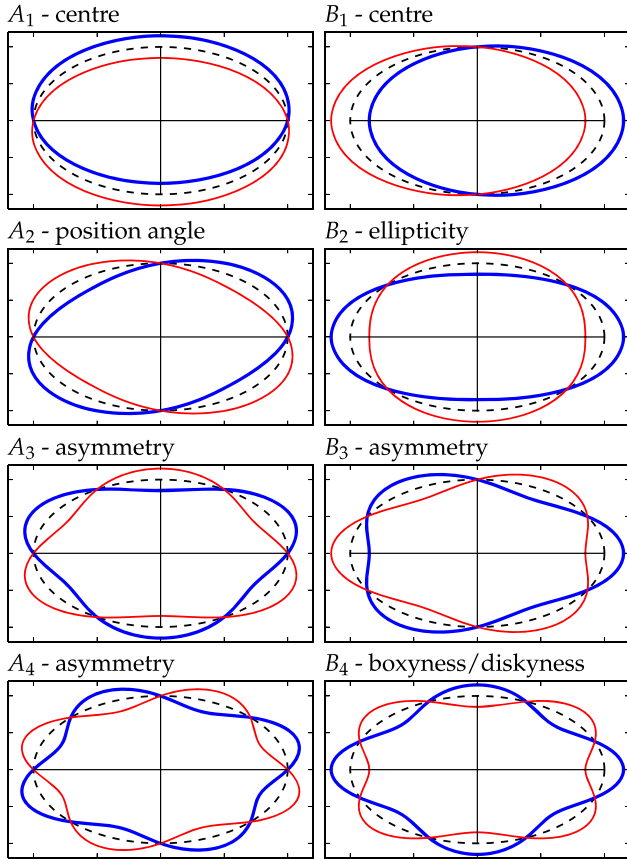
Figure 1. Physical significance of the first four harmonic corrections to an elliptical isophote. Positive coefficients are illustrated in blue (thick) while negative coefficients in red (thin). The reference isophote is plotted in black (dotted) in each panel.

2. ISOPHOTE FITTING

Among the early efforts to express departures from pure elliptical shapes in mathematical form, the work of Carter (1978) was to become key in modeling more refined and realistic galaxy isophotes. This work proposed adding perturbations to an ellipse as a function of azimuthal angle ϕ, in the same way as in a Fourier series decomposition

$$I(\phi) = \langle I_{\mathrm{ell}} \rangle + \sum_{n} \left[A_n \sin(n\phi) + B_n \cos(n\phi) \right], \qquad (1)$$

where $I(\phi)$ is the intensity profile along the isophote, expressed as a function of (central) azimuthal angle, $\langle I_{\mathrm{ell}} \rangle$ is the average intensity of the purely elliptical path, and the sum represents Fourier harmonic perturbations to $\langle I_{\mathrm{ell}} \rangle$, with n being the harmonic (integer) order. Note that perturbing the *intensity distribution* in this way is equivalent to distorting the *physical shape* of the isophote. The two cases are used interchangeably throughout for illustrative purposes.

This formalism is particularly elegant because the coefficients of the Fourier harmonics (A_n and B_n) carry physical meaning. This is illustrated in Figure 1 for the first four harmonic orders. Here we observe how the harmonics bring corrections to the ellipse's center ($n = 1$), the ellipticity, and position angle (PA) ($n = 2$), as well as capturing various types of asymmetries and the boxy or disky feature (the B_4 coefficient).

These principles were later detailed into a full isophote fitting algorithm in the seminal paper of Jedrzejewski (1987a; also in Jedrzejewski 1987b). The reader is referred to these works for detailed descriptions of the algorithm, which is only briefly outlined below. In this method, nested isophotes (not necessarily concentric) are fitted at several pre-defined points along the semimajor axis (denoted by a) of a galaxy in a CCD image. At each of these points, the isophote starts as a pure ellipse defined by initial guess-values for its geometric parameters, namely center position (x_0, y_0), PA, and ellipticity ($e = 1 - b/a$, where b is the semiminor axis). The image is then sampled along this elliptical path, giving the one-dimensional (1D) intensity distribution as a function of azimuthal angle $I_{\mathrm{data}}(\phi)$, which is first modeled by the right-hand side of Equation (1), but restricted to $n \in \{1, 2\}$, i.e.,

$$I(\phi) = \langle I_{\mathrm{ell}} \rangle + \sum_{n=1}^{2} \left[A_n \sin(n\phi) + B_n \cos(n\phi) \right]. \qquad (2)$$

After a least-squares minimization of the quantity S in Equation (3), the best-fit values of the harmonic coefficients are used to update the geometric parameters of the ellipse, and then $\langle I_{\mathrm{ell}} \rangle$.

$$S = \sum_{i} \left[I_{\mathrm{data}}(\phi_i) - I(\phi_i) \right]^2. \qquad (3)$$

The minimization iterates until a minimum rms criterion is met. By only considering the first two harmonics (center, PA, and e), this section of the algorithm essentially computes the best-fitting pure ellipse on the data isophote corresponding to this semimajor axis radius. Finally, higher order harmonic perturbations to the ellipse ($n \geqslant 3$) are fitted (sequentially) through the same iterative minimization.

A powerful and robust implementation of this algorithm is in the Image Reduction and Analysis Facility (IRAF[1]) external software package ISOPHOTE, developed by the Space Telescope Science Data Analysis System[2] (STSDAS). The main tasks in this package (frequently referred to in the remainder of this work) are the isophote fitting task ELLIPSE, and the task BMODEL, which builds a two-dimensional (2D) galaxy model based on the parameters obtained by ELLIPSE. This software has had considerable success since its release, performing admirably when modeling the type of galaxies it was designed to work with, which are objcts characterized, in general, by relatively low ellipticity ($e \lesssim 0.5$) or, for higher e, with isophotes very close to elliptical (low harmonic amplitudes). These are typically early-type galaxies with no (or with rather face-on) disks. The ELLIPSE task also performs quite well when modeling (late-type) disk galaxies viewed face-on, after the appropriate masking of biasing features such as dust lanes.

However, for galaxies with more complex shapes or, in particular, for disk galaxies viewed at relatively high inclination or edge-on, ELLIPSE (and BMODEL) begin to break down and give rise to residual images marked by ubiquitous cross-like patterns or characteristic, alternating regions of excess and deficit light (see Sections 3.3 and 4).

Obviously, it is desirable to correctly model a galaxy's light distribution. A good model provides physical insight into the galaxy itself, but moreover, subtracting an accurate model from an image allows for the possibility to perform meaningful
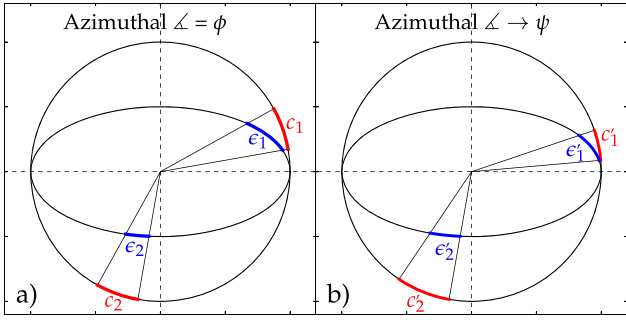
Figure 2. Panel (a): equal polar opening angles (ϕ) define equal arc lengths on a circle ($c_1 = c_2$) but not on an ellipse ($\epsilon_1 \neq \epsilon_2$). Panel (b): when the same opening angles are transformed to the "eccentric anomaly" (ψ), they change as a function of ϕ such that they define equal arc lengths on an ellipse ($\epsilon'_1 = \epsilon'_2$), but no longer on the circle ($c'_1 \neq c'_2$). ψ therefore samples an ellipse uniformly.

studies of substructures still remaining after the subtraction, such as star clusters, globular clusters (GCs), or optical counterparts to X-ray/radio sources. In the case of edge-on galaxies, a model where the light intensity is significantly underestimated along the major axis of the galaxy introduces errors in the surface brightness profile, which is typically measured (and in fact output by ELLIPSE) along a, and is one of the main quantities of interest provided by isophote fitting programs. The surface brightness profile is essential in galaxy decomposition and is routinely used to quantify galaxy components and characterize structural scaling relations (see the review article of Graham 2013 and the references therein).

3. A NATURAL ANGULAR METRIC

The reason why isophote-fitting algorithms like ELLIPSE fail in the regime of high e and high harmonic amplitudes is traced back to the incorrect manner in which a quasi-elliptical isophote path is parameterized and sampled. The task ELLIPSE splits the isophote into sectors as it would a circle: it divides the azimuthal range ($\phi \in [0; 2\pi]$) uniformly, in equal bins. While the sectors (arc lengths) corresponding to equal steps in ϕ are all equal for a circle, they are not for an ellipse, but are actually longest along the major axis and shortest along the minor axis (see Figure 2, left panel). This causes the isophote to be too coarsely sampled along a (in the case of edge-on galaxies, a corresponds to the plane of the disk, and thus needs to be very finely sampled as it contains most of the light), which then leads to bright streaks in residual images.

3.1. The Eccentric Anomaly

This work introduces a new isophote fitting formalism implemented in a new IRAF task ISOFIT, where the Fourier harmonics that quantify deviations from perfect ellipses are expressed as a function of an angular parameter more natural to elliptical shapes, namely the "eccentric anomaly," henceforth denoted by ψ. The eccentric anomaly is frequently used in celestial mechanics to describe the position of a point orbiting on an elliptical path, in canonical form (i.e., where the angle is defined from the orbit center, not from one focus), or more generally to express the parametric equation of an ellipse. It is the "natural" angular coordinate for ellipses, and the ψ coordinate of a point on an ellipse is in fact related to its azimuthal/plane-polar angular coordinate (denoted as ϕ throughout this paper) through the ellipticity $e \equiv 1 - b/a$,
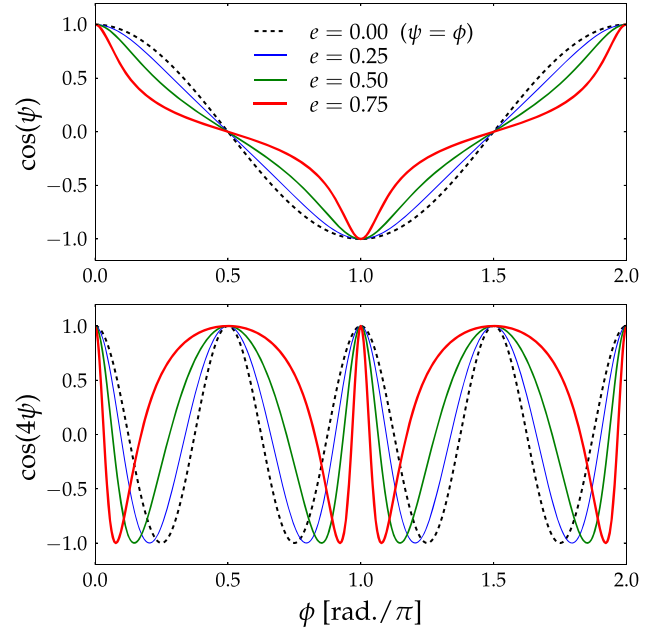

Figure 3. Top: the cosine of the "eccentric anomaly" ψ, for different values of ellipticity (e) plotted against the polar angle ϕ. The amplitude of this harmonic (B_1 in Figure 1) controls the center position of the isophote. Bottom: the cosine of 4ψ, for the same values of e as in the top panel. The amplitude of this harmonic (B_4 in Figure 1) controls the boxyness/diskyness of the isophote.

such that

$$\psi = -\arctan\left(\frac{\tan(\phi)}{1 - e}\right). \tag{4}$$

By transforming from ϕ to ψ, the isophotes are sampled uniformly along the entire azimuthal range (Figure 2, right-hand panel), and the Fourier corrections are expressed as

$$I(\psi) = \langle I_{\rm ell} \rangle + \sum_n \left[A_n \sin(n\psi) + B_n \cos(n\psi)\right]. \tag{5}$$

Furthermore, the Fourier harmonics correct the isophotal shape quite differently. This is illustrated in Figure 3, where the top panel shows how the cosine form of ψ (which enters in Equation (5)) changes as the ellipticity changes from $e = 0$ ($\psi = \phi$) to high ellipticity. The bottom panel illustrates how the cosine part of the $n = 4$ harmonic (i.e., boxyness/diskyness) acts sharply at the major axis (defined to correspond to $\psi = 0$, 2π, and $\psi = \pi$) and more softly along the minor axis ($\psi = \pi/2$, and $\psi = 3\pi/2$), as the ellipticity increases. The more flattened (i.e., high e) an isophote, the sharper the harmonic correction around a and the softer the correction around b. This is precisely what is required, since a disk galaxy viewed edge-on has a very bright but thin disk dominating the light along a, while along and around the minor axis b the light is dominated by a spheroidal bulge. The lower panel in Figure 3 thus illustrates how the "lemon-shaped" contours in the lower-right panel of Figure 1 can be made more "pointy" along the major axis.

A concrete example of harmonic terms characterizing an isophote shape is given in Figure 4, which also highlights the difference between using the generic polar angle (ELLIPSE) and eccentric anomaly (ISOFIT) to express the Fourier corrections. Here we notice how the angle transformation ($\phi \rightarrow \psi$) makes the A_2 correction correspond more to a rotation (change in PA),
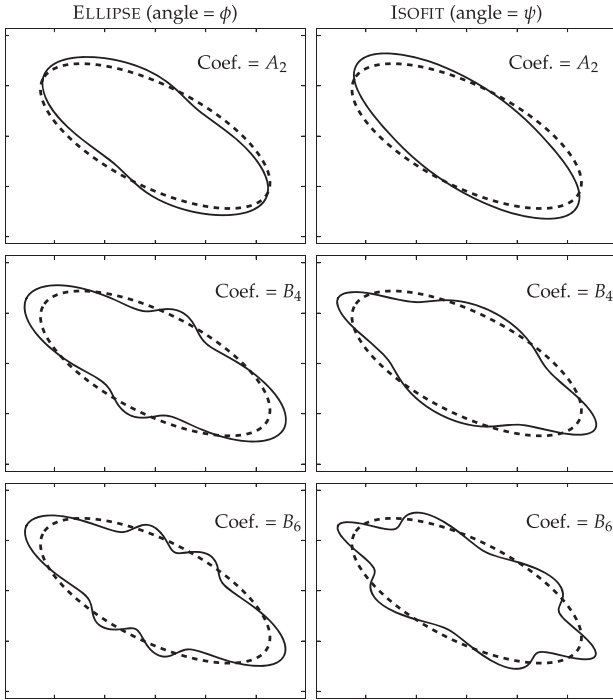
Figure 4. Examples of three harmonic corrections to an elliptical isophote, expressed as a function of polar angle ϕ (left panels) and in the new formalism (as a function of ψ; right panels), for values of $e = 0.65$ and $A_2 = B_4 = B_6 = 0.15$, chosen to be relatively high to clearly illustrate the effect. In every panel, the reference ellipse is displayed with a dashed line.

and the B_4 correction resemble more a disky, lemon- or diamond-shaped contour. The lower two panels show a higher ($n = 6$) harmonic, which may carry physical meaning in edge-on galaxies with so-called X-shaped or "peanut" bulges. This tentative point is further explored in Section 4.1 by modeling such a galaxy.

3.2. Implementation in IRAF

In order to model galaxy isophotes according to the formalism discussed in the previous section, the source code of the IRAF package Isophote was modified at the harmonic fitting level (Ellipse) and 2D galaxy model building (Bmodel). An angular parameter similar to the eccentric anomaly has been used in other galaxy-modeling codes, most notably in Galfit (Peng et al. 2010), where it takes a slightly different form (the Fourier formalism distorts the coordinate grid rather than the intensity distribution) and the authors consider only the cosine of the angle plus a phase in expressing the harmonics.

The Ellipse task was modified and renamed Isofit in order to differentiate the new formalism from the standard Ellipse. When fitting for the harmonic coefficients, Isofit now defines the isophotes as a function of the eccentric anomaly ψ by transforming the azimuthal angle ϕ according to Equation (4) and applying the appropriate sign correction to each angle quadrant. Additionally, all harmonic corrections of $n \geqslant 2$ are now added *simultaneously*, in contrast to Ellipse, which fitted $n > 2$ harmonics sequentially. By fitting the harmonics simultaneously, all orders contribute together to construct the isophote (just as in a Fourier decomposition), rather than each individual order being a "best-attempt" at capturing the dominant components of the galaxy light distribution. For

example, in the particular case when the dominant component is a bright, thin disk along the major axis (i.e., an edge-on galaxy), we have seen in Figure 1 and in Figure 4 (bottom two panels), and one can also deduce from Equation (1), that every even-n B_n harmonic provides a correction at the positions corresponding to a ($\psi = 0$ and $\psi = \pi$). Therefore, by fitting them sequentially each coefficient is optimized to best capture the disk feature rather than all orders contributing together to model less obvious features over the whole azimuthal range.

In Ellipse, the harmonics are chosen by the user and their number is technically unlimited. This same flexibility in terms of choice is kept in Isofit, though the simultaneous fitting does limit the number of useful harmonics. Nevertheless, in practice, the harmonic amplitude decreases with increasing n and usually asymptotes to zero for $n \sim$ 10–12 and above, even for extremely thin edge-on disks. Furthermore, in the majority of cases, odd-n harmonics bring little-to-no refinement to the isophote shapes (unless the galaxy has significant asymmetries), so by restricting the choice to only even orders, one can reliably fit harmonics up to $n = 12$ and obtain accurate models, as is demonstrated in Section 3.3 below.

In addition to Ellipse, the auxilliary task Bmodel ("build model") was modified and renamed Cmodel ("construct model"). The task Cmodel considers all harmonics included by the user (Bmodel only used $n \leqslant 4$) and generates a 2D model of the galaxy based on the fitting results output by Isofit. The harmonic corrections are applied as a function of ψ, which is obtained as before. In the regime $e \to 0$, the standard Ellipse result is recovered, since in this limit $\psi = \phi$.

3.3. Detailed Example in Practice: the Edge-on Galaxy ESO 243-49

The ideal test-cases, which best highlight the improvements brought by the formalism discussed in this work, are edge-on disk galaxies. These galaxies are characterized by diamond-like or lemon-like isophote shapes, which deviate strongly from pure ellipses. They are the objects for which the standard version of Ellipse gives the least accurate results in both 1D (systematically underestimated major-axis surface brightness profiles) and 2D (cross-like features in residual images).

The S0 galaxy ESO 243-49 was chosen as the test-case for the new tasks Isofit and Cmodel. This edge-on galaxy has been intensly studied following the discovery of a source of hyperluminous X-ray emission (referred to as HLX-1) associated with a potential intermediate-mass black hole within the galaxy but outside the nuclear region (Farrell et al. 2009; Webb et al. 2010). The fact that HLX-1 was found to have an optical counterpart (Soria et al. 2010) makes this galaxy particularly interesting to model, as one of the aims of this work is to achieve high-quality 2D galaxy models and, after subtracting them from the image data, to perform accurate photometry on the remaining substructure (such as HLX-1) left behind in the residual image. Additionally, ESO 243-49 also displays a relatively large number of star clusters both in the plane of the disk and outside, as well as a dust disk in the nucleus, also viewed edge-on. The image data for ESO 243-49 was retrieved from the Hubble Legacy Archive[3] and consisted of an *H*-band image taken with the Wide Field Camera 3 (WFC3, IR channel, *F*160*W* filter, PI: S. A. Farrell) on the *Hubble Space Telescope* (*HST*).
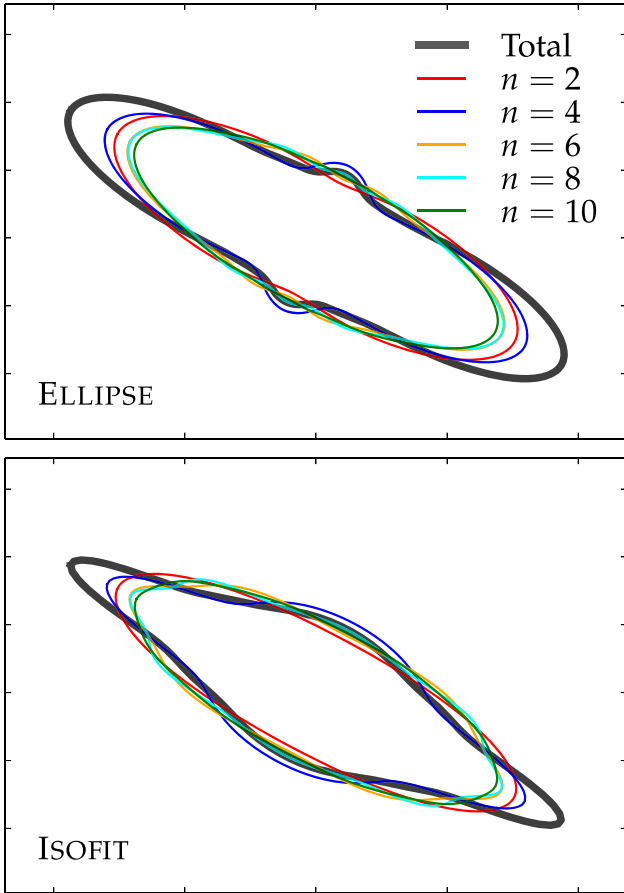
---

[3] http://hla.stsci.edu

Figure 5. Example of how an isophote of ESO 243-49 (thick black line) is constructed from several harmonic orders, with the standard $I(\phi)$ formalism (top) and the new $I(\psi)$ formalism (bottom). The different harmonic orders, denoted by n, refer to Equation (1) (top) and Equation (5) (bottom).

To fully showcase the improvements brought by the new formalism, the image was modeled first with the standard ELLIPSE/BMODEL and then with ISOFIT/CMODEL. Both versions were run, where applicable, with identical initial conditions.

3.3.1. Constructing the Isophotes

An important observation concerning the construction of each isophote is that, due to the use of the polar angle ϕ instead of ψ to define the isophote in ELLIPSE, the high-order ($n \gtrsim 4$) harmonics do very little to improve its shape (see Figure 4, bottom-left panel). This is in part why, generally, higher order harmonics have not been used in the literature and it has been assumed that they are not important. This is illustrated in the top panel of Figure 5, which shows a single isophote and its constituent *even* Fourier contributions for $2 \geqslant n \geqslant 10$. This isophote was constructed from the harmonic coefficients computed by ELLIPSE while modeling ESO 243-49. The bottom panel in Figure 5 displays an isophote constructed at the same semimajor axis, but with the new formalism of ISOFIT proposed in this work. Here we see how each upper harmonic order brings a new level of refinement to the final shape, as one expects in fact from a Fourier analysis. The ability of each of these corrections to describe the actual isophote shape (at this semimajor axis) in ESO 243-49 will become apparent in Section 3.3.3.
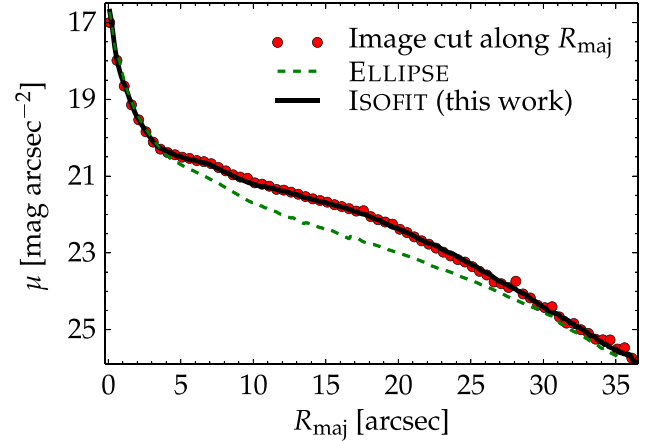

Figure 6. Major axis surface brightness profile of ESO 243-49. The standard ELLIPSE task systematically underestimates the profile in the range of 5–30 arcsec (where the disk dominates), by as much as a factor of two in surface brightness occurring at $R_{maj} = 16.5$ arcsec. See the lower panels of Figure 7 to understand this.

3.3.2. 1D Improvements

A very useful quantity routinely extracted from galaxy images with the use of isophote fitting tools is, of course, the surface brightness profile $\mu(R)$—the radial distribution of light in the galaxy. This quantity is frequently used when performing 1D structural decompositions (e.g., bulge/disk) of galaxies. Oftentimes, μ is measured along the major axis of the galaxy. For edge-on galaxies, this is precisely the locus where light is systematically underestimated when using improperly defined isophote shapes. In such cases (and the test-case ESO 243-49 is a prime example), one must resort to estimating $\mu(R)$ by taking a crude "cut" along the image major axis, which is undesirable for several reasons. First, this method is noisy, because of, e.g., dust, star clusters or foreground stars that happen to be located in the plane of the disk. Furthermore, when taking a cut, one obtains a single measurement of the brightness at each radial position, whereas by fitting the isophote, one obtains a value for the brightness at a given R, which is the average value across the whole azimuthal range. Second, a cut is a less accurate representation of the major axis surface brightness profile because, in general, the PA of the isophotes does not remain constant with increasing radius (the isophotes sometimes follow features such as bars; see Section 4.2), so a 1D cut capturing this effect must be a curve, not a line.

Figure 6 shows how the use of the old formalism in ELLIPSE systematically underestimates the major axis surface brightness profile of the test-case galaxy ESO 243-49, compared with a (constant PA) direct cut taken along the disk plane and assumed to be a more realistic approximation of the true $\mu(R_{maj})$. The discrepancy is most prominent across the range ($5 \lesssim R_{maj} \lesssim 30$ arcsec) where the disk light dominates. The formalism presented in this work does remarkably better and is the closest and most accurate representation of $\mu(R_{maj})$, for the reasons explained above. The discrepancy between the profiles computed with ELLIPSE and ISOFIT is maximal at $R_{maj} = 16.5$ arcsec, where ELLIPSE underestimates μ by 0.77 mag arcsec^{-2}, which is a factor of two in surface brightness.

Such a discrepancy propagates into the bulge/disk decompositions and leads to wrong results. Judging by the shape of
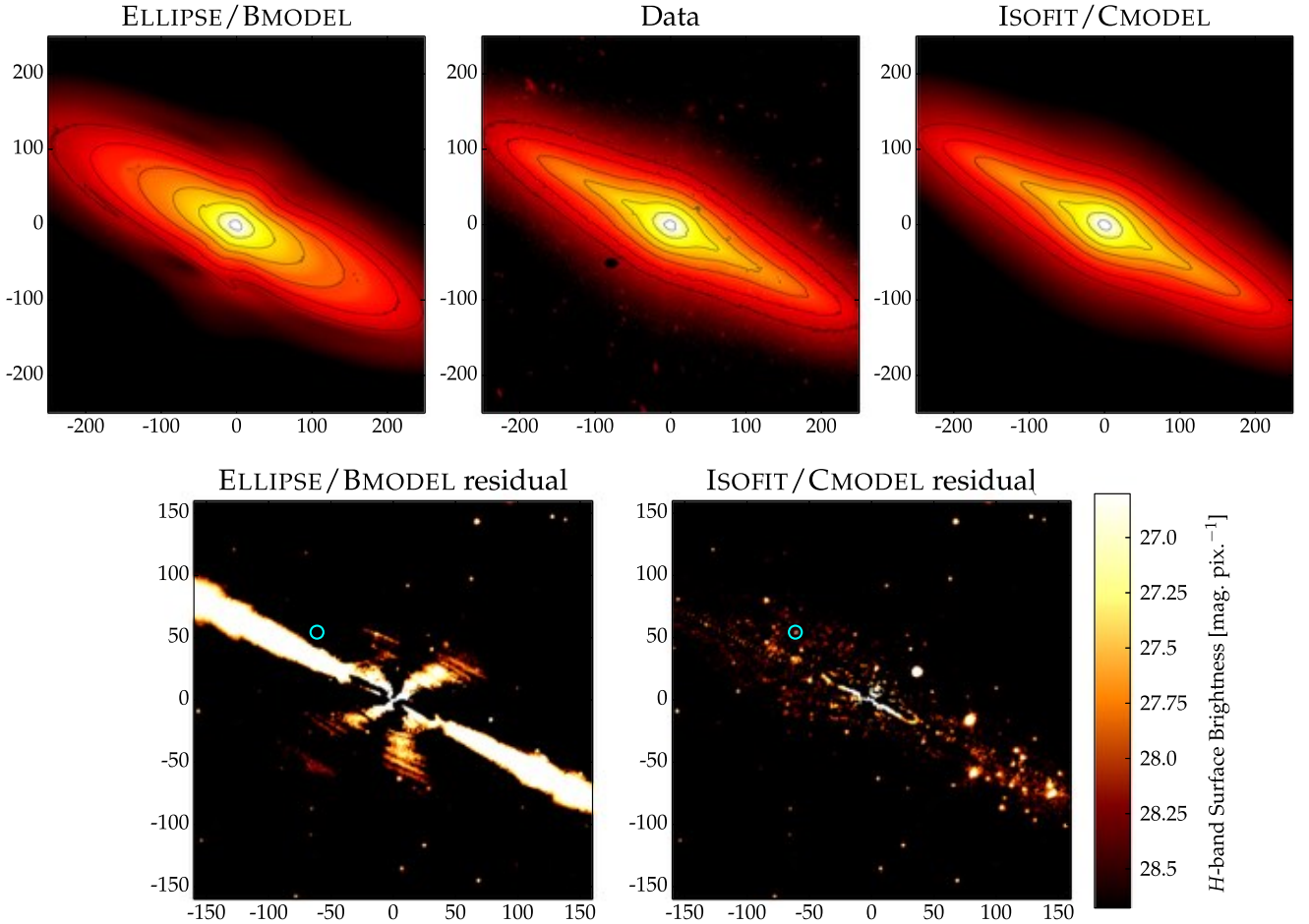
ELLIPSE / BMODEL

Data

ISOFIT / CMODEL

ELLIPSE / BMODEL residual

ISOFIT / CMODEL residual

Figure 7. Top panels: 2D model of the galaxy ESO 243-49 constructed with the old formalism of ELLIPSE and BMODEL (top-left), the *HST* image of ESO 243-49 (top-center) and the 2D model constructed with ISOFIT and CMODEL (top-right). Bottom panels: residual images obtained after subtracting the BMODEL-based galaxy model (bottom-left) and the new CMODEL-based galaxy model (bottom-right) from the galaxy image. The position of the optical counterpart of HLX-1 is marked with the cyan circle in both residual maps. The higher harmonic terms were turned on and used to construct both models. However, the old formalism used in ELLIPSE/BMODEL fails due to the reasons detailed in Section 3.

the underestimated profile (the green dashed curve in Figure 6), the disk component appears to follow an exponential form. If modeled as such, it would eat into and impact the fit of the central bulge (its brightness, concentration, effective radius, etc.). When considering the correct profile (black solid curve in Figure 6), the disk component is, in reality, more appropriately described by an inclined disk model (a Sérsic function with $n_{Sérsic} < 1$; Pastrav et al. 2013), which leads to quite a different decomposition result, with a brighter and more concentrated (higher Sérsic index) bulge. When performing bulge/disk decompositions, it is common for the major-axis surface brightness profile, $\mu(R_{maj})$, to be mapped onto the "equivalent" axis R_{eq}. This mapping is equivalent to transforming each isophote of semimajor axis R_{maj} into a circle of equal enclosed area, which then has a radius R_{eq}. This way, one can use azimuthal symmetry to compute *integrated* quantities from $\mu(R_{eq})$, including the magnitudes of the model components that are fit to this profile. This is fully consistent with the formalism implemented in this work because the Fourier harmonic perturbations change the shape of the isophote but conserve its area. This is demonstrated in the Appendix.

A final note on the 1D aspect of this work is that using the correct angular metric to express the isophotes makes it

possible to obtain the surface brightness profile not just of the major axis, but also the minor axis or in fact any direction, directly by using $\langle I_{ell} \rangle$ and the harmonic coefficients (all provided by ISOFIT) in Equation (5), for any azimuthal angle. This was not possible before, and we can readily see it just by inspecting the single isophote shown in the upper panel of Figure 5 (the shape as a function of azimuthal angle is wrong).

3.3.3. 2D Improvements

The auxilliary task BMODEL in the IRAF package ISOPHOTE has been routinely used in the past to generate two-dimensional models of galaxies, based on the 1D information computed by ELLIPSE. Due to the improper angular metric employed, the residuals obtained from subtracting these 2D models from galaxy images are notorious for displaying obvious artificial features, in particular, for systems with strong departures from pure elliptical shapes. In this subsection, BMODEL and the new task CMODEL, are both run on the test-case galaxy ESO 243-49. The input information for BMODEL consisted of the best-fit generated by ELLIPSE, while the input for CMODEL consisted of the best-fit generated by ISOFIT. The results are shown in Figure 7.

We can clearly recognize in the upper-left panel of Figure 7 the wrong shape of a disky isophote resulting from improperly defined ellipses (we noticed this in Figures 4 and 5). The inevitable consequence is that when such a model is subtracted from the galaxy image, the resulting residual map is contaminated by artificial features (for ESO 243-49, the residual image is dominated by such an artificial feature along the disk plane, which is quite obvious in the bottom-left panel of Figure 7).

It is immediately apparent that CMODEL (top-right and bottom-right panels in Figure 7) achieves a remarkably better representation of the galaxy light distribution than the previous standard (BMODEL). With CMODEL, it is now possible to construct realistic and accurate 2D models of galaxies. Having such models can bring considerable insight into the structure and morphology of galaxies and also enables meaningful studies of the substructure left behind after subtracting the accurate model from the image. Regarding the latter, CMODEL makes it possible to easily identify the optical counterpart of the X-ray source HLX-1 and compute its near-infrared brightness. This was done with the software Aperture Photometry Tool (Laher et al. 2012), resulting in the apparent H-band magnitude $m_H = 22.68 \pm 0.27$ (in the Vega magnitude system).

4. NEW SCIENCE—CASE STUDIES

This section demonstrates the much broader applicability of the new technique to describing virtually any galaxy. Four additional galaxies are modeled, chosen to be representative of a specific class that presents scientific interest and is the object of active current research. The following is by no means an exhaustive study of each class, but it is meant to merely illustrate the usefulness of the method introduced in this work, and to highlight some tentative ways to investigate such galaxies and quantify their properties.

4.1. Peanut/X-shaped Bulges and Boxy+Disky Isophotes

The bulges of many nearby galaxies have been observed to display non-elliptical shapes, particularly obvious in (but not restricted to) galaxies where the bulge is embedded in a large scale disk. These bulges are commonly referred to as boxy, peanut-shaped, or X-shaped, and have been amply studied both observationally and with simulations (e.g., de Vaucouleurs 1974; Combes & Sanders 1981; Bureau & Freeman 1999; Bureau et al. 2006—see Laurikainen & Salo 2015 for a recent review). In terms of formation scenarios, it is believed that this structural feature has a kinematical origin, resulting from the re-organization of stellar orbits within the bulge, and is possibly related to the formation of bars. Because peanut/X-shaped bulges are especially obvious when the galaxies are viewed edge-on, these objects make ideal candidates for the modeling technique described in this work.

A representative galaxy, known to have an X-shaped bulge, was chosen to be modeled in this section, namely NGC 2549. The imaging data was retrieved from the HLA, and consisted of an R-band HST image taken with the Wide Field and Planetary Camera 2 (WFPC2, filter F702W; PI: W. Jaffe). As before, the galaxy was modeled with the old method (standard ELLIPSE, BMODEL) and the new technique (ISOFIT, CMODEL), both run with identical starting conditions. The results are displayed in Figure 8.

As mentioned in Section 3, one of the goals of this work is to investigate whether a galaxy's more complex morphological features are encoded in its isophotal structure, and can therefore be quantified through the Fourier coefficients. While the B_4 harmonic coefficient has been shown in the past to correlate with structural and physical properties of elliptical galaxies, the higher orders and late-type galaxies have been left quite unexplored (largely due to the improper expression of the isophote contours). With this new formalism it is now possible to explore this parameter space.

If we observe the isophote contours of NGC 2549 in the upper panels (center and right) of Figure 8, we notice how the isophotes transition from boxy (inner) to disky (outer). However, the shapes at the transition are not elliptical (even though $B_4 = 0$), but rather a combination of boxy *and* disky (green contour), reminiscent of the B_6-corrected ellipse illustrated in Figure 4 (bottom right panel). The transition occurs precisely in the radial range where the X-shape/peanut feature is most obvious in the image. Since it is clear that higher-order harmonics are necessary to capture this morphological feature, the harmonic coefficients actually "measure" the *peanutness* in this way. This is an important result: with the degree of peanutness quantifiable this way, it is now possible to directly and quantitatively compare observations of real galaxies with simulations (such as, e.g., Athanassoula 2005, 2015).

A second galaxy, NGC 3610, which displays a combination of boxy *and* disky isophotes was modeled in this section. This galaxy is consistent with having a thick boxy bulge, i.e., the extent of the disk component is less than or comparable to that of the bulge. In this work, the terminology "boxy/peanut (B/P) bulge" is avoided, however, precisely because boxyness is expressed through B_4, whereas the isophotes of these structures are associated with different/additional harmonics. Instead, these structures are referred to as X-shaped/peanut (X/P) bulges. The data was again retrieved from the HLA, and consisted of an I-band image taken with WFPC2 (filter $F814W$; PI: B. Whitmore). The resulting models and residual maps corresponding to this galaxy are displayed in Figure 9. Once again, the standard ELLIPSE cannot model the higher harmonic orders, and the residual image is dominated by an artificial streak along the disk plane.

Figure 10 displays the B_4 and B_6 coefficients of NGC 2549 and NGC 3610, computed with ISOFIT, because they change with radius (along the major axis). The coefficients are re-normalized by the local gradient and local semimajor axis length (Equation (6)), such that

$$B_n \rightarrow -B_n \left(a \frac{\partial I}{\partial a} \right)^{-1}, \qquad (6)$$

where a is the local semimajor axis length of the ellipse. This is a common way of expressing the coefficients as (dimensionless) deviations from ellipticity, as opposed to concrete intensity corrections. The transition between boxy and disky isophotes (B_4 crossing 0) occurs in both galaxies, and also B_6 has non-zero amplitude for most of the radial range, which indicates that it plays a part in capturing the isophote shape.
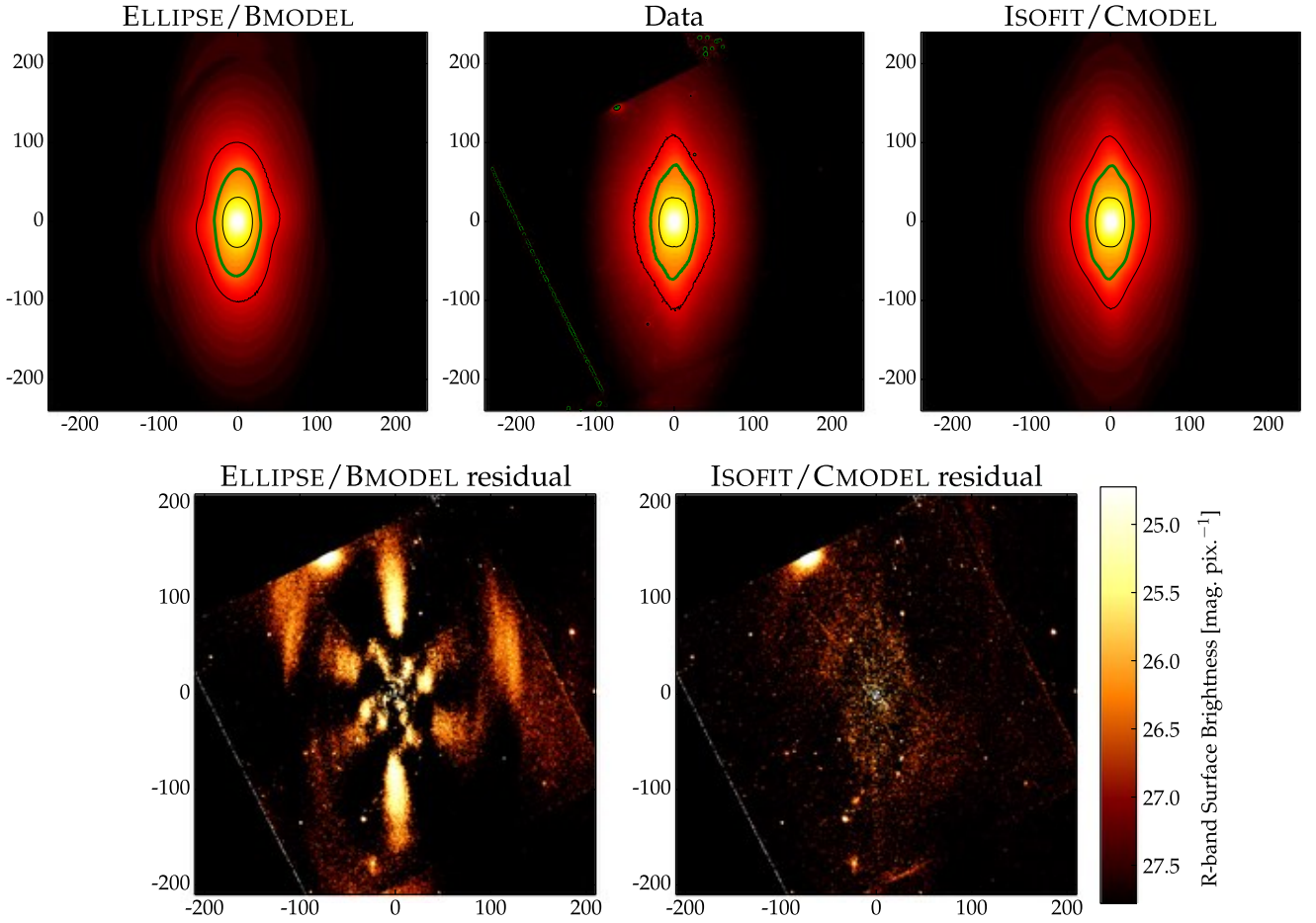
Figure 8. NGC 2549: a galaxy with a known X-shaped bulge. The panels are arranged analogously to Figure 7. The upper panels use a segmented colormap to better highlight the X-shaped bulge feature, and only three contours are overplotted: the inner and outer black contours have boxy and disky shapes, respectively. The middle contour (green) is a combination of both and needs higher orders to be properly modeled.

Such accurate information was not available with the old formalism used in IRAF.

4.2. Photometry of Galaxy Substructure

Perhaps the most basic use of a high-quality model of a galaxy is the study of residual substructure, such as star clusters, GCs, satellites, streams, etc. Once the model is subtracted from the original image, all of this substructure is left behind in the residual image. We have seen in Section 3.3 that CMODEL makes it possible to perform photometry on residual images quite straightforwardly with tools such as the Aperture Photometry Tool. In this section, we qualitatively explore this further, and extend the study to modeling galaxies with more complex isophotal structures such as misaligned bars. To begin with, the interesting barred lenticular (SB0) galaxy NGC 936 (Muñoz-Mateos et al. 2015) was the first candidate to be modeled. Due to this galaxy's orientation (slightly inclined but close to face-on view) and components (bulge, disk, and *barlens*; see Laurikainen et al. 2011), its isophote structure is relatively complicated. The data was retrieved from the publicly available archive of the *Spitzer* Survey of Stellar Structure in Galaxies (S4G[4]), and consisted of an infrared (3.6 μ) *Spitzer* observation (IRAC 1 instrument, PI:

K. Sheth). Figure 11 displays the results: the isophote shape starts off close to elliptical in the central regions, then it transitions to lemon-shaped and parallelogram-shaped (when capturing the barlens) and finally returns to a shape close to elliptical, when the barlens no longer dominates and the disk takes over. The isophotes also rotate in PA with increasing radius, a process that is again driven by the barlens. Because of all these strong deviations from ellipticity, the 2D model built with BMODEL fails to reproduce the light distribution in this galaxy and after its subtraction from the image, a residual map remains that is heavily contaminated by twisting features, both positive and negative. The much more realistic 2D model built with CMODEL (top right) and the associate residual map (bottom right) demonstrate that the formalism proposed here is not limited to edge-on systems, but can competently handle any type of galaxy. With such good quality results, it is now possible to make stronger claims about galaxy morphology and also gain better insight into the substructure than before. The previous contaminated residual images made it difficult to analyze GCs because the artificial features often hid them in oversubtracted regions or covered them through the bright artificial streaks. This not a problem because, with our new approach, it is now possible to perform GC number statistics (e.g., GC number density radial profiles) as well as more accurate photometry.
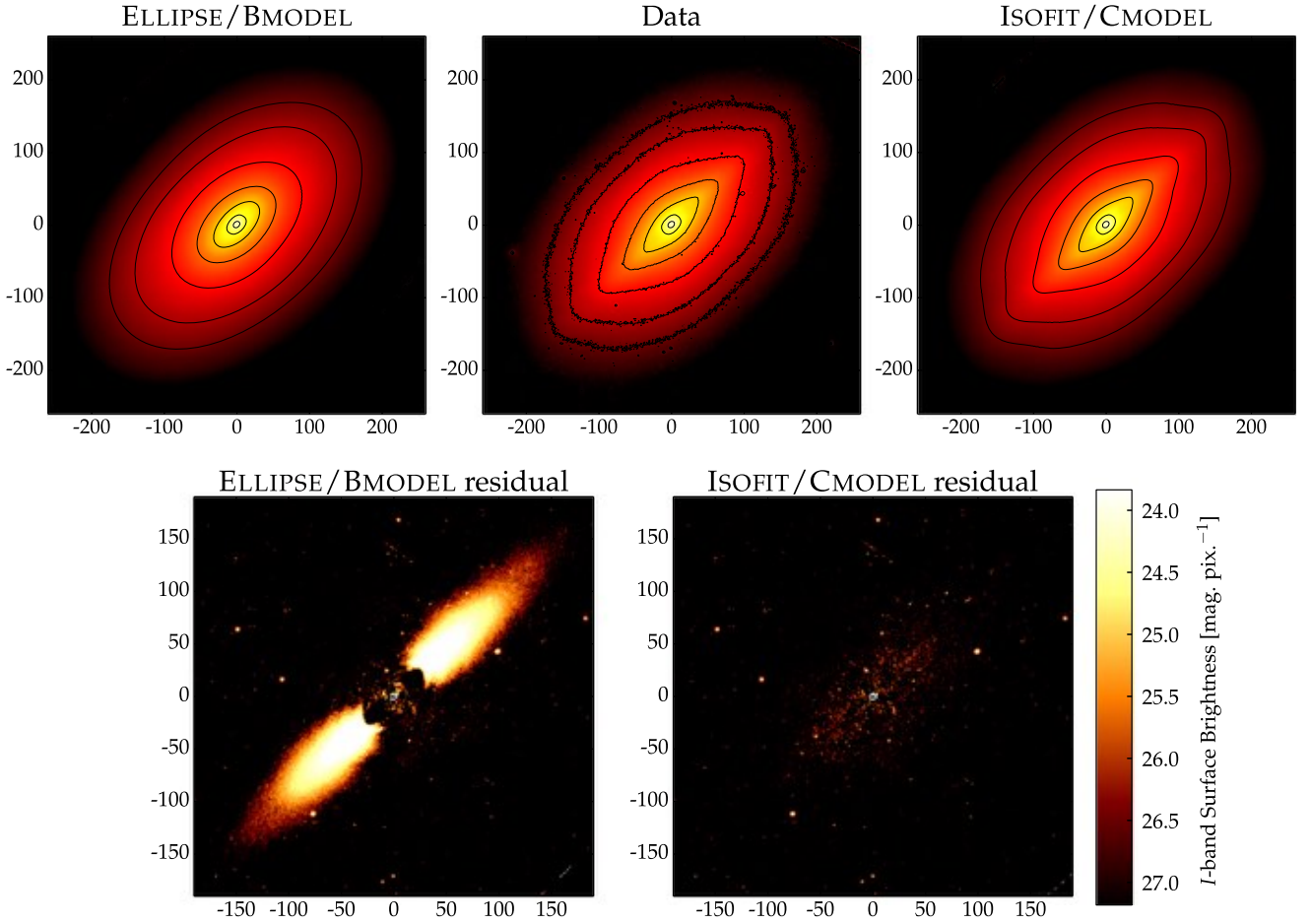
---

[4] http://irsa.ipac.caltech.edu/data/SPITZER/S4G/

Figure 9. NGC 3610. The panels are arranged analogously to Figure 7. The isophote shapes require higher-order harmonics to properly capture the combination of both boxyness ("square" along the minor axis) and diskyness ("pointy" along the major axis due to the embedded, nearly edge-on disk) within the same isophote.
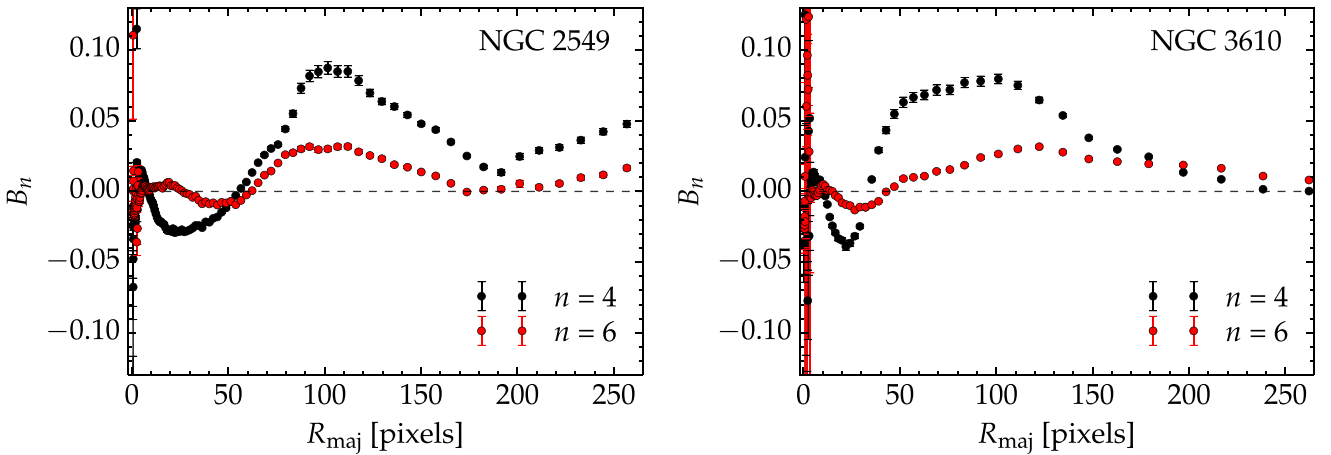

Figure 10. Fourth and sixth Fourier coefficient profiles corresponding to the isophotes of NGC 2549 (left panel) and NGC 3610 (right panel), normalized by the local semimajor axis and intensity gradient (see Equation (6)) and plotted as a function of semimajor axis length. In NGC 2549, there is a transition between boxy (negative B_4 at $R_{maj} \lesssim 50$ pixels) and disky (positive B_4 at $R_{maj} \gtrsim 50$ pixels) isophotal shapes, and the higher order B_6 term is required to capture the "peanut" feature. NGC 3610 has a similar transition in B_4 and also requires a B_6 contribution.

The second galaxy modeled in this section was deliberately chosen from a survey dedicated to GC studies, namely the SLUGGS[5] survey (Usher et al. 2012; Brodie et al. 2014). The

galaxy in question, NGC 4111, is another example of a disk viewed at close to 90° inclination, and is in fact the "flattest" galaxy modeled in this paper. The data was again retrieved from the S4G archive, and consisted of an infrared (4.5 μ) *Spitzer* observation (IRAC 2 instrument, PI: K. Sheth). The
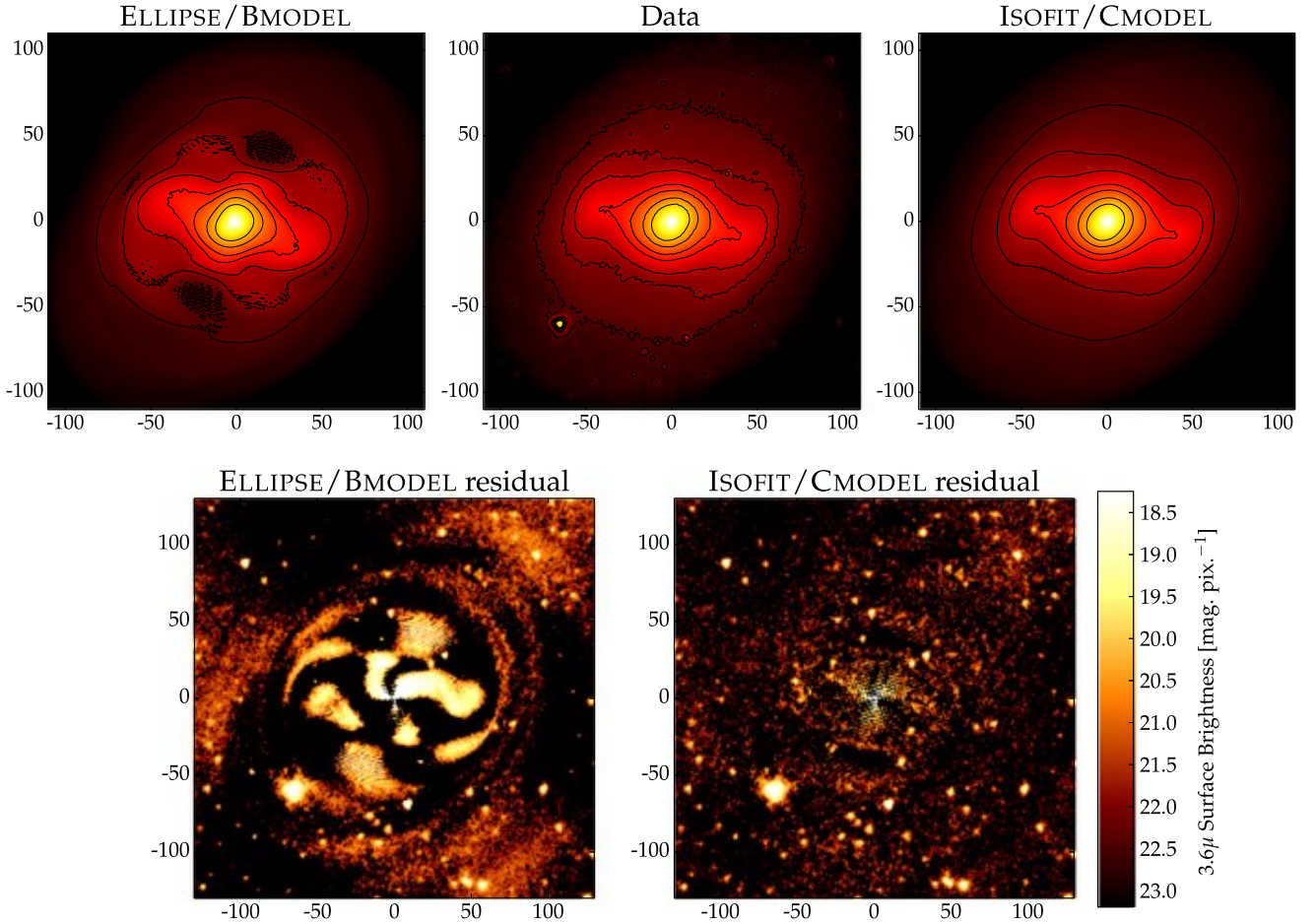
---

5 http://sluggs.swin.edu.au/

Figure 11. NGC 936: an SB0 galaxy with a barlens and complex isophotes. The panels are arranged analogously to Figure 7. The barlens induces strong departures from pure elliptical shapes, as well as substantial (close to 90°) isophote rotation.

results are displayed in Figure 12, where again we notice the contaminated residual image produced with BMODEL as well as the "cleaner" residual obtained with with CMODEL.

5. SUMMARY AND OUTLOOK

This paper proposes a new formalism in which the isophotes of galaxies are expressed as a function of an angular parameter more natural to ellipses, namely the "eccentric anomaly." This replaces the use of the polar angle and significantly improves past algorithms, such as the IRAF tasks ELLIPSE and BMODEL. Isohotes with significant deviations from pure ellipses can now be accurately modeled, opening the door to new science.

This new formalism is implemented in the tasks ELLIPSE and BMODEL, which are renamed ISOFIT and CMODEL, respectively, in order to differentiate the new implementation from the old standard. The method is tested on an edge-on galaxy, ESO 243-49, and is found to bring considerable improvements in both 1D (major axis surface brightness profile) and 2D (model and residual image). Specifically, with ISOFIT, the true surface brightness profile of ESO 243-49 is recovered, in shape and normalization, while, with ELLIPSE, it was systematically underestimated, the discrepancy reaching a maximum of 0.77 mag arcsec^{-2} (a factor of $\sim$2 in brightness) at $R_{\mathrm{maj}} = 16.5$ arcsec for the galaxy in question. In addition, the second new task CMODEL was found to produce a realistic 2D representation of the light distribution, which, after being

subtracted from the image, left behind a high quality residual image on which photometry was possible. The H-band apparent magnitude of the optical counterpart of HLX-1 was measured to be $m_H = 22.68 \pm 0.27$ mag.

This work makes it possible to study a wide range of photometrically interesting objects, and two particular scientific applications (beyond galaxies with near edge-on disks) were further considered: galaxies with X-shaped/peanut bulges, and photometry of galaxy substructure. By expressing isophotes with a more natural metric, the higher order Fourier moments now carry meaning and can potentially quantify morphological features such as the peanut feature in galaxy bulges. This conclusion, however, is only based on the two galaxies modeled in the paper and an exhaustive and more quantitative study on a larger sample is reserved for future work to confirm this hypothesis. While the full power of this new formalism is most obvious in edge-on galaxies, it is not limited to these systems, and in fact is fully applicable to any galaxy. The task ISOFIT is capable of capturing complex isophote shapes with high deviations from ellipticity and, in the limit of low ellipticity or low deviations from ellipticity, the results of ELLIPSE are fully recovered.

The case-studies discussed in the above sections represent a small sample of the much wider range of science made possible by the better mathematical description of isophotal structure used in ISOFIT. Section 3.3.3 illustrates how the accurate
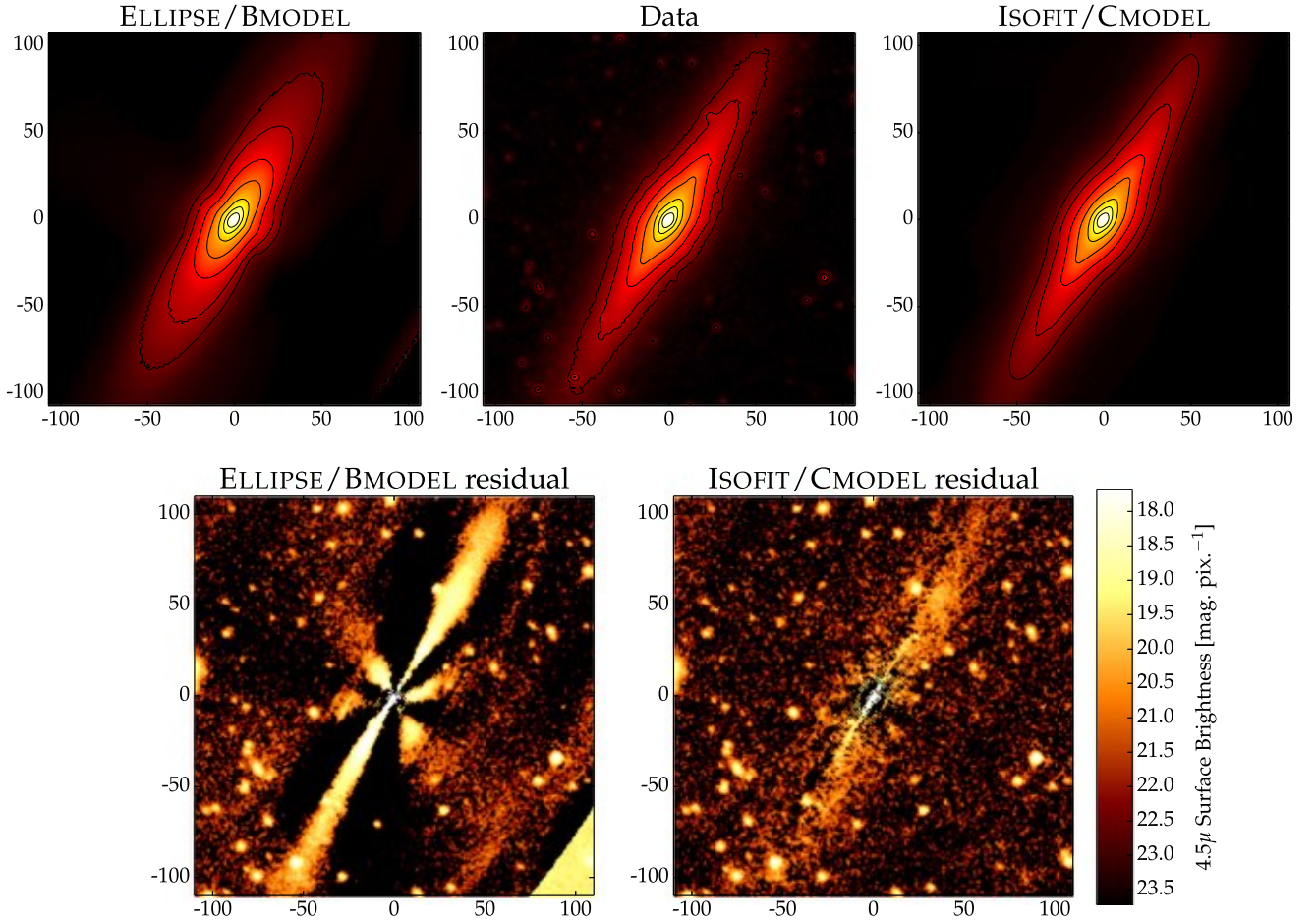
Figure 12. NGC 4111: an edge-on galaxy surrounded by globular clusters. The panels are arranged analogously to Figure 7. The artificial cross in the residual obtained from BMODEL (bottom left) makes it hard to detect all of the globular clusters and contaminates the computation of their brightness. Application of the new CMODEL obtains a much better residual image (bottom right).

modeling of the galaxy ESO 243-49 with ISOFIT and CMODEL makes it possible to characterize the optical counterpart of the hyperluminous X-ray source HLX-1. This case-study can be extended to a systematic study of such objects, by, e.g., cross-correlating the positions of similar X-ray sources (from X-ray databases) with the positions of nearby galaxies.

Another potential application involves the modeling of compact, low-mass early-type galaxies. Current investigations on such galaxies (e.g., Guérou et al. 2015) still model them with ELLIPSE and thus fail to capture interesting features such as embedded disks, which in turn leads to the familiar cross-pattern in residual maps. Because of this, often times the harmonics are deliberately not included, and the presence of disks/diskyness is pointed out by the cross pattern in the residual image.

Additionally, recent studies have shown that the bulge of the Milky Way has an X/peanut-shaped structure (Di Matteo et al. 2015; Qin et al. 2015; Wegg et al. 2015). Since this makes it the nearest X/P bulge in an edge-on galaxy, it is a prime candidate to study with ISOFIT and investigate potential connections between the X/P characteristic and $n > 4$ Fourier coefficients.

Finally, these new galaxy modeling tools can be applied to the interesting shell-galaxies (e.g., Forbes et al. 1994; Del Burgo et al. 2008). These are elliptical galaxies marked with

shell-like or ring-like structures, thought to be the remnants of past merger events.

All of these constitute extensive projects in their own right and are deferred to future work.

APPENDIX

The formalism proposed in this work is fully consistent with re-mapping the major-axis surface brightness profile $\mu(R_{maj})$, computed by ISOFIT, onto the "equivalent axis" R_{eq}. The "equivalent radius" R_{eq} is the radius of the "circularized" isophote of semimajor axis length R_{maj} such that the circle encloses an equal area as that of the isophote. This transformation is routinely performed on $\mu(R_{maj})$ following a bulge/disk decomposition of $\mu(R_{maj})$, because it allows the use
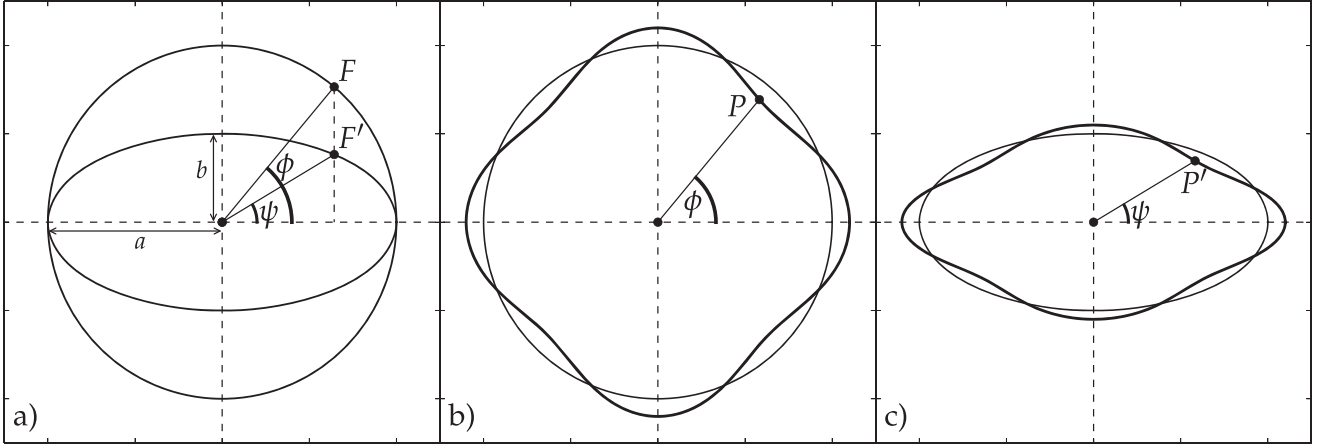
Figure 13. Panel (a): when the circle of radius a is "squeezed" along the y-axis by a factor b/a, it results in an ellipse of semiminor axis b and semimajor axis a. The point F on the circle (defined by ϕ) corresponds to F' on the ellipse, which is described by the "eccentric anomaly ψ." Panel (b): the circle in panel (a) distorted through Equation (9), with $n = 4$, $A_n = 0$, $B_n = 0.1$ (thick line). A point P along the circumference is defined by the polar angle ϕ. Panel (c): when the distorted circle in panel (b) is "squeezed" into a distorted ellipse, the same point (now denoted by P') is now defined by the "eccentric anomaly" ψ.

of circular symmetry in computing the integrated surface brightness (i.e., the magnitude) of the model components. The deviations from a purely elliptical shape brought by the ISOFIT formalism *conserve* the enclosed area, as is demonstrated below.

(I) Consider a surface enclosed in a circle of radius a. In plane-polar coordinates, where r is the radial coordinate and ϕ the azimuthal coordinate, the surface element dS is given by

$$dS = r dr d\phi. \tag{7}$$

The total area $\mathcal{A}$, obtained by integrating dS in the range of $r \in [0, a]$ and $\phi \in [0, 2\pi]$ is the usual

$$\mathcal{A} = \int_0^a \int_0^{2\pi} r \, dr d\phi = \pi a^2. \tag{8}$$

(II) Consider re-scaling the circle along the y-axis by a factor b/a. The resulting shape is an ellipse with semimajor axis a and semiminor axis b (Figure 13, panel (a)). Moreover, the area $\mathcal{A}$ is also re-scaled by the same factor: $\mathcal{A}_{\text{ell}} = \mathcal{A} \, b/a = \pi a^2 (b/a) = \pi ab$, the usual expression for the area of an ellipse. Furthermore, a point F on the circle (defined by a central angle ϕ) becomes the point F' on the ellipse, and is now defined by a central angle ψ. The two angles are related to each other through the axis ratio b/a or ellipticity $e = 1 - a/b$, through Equation (4). This is in fact the geometric definition of the "eccentric anomaly" ψ.

(III) Consider again the circular surface, but perturbed with a set of sinusoidal waves, as a function of the polar angle (e.g., Figure 13, panel (b)), such that

$$r(\phi) = r [1 + A_n \sin(n\phi) + B_n \cos(n\phi)], \tag{9}$$

where A_n, B_n are constant coefficients and n is an integer. The new surface element (denoted as dS') becomes

$$dS' = r [1 + A_n \sin(n\phi) + B_n \cos(n\phi)] dr d\phi. \tag{10}$$

As before, the total area of the perturbed shape (denoted as $\mathcal{A}'$) is given by integrating the surface element in the same limits:

$$
\begin{aligned}
\mathcal{A}' &= \int_0^a \int_0^{2\pi} r [1 + A_n \sin(n\phi) + B_n \cos(n\phi)] \, dr d\phi \\
&= \int_0^a \int_0^{2\pi} r \, dr d\phi + A_n \int_0^a \int_0^{2\pi} r \sin(n\phi) dr d\phi \\
&\quad + B_n \int_0^a \int_0^{2\pi} r \cos(n\phi) dr d\phi \\
&= \pi a^2 + \frac{a^2}{2} \int_0^{2\pi} \sin(n\phi) d\phi + \frac{a^2}{2} \int_0^{2\pi} \cos(n\phi) d\phi \\
&= \pi a^2 + \frac{a^2}{2n} [-1 + 1 + 0 - 0] \\
&= \pi a^2 \equiv \mathcal{A}, \; \forall \; n.
\end{aligned}
\tag{11}
$$

The sinusoidal functions change the area as a function of ϕ but the net change is zero over the full range $[0, 2\pi]$, i.e., the positive "bumps" are cancelled out by the negative "dips" over the whole azimuthal range, independently of the choice of n.

(IV) Consider now the perturbed shape "squeezed" along the y direction by a factor of b/a (Figure 13, panels (b) and (c)), in the same way as the circular shape was re-scaled (panel (a)). A point P on the perturbed circle, which was described by the polar angle ϕ (panel (b)), becomes the point P' on the perturbed ellipse (panel (c)), described by the eccentric anomaly ψ as before. This is at the heart of the the new formalism—a Fourier wave on a circle needs a different coordinate system on the corresponding ellipse. As a consequence of the re-scaling ("squeezing"), all areas (in panel (b)) are reduced by the same factor (b/a) in panel (c). The area inside and outside of the ellipse is thus reduced by b/a, but there is still, obviously, an equal amount of area inside and outside. The area of the ellipse is therefore conserved following the perturbation.

(V) From the output of ISOFIT ($\langle I_{\text{ell}} \rangle$, R_{maj} and A_n, B_n—see Section 2 for the explanation) the major axis surface brightness profile $\mu(R_{\text{maj}})$ can be constructed in two equivalent ways.

1. By applying the perturbations to the intensity/surface brightness ($I_{\psi=0} \neq \langle I_{\text{ell}} \rangle$)—keeping the isophote shape

elliptical and distorting the intensity distribution along its circumference. This is in fact how Isofit works.

2. By keeping $\langle I_{\mathrm{ell}} \rangle$ fixed and applying the corrections to R_{maj}—distorting the ellipse shape and keeping the intensity fixed. This step additionally requires the intensity gradient, which is also provided by Isofit (Ellipse also computes all of these quantities, though with incorrect A_n, B_n), to re-normalize the coefficients (such that they correspond to R_{maj} perturbations).

Performing the distortion the second way is analogous to case (IV): a given isophote is a distorted ellipse whose area is the same as that of the original, pure ellipse ($\mathcal{A}_{\mathrm{iso}} = \mathcal{A}_{\mathrm{ell}} = \pi a b = \pi a^2 (1-e) \equiv \pi R_{\mathrm{maj}}^2 (1-e)$). The intensity associated with this isophote area is $\langle I_{\mathrm{ell}} \rangle$ (which is converted into the surface brightness μ_{ell}). Therefore, if the area is expressed as a circular area, its radius R_{eq} can be obtained as

$$\pi R_{\mathrm{eq}}^2 = \pi R_{\mathrm{maj}}^2 (1-e) \tag{12}$$

$$R_{\mathrm{eq}} = R_{\mathrm{maj}} \sqrt{1-e}. \tag{13}$$

With the surface brightness profile now expressed along the equivalent axis, it is straightforward to compute magnitudes in the usual fashion.

REFERENCES

Alamo-Martinez, K. A., Blakeslee, J. P., Jee, M. J., et al. 2013, ApJ, 775, 20
Athanassoula, E. 2005, MNRAS, 358, 1477
Athanassoula, E. 2015, arXiv:1503.04804
Bender, R. 1988, A&A, 193, L7
Bender, R., Surma, P., Doebereiner, S., Moellenhoff, C., & Madejsky, R. 1989, A&A, 217, 35
Brodie, J. P., Romanowsky, A. J., Strader, J., et al. 2014, ApJ, 796, 52
Bureau, M., Aronica, G., Athanassoula, E., et al. 2006, MNRAS, 370, 753
Bureau, M., & Freeman, K. C. 1999, AJ, 118, 126
Capaccioli, M., Spavone, M., Grado, A., et al. 2015, arXiv:1507.01336
Carter, D. 1978, MNRAS, 182, 797
Carter, D. 1987, ApJ, 312, 514
Chies-Santos, A. L., Larsen, S. S., Wehner, E. M., et al. 2011, A&A, 525, A19
Combes, F., & Sanders, R. H. 1981, A&A, 96, 164
Davies, R. L., Efstathiou, G., Fall, S. M., Illingworth, G., & Schechter, P. L. 1983, ApJ, 266, 41
de Vaucouleurs, G. 1974, in IAU Symp. 58, The Formation and Dynamics of Galaxies, ed. J. R. Shakeshaft (Dordrecht: Reidel), 335
Del Burgo, C., Carter, D., & Sikkema, G. 2008, A&A, 477, 105
Di Matteo, P., Gómez, A., Haywood, M., et al. 2015, A&A, 577, A1
Farrell, S. A., Webb, N. A., Barret, D., Godet, O., & Rodrigues, J. M. 2009, Natur, 460, 73
Forbes, D. A., Thomson, R. C., Groom, W., & Williger, G. M. 1994, AJ, 107, 1713
Graham, A. W. 2013, in Planets, Stars and Stellar Systems Vol. 6, ed. T. D. Oswalt & W. C. Keel (Dordrecht: Springer), 91
Guérou, A., Emsellem, E., McDermid, R. M., et al. 2015, ApJ, 804, 70
Hubble, E. P. 1926, ApJ, 64, 321
Jaffe, W., Ford, H. C., O'Connell, R. W., van den Bosch, F. C., & Ferrarese, L. 1994, AJ, 108, 1567
Janowiecki, S., Mihos, J. C., Harding, P., et al. 2010, ApJ, 715, 972
Jeans, J. H. 1919, Problems of Cosmogony and Stellar Dynamics (Cambridge: Cambridge Univ. Press)
Jeans, J. H. 1928, Astronomy and Cosmogony (Cambridge: Cambridge Univ. Press)
Jedrzejewski, R. I. 1987a, MNRAS, 226, 747
Jedrzejewski, R. I. 1987b, in IAU Symp. 127, Structure and Dynamics of Elliptical Galaxies, ed. P. T. de Zeeuw (Dordrecht: Reidel), 37
Laher, R. R., Gorjian, V., Rebull, L. M., et al. 2012, PASP, 124, 737
Lauer, T. R. 1985, MNRAS, 216, 429
Laurikainen, E., & Salo, H. 2015, arXiv:1505.00590
Laurikainen, E., Salo, H., Buta, R., & Knapen, J. H. 2011, MNRAS, 418, 1452
Muñoz-Mateos, J. C., Sheth, K., Regan, M., et al. 2015, ApJS, 219, 3
Nieto, J.-L., Bender, R., & Surma, P. 1991, A&A, 244, L37
Pastrav, B. A., Popescu, C. C., Tuffs, R. J., & Sansom, A. E. 2013, AAP, 553, A80
Peletier, R. F., Davies, R. L., Illingworth, G. D., Davis, L. E., & Cawson, M. 1990, AJ, 100, 1091
Peng, C. Y., Ho, L. C., Impey, C. D., & Rix, H.-W. 2010, AJ, 139, 2097
Peng, E. W., Ferguson, H. C., Goudfrooij, P., et al. 2011, ApJ, 730, 23
Qin, Y., Shen, J., Li, Z.-Y., et al. 2015, arXiv:1503.06774
Reda, F. M., Forbes, D. A., Beasley, M. A., O'Sullivan, E. J., & Goudfrooij, P. 2004, MNRAS, 354, 851
Reda, F. M., Forbes, D. A., & Hau, G. K. T. 2005, MNRAS, 360, 693
Rothberg, B., & Joseph, R. D. 2004, AJ, 128, 2098
Soria, R., Hau, G. K. T., Graham, A. W., et al. 2010, MNRAS, 405, 870
Usher, C., Forbes, D. A., Brodie, J. P., et al. 2012, MNRAS, 426, 1475
Webb, N. A., Barret, D., Godet, O., et al. 2010, ApJL, 712, L107
Wegg, C., Gerhard, O., & Portail, M. 2015, MNRAS, 450, 4050

3

Quantifying (X/Peanut)–shaped Structures in Edge-on Galaxies

We have seen in Chapter 2 how the Fourier expansion of a galaxy's isophotes can capture, and quantify, specific structural properties, such as the presence of discs, bars and their strength, triaxiality in early-type galaxies, etc. The re-formulation, in Ciambur (2015), of this mathematical description has allowed for a more accurate representation of a galaxy's surface photometry, but, moreover, it has opened the door for studying higher-order terms ($n > 4$ in Equation 1.3), as measures of more complex structures. In Chapter 2 we have briefly explored the possible connection between the amplitude of the 6th order cosine term (B_6) and X/P structures in edge-on disc galaxies. Here we develop on this idea, and present a comprehensive framework for quantifying X/P features directly from photometric data, through their imprint in the galaxy's isophotes.

X/P structures (or boxy/peanut/X–shaped "bulges", as they are often confusingly referred to) are characteristic bi-lobed, "peanut"–shaped structures observed in barred disc galaxies (Jarvis 1986; Lütticke et al. 2000; Laurikainen et al. 2011; Buta et al. 2015), that develop from the vertical thickening of galactic bars outside the plane of the disc in which they are embedded. Simulations indicate that they result naturally from internal orbital resonances or bar-buckling instabilities (Combes & Sanders 1981; Raha et al. 1991; see §1.2.2). They can be quite prominent when the disc galaxy in which they reside is viewed in edge-on projection, while at higher inclinations, they are generally believed to assume the morphology of a barlens (Laurikainen et al. 2011; Athanassoula et al. 2015; Laurikainen & Salo 2017). Their obvious prevalence in the barred galaxy population (up to ∼87% in S0–Sb types; Erwin & Debattista 2013) indicates that the X/P instability is a common secular process, which may play an important role in the host galaxy's (chemo-)

dynamical evolution. Nevertheless, analysing these structures in detail in real galaxies has proved challenging in the past, with most studies relying on qualitative approaches such as visual inspection of the image, or of its unsharp mask[1] (e.g., Aronica et al. 2003).

In this Chapter we quantitatively examine the isophotal structure of a sample of edge-on disc galaxies, previously identified in the literature to host peanut structures. We obtained archival images from the S^{4}G (Sheth et al. 2010) and SDSS (DR9; Ahn et al. 2012) surveys, as well as *Hubble* Space Telescope observations[2], which we analysed with ISOFIT, extracting the galaxies' surface brightness profiles as well as their isophote geometric parameters. As predicted in Chapter 2, we identified the B_6 harmonic as a clear tracer of the X/P structure, and developed a framework to quantify the radial and vertical extent of the structure, as well as the integrated strength of the X/P instability, from the radial B_6 profile. We additionally performed photometric decompositions for each galaxy, with the method presented in Chapter 5. Studying the X/P parameter space revealed structural scaling relations between the peanut in-plane length, off-plane height and integrated strength, which are discussed and interpreted from a secular evolution standpoint (e.g., formation, radial drift/growth, recurrent buckling phases; Martinez-Valpuesta et al. 2006; Quillen et al. 2014). Moreover, all parameters were normalised by the exponential scale length of each galaxy's disc, as obtained from the decompositions. This removed uncertainties arising from errors in distance measurements, while preserving the trends between X/P parameters – suggesting that peanuts "know" about their host disc.

The advantages of this method are its sensitivity to faint structures, its accuracy, but also its applicability to both galaxy images and projected density maps from numerical simulations, which can in principle add observational constraints (such as the scaling relations) to the theory (this is discussed further in Chapter 7). The sensitivity of ISOFIT led to the discovery of previously unknown, "nested", X/P structures co-existing in the same galaxy. We found this peculiar configuration in two galaxies in our sample (NCG 128 and NGC 2549). Their decomposition additionally showed that they are double-barred galaxies (e.g., Friedli et al. 1996; Erwin 2011), consolidating the peanut–bar connection (§1.2.2).

The remainder of this Chapter consists of the article "*Quantifying the (X/Peanut)–*

---

[1] Note that since the publication of the article presented in this Chapter, Laurikainen & Salo (2017) have applied the unsharp masking technique to observed and simulated X/P galaxies, to measure their radial and vertical extent.

[2] http://hla.stsci.edu

Shaped Structure in Edge-on Disc Galaxies: Length, Strength, and Nested Peanuts", by B. C. Ciambur and A. W. Graham, as it appears in Monthly Notices of the Royal Astronomical Society, Vol. 459, pp. 1276–1292 (2016).

Quantifying the (X/peanut)-shaped structure in edge-on disc galaxies: length, strength, and nested peanuts

Bogdan C. Ciambur⋆ and Alister W. Graham

Centre for Astrophysics and Supercomputing, Swinburne University of Technology, Hawthorn, VIC 3122, Australia

ABSTRACT

X-shaped or peanut-shaped (X/P) bulges are observed in more than 40 per cent of (nearly) edge-on disc galaxies, though to date a robust method to quantify them is lacking. Using Fourier harmonics to describe the deviation of galaxy isophotes from ellipses, we demonstrate with a sample of 11 such galaxies (including NGC 128) that the sixth Fourier component (B_6) carries physical meaning by tracing this X/P structure. We introduce five quantitative diagnostics on the radial B_6 profile, namely: its 'peak' amplitude (Π_{max}); the (projected major-axis) 'length' where this peak occurs ($R_{\Pi,\,max}$); its vertical 'height' above the disc plane ($z_{\Pi,\,max}$); a measure of the B_6 profile's integrated 'strength' (S_Π); and the B_6 peak 'width' (W_Π). We also introduce different 'classes' of B_6 profile shape. Furthermore, we convincingly detect and measure the properties of multiple (nested) X/P structures in individual galaxies which additionally display the signatures of multiple bars in their surface brightness profiles, thus consolidating further the scenario in which peanuts are associated with bars. We reveal that the peanut parameter space ('length', 'strength' and 'height') for real galaxies is not randomly populated, but the three metrics are inter-correlated (both in kpc and disc scalelength h). Additionally, the X/P 'length' and 'strength' appear to correlate with ($v_{rot}/\sigma_\star$), lending further support to the notion that peanuts 'know' about the galactic disc in which they reside. Such constraints are important for numerical simulations, as they provide a direct link between peanuts and their host disc. Our diagnostics reveal a spectrum of X/P properties and could provide a means of distinguishing between different peanut formation scenarios discussed in the literature. Moreover, nested peanuts, as remnants of bar buckling events, can provide insights into the disc and bar instability history.

Key words: galaxies: bulges – galaxies: fundamental parameters – galaxies: peculiar – galaxies: structure.

1 INTRODUCTION

Quite apart from the spheroid-shaped bulges observed at the cores of many disc galaxies, some galaxy bulges display a characteristic bi-lobed, boxy or X-like shape if viewed in projection close to edge-on (for example, the famous IC 4767 – 'the X-galaxy'; Whitmore & Bell 1988). Shortly after this class of galaxy was noticed (Burbidge & Burbidge 1959) they were coined 'peanut' bulges by de Vaucouleurs & de Vaucouleurs (1972), and have since been found to occur in a significant fraction of galaxies (e.g. Lütticke, Dettmar & Pohlen 2000 found that >40 per cent of disc galaxies in close to edge-on orientation and ranging from S0 to Sd have (peanut/X)-shaped bulges; see also Jarvis 1986 and Buta et al. 2015). Additionally, more recent works suggest that the bulge of our own Galaxy is

peanut-shaped (Sellwood 1993; Dwek et al. 1995; Ness et al. 2012; Wegg, Gerhard & Portail 2015).

The early analyses (based on *N*-body simulations) of Combes & Sanders (1981), Combes et al. (1990) and Raha et al. (1991), suggested that peanuts arise naturally from the thickening and/or buckling of galactic bars, or vertical resonance mechanisms, such as the Inner Lindblad Resonance (ILR). Observational support for the peanut-bar link quickly followed (e.g. Shaw 1987; Dettmar & Barteldrees 1990; Kuijken & Merrifield 1995; Bureau & Freeman 1999; Bureau & Athanassoula 2005), the fraction of barred disc galaxies (~45 per cent; Aguerri, Méndez-Abreu & Corsini 2009) being found to be close (within a few per cent) to that of X/P hosts. Other than their characteristic morphology, X/P bulges also exhibit specific kinematic signatures in face-on orientation (Debattista et al. 2005; Méndez-Abreu et al. 2008), as well as cylindrical rotation, i.e. almost constant rotational velocity in the direction perpendicular to the disc plane (e.g. Molaeinezhad et al. 2016 and

⋆ E-mail: bciambur@swin.edu.au

references therein). The field has advanced significantly, with three-dimensional simulations becoming ever more refined (e.g. Quillen et al. 2014; Athanassoula et al. 2015; Li & Shen 2015) and peanuts being detected at lower inclinations (e.g. Erwin & Debattista 2013). For a more in-depth overview, we refer the reader to the review articles of Laurikainen & Salo (2016) and Athanassoula (2016), and references therein.

Quantifying X/P structures in real galaxies has proved a challenging feat, with most observational studies relying on qualitative methods, such as visual inspection. Several quantitative diagnostics have been attempted, particularly: determining whether isophotes crossing the minor axis are 'pinched' or concave (Williams, Bureau & Cappellari 2009), examining one-dimensional cuts parallel to the disc plane (D'Onofrio et al. 1999; Athanassoula 2005) or looking for the peanut imprint in the fourth Fourier component (B_4) of isophotes (Beaton et al. 2007; Erwin & Debattista 2013). However, all of these approaches are problematic. As we will show in Section 4, many peanut galaxies do not exhibit a very prominent X/P feature compared to the disc and spheroid. As such, their photometric structure is dominated by the combination of the latter two, thus most often resulting in straight (parallel to the disc plane) or even convex isophotes which cross the minor axis[1] (where the shape is dominated by the spheroid), despite the presence of an X/P. Taking cuts parallel to the disc plane also works best only for strong peanuts, and further suffers from noise from, e.g. substructure, seeing, etc. Finally, B_4 usually measures the boxyness or discyness of isophotes. However, X/P structures are believed to be different to boxy ellipticals (Combes et al. 1990), and in fact for edge-on galaxies the disc makes the isophotes discy, i.e. when the isophote crosses the major axis, it is highly convex (not concave, as would be the case for boxy isophotes).

In this work, we propose a method which is more accurate, easy to automate, can probe fainter peanuts and is well suited to compare observations (galaxy isophotes) with simulations (projected isodensity contours). Ciambur (2015, hereafter C15), recently suggested that, just as B_4 quantifies boxyness or discyness, so the sixth Fourier component of isophotes (B_6) carries physical meaning, capturing the X/P feature. In this paper, we show that B_6 does trace X/peanut structures remarkably well and provides a wealth of information about them.

The paper is structured as follows. In Section 2, we define our five diagnostics, based on the radial B_6 profile, and we additionally present them in the context of peanut formation theory. Section 3 details our sample of eleven galaxies with known X/P structures, obtained from the literature. Section 4 provides a detailed demonstration of X/P structure quantification using a well-known peanut galaxy, NGC 128, as well as the results for the full sample. We interpret and discuss our results in Section 5, and finally, we re-iterate our main findings and conclude with Section 6. Throughout this paper, we assume a flat Universe cosmology with $\Omega_m = 0.27$ and $H_0 = 70$ km s^{-1} Mpc^{-1}.

2 THEORY AND QUANTITATIVE X/P PARAMETERS

Bars in discs are dynamically unstable, and are susceptible to buckling outside of the disc plane. Numerical simulations have shown

---

[1] There are of course exceptions, most notably NGC 128, in which the peanut is the dominant component, and the isophotes crossing the minor axis are highly concave.

that bar buckling is one channel through which disc galaxies can develop X/P structures (Raha et al. 1991; Merritt & Sellwood 1994). In such cases, the bar buckles and forms a peanut in the inner regions (Athanassoula & Martinez-Valpuesta 2009) and the stronger the buckling, the more pronounced is the resulting peanut. Another scenario which also arose from *N*-body simulations is that the peanut is actually due to a resonance mechanism (e.g. Combes & Sanders 1981; Combes et al. 1990), in particular a vertical ILR. The X/P shape is given by stellar orbits undergoing a 2:1 vertical Lindblad Resonance:

$$\Omega_{p,b} = \Omega - \frac{\nu_z}{2},\qquad(1)$$

where $\Omega_{p,b}$ is the pattern rotation frequency of the bar, Ω is the circular rotation frequency of stars in the disc, and ν_z is their vertical oscillation frequency. Essentially, there is a 'sweet spot' in radius where the vertical component of stellar orbits is resonant with the bar's pattern speed, and for the 2:1 resonance, the stellar orbits oscillate twice per bar rotation (i.e. each time the two ends of the bar pass underneath). As this is a resonance, this vertical motion enhancement causes the orbits of these stars to 'puff' out of the disc plane at these two points, thus leading to the observed peanut shape in an edge-on projection. Finally, Patsis et al. (2002) explore *N*-body simulations where X/P bulges develop without a bar at all.

In order to disentangle the various mechanisms and thus constrain galaxy dynamics, it is obviously interesting to measure a number of peanut properties: the radius where it is most prominent, how high above the disc plane it reaches, and how strong it is, in real galaxies. Our methodology provides a framework for measuring these quantities and thus allows us to probe the theory via direct observations, as well as comparing real X/P galaxies among themselves. This framework is based on the azimuthal profiles of galaxy isophotes. Throughout our work, we employed the quasi-elliptical isophote fitting software ISOFIT, introduced in C15. As detailed in C15, ISOFIT provides a superior description of isophote deviations from pure ellipses (which real galaxy isophotes are observed to have), than its predecessor, ELLIPSE. These deviations are mathematically expressed as Fourier harmonics, and in ISOFIT, they are expressed as a function of the eccentric anomaly (ψ) of the ellipse, such that:

$$R'(\psi) = R(\psi) + \sum_n [A_n\sin(n\psi) + B_n\cos(n\psi)],\qquad(2)$$

where $R(\psi)$ is the angle-dependent radial coordinate of a pure ellipse, n is the harmonic order and ψ is the azimuthal angular coordinate (see Fig. 1). The angle ψ is related to the usual polar coordinate ϕ as follows. If a point on a circle is defined in polar co-ordinates (r, ϕ), and the circle is 'flattened' in one direction such that it becomes an ellipse, then the same point has the new co-ordinates $(R(\psi), \psi)$. By using the eccentric anomaly as the angular coordinate, ISOFIT drastically improves on previous isophote-fitting algorithms, such as ELLIPSE.

Note that generally the harmonic coefficients (A_n, B_n) can have either units of length (assumed in equation 2), or intensity (as ISOFIT uses and outputs), or they can be dimensionless. Fortunately, it is relatively easy to alternate between units if the isophote semimajor axis and local intensity gradient are known. As usually done in the literature, we plot the dimensionless coefficients (i.e. B_n in units of intensity, re-normalized by the isophote semimajor axis (a) and local intensity gradient $-\partial I/\partial a$), as given by

$$B_n \to -B_n \left(a\frac{\partial I}{\partial a}\right)^{-1}; \quad A_n \to -A_n \left(a\frac{\partial I}{\partial a}\right)^{-1}.\qquad(3)$$
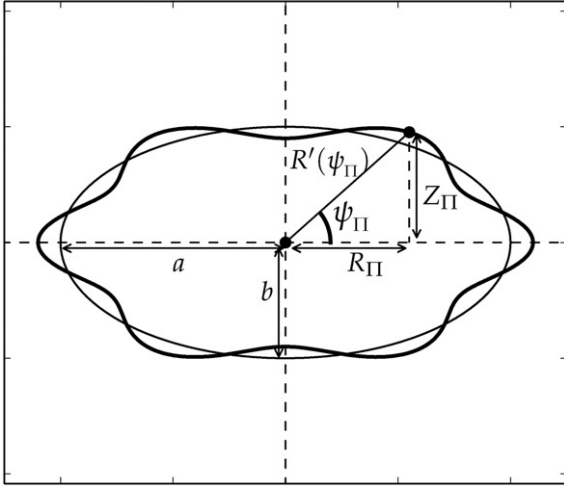
Figure 1. An isophote with the characteristic X/P shape (thick curve), obtained by perturbing an elliptical isophote ($e = 0.4$, thin curve) with the sixth Fourier harmonic ($B_6 = 0.1$). The projected radial 'length' of the peanut, R_Π, is defined here, as is its projected 'height' above the disc plane, Z_Π.
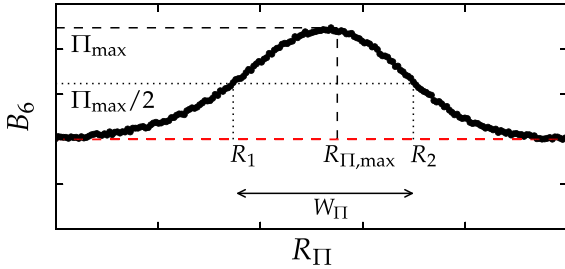

Figure 2. A schematic example of a $B_6(R_\Pi)$ profile (see Fig. 1 for the definition of R_Π), which illustrates the main elements used in defining the five X/P metrics, i.e. the peanut 'peak' (Π_{max}), the projected 'length' ($R_{\Pi,\,max}$), the peak 'width' (W_Π). The peanut 'strength' (S_Π) is the area under the profile enclosed by R_1 and R_2. As with the X/P length, the peanut 'height' ($z_{\Pi,\,max}$) also corresponds to the isophote with maximum B_6 amplitude (Π_{max}).

In the past, quantitative studies of galactic bars have been performed on similar principles, most notably in Ohta, Hamabe & Wakamatsu (1990), Regan & Elmegreen (1997) and Aguerri, Beckman & Prieto (1998) (the latter in particular use diagnostics for bar length and strength derived from isophotal $n = 2$ Fourier terms), but see also Schwarz (1984) and Buta, Laurikainen & Salo (2004). Out of all the Fourier coefficients of equation (2), the sixth cosine coefficient B_6 is of particular interest in our work quantifying X/peanut-shaped features. C15 already suggested that B_6 may trace the X/P feature in galaxies, and qualitatively explored this possibility (see e.g. their Fig. 4). Here we demonstrate that this is indeed the case, and we define the following peanut diagnostics, derived from the B_6 profile (see Fig. 2).

(i) $\Pi_{max}(= B_{6,\,max})$ – the X/P peak, equal to the maximum B_6 amplitude. The quantity B_6, like all the A_n and B_n coefficients, is a function of radius, such that each isophote has its own value.

(ii) $R_{\Pi,\,max}$ – the projected X/P length, equal to the (major-axis) radius where Π_{max} occurs. Note that the true length of a peanut ($l_{\Pi,\,max}$) is only measurable from a galaxy image when the bar is viewed perfectly side-on. As the bar's viewing angle (α in our

notation) is unknown, we can only calculate a lower limit of the peanut length, that is, the projected radius $R_{\Pi,\,max} = l_{\Pi,\,max} \sin(\alpha)$ ($\alpha = 0°$ for end-on and $90°$ for side-on orientation). This latter quantity is straightforward to compute from equation (2):

$$R_{\Pi,max} = R'(\psi_\Pi)\cos(\psi_\Pi), \qquad (4)$$

calculated at the isophote with maximum B_6 amplitude, and where ψ_Π is the eccentric anomaly angle of the peanut, given by

$$\psi_\Pi = -\arctan\left[\frac{\tan(2\pi/6)}{1 - \epsilon}\right], \qquad (5)$$

with ϵ being the isophote ellipticity.

(iii) $z_{\Pi,\,max}$ – the X/P height, equal to the vertical extent above the disc plane computed from the isophote where Π_{max} occurs:

$$z_{\Pi,max} = \frac{Z_{\Pi,max}}{\sin(i)} = \frac{R'(\psi_\Pi)\sin(\psi_\Pi)}{\sin(i)}, \qquad (6)$$

where $Z_{\Pi,\,max}$ is the projected height and i is the inclination angle of the galaxy's disc (such that $90°$ corresponds to edge-on). Since X/P structures arise from vertical oscillations ($\perp$ to the disc plane), the observed vertical extent is diminished in proportion to the observed disc inclination. We correct for this effect for non-edge-on galaxies in our sample through the use of equation (6), thus recovering the true vertical extent of the peanut, $z_{\Pi,\,max}$. We illustrate how $R_{\Pi,\,max}$ and $Z_{\Pi,\,max}$ are derived from an isophote in Fig. 1.

(iv) S_Π – the integrated strength of the X/P feature, which we define as

$$S_\Pi = 100 \times \int_{R_1}^{R_2} B_6(R)\mathrm{d}R, \qquad (7)$$

where R_1 and R_2 are the (major-axis) radii enclosing the part of the $B_6(R)$ profile higher than the peak half-maximum[2] ($\Pi_{max}/2$).

(v) W_Π – the X/P peak width, is the radial extent $R_2 - R_1$.

Although the harmonic profiles are typically plotted as a function of the isophotal semimajor axis, i.e. 'a' in Fig. 1, we plot B_6 as a function of R_Π [see equation (4) and Fig. 1].

In our analysis, an X/P feature can be 'strong' in two ways: when it displays a high B_6 amplitude, or if the peak in the B_6 profile is extended over a large radial range (i.e. a large W_Π). This will be more clear when we present actual B_6 profiles in the following sections, and is illustrated here schematically in Fig. 2. Both of these cases are accounted for in our definition of the peanut strength diagnostic, S_Π. We chose to perform the integral in equation (7) within the half-maximum limits so that the X/P feature is well separated from other potential components or the noise in the B_6 profile, as B_6 approaches zero. Throughout this work, we provide the X/P length, height, strength and peak width both in the usual angular units (arcsec), in kiloparsecs and in units of the disc exponential scalelength h. We prefer the latter, since it is more insightful from a galaxy structure perspective, and is independent of the distance to the galaxy.

Perhaps the most important advantage of our method is that it is simple, practical, and constitutes an objective and accurate way of measuring X/P structures. Moreover, it is not restricted to the strongest and most visibly obvious X/P bulges, but can detect and measure weaker structures, in regions of the galaxy where additional components (such as the bulge or the disc) dominate the isophotes.

---

[2] Variations of this can readily be envisaged, and we tested a few but preferred $\Pi_{max}/2$.

Table 1. The X/P sample.

Galaxy (peanut)	Telescope (filter)	Type	Scale (pc arcsec^{-1})	Inclination i ($^\circ$)	v_{rot} (km s^{-1})	$\sigma_\star$ (km s^{-1})	M_K (mag)
NGC 128 (a, b)	*HST, NIC*3 (*F160W*)	S0 pec	288	78	180±40*	211±32	−25.35±0.15
NGC 128 (b)	SDSS (r)						
NGC 678	*Spitzer* (3.6μ)	SB(s)b?	193	90	195±29	133±20	−24.29±0.15
NGC 2549 (a)	*HST* (*F702W*)	SA0^0(r)	95	75	160±10*	143±22	−23.40±0.15
NGC 2549 (b)	SDSS (r)						
NGC 2654	*Spitzer* (3.6μ)	SBab:	117	81	236±10	–	−23.45±0.15
NGC 2683	*Spitzer* (3.6μ)	SA(rs)b	32	82	218±7	118±18	−22.75±0.15
NGC 3628	*Spitzer* (4.5μ)	Sb pec	43	90	230±5	81±12	−23.67±0.15
NGC 4111	SDSS (i)	SA0$^+$(r):	75	90	89±6	147±22	−23.41±0.15
NGC 4469	SDSS (z)	SB(s)0/a?	19	75	18±9	107±16	−19.93±0.20
NGC 4710	*Spitzer* (3.6μ)	SA0$^+$(r)?	71	90	150±36	117±18	−23.25±0.15
NGC 7332	SDSS (r)	S0 pec	96	80	186±28	128±19	−23.47±0.15
ESO 443-042	*Spitzer* (4.5μ)	Sb:	175	90	191±8	–	−23.11±0.15

*v_{rot} of stars

3 DATA

It is difficult to decide upon the optimal observational data for edge-on peanut galaxies. An important consideration is dust obscuration, which is likely to be a problem for peanut galaxies because they are disc galaxies viewed, in the majority of cases, at high inclination or close to edge-on. Therefore, were their discs to have embedded dust lanes (which is quite common in actively star-forming spirals), the undesired obscuration would have a maximal impact. Opting for near-infrared (NIR) imaging has the advantage of revealing X/P structures which may be contaminated (or even completely obscured) in the visible bands by dust (Quillen et al. 1997). However, the disadvantage of NIR data is a broader point spread function (PSF), often with strong Airy rings. Should a galaxy contain a large number of point-like or (small) resolved objects (such as a bright active galactic nucleus, star clusters, etc.), their light is spread by the instrumental PSF into the diffuse galaxy light (i.e. the peanut, bulge, disc) and thus introduces noise/bias in the true shape of these components. To diminish this effect, shorter wavelengths are preferable, particularly since determining the shape of the peanut accurately makes it possible to detect weak or nested peanuts, which would otherwise be lost in the noise.

We compiled a sample of 11 nearly edge-on galaxies with known X/P structures from the literature (Sandage 1961; Tsikoudi 1980; Jarvis 1986; de Souza & Dos Anjos 1987; Shaw 1987; Shaw, Dettmar & Barteldrees 1990). We sourced the imaging for our sample from three archives, namely (i) the Hubble Legacy Archive[3] for visible and NIR imaging taken with the *Hubble Space Telescope* (*HST*) (ii) Data Release 9 (Ahn et al. 2012) of the Sloan Digital Sky Survey[4] (SDSS), where we generally opted for the redder bands (r, i, z), and (iii) the *Spitzer* Survey of Stellar Structure in Galaxies[5] (S^{4}G; Sheth et al. 2010; Buta et al. 2015) for NIR imaging (3.6μ and 4.5μ). We decided on the optimal source on a case-by-case basis, depending on the image availability, level of dust obscuration and field of view size. For NGC 128 and NGC 2549, we made use of more than one image.

Table 1 lists the full sample, together with the source archive and bandpass (filter), as well as the morphological classification from the Third Reference Catalogue of Bright Galaxies[6] (de Vaucouleurs et al. 1991, hereafter RC3). The inclination angle i of each galaxy is also listed, and was calculated from the axis ratio reported in Salo et al. (2015) for the S^{4}G galaxies, and in RC3 for the remainder, while assuming an intrinsic thickness of an edge-on disc of 0.22 (Unterborn & Ryden 2008). The intrinsic thickness is degenerate with the inclination: when a disc approaches an edge-on viewing angle, its axis ratio is dominated by its natural thickness. For this reason, all our galaxies with an RC3 value of $b/a < 0.22$ are assumed to be exactly edge-on ($i = 90^\circ$). Additionally, Table 1 lists the physical scale (pc arcsec^{-1}) of each image, corrected for infall into the Virgo Cluster and the Great Attractor, as provided by the NASA/IPAC Extragalactic Database[7] (NED), plus the 2*MASS*[8] K-band magnitude (M_K) of each galaxy, as listed in NED. Finally the gas rotational velocity (v_{rot}) and the stellar velocity dispersion ($\sigma_\star$) were retrieved from the HyperLeda[9] (Makarov et al. 2014) data base and are also listed in Table 1 for each galaxy. We used the v_{rot} of the gas reported by Giovanelli et al. (1986), Giovanelli et al. (2007), Haynes et al. (2011) and Braun, Thilker & Walterbos (2003) for NGC 678, NGC 4710, NGC 4469 and NGC 7332, respectively; the stellar rotational velocity reported by Bertola & Capaccioli (1977) and Simien & Prugniel (1997) for NGC 128 and NGC2549; and gas rotational velocities values reported by Courtois et al. (2009) for the rest of the sample.

In Table 1, those galaxies where an inner, nested peanut was found, are henceforth labelled with (a) for the inner peanut and (b) for the outer.

4 ANALYSIS

4.1 Methodology: modelling a strong peanut – NGC 128

Here we demonstrate our analysis of X/P bulges on the interesting, well known peanut galaxy NGC 128. This peculiar lenticular galaxy displays a very pronounced X/P structure (Fig. 3) and is in fact the first galaxy where such a feature was noted (Burbidge & Burbidge 1959).

The first image that we modelled was the SDSS r-band image. Using ISOFIT, nested isophotes were fit at increasing major-axis steps, each having full freedom in varying their geometric parameters, such as centre position, ellipticity (ϵ) and position angle (PA). ISOFIT distorts the purely elliptical shapes at each radial location through

---

[3] http://hla.stsci.edu
[4] https://www.sdss3.org/dr9/
[5] http://irsa.ipac.caltech.edu/data/SPITZER/S4G/
[6] http://vizier.u-strasbg.fr

[7] https://ned.ipac.caltech.edu
[8] http://www.ipac.caltech.edu/2mass/
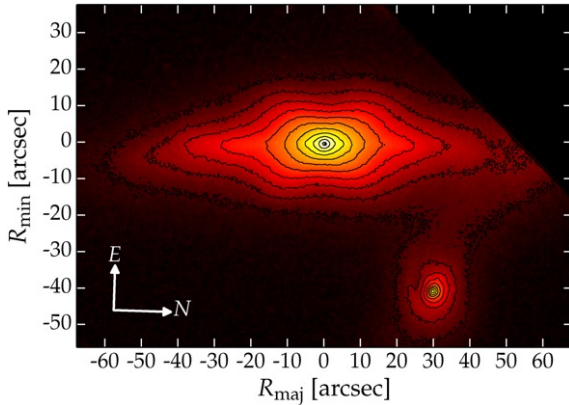[9] http://leda.univ-lyon1.fr

Figure 3. NGC 128 in the SDSS *r* band. This galaxy has a peculiar disc morphology, particularly at $R \gtrsim 40$ arcsec, which is likely related to its interaction with the companion galaxy NGC 127, also displayed here (to the west).

Fourier terms (equation 2) whose number (1 to *n*) are chosen at the start of the run. The modes chosen for our analysis were $n = 2, 3, 4, 6, 8,$ and 10. Briefly, $n = 2, 3,$ and 4 are the standard harmonics used in the literature ($n = 2$ fits the ϵ and PA, $n = 3$ fits for asymmetry and $n = 4$ for boxyness/discyness), whereas $n = 6, 8, 10$ are higher order terms which in general are negligible but for peanut galaxies are relevant ($n = 6$ is in fact crucial since this is the harmonic which describes the X/P feature, as we will show). Because odd-numbered harmonics capture ever more complicated asymmetries, we did not include $n > 3$ odd terms.

The first aspect analysed from our isophotal study was the major-axis surface brightness profile $\mu(R_{maj})$, which we subsequently decomposed into galaxy components. There is a long history of using analytical functions to describe the radial surface brightness profiles of galaxies and their components (see Graham 2013 for a review), with multicomponent (≥ 2) decompositions routinely fit these days (e.g. Laurikainen et al. 2014; Savorgnan & Graham 2016). The decomposition was performed with the software PROFILER (Ciambur, in preparation). PROFILER constructs a model $\mu(R_{maj})$ from user-defined analytical functions (such as Sérsic, exponential, Gaussian, etc.) each of which is intended to describe a particular photometric component (e.g. the disc, the bulge). The model is built by adding together all the components and then convolving the resulting profile with the instrumental PSF. This process is iterated until the best-fitting solution is found. PROFILER employs the Levenberg–Marquardt (Marquardt 1963) minimization algorithm, as well as a hybrid (fast Fourier transform-based + direct) convolution scheme. PROFILER has many desirable features, such as a fast minimization process (chiefly due to its efficient convolution scheme), an intuitive graphical user interface, and several options for the choice of PSF profile, specifically Gaussian or Moffat (Moffat 1969) functions, or any user-provided profile in the form of a table of values. For NGC 128, the PSF was characterized by fitting Gaussian profiles to bright unsaturated stars in the image, with the IRAF task IMEXAMINE.

The decomposition of NGC 128's surface brightness profile is shown in the top panel of Fig. 4. In addition to the spheroid component (red curve) and inclined disc component (blue curve), the profile also displays the signatures of two bar components, plotted in cyan. While multiple, nested, bars are known to occur in some galaxies (Friedli et al. 1996; Erwin et al. 2001; Erwin 2011), this instance is particularly interesting as the bulge of NGC 128 is peanut-shaped, and X/P structures are known to be associated with bars. Martinez-Valpuesta, Shlosman & Heller (2006) show how, in
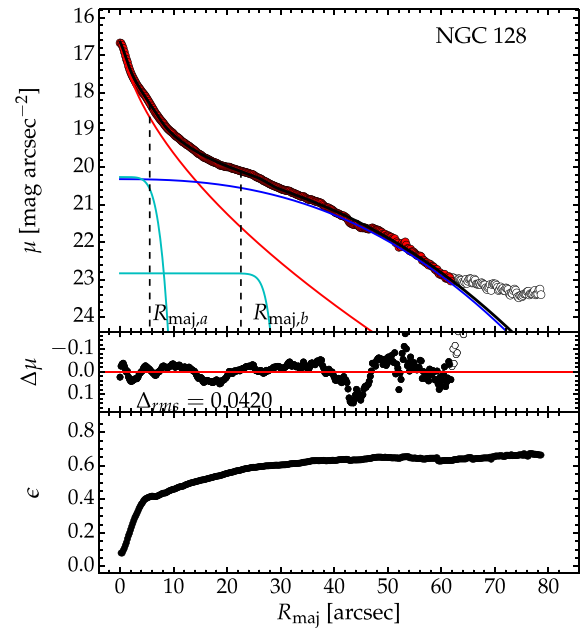
Figure 4. Top: the surface brightness profile of NGC 128, extracted from the SDSS *r*-band image, and decomposed into its constituent components: spheroid (red), edge-on disc (blue) and two bars (cyan). The dashed vertical lines correspond to the semimajor axis lengths of the isophotes associated with the inner (*a*) and outer (*b*) X/P structures. Middle: the residual profile (data – model). Bottom: the isophote ellipticity profile.

their simulations, bars can undergo recurrent buckling events, each giving rise to a progressively longer peanut-shaped structure, but the X/P structures themselves do not co-exist (they occur as single structures at different times, not a nested structure). For NGC 128 though, as we will show below, each of the two co-existing bars has its own corresponding peanut.

The second image that we investigated was a higher resolution image of NGC 128, taken with the *NICMOS*-3 (*NIC*3) instrument on board the *HST*. While the field of view is small, the better spatial resolution at smaller radii is ideal to showcase the X/P feature of this galaxy, and measure it more accurately than from the SDSS *r* band. Again, the modelling was performed with ISOFIT, and additionally, a two-dimensional reconstruction of the image was generated with the IRAF task CMODEL (also introduced in C15). NGC 128 and the reconstructed image are displayed in Fig. 5. The residual image (data minus reconstruction) is shown in Fig. 6.

If we were to generate a perfect model of the galaxy, then subtracting it from the image would produce a residual map in which the distribution of pixel values is centred on zero, and has some inevitable dispersion due to the noise in the data. However, failing to adequately capture a given photometric component leads to systematics in the residual, which broaden the pixel distribution and cause it to depart from a (narrow) Gaussian shape. We can discern which is the harmonic that captures the X-shape/peanut-shape from Fig. 6. The figure shows the distribution of pixel values in the residual image (left-hand panels) and the residual image itself (right-hand panels), for five values of the maximum harmonic order chosen in ISOFIT. The first (top) case corresponds to purely elliptical isophotes ($n = 0$),[10] for which the residual image displays obvious (and essentially expected) X-shaped systematics. The latter are reflected

---

[10] Strictly speaking, ISOFIT does use the $n = 2$ harmonic to adjust the ellipticity (ϵ) and PA of ellipses as they are fitted. However, once adjusted,
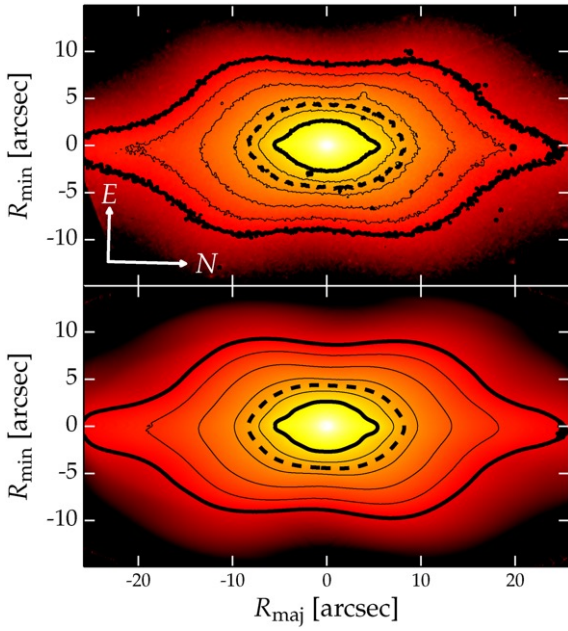
Figure 5. The *HST*/*NIC*3 image of NGC 128 (top) and the reconstruction with ISOFIT/CMODEL (bottom). The residual image resulting from subtracting the reconstruction from the image can be seen in the lower panel of Fig. 6. Both panels have contours overlaid (at the same intensity levels), to highlight the isophote shapes. The two solid thick contours represent the isophotes corresponding to the two peaks in the B_6 harmonic amplitude (see Fig. 7), while the thick dashed contours represent the isophote with the minimum B_6 amplitude between the two peaks.

in the relatively broad dispersion of the pixel distribution (the red curve), which also appears to be bi-modal: the bright features are compensated by dark features, each giving rise to its own peak. It is notable that upgrading the model's level of sophistication to the use of $n \leq 4$, i.e. the standard boxyness/discyness terms, does little to nothing to improve the fit. The dispersion is just as broad, still bi-modal, and the X-shape just as pronounced (Fig. 6, middle panels). This clearly shows that, for edge-on galaxies, the X/P feature cannot be quantified with the B_4 harmonic term. It is only when the sixth harmonic is included that the pixel distribution suddenly approaches a Gaussian shape, with a dispersion 2.3 times narrower than the $n \leq 4$ case (2.5 times narrower than for the pure ellipse model), and the X-shaped feature is adequately captured. The pixel distribution resulting from our highest quality model (corresponding to $n \leq 10$) is overplotted in black in all panels of Fig. 6. In passing, we note how ISOFIT/CMODEL enable the easy visual identification of a background spiral galaxy in the image of NGC 128.

The role played by B_6 is even more apparent when we plot the radial profiles of the harmonic coefficients. We show the even-n cosine coefficients output by ISOFIT in Fig. 7, for the range of harmonic orders $4 \leq n \leq 10$.

In Fig. 7, B_4 (which models boxyness/discyness, as usual) contributes significantly to the isophote shape. The B_4 profile indicates a transition from discy ($B_4 > 0$) to boxy ($B_4 < 0$) to discy again with increasing R_{maj}. However, it is not this harmonic which captures the X/P feature, but in fact the B_6 harmonic (Fig. 6). It is clear

the old ellipses distorted by $n = 2$ become new ellipses with no distortions ($n = 0$) but updated ϵ and PA.

that B_6 dominates over all other coefficients at $R_{maj} \gtrsim 20$ arcsec. This is in fact the locus where the peanut is most prominent, as we show in Fig. 5 through the outer thick contour (which corresponds to Π_{max}) overlayed on the data and the reconstructed image. As R_{maj} decreases, so does the B_6 amplitude, mirroring the isophotes becoming more elliptical (slightly boxy) and the peanut shape less and less apparent. The higher order harmonics are comparatively low-level, and most likely only serve to refine the final isophote shape, as we shall discuss below.

It is worth noting that at $R_{maj} \sim 5$ arcsec, there is another peak in the B_6 profile. While this is a radius where the isophote has contributions from other harmonic orders, it is likely that there is in fact a second, nested X/P structure in these inner regions. The use of ISOFIT, therefore, is essential in identifying and measuring very faint X/P structures that would otherwise not be detected.

Curiously, a faint 8-prong pattern is evident in the central ~ 6 arcsec of the residual image, when employing the $n \leq 6$ model (Fig. 6, third panel down). As the $n = 6$ harmonic describes the X/P shape, the $n = 8$ term then captures this fainter eight-spoked feature (see Fig. 7, third panel down). One can speculate that the latter pattern may reflect that in the central ~ 6 arcsec, the spheroid component contributes to the isophote shapes along the minor axis, and thus the spheroid, disc an peanut together induce a total of eight 'bumps' in the shapes of the inner isophotes: two from the disc (along the major axis), two from the bulge (along the minor axis) and four from the peanut's X-like 'arms'. This pattern might also be caused by the fact that the two nested X shapes are slightly offset from each other, i.e. they do not necessarily have the same point of origin and certainly do not have the same opening angle ψ of the X 'arm' relative to the major axis (see Table 2). This offset may therefore cause these low-level, leftover systematics, which are corrected by the higher order harmonics.

The five X/P diagnostics of NGC 128 were computed from both the *HST*- and SDSS-derived B_6 profiles (Figs 7 and 8). This was necessary because, due to the small field of view of the *HST* image, the integrated strength of the main (outer) peanut could not be measured reliably [R_2 from equation (7) corresponds to an isophote semimajor axis of ~ 38 arcsec, outside of the *NIC*3 CCD]. It also provided a consistency check for Π_{max}, $R_{\Pi, max}$ and $z_{\Pi, max}$ from two different images of the same galaxy. In addition to the main outer peanut, we also measured the five quantities for the inner peanut. The results are tabulated in Tables 2 and 3.

Figs 4 and 7 nicely show how the two X/P structures of NGC 128 are associated with its two bars. This is indicated through the major-axis radii of the isophotes corresponding to the two peanuts of this galaxy, namely $R_{maj, a}$ for the inner peanut and $R_{maj, b}$ for the outer. We draw the reader's attention to the fact that, for a given isophote, the projected peanut radius R_Π is different to the isophote's major-axis radius R_{maj}, the latter being always longer than the former (see Fig. 1). In Figs 4 and 9, we follow the standard practice of plotting the surface brightness profile as a function of isophote semimajor axis, i.e. R_{maj}. For consistency, we indicate in these two plots the R_{maj} of the isophotes having the maximum B_6 value, corresponding to the two peanuts. These two radii clearly correspond visually to approximately the ends of the inner and outer bars (i.e. the radii where the bar profiles cease to be flat and start to drop off in surface brightness), respectively, though we recognize that the actual peanut lengths are shorter than the bars, which is in agreement with simulations (see the review article by Athanassoula 2016, and also Athanassoula & Misiriotis 2002; Martinez-Valpuesta et al. 2006).
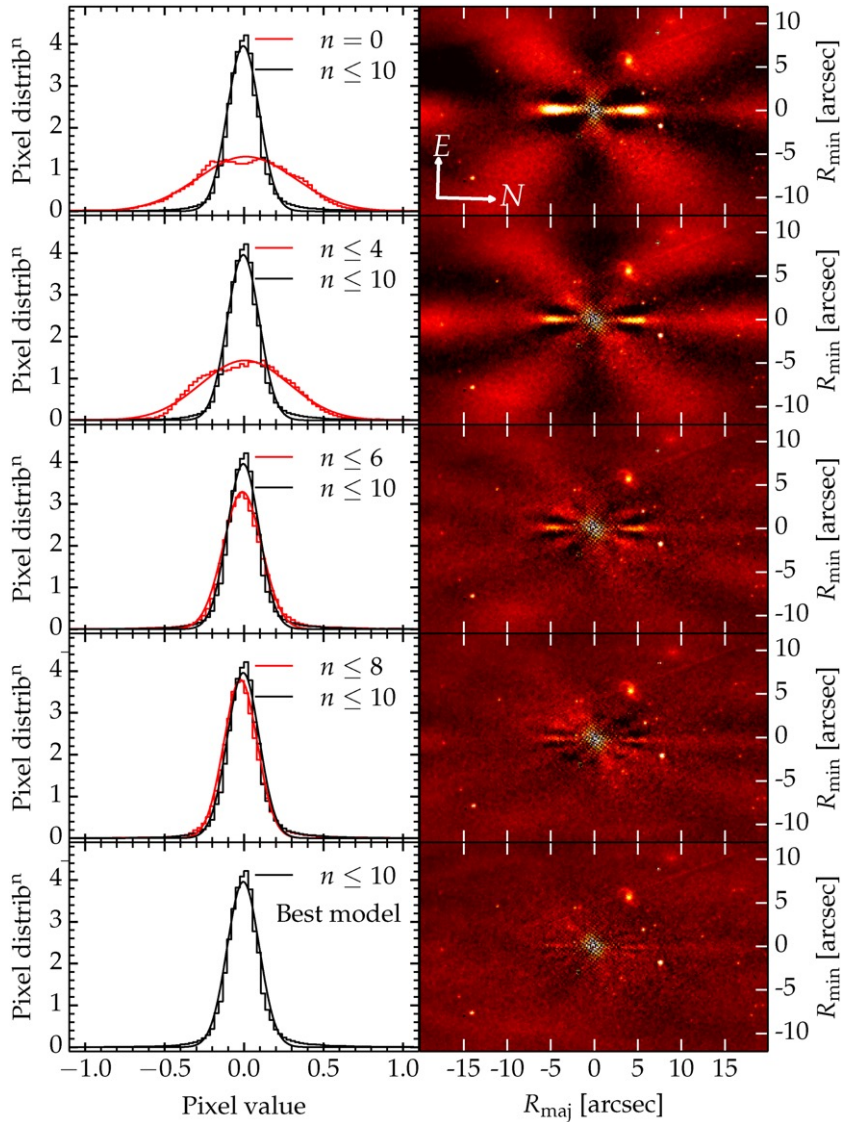
Figure 6. Finding the harmonic order which captures the X/P feature in NGC 128, based on the *NIC*3 image. Left-hand panels – the red curves represent the pixel distribution in the residual image for five upper limits in the number of harmonic terms, from top to bottom: $n = 0$, i.e. no harmonic terms, purely elliptical isophotes (top), $n \leq 4$ (middle), $n \leq 6$, $n \leq 8$ and our preferred model, $n \leq 10$ (bottom). The black curve is the same in all five panels, and represents the pixel distribution corresponding to the residual image from the highest quality model (i.e. the bottom panel), which corresponds to the reconstruction in Fig. 5 and is adopted throughout our work. Right-hand panels – residual profiles associated with the five cases considered on the left-hand side.

4.2 The full galaxy sample

Having now detailed the analysis and quantification of X/P structures in our case study of NGC 128, we now present the remaining galaxies. While NGC 128 hosts a remarkably strong and obvious peanut structure, this is not necessarily the case for all such galaxies (moreover, its inner peanut was hidden under the luminosity of the bulge and disc). Peanut bulges come in a wide range of shapes and sizes: some puffing up strongly outside the disc plane and showing a clear X-shape (e.g. NGC 3628, ESO 443-042), others (e.g. NGC 2654, NGC 2683) displaying so-called spurs (Erwin & Debattista 2013), some barely perturbing the discy/lenticular shape of their host [e.g. NGC 2549 (*b*)] while others showing peanut-like isophotes 'pinched' along the minor axis (e.g. NGC 128, NGC 4469). Nevertheless, our method of isophotal analysis proved robust for all of these cases, as the peanut invariably left its imprint on the radial B_6 profiles of these galaxies.

The results of the isophotal analysis (image, reconstruction, residual and B_6 profile) for each individual galaxy are shown in Appendix

A (Fig. A1), while we report the peanut diagnostics in Table 2. Before proceeding, provide some additional remarks concerning some of the galaxies in our sample.

(i) NGC 2549 – this is the second galaxy where we detect both an inner and an outer X/P structure. As for NGC 128, we denote the inner peanut with (*a*) and the outer with (*b*). Also similarly to NGC 128, we measured the diagnostics for (*a*) from an *HST* image, this time taken with the Wide Field (WF) + Planetary Camera (PC), WFPC 2. We refer the reader to fig. 8 in C15 to see the image, reconstruction and residual, and their fig. 10 to see the B_6 profile. However, because the peak in the outer peanut coincided spatially with the gap between the WF and PC chips, we again opted to model peanut (*b*) using the SDSS *r*-band image. We show the latter in Fig. A1 with an increased number of contours overplotted, to aid the eye in making out the inner peanut. Although we also see the signature of peanut (*a*) in the SDSS B_6 profile, we prefer the higher spatial resolution (and lower seeing) of the *HST* image for measuring it, since poorer seeing smears out and systematically
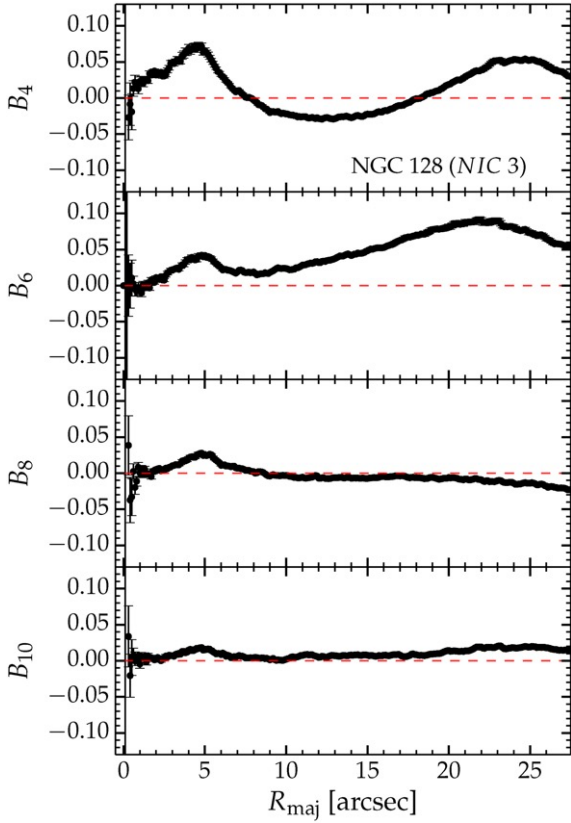
Figure 7. Dimensionless (see equation 3) even harmonic cosine coefficients (B_n) of the order of $4 \leq n \leq 10$, plotted as a function of isophote semimajor axis. B_4 represents boxyness/discyness, while B_6 captures the peanut shape and dominates in amplitude over the other harmonic orders at $R_{\mathrm{maj}} \sim 10$–25 arcsec (see also Fig. 8), where the X/P feature is most prominent. The higher orders have comparatively low amplitudes, and serve to refine the final isophote shape through small perturbations to the elliptical shape. Data extracted from the *NIC*3 image (Fig. 5).

underestimates the X/P peak (we see this in Table 2, where the B_6 profile of NGC 128 has lower amplitude for both peanuts in the SDSS data compared to the *HST* data). Again, we indicate the major-axis radii of peanuts (*a*) and (*b*) on the surface brightness profile
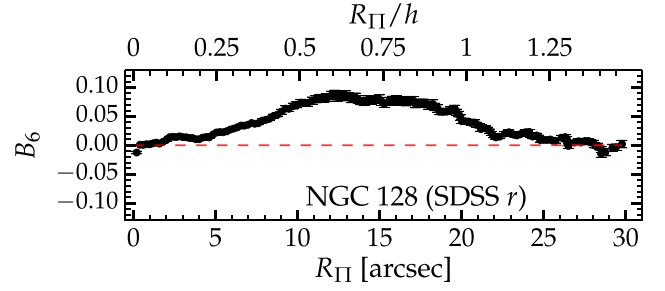
Figure 8. Extended B_6 profile of NGC 128, derived from the SDSS *r*-band image (Fig. 3).

decomposition (Fig. 9), and again we see that both radii match approximately the ends of the two bars: ∼10 arcsec for bar (*a*) (in good agreement with the range 8–10 arcsec reported in Laurikainen et al. 2011) and ∼30 arcsec for bar (*b*).

(ii) NGC 2654 and NGC 2683 – both of these galaxies display regions of comparatively low brightness, bordered by 'spurs', along the major axis on either side of the 'bulge', suggesting that they are boxy/peanut (Erwin & Debattista 2013) or barlens galaxies (Laurikainen et al. 2014; Athanassoula et al. 2015) viewed close to, but not exactly, edge-on, with a thin bar aligned such that its viewing angle $\alpha < 90°$ (i.e. not exactly side-on).

(iii) NGC 4111 – this galaxy appears to host an inner peanut as well, at ∼2 arcsec, in the SDSS *i*-band image. However, a closer inspection reveals an edge-on dust torus perpendicular to the disc plane at precisely this spatial scale. The obscuration which this induces causes the isophotes to appear 'pinched', just as they would if an inner peanut were there. Therefore, we chose to not classify this as an inner peanut, at least not until higher resolution NIR imaging is available (NB: the 'inner peanut' does not show at all in the B_6 profile extracted from the *Spitzer* imaging, both 3.6 and 4.5μ).

(iv) NGC 4469 – the major axis of this galaxy is heavily obscured by dust. As there is no NIR image available, we used the reddest SDSS passband (*z*) image, which has relatively poor S/N, and still shows the dust slightly, in the inner regions (see residual map). Nevertheless, the B_6 profile, though noisy, is robust and very nicely shows the peanut signature.

Table 2. The X/P diagnostics, in kpc.

Galaxy	h (arcsec, kpc)	$\Pi_{\max}$ (kpc)	$R_{\Pi,\,\max}$ (kpc)	$z_{\Pi,\,\max}$ (kpc)	S_Π (kpc)	W_Π (kpc)	ψ (°)	Shape
NGC 128 (*a*)[†]	–	0.042 ± 0.003	0.72 ± 0.02	0.70 ± 0.02	1.68 ± 0.59	0.53 ± 0.06	43.49	Hump
NGC 128 (*b*)[†]	–	0.091 ± 0.004	3.44 ± 0.02	2.58 ± 0.02	–	–	36.29	–
NGC 128 (*b*)[‡]	–	0.087 ± 0.008	3.54 ± 0.04	2.66 ± 0.09	24.64 ± 6.62	3.42 ± 0.24	36.39	HoP
NGC 678	$47.92 \pm 7.69, 9.25 \pm 1.48$	0.054 ± 0.006	2.67 ± 0.11	2.30 ± 0.11	5.51 ± 2.78	1.27 ± 0.31	40.72	Pyramid
NGC 2549 (*a*)[†]	$43.56 \pm 0.58, 4.14 \pm 0.06$	0.037 ± 0.002	0.53 ± 0.01	0.50 ± 0.01	0.96 ± 0.06	0.33 ± 0.02	42.35	Hump
NGC 2549 (*b*)[‡]	$43.56 \pm 0.58, 4.14 \pm 0.06$	0.030 ± 0.002	1.57 ± 0.03	1.12 ± 0.03	1.80 ± 0.60	0.76 ± 0.08	34.53	Hump
NGC 2654	$31.52 \pm 0.36, 3.69 \pm 0.04$	0.066 ± 0.008	2.25 ± 0.04	1.11 ± 0.07	4.31 ± 2.15	0.77 ± 0.19	26.08	HoP
NGC 2683	$87.18 \pm 4.5, 2.79 \pm 0.14$	0.036 ± 0.003	1.80 ± 0.04	0.95 ± 0.02	2.76 ± 0.66	0.93 ± 0.05	27.47	Saw-tooth
NGC 3628	$68.09 \pm 1.41, 2.93 \pm 0.06$	0.055 ± 0.007	3.08 ± 0.03	1.13 ± 0.03	6.74 ± 1.21	1.79 ± 0.07	20.05	Top-hat
NGC 4111	$30.51 \pm 0.34, 2.29 \pm 0.03$	0.035 ± 0.003	0.92 ± 0.02	0.56 ± 0.02	1.78 ± 0.59	0.62 ± 0.06	31.08	Hump
NGC 4469	$40.94 \pm 1.55, 0.78 \pm 0.03$	0.067 ± 0.007	0.69 ± 0.01	0.38 ± 0.01	1.36 ± 0.34	0.26 ± 0.02	27.78	Hump
NGC 4710	$31.05 \pm 0.25, 2.21 \pm 0.02$	0.059 ± 0.015	1.21 ± 0.08	0.60 ± 0.08	2.71 ± 1.22	0.60 ± 0.11	26.24	HoP
NGC 7332	$20.30 \pm 0.15, 1.95 \pm 0.01$	0.037 ± 0.003	1.44 ± 0.03	0.86 ± 0.06	3.10 ± 0.88	1.06 ± 0.08	30.36	Hump
ESO 443-042	$36.13 \pm 1.12, 6.32 \pm 0.20$	0.109 ± 0.045	3.32 ± 0.20	0.87 ± 0.20	8.93 ± 4.79	1.02 ± 0.28	14.38	HoP

[†]from *HST* image, [‡]from SDSS image

Note. Due to the non-exponential disc in NGC 128, we do not have an (exponential) scalelength h value.

Table 3. The X/P diagnostics, in units of h and arcsec.

Galaxy	$R_{\Pi, \max}$ (units of h, arcsec)	$z_{\Pi, \max}$ (units of h, arcsec)	S_Π (units of h, arcsec)	W_Π (units of h, arcsec)
NGC 128 (a)[†]	0.12 ± 0.01, 2.50 ± 0.15	0.12 ± 0.01, 2.43 ± 0.15	$-$, 5.8 ± 2.1	$-$, 1.8 ± 0.2
NGC 128 (b)[†]	0.59 ± 0.01, 11.95 ± 0.15	0.44 ± 0.01, 8.97 ± 0.15	$-$	$-$
NGC 128 (b)[‡]	0.61 ± 0.03, 12.28 ± 0.59	0.46 ± 0.03, 9.25 ± 0.59	$-$, 85.6 ± 23.0	$-$, 11.9 ± 0.9
NGC 678	0.29 ± 0.05, 13.83 ± 1.13	0.25 ± 0.09, 11.90 ± 1.13	0.60 ± 0.30, 28.6 ± 14.4	0.14 ± 0.03, 6.6 ± 1.6
NGC 2549 (a)[†]	0.13 ± 0.04, 5.60 ± 0.15	0.12 ± 0.01, 5.29 ± 0.15	0.23 ± 0.06, 10.1 ± 2.6	0.08 ± 0.01, 3.5 ± 0.2
NGC 2549 (b)[‡]	0.38 ± 0.02, 16.51 ± 0.59	0.27 ± 0.02, 11.77 ± 0.59	0.43 ± 0.15, 18.9 ± 6.3	0.19 ± 0.02, 8.0 ± 0.9
NGC 2654	0.61 ± 0.04, 19.19 ± 1.13	0.30 ± 0.04, 9.51 ± 1.13	1.17 ± 0.58, 36.8 ± 18.4	0.21 ± 0.05, 6.6 ± 1.6
NGC 2683	0.65 ± 0.07, 56.32 ± 1.13	0.34 ± 0.07, 29.57 ± 1.13	0.99 ± 0.24, 86.1 ± 20.7	0.34 ± 0.02, 29.2 ± 1.6
NGC 3628	1.05 ± 0.05, 71.69 ± 1.13	0.38 ± 0.05, 26.16 ± 1.13	2.30 ± 0.41, 156.7 ± 28.1	0.61 ± 0.02, 41.6 ± 1.6
NGC 4111	0.40 ± 0.02, 12.30 ± 0.59	0.24 ± 0.02, 7.41 ± 0.59	0.78 ± 0.26, 23.8 ± 7.8	0.27 ± 0.03, 8.3 ± 0.9
NGC 4469	0.89 ± 0.04, 36.32 ± 0.59	0.48 ± 0.07, 19.81 ± 0.59	1.75 ± 0.44, 71.6 ± 18.1	0.33 ± 0.02, 13.5 ± 0.8
NGC 4710	0.55 ± 0.03, 17.08 ± 1.13	0.27 ± 0.04, 8.42 ± 1.13	1.23 ± 0.55, 38.2 ± 17.2	0.27 ± 0.05, 8.5 ± 1.6
NGC 7332	0.74 ± 0.03, 15.00 ± 0.59	0.44 ± 0.03, 8.92 ± 0.59	1.59 ± 0.45, 32.2 ± 9.2	0.55 ± 0.04, 11.1 ± 0.8
ESO 443-042	0.55 ± 0.04, 19.96 ± 1.13	0.14 ± 0.04, 5.11 ± 1.13	1.41 ± 0.76, 51.1 ± 27.4	0.16 ± 0.04, 5.9 ± 1.6

[†] from *HST* image, [‡] from SDSS image
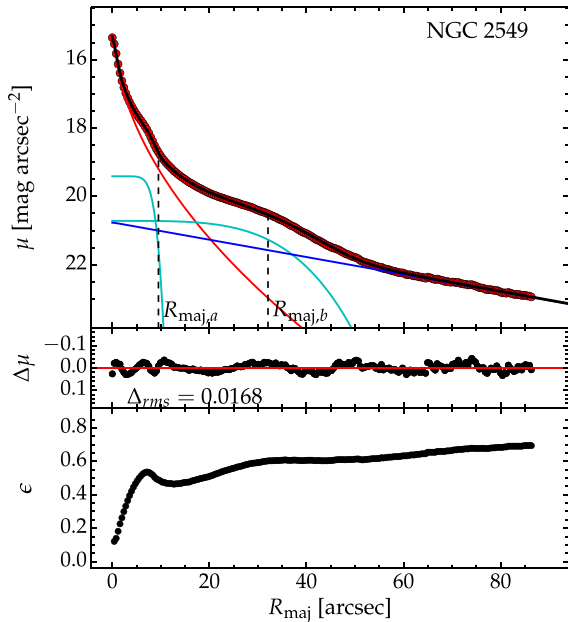
Figure 9. The decomposition of the SDSS r-band surface brightness profile of NGC 2549. Apart from a Sérsic (spheroid) and an exponential (disc) component, the profile also shows the signatures of two bars, modelled with Sérsic functions of low n (~ 0.1–0.2), and plotted as the cyan curves. As in Fig. 4, the major-axis radii of the isophotes associated with the two peanuts ($R_{\mathrm{maj},\,a}$ and $R_{\mathrm{maj},\,b}$) are indicated as vertical dashed lines.

(v) NGC 4710 – the image of this galaxy (and, much more obviously, the residual image) shows two pronounced stripes, which were attributed to dark stripes on the CCDs caused by a bright star (there are two because the image is a mosaic of different individual exposures).

For each galaxy in the sample, we extracted the major-axis surface brightness profile, $\mu(R_{\mathrm{maj}})$, and decomposed it with PROFILER to obtain the disc scalelength. As we have discussed above, X/P structures are closely associated with the galactic discs in which they are embedded. If a disc buckles and gives rise to a bar, which also buckles and gives rise to a peanut, the peanut may reflect the disc's fundamental properties. A pertinent question, therefore, is: are the peanut's metrics (size, shape) random, or do they depend on

their host disc's properties? We address this question by measuring the disc's scalelength h, and expressing the peanut height, projected length, peak width and integrated strength in units of h, as well in kiloparsecs. Because our test-case galaxy, NGC 128, displays very unusual (warped) morphology, and the surface brightness profile of its disc is not exponential, but Sérsic ($n \sim 0.4$; see Fig. 4), it is not meaningful to assign it a scalelength. As such, we only report values of h for the rest of the galaxies in our sample.

The PSF profiles used to convolve the model $\mu(R_{\mathrm{maj}})$ were always characterized from bright stars in the image of each galaxy. A second example of a PROFILER decomposition is shown for NGC 2549 in the top panel of Fig. 9, where the model consisted of a bulge (Sérsic function, red curve), a disc (exponential, blue curve) and a bar associated with each of the two peanuts (Ferrers functions – Ferrers 1877, cyan curves), once again nicely confirming the bar-peanut connection in this second galaxy with a nested peanut structure.

4.3 Scaling relations

The data show a remarkably tight correlation between $R_{\Pi,\,\max}$ and the integrated peanut strength S_Π (i.e. the area under the B_6 curve). We display this relationship in the upper panels of Fig. 10. As B_6 is dimensionless, with any radial dependence normalized out through equation (3), it is independent of $R_{\Pi,\,\max}$, and therefore so is S_Π, which is derived from the profile. This relation implies that stronger peanuts are located further out in a galaxy, and it is further surprising that, while reasonably tight in units of kpc, it also holds when expressing both quantities in units of the disc scalelength h (Fig. 10, top-left panel). This suggests that when a disc defined by a scalelength h buckles and forms a bar, which in turn gives rise to a peanut, the resulting peanut still retains the information about its parent disc's scalelength. This is consistent with the scenario proposed by Bureau et al. (2006), who suggest that the different components of galaxies with X/P features (including the peanut component itself) are dynamically coupled, and most likely all originated from the disc material.

We performed basic linear fits to all the trends plotted in Fig. 10, which we show as equations (8), (9), (10) and (11). As NGC 128 (b) appears to be an outlier from all the trends, we excluded it from the fits. The fact that this galaxy is an outlier is not entirely surprising considering its peculiarity. More specifically, in addition to its visibly distorted morphology, there is also evidence that it
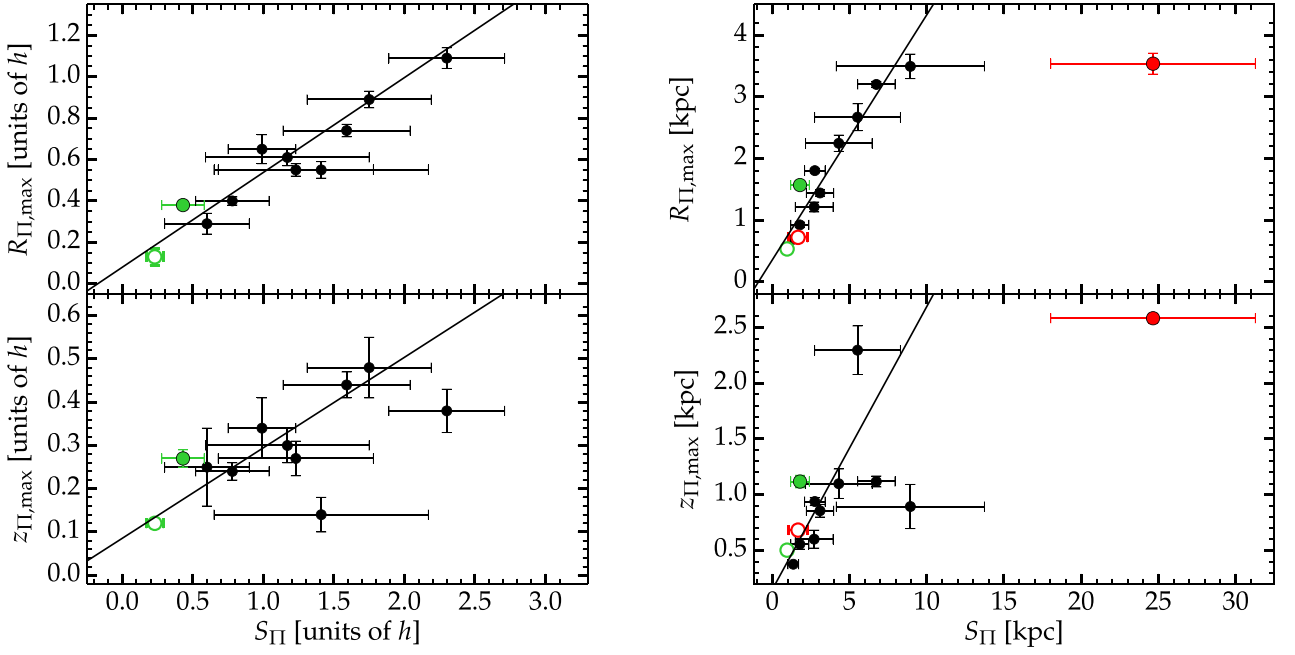
Figure 10. Left: projected radial length (top), and vertical height above the disc plane (bottom) of the X/P structures, as a function of integrated strength S_Π, all in units of the disc scalelength h. Right: the same quantities as in the left-hand panels, but plotted in kpc. Red symbols correspond to NGC 128 while green symbols correspond to NGC 2549; filled circles correspond to outer peanuts whereas open circles to inner peanuts. The linear relations shown are given by equations (8)–(11), and exclude the outer, outlying peanut of NGC 128.

hosts a counter-rotating gas disc, tilted at ~26° from its major axis (Emsellem & Arsenault 1997). Perhaps NGC 128 is an example of the scenario proposed by Binney & Petrou (1985), who argue that galaxy interactions (slow accretion: galactic cannibalism) may if not generate, then at least enhance the peanut shape. NGC 128 is just such a galaxy, and we deliberately show its companion NGC 127 in Fig. 3, which visibly exchanges material with it. In fact, several of our galaxies display somewhat distorted (S-shaped) disc planes, possibly indicating instability due to tidal interaction (e.g. NGC 7332). Note that we expect non-symmetric harmonics (both A_n and B_n coefficients) in galaxies observed in the process of bar-buckling. For such cases, the dominant shape of the instability would be a strong banana shape, which would likely be described by, e.g. $n = 3$ or, if the disc is comparatively bright at those radial scales, by $n = 5$ (in edge-on disc projection, side-on bar projection).

All the linear regressions were performed with the bisector method. The fit uncertainties were computed through bootstrap re-sampling (10 000 samples), which is best suited for such sparse data.

$$\frac{R_{\Pi,\text{max}}}{\text{kpc}} = (0.03 \pm 0.08) + (0.53 \pm 0.07)\frac{S_\Pi}{\text{kpc}} \qquad (8)$$

$$\frac{R_{\Pi,\text{max}}}{h} = (0.08 \pm 0.07) + (0.46 \pm 0.05)\frac{S_\Pi}{h} \qquad (9)$$

$$\frac{z_{\Pi,\text{max}}}{\text{kpc}} = (0.15 \pm 0.17) + (0.25 \pm 0.09)\frac{S_\Pi}{\text{kpc}} \qquad (10)$$

$$\frac{z_{\Pi,\text{max}}}{h} = (0.09 \pm 0.06) + (0.21 \pm 0.05)\frac{S_\Pi}{h}. \qquad (11)$$

That the peanut strength correlates with both its height and its length is not surprising, given that the latter two appear to be
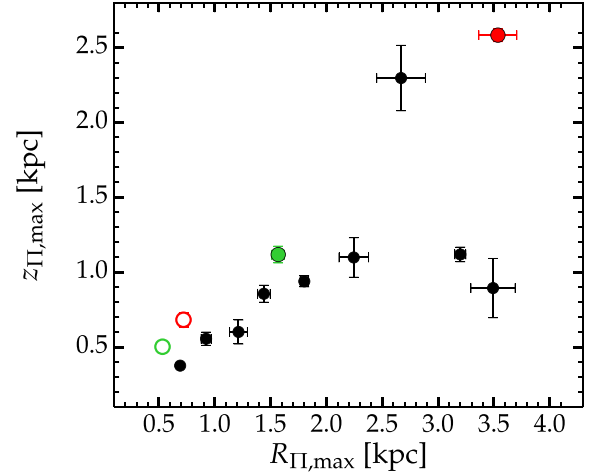

Figure 11. The smaller peanuts appear to follow a characteristic ratio of $z_{\Pi,\text{max}}/R_{\Pi,\text{max}}$ of ~0.5–0.6, while the larger peanuts appear to deviate from this. As in Fig. 10, the green symbols correspond to NGC 2549, while the red symbols correspond to NGC 128, and filled circles correspond to outer peanuts whereas open circles to inner peanuts.

correlated to each other. As shown in Fig. 11, the shorter ($R_{\Pi,\text{max}} \lesssim 2.5$ kpc) X/P structures follow a characteristic height-to-length ratio of ~0.5–0.6, which breaks down for the longer X/P structures. While the bar orientation [the $\sin(\alpha)$ term mentioned prior to equation (4)] may impact this trend, driving down the observed projected length if not viewed perfectly side-on, the discrepancies can be perhaps also understood from the point of view of the peanut's age or additional, non-secular processes, as we will speculate in Section 5.

In terms of the peanut height above the disc ($z_{\Pi,\text{max}}$), we found that for all galaxies in our sample this lies in the range $0.1h \leq z_\Pi \leq 0.5h$, or equivalently, within ~2.6 kpc. The stronger peanuts also
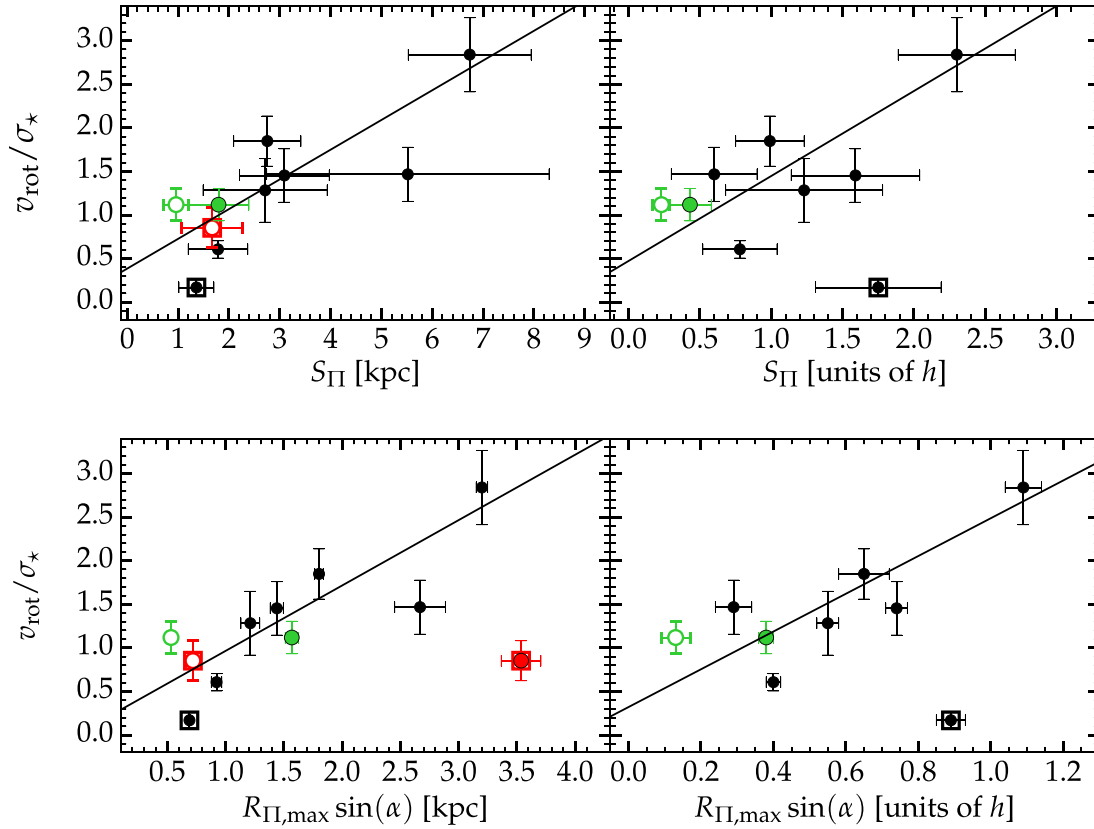
Figure 12. Top: the v/σ ratio as a function of peanut strength. The colour scheme is analogous to Figs 10 and 11. Data points enclosed in squares were excluded from the linear fits (see Section 4.3), which are given by equations 12 and 13).The data point corresponding to the outer peanut of NGC 128 is a significant outlier of this trend, and is outside (to the right of) the plot area (it was excluded from the fits, where applicable). Bottom: the v/σ ratio as a function of peanut length.

seem to reach greater heights above the disc plane, though this trend is not as tight as the location–strength relation.

4.3.1 Peanut-disc scaling relations

Just as 'bar strength' has been tested for correlations with properties of the host disc, such as star formation (e.g. Martinet & Friedli 1997; Aguerri 1999), nuclear activity (e.g. Laurikainen, Salo & Rautiainen 2002; Laurikainen, Salo & Buta 2004; Cisternas et al. 2013), central velocity dispersion (Das et al. 2008), various gaseous features (e.g. Peeples & Martini 2006; Kim, Seo & Kim 2012; see also Athanassoula, Machado & Rodionov 2013), etc., we can now test for correlations between peanut strength and the physical characteristics of the host disc. It is hoped that this will provide a further quantitative setting for testing the different mechanisms proposed for peanut formation, and thus a deeper understanding of their evolutionary path.

We observed a positive, though weak, correlation of the galaxy's $v_{\rm rot}/\sigma_{\star}$ (Fig. 12). This trend shows, in essence, that peanuts are more pronounced in faster rotating galaxies, once more pointing towards their link with the host disc. As before, we performed linear (bisector method) fits to the relations in Fig. 12, and estimated the uncertainties via bootstrap re-sampling. We show the relations as equations (12) and (13). We note, however, the exclusion of five data points from these fits, namely NCG 2654 and ESO 443-042, as we lacked values for their velocity dispersion, $\sigma_{\star}$; NGC 128(a) and (b), because of ambiguities arising from this galaxy's complicated

morphology (see Section 5); and NGC 4469, as we find that its reported value of $v_{\rm rot} = 18 \pm 9$ km s^{-1} is implausibly low for a rotation-supported, edge-on disc galaxy.

$$\frac{v_{\rm rot, \, gas}}{\sigma_{\star}} = (0.21 \pm 0.30) + (0.75 \pm 0.16)\frac{R_{\Pi,\max}}{\rm kpc}$$

$$= (0.32 \pm 0.48) + (2.17 \pm 0.82)\frac{R_{\Pi,\max}}{h} \qquad (12)$$

$$\frac{v_{\rm rot, \, gas}}{\sigma_{\star}} = (0.39 \pm 0.25) + (0.34 \pm 0.06)\frac{S_{\Pi}}{\rm kpc}$$

$$= (0.47 \pm 0.28) + (0.98 \pm 0.18)\frac{S_{\Pi}}{h}. \qquad (13)$$

We did not find any correlation between any of our X/P diagnostics and the galaxy global, K_s-band magnitude.

5 DISCUSSION

Having diagnosed and quantified the X/P features in our galaxy sample, we now shift the focus of the paper to discussing the information encoded in our peanut diagnostics.

Most studies in the literature invoke either the buckling of bars (Raha et al. 1991) or vertical Lindblad Resonances (Combes et al. 1990) to describe essentially the same class of objects. While numerical simulations have been resoundingly successful at reproducing, visually, X/P-like structures, direct comparisons between

observations and simulations have seldom been performed. As such, it remains an open question which physical mechanism is responsible for which type of X/P structure. Our study aims, among other things, to provide a set of useful measurements from real X/P galaxies which can act as constraints for *N*-body simulations of galactic dynamics (e.g. Saha & Gerhard 2013).

The first point to note is that our sample galaxies are remarkably heterogeneous in terms of their radial B_6 profile shape. While all show an unambiguous peak in B_6, which is the mark of the peanut, the peak can be shaped like a hump (e.g. NGC 128*a*, NGC 2549*a* and *b*, NGC 4111), hump-on-plateau (NGC 128*b*, NGC 2654, NGC 4710, ESO 443-042), top-hat (NGC 3628), saw-tooth (steady rise followed by sharp decline; NGC 2683, NGC 4469) or even pyramid (NGC 678). This is not very surprising since bars (and triaxial ellipsoids in general) can host a large variety of orbit families (Patsis, Skokos & Athanassoula 2002; Patsis & Katsanikas 2014a; Patsis & Katsanikas 2014b; Valluri et al. 2016), each of which potentially leaving its characteristic imprint on the photometric morphology of the host galaxy.

If a bar buckles, it forms a peanut in the inner regions (Raha et al. 1991; Athanassoula & Martinez-Valpuesta 2009), and one would expect a relatively flat B_6 profile (e.g. top-hat) along the entire peanut length. On the other hand, a resonance mechanism usually occurs in a narrow radial range, thus corresponding to a comparatively sharper peanut peak (e.g. hump or pyramid). It would be interesting to see from simulations (i) whether there is a characteristic B_6 shape for each of the two phenomenologies, and (ii) how the shape evolves with time.

We might be observing peanuts at different stages of their lifetime, i.e. newly formed or old. As these features have been shown to drift outwards with time (Quillen et al. 2014), the radial length $R_{\Pi, max}$, coupled with the peak width, W_Π, of the B_6 profile, might be an indicator of their age. The latter point is supported by noticing that for the two galaxies which host nested peanuts (NGC 128 and NGC 2549), the inner peanut (which is presumably the younger) has a narrower span than the outer, presumably older X/P structure. For this work, however, we are limited by projection effects and can only measure the projected peanut length, $R_{\Pi, max} = l_{\Pi, max} \sin(\alpha)$. This aspect is a strong restriction to any conclusions we may draw from Figs 10 to 12. For now, we speculate that we may see tentative evidence of radial drift (starting from the 'characteristic ratio' and moving out in radius while keeping the same height) or length/height enhancements due to external, non-secular processes, such as tidal interactions), though we require additional information on the bar's orientation in the disc plane to draw any conclusions. The key to constraining α may lie in applying our method to edge-on (disc) projections of simulated galaxies viewed at different bar angles α, ranging from side-on to end-on. The B_6 profiles, which may contain information about α, could easily be recovered from isodensity contours of the simulation projections (rather than isophotes). Such a study exceeds the scope of this paper, however, and we defer it for future works.

6 CONCLUSIONS

In this work, we define five quantitative diagnostics of X/P structures in edge-on galaxies, based on the sixth Fourier mode (B_6) of their isophotes: (i) the peak amplitude of the B_6 radial profile, Π_{max}, (ii) its projected length along the major-axis, $R_{\Pi, max}$, (iii) its height above the disc plane, $z_{\Pi, max}$, (iv) the integrated strength, S_Π (equation 7), and (v) the width of the B_6 peak, W_Π. Additionally, we introduce a qualitative classification of X/P galaxies, based on the shape of the B_6 profile.

We demonstrate our methodology on NGC 128, a galaxy with a very strong peanut, and extend our analysis to a sample of 11 other galaxies known to host such structures. This technique is accurate, easy to implemented and automate, and it performs best when using imaging with low dust obscuration (dust-free galaxies or NIR wavelengths).

Our main findings can be summarized as follows.

(i) The $n = 4$ Fourier harmonic of isophotes (B_4) does not describe the X/peanut-shaped structure. Out of all the Fourier harmonics tested ($0 \leq n \leq 10$), it is the $n = 6$ order (B_6 term) which captures the peanut.

(ii) We detect, for the first time, nested peanuts (one inner and one outer) in 2 of the 11 galaxies of our sample, namely NGC 128 and NGC 2549.

(iii) The galaxies in our sample are quite heterogeneous in terms of their B_6 profile shapes (which range from hump-shaped, hump-on-plateau, top-hat, saw-tooth and pyramid, in our classification scheme). We speculate that these may provide insight into disentangling between the various peanut formation scenarios in the literature.

(iv) We identified trends between peanut projected length and strength, and between peanut height and strength. The stronger peanuts are located at larger radii and reach greater heights above the disc plane. These trends hold when expressed in units of kpc and disc scalelength, indicating that peanuts 'know' about the disc in which they live. Together with an apparently characteristic height-to-length ratio for small peanuts, this constitutes valuable constraints for simulations.

(v) We additionally identified a positive, though weak, correlation between peanut parameters (length and strength) and the galaxy's $v_{rot}/\sigma_\star$, such that faster rotating galaxies tend to host larger and more pronounced X/P structures. This provides yet more support for the peanut-host disc link, but would benefit from more data.

There are many catalogues of edge-on disc galaxies (e.g. Dalcanton & Bernstein 2002; Kregel, van der Kruit & Freeman 2005; Kautsch et al. 2006; Yoachim & Dalcanton 2006; Comerón et al. 2011; Bizyaev et al. 2014) including even the late-type ultra-flat galaxies (Karachentseva et al. 2016) that can now be quantitatively analysed for the presence of X-shaped features. ISOFIT is also well placed to both search for and quantify, in addition to cataloguing, banana-shaped (in projection) bars in the act of buckling in real galaxies, through non-symmetric harmonic terms.

Additionally, kinematic follow-up of nested peanuts may be insightful, and several integral field spectrographs such as the Calar Alto Legacy Integral Field Area (Sánchez et al. 2012); the Sydney-AAO Multi-object Integral field spectrograph (Croom et al. 2012), the Mapping Nearby Galaxies survey (Bundy et al. 2015), or the Multi-Unit Spectroscopic Explorer (MUSE; Bacon et al. 2010) are ideal for this task (see for example Gonzalez et al. 2016, who study the X/P galaxy NGC 4710 with the MUSE instrument).

Furthermore, this method allows for direct comparisons between real, observed galaxies and simulations. Used in conjunction, an observational approach, coupled with *N*-body simulations, have the potential to disentangle the various X/P formation mechanisms proposed in the literature.

Such studies, however, are beyond the scope of this paper and, along with a study of the Milky Way's own peanut-shaped bulge, we defer them for future works.

ACKNOWLEDGEMENTS

REFERENCES

Aguerri J. A. L., 1999, A&A, 351, 43

Aguerri J. A. L., Beckman J. E., Prieto M., 1998, AJ, 116, 2136

Aguerri J. A. L., Méndez-Abreu J., Corsini E. M., 2009, A&A, 495, 491

Ahn C. P. et al., 2012, ApJS, 203, 21

Athanassoula E., 2005, MNRAS, 358, 1477

Athanassoula E., 2016, Astrophysics and Space Science Library, Vol. 418, Galactic Bulges. Springer Int. Publ., Switzerland, p. 391

Athanassoula E., Martinez-Valpuesta I., 2009, in Contopoulos G., Patsis P. A., eds, Boxy/peanut Bulges : Formation, Evolution and Properties, Springer-Verlag, Berlin, Heidelberg, p. 77

Athanassoula E., Misiriotis A., 2002, MNRAS, 330, 35

Athanassoula E., Machado R. E. G., Rodionov S. A., 2013, MNRAS, 429, 1949

Athanassoula E., Laurikainen E., Salo H., Bosma A., 2015, MNRAS, 454, 3843

Bacon R. et al., 2010, in McLean I. S., Ramsay S. K., Takami H., eds, Proc. SPIE Conf. Ser. Vol. 7735, Ground-based and Airborne Instrumentation for Astronomy III, SPIE, Bellingham, p. 773508

Beaton R. L. et al., 2007, ApJ, 658, L91

Bertola F., Capaccioli M., 1977, ApJ, 211, 697

Binney J., Petrou M., 1985, MNRAS, 214, 449

Bizyaev D. V., Kautsch S. J., Mosenkov A. V., Reshetnikov V. P., Sotnikova N. Y., Yablokova N. V., Hillyer R. W., 2014, ApJ, 787, 24

Braun R., Thilker D., Walterbos R. A. M., 2003, A&A, 406, 829

Bundy K. et al., 2015, ApJ, 798, 7

Burbidge E. M., Burbidge G. R., 1959, ApJ, 130, 20

Bureau M., Athanassoula E., 2005, ApJ, 626, 159

Bureau M., Freeman K. C., 1999, AJ, 118, 126

Bureau M., Aronica G., Athanassoula E., Dettmar R.-J., Bosma A., Freeman K. C., 2006, MNRAS, 370, 753

Buta R., Laurikainen E., Salo H., 2004, AJ, 127, 279

Buta R. J. et al., 2015, ApJS, 217, 32

Ciambur B. C., 2015, ApJ, 810, 120 (C15)

Cisternas M. et al., 2013, ApJ, 776, 50

Combes F., Sanders R. H., 1981, A&A, 96, 164

Combes F., Debbasch F., Friedli D., Pfenniger D., 1990, A&A, 233, 82

Comerón S. et al., 2011, ApJ, 741, 28

Courtois H. M., Tully R. B., Fisher J. R., Bonhomme N., Zavodny M., Barnes A., 2009, AJ, 138, 1938

Croom S. M. et al., 2012, MNRAS, 421, 872

D'Onofrio M., Capaccioli M., Merluzzi P., Zaggia S., Boulesteix J., 1999, A&AS, 134, 437

Dalcanton J. J., Bernstein R. A., 2002, AJ, 124, 1328

Das M., Laurikainen E., Salo H., Buta R., 2008, Ap&SS, 317, 163

de Souza R. E., Dos Anjos S., 1987, A&AS, 70, 465

de Vaucouleurs G., de Vaucouleurs A., 1972, Mem. R. Astron. Soc., 77, 1

de Vaucouleurs G., de Vaucouleurs A., Corwin H. G., Jr, Buta R. J., Paturel G., Fouqué P., 1991, Third Reference Catalogue of Bright Galaxies. Volume I: Explanations and references. Volume II: Data for galaxies between 0^h and 12^h. Volume III: Data for galaxies between 12^h and 24^h. Springer, New York, NY (RC3)

Debattista V. P., Carollo C. M., Mayer L., Moore B., 2005, ApJ, 628, 678

Dettmar R.-J., Barteldrees A., 1990, in Jarvis B. J., Terndrup D. M., eds, Eur. South. Obs. Conf. Workshop Proc., Vol. 35, ESO/CTIO Workshop on Bulges of Galaxies. ESO, Garching, p. 259

Dwek E. et al., 1995, ApJ, 445, 716

Emsellem E., Arsenault R., 1997, A&A, 318, L39

Erwin P., 2011, Mem. Soc. Astron. Ital. Suppl., 18, 145

Erwin P., Debattista V. P., 2013, MNRAS, 431, 3060

Erwin P., Vega Beltrán J. C., Beckman J., Sparke L. S., 2001, in Knapen J. H., Beckman J. E., Shlosman I., Mahoney T. J., eds, ASP Conf. Seri. Vol. 249, The Central Kiloparsec of Starbursts and AGN: The La Palma Connection, Astron. Soc. Pac, San Francisco, p. 85

Ferrers N. M., 1877, Q. J. Pure Appl. Math., 14

Friedli D., Wozniak H., Rieke M., Martinet L., Bratschi P., 1996, A&AS, 118, 461

Giovanelli R., Myers S. T., Roth J., Haynes M. P., 1986, AJ, 92, 250

Giovanelli R. et al., 2007, AJ, 133, 2569

Gonzalez O. A. et al., 2016, preprint (arXiv:1603.02546)

Graham A. W., 2013, in Oswalt T. D., Keel W. C., eds, Elliptical and Disk Galaxy Structure and Modern Scaling Laws, Springer Science+Business Media, Dordrecht, p. 91

Haynes M. P. et al., 2011, AJ, 142, 170

Jarvis B. J., 1986, AJ, 91, 65

Karachentseva V. E., Kudrya Y. N., Karachentsev I. D., Makarov D. I., Melnyk O. V., 2016, Astrophys. Bull., 71, 1

Kautsch S. J., Grebel E. K., Barazza F. D., Gallagher J. S., III, 2006, AAP, 445, 765

Kim W.-T., Seo W.-Y., Kim Y., 2012, ApJ, 758, 14

Kregel M., van der Kruit P. C., Freeman K. C., 2005, MNRAS, 358, 503

Kuijken K., Merrifield M. R., 1995, ApJ, 443, L13

Laurikainen E., Salo H., 2016, Astrophysics and Space Science Library, Vol. 418, Galactic Bulges. Springer Int. Publ., Switzerland, p. 77

Laurikainen E., Salo H., Rautiainen P., 2002, MNRAS, 331, 880

Laurikainen E., Salo H., Buta R., 2004, ApJ, 607, 103

Laurikainen E., Salo H., Buta R., Knapen J. H., 2011, MNRAS, 418, 1452

Laurikainen E., Salo H., Athanassoula E., Bosma A., Herrera-Endoqui M., 2014, MNRAS, 444, L80

Li Z.-Y., Shen J., 2015, ApJL, 815, 20

Lütticke R., Dettmar R.-J., Pohlen M., 2000, A&AS, 145, 405

Makarov D., Prugniel P., Terekhova N., Courtois H., Vauglin I., 2014, A&A, 570, A13

Marquardt W. D., 1963, J. Soc. Ind. Appl. Math., 11, 431

Martinet L., Friedli D., 1997, A&A, 323, 363

Martinez-Valpuesta I., Shlosman I., Heller C., 2006, ApJ, 637, 214

Méndez-Abreu J., Corsini E. M., Debattista V. P., De Rijcke S., Aguerri J. A. L., Pizzella A., 2008, ApJ, 679, L73

Merritt D., Sellwood J. A., 1994, ApJ, 425, 551

Moffat A. F. J., 1969, A&A, 3, 455

Molaeinezhad A., Falcón-Barroso J., Martínez-Valpuesta I., Khosroshahi H. G., Balcells M., Peletier R. F., 2016, MNRAS, 456, 692

Ness M. et al., 2012, ApJ, 756, 22

Ohta K., Hamabe M., Wakamatsu K.-I., 1990, ApJ, 357, 71

Patsis P. A., Katsanikas M., 2014a, MNRAS, 445, 3525

Patsis P. A., Katsanikas M., 2014b, MNRAS, 445, 3546

Patsis P. A., Skokos C., Athanassoula E., 2002, MNRAS, 337, 578

Patsis P. A., Athanassoula E., Grosbøl P., Skokos C., 2002, MNRAS, 335, 1049

Peeples M. S., Martini P., 2006, ApJ, 652, 1097

Quillen A. C., Kuchinski L. E., Frogel J. A., DePoy D. L., 1997, ApJ, 481, 179

Quillen A. C., Minchev I., Sharma S., Qin Y.-J., Di Matteo P., 2014, MNRAS, 437, 1284

Raha N., Sellwood J. A., James R. A., Kahn F. D., 1991, Nature, 352, 411

Regan M. W., Elmegreen D. M., 1997, AJ, 114, 965

Saha K., Gerhard O., 2013, MNRAS, 430, 2039

Salo H. et al., 2015, ApJS, 219, 4

Sánchez S. F. et al., 2012, A&A, 538, A8

Sandage A., 1961, The Hubble Atlas of Galaxies. Carnegie Institution, Washington

Savorgnan G. A. D., Graham A. W., 2016, ApJS, 222, 10

Schwarz M. P., 1984, MNRAS, 209, 93

Sellwood J. A., 1993, in Holt S. S., Verter F., eds, AIP Conf. Ser. Vol. 278, Back to the Galaxy. Am. Inst. Phys., New York, p. 133

Shaw M. A., 1987, MNRAS, 229, 691

Shaw M., Dettmar R.-J., Barteldrees A., 1990, A&A, 240, 36

Sheth K. et al., 2010, PASP, 122, 1397

Simien F., Prugniel P., 1997, A&AS, 126

Tsikoudi V., 1980, ApJS, 43, 365

Unterborn C. T., Ryden B. S., 2008, ApJ, 687, 976

Valluri M., Shen J., Abbott C. G., Debattista V. P., 2016, ApJ, 818, 141

Wegg C., Gerhard O., Portail M., 2015, MNRAS, 450, 4050

Whitmore B. C., Bell M., 1988, ApJ, 324, 741

Williams M. J., Bureau M., Cappellari M., 2009, MNRAS, 400, 1665

Yoachim P., Dalcanton J. J., 2006, AJ, 131, 226

APPENDIX A: MODELLING THE GALAXIES

In this section, we show the results of our ISOFIT/CMODEL analysis for each of the galaxies in our sample. Specifically, in each panel of Fig. A1, we show the galaxy image and its orientation, the image reconstruction made with CMODEL, the residual image obtained by subtracting the reconstruction from the original image and, at the bottom, the B_6 profile as a function of peanut radius (see Fig. 1). The image and its reconstruction both have their respective isophote contours overlayed (at identical levels), and the thicker contour corresponds to the maximum B_6 amplitude (Π_{max}).
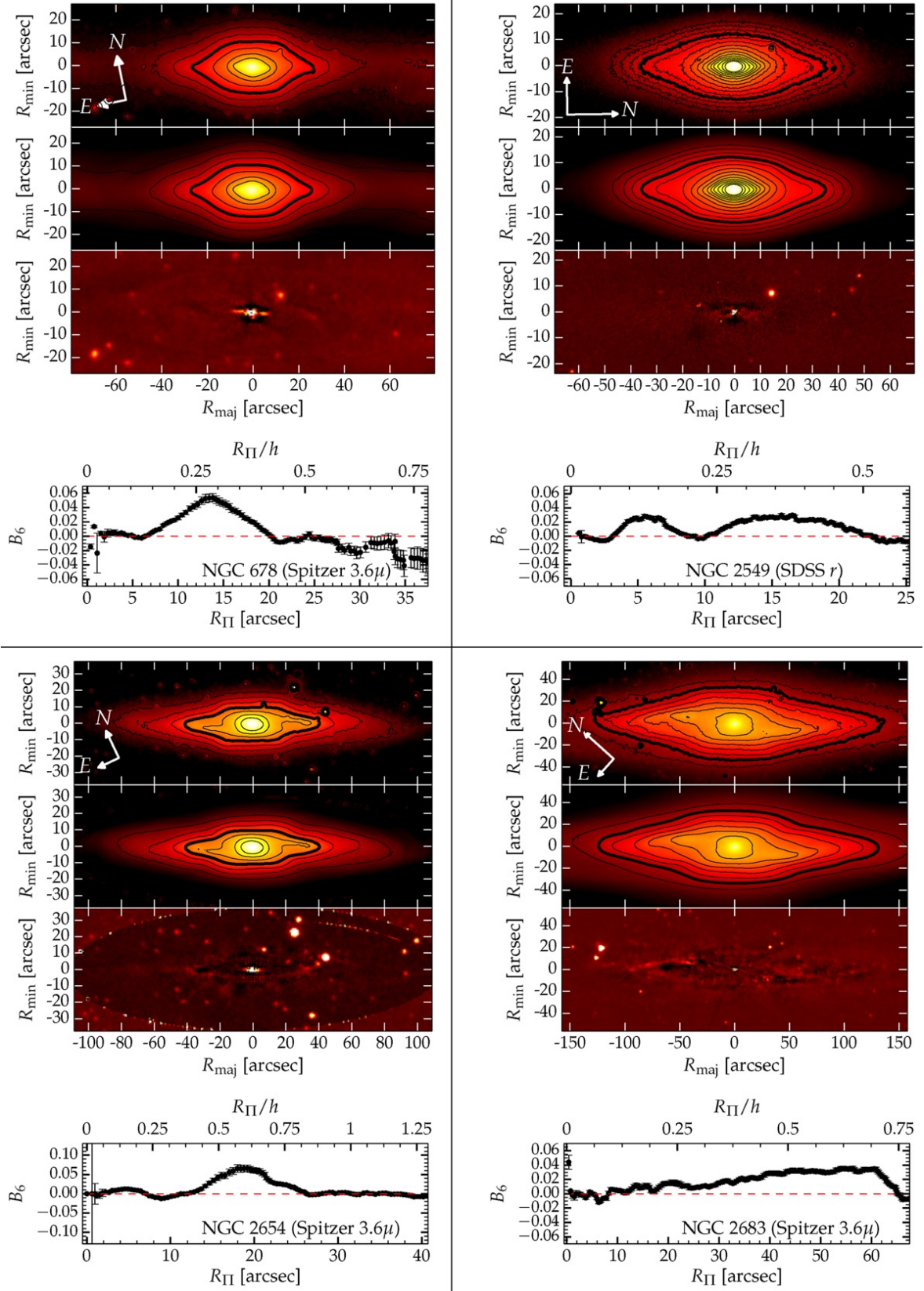
Figure A1. Each quadrant, from top to bottom panel: image, model, residual and B_6 profile. Thick contours correspond to Π_{max} (the isophote with maximal B_6 amplitude).
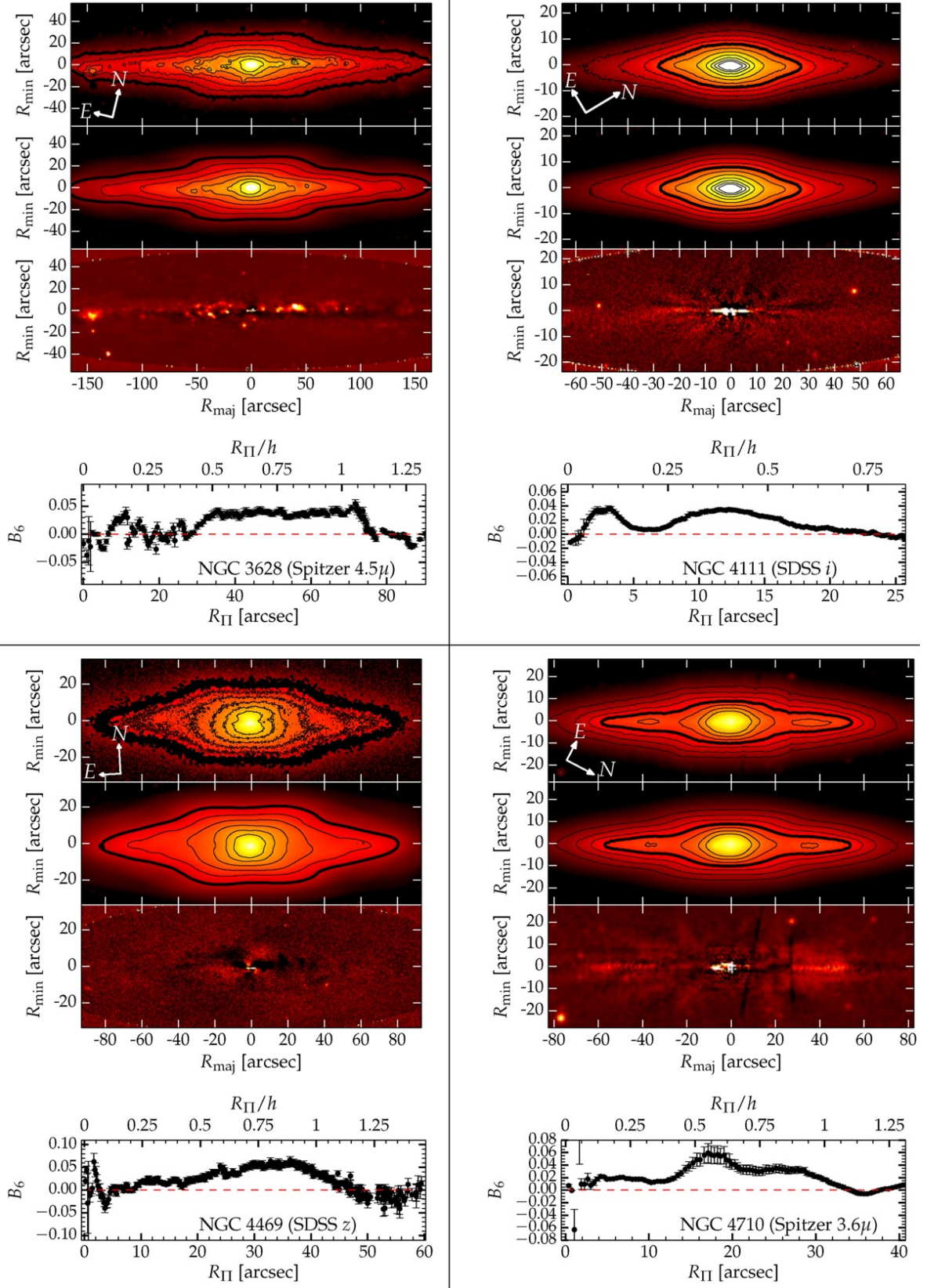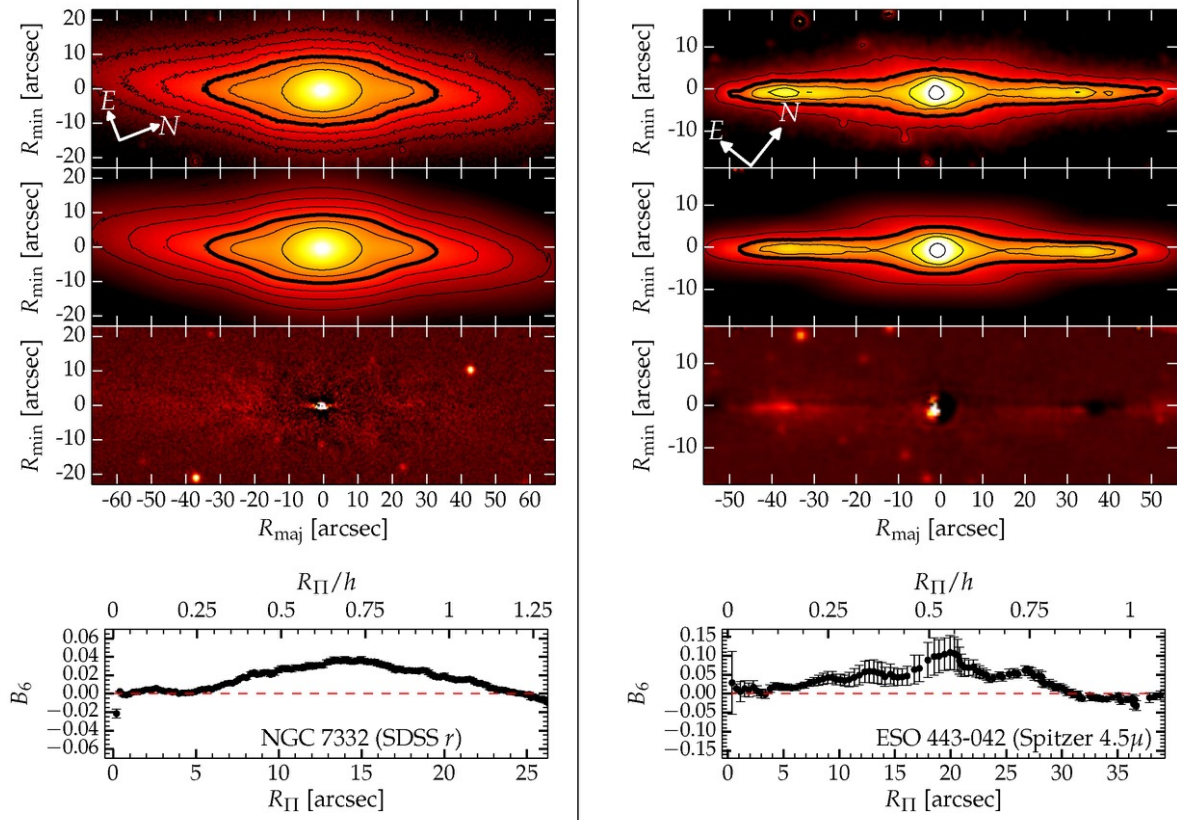
Figure A1 – *continued*.

Figure A1 *– continued.*

This paper has been typeset from a TEX/LATEX file prepared by the author.

4

Quantifying the Milky Way's Bar & (X/Peanut)–shaped Structure

In Chapter 3 we developed a comprehensive method to quantify X/P structures in edge–on disc galaxies, directly from photometric data. Here we turn our attention to the closest such peanut feature, that of our own Milky Way galaxy (Dwek et al. 1995; McWilliam & Zoccali 2010; Ness & Lang 2016, etc.). The Sun's placement within the Milky Way's stellar disc provides a unique close-up perspective of the X/P–shaped "bulge" emerging from the plane of the disc, in the direction of the Galactic Centre (GC) (Figure 1.2). However, inside the disc, the intervening stars and obscuring dust make it difficult to disentangle the in-plane stellar distribution (including the Galactic bar), and thus constrain the Milky Way's global morphology. Progress in this area has been made through in-plane, near-infrared star counts (Hammersley et al. 1994) or by analysing stellar populations that are tracers of structure, in the inner ~ 5 kpc (e.g., López-Corredoira et al. 2007; Wegg et al. 2015). To date the geometry (intrinsic size and orientation) of the "bulge" and long bar – the dominating components in this region – have remained disputed (§1.1.3).

In this Chapter, we tackle this problem with a new approach: by exploiting the two–dimensional information encoded in the X/P structure, and accurately quantifying it with the method presented in Chapter 3, we infer the properties of the long bar, from which it is expected to have formed. We run our analysis on WISE (Wide-field Infrared Survey Explorer; Wright et al. 2010; Lang 2014) images of the Milky Way, in two photometric bands (3.4 and 4.6 μm), to mitigate dust effects and ensure a robust and self-consistent analysis. One important difference between the Milky Way and the sample of Ciambur & Graham (2016) is that the Galaxy's X/P structure is oriented at an angle with respect to the Sun–(GC) line of sight. Coupled with its relatively close proximity, the inclination

induces an *East–West* asymmetry (in Galactic co-ordinates) in the isophotes about the GC, such that the near-side appears larger in projection than the far–side. This warranted a separate treatment of the two hemispheres. Measuring the projected radius of the X/P structure in the two directions provided a direct constraint on the orientation angle, and thus allowed the recovery of the *intrinsic* length of the peanut.

Building upon the theoretically-based X/P formation scenarios, where peanuts arise due to vertical buckling instabilities in the inner regions of bars (§1.2.2), we suggest that the Milky Way's X/P bulge is no different, i.e. it is the central part of, and thus aligned with, the long bar (see also Gerhard & Martinez-Valpuesta 2012; Wegg et al. 2015). More-over, recent studies indicate that X/P structures typically extend out to $\approx$ half the length of bars (Laurikainen & Salo 2017; Erwin & Debattista 2017). Bearing all this in mind, we treated the X/P structure as a proxy of the long bar, and thus inferred the geometry of the latter from our measurements of the former.

Finally, we explored how the parameters of the Milky Way's peanut compare with those of external galaxies, specifically the edge-on, X/P galaxy sample studied in Chapter 3. Correcting to a side-on view of the bar/peanut, we computed an average radial B_6 profile of the Milky Way, from which we extracted all the quantitative diagnostics of the X/P structure. As before, we normalised the X/P length, height and integrated strength by the exponential scale length of the disc, which we measured from the same data set by modelling the integrated (along the line-of-sight) light profile along the disc mid-plane, ac-counting for individual spiral arms. The Milky Way is broadly consistent with the scaling relations presented in the previous Chapter (Ciambur & Graham 2016), though appears to have a marginally stronger peanut than expected. This may indicate an X/P enhancement due to the Galaxy's interactions with its satellites, while, in addition, tentative evidence is presented that the buckling phase of the Milky Way's bar may have been recent.

The remainder of this Chapter consists of the article "*Quantifying the (X/Peanut)– Shaped Structure of the Milky Way – New Constraints on the Bar Geometry*", by B. C. Ciambur, A. W. Graham and J. Bland-Hawthorn, submitted to Monthly Notices of the Royal Astronomical Society, (under review).

Quantifying the (X/peanut)–shaped Structure of the Milky Way – New Constraints on the Bar Geometry

Bogdan C. Ciambur[1]⋆, Alister W. Graham[1], Joss Bland-Hawthorn[2]

[1] *Centre for Astrophysics and Supercomputing, Swinburne University of Technology, Hawthorn, VIC 3122, Australia*
[2] *Sydney Institute for Astronomy, School of Physics A28, University of Sydney, NSW 2006, Australia*

10 August 2017

ABSTRACT

The nature, size, and orientation of the Milky Way's bar and 'bulge' have been the subject of conflicting interpretations in the literature. Here we present a novel approach to inferring the properties of the long bar, which extends beyond the inner 'bulge', by using information encoded in the Galaxy's X/peanut (X/P)-shaped structure. We perform a quantitative analysis of the X/P feature seen in WISE wide-field images, at 3.4 μm and 4.6 μm, by measuring the deviations of the isophotes from pure ellipses and using the radial profile of their sixth order Fourier harmonic (cosine term, B_6). In addition to the vertical height and integrated 'strength' of the observed X/P instability, we report an intrinsic radius $R_{\Pi,\text{int}} = 1.67 \pm 0.27$ kpc, and an orientation angle of $\alpha = 37^{\circ}{}^{+7^{\circ}}_{-10^{\circ}}$ with respect to our line-of-sight to the Galactic Centre. Based on X/P-structures observed in other galaxies, we assume that the Milky Way's X/P-structure is intrinsically symmetric, aligned with the long Galactic bar, and that its size is correlated with this bar. The implications for the Galactic bar are that it is oriented at a 37° angle and has a radius of ≈4.2 kpc, but possibly as low as ≈3.2 kpc. We have investigated how the Milky Way's X/P-structure compares with analogues in other galaxies, and find that it is consistent with recently established scaling relations, though with a marginally stronger X/P instability than expected. We additionally perform a photometric decomposition of the Milky Way's major axis surface brightness profile, accounting for spiral structure, and determine an average disc scale length of $h = 2.54 \pm 0.16$ kpc.

Key words:
Galaxy: bulge – Galaxy: disc – Galaxy: fundamental parameters – Galaxy: structure

1 INTRODUCTION

Although the Sun's placement within the Galactic disc offers a restricted perspective of the Galaxy's central structural components, it has become generally accepted that the Milky Way is a barred galaxy (see Gerhard 2002 and Merrifield 2004 for reviews on the topic). Nevertheless, a consensus has yet to be reached on the exact details of its central components. There are conflicting interpretations in the literature with regard to the nature and geometry of the Galactic 'bulge': whether it is a classical or pseudo-bulge or both, the primary bar or the inner part of a longer, thinner bar, etc. The notion of a long, thin bar extending beyond the triaxial 'bulge' region ($10^{\circ} < l < 30^{\circ}$) was introduced by Hammersley et al. (1994), who found evidence for such

a structure from star counts in the Galactic plane. Building upon this, Hammersley et al. (2000), López-Corredoira et al. (2001, 2007) and Cabrera-Lavers et al. (2007, 2008) confirmed and characterised this long bar. Using red clump giant (RCG) stars – which are approximate standard candles (Stanek et al. 1994) – as tracers of the bar's structure, they obtained a bar approximately 4 – 4.5 kpc long and inclined at close to ∼ 43° with respect to the Sun–(Galactic Centre) line-of-sight (see also Sevenster et al. 1999). While other studies have reported lower bar viewing angles (38° ± 6° in Zasowski 2012; 30° ± 10° in Francis & Anderson 2012), these results nevertheless point to a misalignment between the newly discovered long bar and the inner triaxial 'bulge', which recent works place at an orientation angle of ∼ 20° – 30° (Babusiaux & Gilmore 2005, Cao et al. 2013, Wegg & Gerhard 2013).

The majority of barred galaxies display 'boxy', or

⋆ E-mail: bciambur@swin.edu.au

X/peanut (X/P)–shaped 'bulges'. These structures occur when orbital resonances (Combes et al. 1990) or buckling (Raha et al. 1991) cause the bars' inner parts to thicken vertically and take the characteristic 'X', or 'peanut' shape when viewed in close to side-on (bar) and edge-on (disc) projection, while in face-on views they often take the form of a 'bar-lens' (Laurikainen et al. 2011, 2014; Athanassoula et al. 2015, Laurikainen & Salo 2017). Recently, Ciambur & Graham (2016) (hereafter CG16) introduced a quantitative framework to characterise the properties of X/P structures, and additionally showed evidence, through a sample of twelve nearby galaxies with X/P 'bulges', that peanuts obey specific scaling relations. As a typical barred spiral galaxy, the Milky Way's 'bulge' too is X/P–shaped (Weiland et al. 1994, Dwek et al. 1995, López-Corredoira, Cabrera-Lavers & Gerhard 2005, Wegg & Gerhard 2013, Ness & Lang 2016). Multiple studies of the distribution, chemistry and kinematics of the stellar populations in the 'bulge' region support its X/P nature (e.g., McWilliam & Zoccali 2010, Ness et al. 2012, Vásquez et al. 2013, Zoccali et al. 2014, Rojas-Arriagada et al. 2014, Williams et al. 2016, Debattista et al. 2017), although see López-Corredoira (2016, 2017), Gran et al. (2016), Joo, Lee & Chung (2017).

From a dynamical point of view, the developing picture asserts that the Milky Way's peanut and long bar are different parts of essentially the same structure, i.e., the X/P structure is the central, vertically thickened part of the long bar (Combes et al. 1990, Martinez-Valpuesta & Gerhard 2011, Romero-Gómez et al. 2011, Zoccali & Valenti 2016), despite the slight misalignment between the two components. In support of this scenario, Wegg, Gerhard & Portail (2015) appear to reconcile this misalignment and find a long bar angle between $28°$ and $33°$, consistent with the orientation of the triaxial 'bulge'.

Since X/P structures arise from, and are thus part of, galactic bars, one can infer information pertaining to the latter by studying the properties of the former. For the Milky Way in particular, the eastern and western hemispheres of the X/P structure, viewed as they are, at different distances relative to the Sun, contain ample information both in the radial (in-plane) and vertical (off-plane) directions with respect to the disc. This in principle can constrain the X/P structure's orientation, and by extension, that of the Galactic bar, relative to the Sun. Moreover, the radial extent of X/P structures in other galaxies appears to correlate well with the length of their associated bars, with recent studies placing the ratio $R_{X/P}/R_{bar} \approx 0.4$–$0.5$ (Lütticke, Dettmar & Pohlen 2000, Laurikainen & Salo 2017, Erwin & Debattista 2017). Careful measurements of the Milky Way's X/P bulge therefore have the potential to reveal the geometry (extent and orientation) of the Galactic bar. This is one of the main goals of this study.

In this paper, we use for the first time the Milky Way's X/P structure as a proxy for the long bar, and thus constrain the latter's spatial extent and orientation angle based on the properties of the former. We characterise in detail the Milky Way's X/P feature and compare it with other nearby analogues. The remainder of the paper is structured as follows. §2 provides a theoretical outline of the methodology employed to extract quantitative diagnostics of the peanut structure, based on Ciambur (2015) (hereafter C15) and Ciambur & Graham (2016), as well as the peanut and

bar geometric parameters. §3 presents the wide-field WISE datasets and the analysis process, and the results are presented in §4, where the Milky Way is also compared with other, local X/P galaxies. The results are interpreted and discussed in §5, and finally we conclude with §6. Throughout this paper we employ Galactic co-ordinates and assume a distance of the Sun to the Galactic Centre of $R_0 = 8.2 \pm 0.1$ kpc (Bland-Hawthorn & Gerhard 2016).

2 THEORY

C15 has suggested that X/P structures likely leave an imprint in the 6th Fourier component of galaxy isophotes, specifically in the cosine term, B_6 (see Figure 1). Subsequently, CG16 demonstrated with a sample of twelve known X/P galaxies that this is indeed the case, and further introduced a methodology for extracting quantitative peanut diagnostics from a galaxy's radial B_6 profile[1].

2.1 The Quantitative X/P Parameters

In this work we apply the CG16 methodology to extract the parameters of the Milky Way's X/P structure. We briefly summarise these diagnostics here, and refer the reader to the aforementioned papers for further details.

(i) the peak value of the B_6 profile, denoted by Π_{max}.

(ii) the projected X/P radius, or half-length (R_Π), corresponding to the (major axis) radius where Π_{max} occurs. Note that the true, intrinsic, radius of a peanut is generally only measurable from a galaxy image when the bar is viewed perfectly side-on, or when its viewing angle (α in our notation) is known. However, as we show in §2.2, it is possible to directly constrain this angle for the special case of the Milky Way, due to our privileged location within the Galactic disc and relative proximity to the bar. Throughout the paper we denote the *intrinsic* (deprojected) radius by $R_{\Pi,int}$, and employ the convention $\alpha = 0°$ for end-on, and $90°$ for side-on, orientation.

(iii) the X/P height (z_Π) above the disc plane, a quantity computed from the isophote where Π_{max} occurs. In general this value depends on the disc's inclination with respect to the line of sight, reaching a maximum when the disc is edge-on. Fortunately, this is the case for the Milky Way, as the Sun is located roughly in the disc's plane with a planar offset of $z_0 = 25 \pm 5$ pc (Jurić et al. 2008).

(iv) the integrated X/P strength (S_Π) defined as:

$$S_\Pi = 100 \times \int_{R_1}^{R_2} B_6(R)dR \,, \qquad (1)$$

where the limits R_1 and R_2 enclose the part of the $B_6(R)$ profile above the peak's half-maximum ($\Pi_{max}/2$), and

(v) the B_6 profile's width (W_Π), equal to the full width at half-maximum (i.e. $R_2 - R_1$).

---

[1] The Fourier coefficients (including B_6) of a galaxy's isophotes vary with radius from the photocentre, such that each isophote has its own value. One can thus extract a radial B_6 profile.
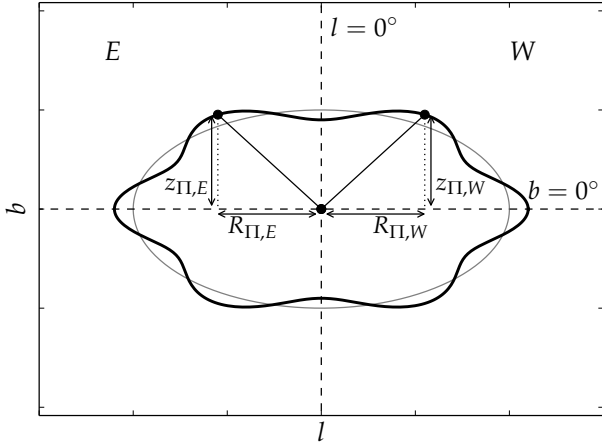
Figure 1. An X/P–shaped isophote (thick black), obtained by distorting an ellipse (thin grey) via a $n = 6$ order Fourier harmonic (cosine term, $B_6 = 0.1$). The X/P projected radius (R_Π) and vertical height (z_Π) above the disc plane (i.e., the $b = 0°$ plane) are derived from the isophote, as shown. Unlike the symmetric (side-on) X/P isophote shown above, the orientation angle and proximity of the Milky Way's X/P structure relative to the Sun induce an asymmetry in its isophotes about the $l = 0°$ axis, such that the near (*East*) side appears larger, in projection, than the far (*West*) side, i.e., $R_{\Pi,E} > R_{\Pi,W}$ and $z_{\Pi,E} > z_{\Pi,W}$ (see also Figure 2).

The galaxy isophote with the strongest B_6 perturbation, i.e., the isophote with semi-major axis associated with the peak of the radial B_6 profile ($\Pi_{\max}$), defines the X/P structure's projected radius (R_Π) and height (z_Π) above the disc, as shown in Figure 1. Note however that Figure 1 shows an X/P–shaped isophote that is symmetric about the $l = 0°$ direction, as it would be observed in an external, edge-on galaxy with its bar oriented perpendicular to the line-of-sight. Our perspective of the Milky Way's X/P structure is from within the disc plane ($b = 0°$), at relatively close proximity, and it is oriented at an angle with respect to the Sun–(Galactic Centre) line-of-sight, as illustrated in Figure 2. This perspective induces an asymmetry in its isophotes, such that the near (*East*) 'half' appears larger, in projection, than the far (*West*) 'half', i.e., $R_{\Pi,E} > R_{\Pi,W}$ and $z_{\Pi,E} > z_{\Pi,W}$. This asymmetry warrants a separate treatment of the eastern and western hemispheres of our data, but offers the possibility to recover the *intrinsic* radius and viewing angle of the X/P structure, as we show in the following subsection.

2.2 The Geometry of the Problem

The geometry of the (Sun – peanut) configuration is illustrated schematically in Figure 2, and shows how the two 'halves' of the peanut[2], which is oriented at an angle α with respect to our line-of-sight to the Galactic Centre (C), have different projected angular sizes. The half nearer to the Sun (*East* of the Galactic Centre) has a larger angular size (β)

[2] This schematic holds for any symmetrically elongated structure viewed at relatively close proximity, such as the Galactic bar itself.

while the more distant half (*West* of the Galactic Centre) appears shorter (γ). The angles β and γ, and the distance between the Sun and the Galactic Centre (i.e., SC $\equiv R_0$) are the only quantities needed to obtain the intrinsic (not apparent) radial extent of the peanut ($R_{\Pi,\text{int}}$) and orientation angle (α), which are given by:

$$R_{\Pi,\text{int}} = \sqrt{R_\beta^2 (1 - \eta) + R_0^2 \eta \left[1 - \frac{(1 - \eta)}{\cos^2(\beta)} \right]}, \qquad (2)$$

where R_β is the projected radius of the peanut eastward of C, on a plane located at a distance R_0 from the Sun, i.e., $R_\beta \equiv R_{\Pi,E} = R_0 \tan(\beta)$, and η is given by the ratio:

$$\eta = \frac{R_\beta - R_\gamma}{R_\beta + R_\gamma}, \qquad (3)$$

where $R_\gamma (\equiv R_{\Pi,W})$ is the analogue of R_β, but westward of C (see Figure 2). The orientation of the peanut structure, i.e., the angle α between the peanut and the line-of-sight towards the Galactic Centre, is given by:

$$\alpha = \cos^{-1}\left(\eta \frac{R_0}{R_\Pi} \right). \qquad (4)$$

The derivation of these equations, based on Stweart's theorem, is provided in Appendix B. Note that this framework operates on the assumption that the X/P structure is essentially 1D, as in Figure 2. However, the bulge is by all accounts triaxial (Pérez-Villegas, Portail & Gerhard 2017), and so its in-plane width, coupled with our perspective of it, adds some uncertainty. For example, in their Fig. 6, López-Corredoira et al. (2007) illustrate how the inclination angle of a triaxial ellipsoid viewed in projection can be over-estimated and, respectively, its intrinsic radius under-estimated, due to the different angular positions of the structure's true, and apparent (projected), ends. This effect is proportional to the in-plane 'thickness' of the elongated structure, and to its length relative to R_0.

3 DATA ANALYSIS

3.1 WISE Data

To measure the properties of the Milky Way's X/P structure, we use two wide-field, infrared images (at 3.4 and 4.6 μm) of the Galaxy, observed with the Wide-field Infrared Survey Explorer (WISE) satellite (Wright et al. 2010, Mainzer et al. 2014). The images are identical to those used in Ness & Lang (2016) except that they cover a slightly wider field of view. They were generated (D. Lang, private communication) by resampling the publicly released NEOWISE-*Reactivation*[3] first-year data, particularly the "unWISE" (Lang 2014) co-adds from Meisner, Lang & Schlegel (2017), into a Galactic coordinate system.

One advantage of this particular dataset is that both images were observed in a wavelength regime where dust effects – obscuration at shorter wavelengths and dust glow at longer – are minimal, though still present (we discuss this
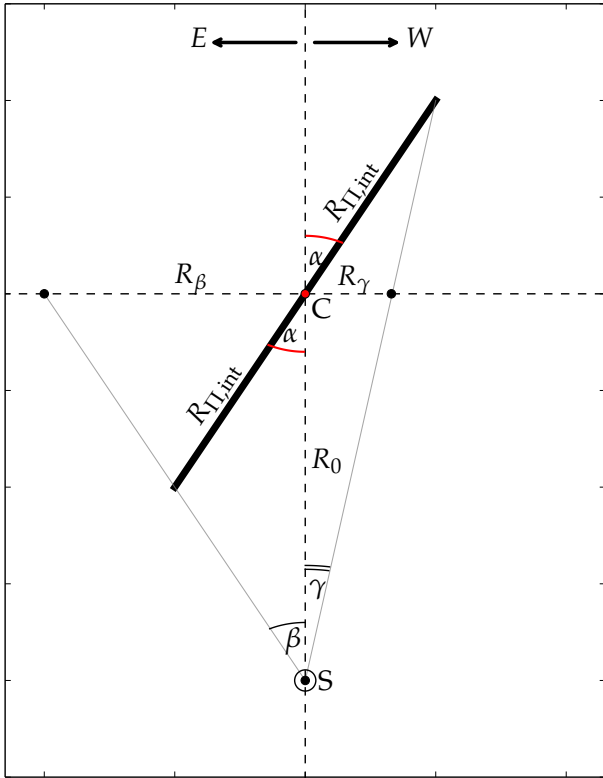
[3] http://neowise.ipac.caltech.edu/

Figure 2. A schematic representation of the (Sun+peanut) configuration, viewed from above the Galaxy. S represents the Sun, C the Galactic Centre, and their separation is denoted by R_0. The thick line represents the peanut structure, which has an intrinsic radius of $R_{\Pi,\mathrm{int}}$, and makes an angle α with the line-of-sight from S to C. Finally, the projected angular sizes of the peanut, to the left (E) and to the right (W) of C, are labelled as β and γ respectively, and correspond to the projected radii R_β and R_γ at a distance R_0.

further in §A2). This can be readily noticed in Figure 3, which shows the raw $3.4\,\mu$m image (panel *a*) and $4.6\,\mu$m image (panel *c*). Moreover, performing our analysis on distinct datasets is useful for checking the robustness of the method, and results, to various biasing aspects, like data quality, or the amount/type of contamination (such as dust obscuration or extended bright sources, e.g., star clusters), which do not affect the two images the same.

3.2 Pre-processing the Raw WISE Images

Before extracting the X/P parameters, both images were pre-processed in order to reduce, as much as possible, contamination from dust or bright sources such as star clusters, both visible in the raw images (Figure 3). This was done by taking advantage of the fact that such contamination is unlikely to occur symmetrically at both positive and negative Galactic latitudes (b and $-b$), i.e, above and below the mid-plane, for a given Galactic longitude l. Each image was traversed pixel by pixel and, wherever a pixel of coordinates (l, b) was determined to have a value significantly offset from its local background (2.5σ above or 2σ below the median within a 15×15 pixel box around the pixel of inter-

est), it was replaced by its symmetric counterpart $(l, -b)$ on the opposite side of the disc mid-plane, provided that the latter pixel was not offset from its local background as well. The results of this pre-processing are displayed in Figure 3, panel *b*) for the $3.4\,\mu$m observation and panel *d*) for the $4.5\,\mu$m image. The pre-processed images were tested against the raw images by performing the subsequent analysis on both sets, and no systematic effect of the pre-processing was found. The various radial profiles extracted from the images (surface brightness profiles, ellipticity and B_6 profiles, etc.) did not differ in shape nor amplitude but only in the noise level, which was noticeably higher in the raw data.

The noise-reduced images were then convolved with a Gaussian kernel to produce a smoother (more diffuse) light distribution. This was done because ISOFIT, like most isophote-fitting codes, was designed to model external galaxies where the light is not discretised (individual stars are not resolved). Several values for the kernel size (dispersion σ) were tested and the value of $\sigma = 5$ pixels was adopted, as it presented the best compromise between undersmoothing (light still discretised) and oversmoothing (erasing structures).

Our relatively close proximity to the bar+peanut gives rise to an apparently asymmetric X/P structure, with a larger limb to the *East* of the Galactic Centre and a smaller one to the *West*, as discussed in §2.2 (see also Figure 3). Consequently, the eastward and westward sides were modelled separately, in both images, by generating mirrored images reflected about the $l = 0°$ axis. We show these four reflected images in Figure 4, where panels *a* and *b* correspond to the near (E) and far (W) side reflections, respectively, for the $3.4\,\mu$m data, while panels *c* and *d* are analogous, but for the $4.6\,\mu$m data. Interestingly, panels *a* and *c* (the reflected near-side of the peanut, at both wavelengths) appear to display a slight additional asymmetry, between the northern and southern hemispheres of the X/P structure. In particular the 'arms' of the X–shape seem to extend further apart at positive latitudes compared to negative latitudes. However, this apparent asymmetry is not evident in the reflected far-side images (panels *b* and *d*).

The final step in preparing the data was to manually mask the four reflected images. In addition to the left-over regions still affected by dust (mostly at $3.4\,\mu$m), the (thin) disc was also masked. While CG16 retained the galaxy discs in their analysis (their 12 galaxies were also oriented nearly edge-on), the situation is different for the Milky Way because we are inside the disc. As such, the radial light profile along the mid-plane appears shallower than it would, were we observing from well outside the disc (i.e., the disc appears comparatively brighter at increasing distance from the centre than it would, were we not observing from within it). In order to avoid any biasing of the isophote shape caused by this effect, we thus excluded the major axis (the range $b = \pm \approx 2°.5$) and relied on the data in the remaining azimuthal range of the isophotes to constrain their shape. This effect is not important for the structural components of interest (bar, peanut) since the Sun is well outside of them. Manually masking the dust-affected regions is common practice in galaxy photometric modelling, and the results are usually robust to the amount of masking (except in extreme cases). This, coupled with the low levels of dust in our data (almost exclusively in the thin disc plane, which was already
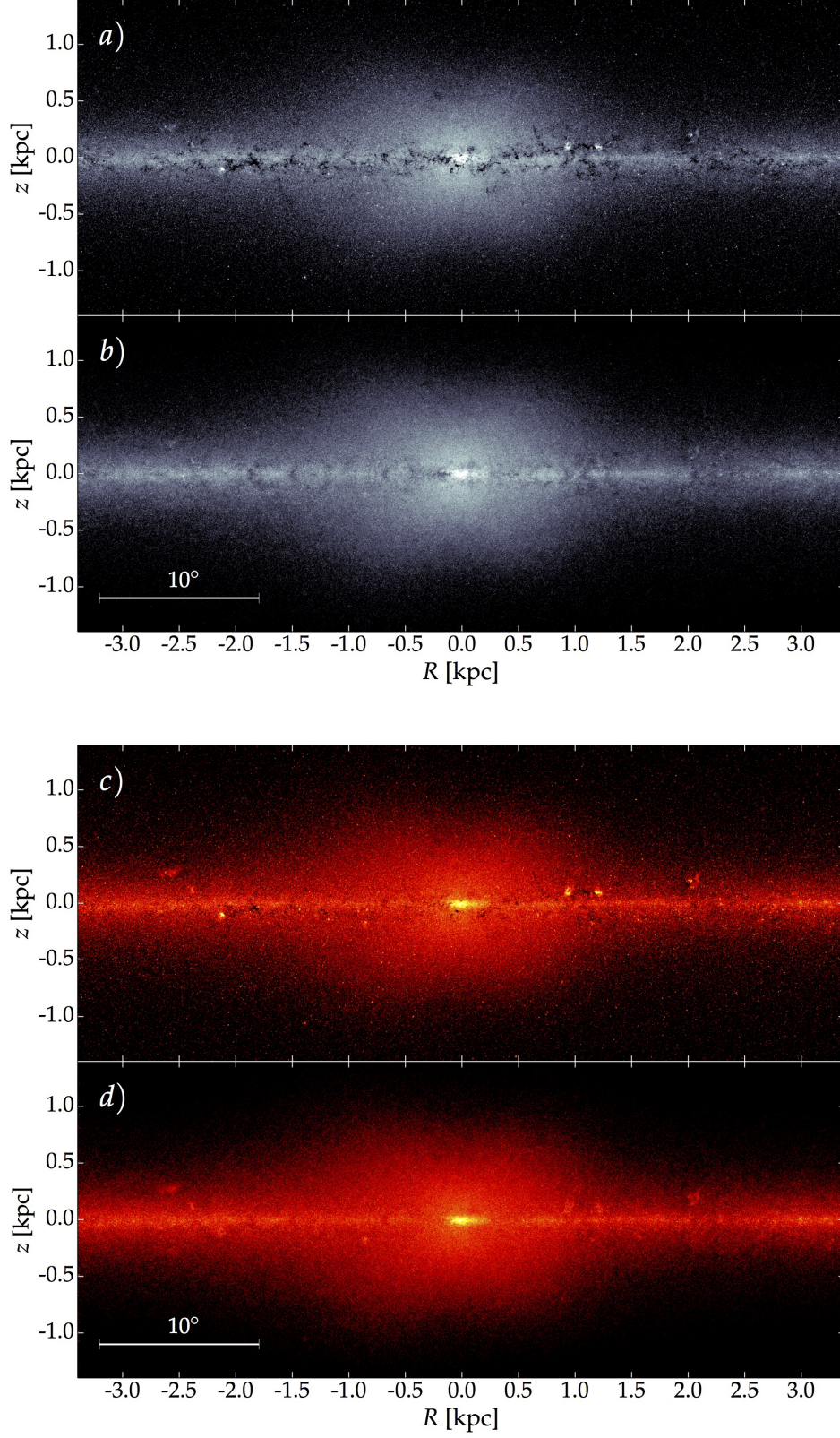
Figure 3. The Milky Way's X/peanut–shaped structure, observed by WISE at $3.4\,\mu$m (a) and $4.6\,\mu$m (c). Scale assumes $R_0 = 8.2$ kpc. Image stretch adjusted to highlight the X/P structure. Panels b) and d) correspond to the results of our pre-processing by symmetric replacement process (see text) intended to reduce contamination from dust or extended sources like star clusters.
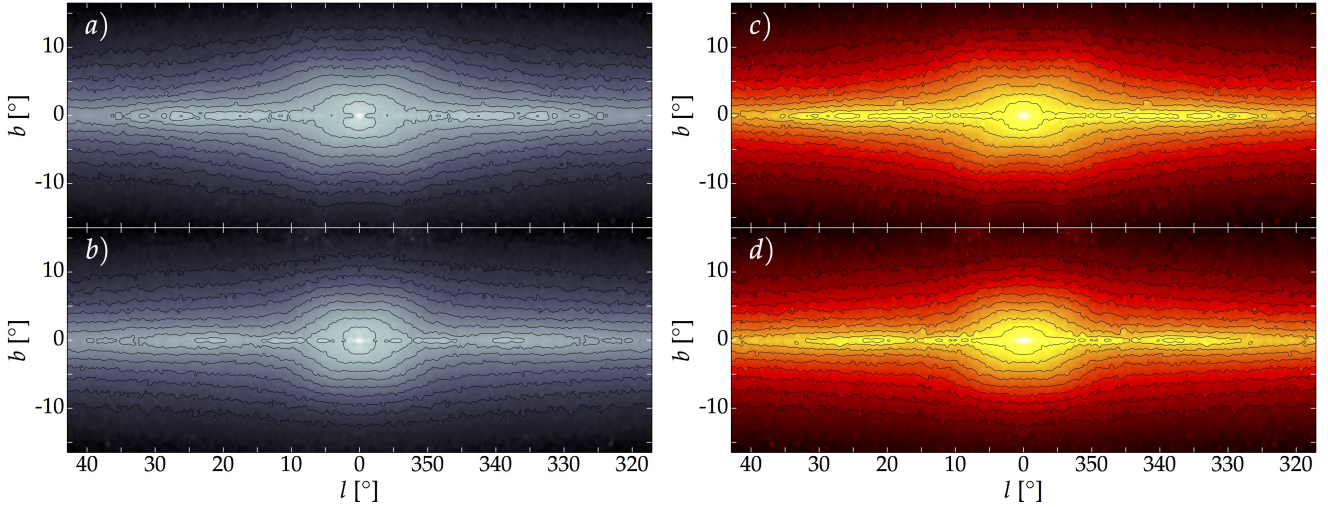
Figure 4. Milky Way images reflected about the $l = 0°$ axis. **Left:** $3.4\,\mu$m image: E hemisphere reflected to the W (a) and vice versa (b). **Right:** $4.6\,\mu$m image: E hemisphere reflected to the W (c) and vice versa (d). Compared to Figure 3, the panels have a larger field-of-view, and the stretch has been adjusted to display a broader dynamical range. The contours are in 0.5 mag steps and the levels are the same in all four panels.

excluded for different reasons), did not warrant a more in-depth treatment of dust for this stage of the analysis.

3.3 Modelling the Milky Way's X/P Structure

The image analysis was performed by running the isophote-fitting task ISOFIT (C15). We ran ISOFIT on the four processed images (E and W reflections, 3.4 and $4.6\,\mu$m, Figure 4), choosing a linear radial sampling step, fixing the isophotes' centre and position angle and allowing the ellipticity to vary.

The four resulting radial B_6 profiles are shown in Figure 5. One can immediately discern the apparent asymmetry in the B_6 profile about the Galactic Centre ($l = 0°$), caused by our perspective of the bar and peanut structure, as discussed in §2.2. The two peaks where the peanut structure is a maximum, indicated by the vertical dashed lines in Figure 5, mark the projected angular sizes of the two peanut limbs, which were computed to be: $\beta = 8°.25 \pm 0°.45$ and $\gamma = 5°.96 \pm 0°.44$. This same methodology for quantifying peanut sizes was employed in CG16. The full range in which the B_6 term is present in the isophotes extends roughly twice as far out ($\approx 16°.5\,W, -10°.5\,E$), at which point both sides curiously display a small 'bump' just before reaching zero. The outer limits of positive B_6 are not of interest for our purposes, however, for several reasons. First, the outer 'edge' of the B_6 signature corresponds to its faint outskirts, where the precise termination point of the feature becomes ambiguous due to noise – this is seen in Figure 5 – or to other photometric components, such as the disc, beginning to dominate the light (the disc is particularly relevant for the Milky Way, since we observe the X/P structure through the disc). Second, previous studies that have measured X/P structures relied on identification techniques (e.g., visual inspection, unsharp masking) that are sensitive to the point where the feature is strongest, not weakest. To keep consistency with the literature, on which we will draw in the following Sections, we remain within the CG16 framework
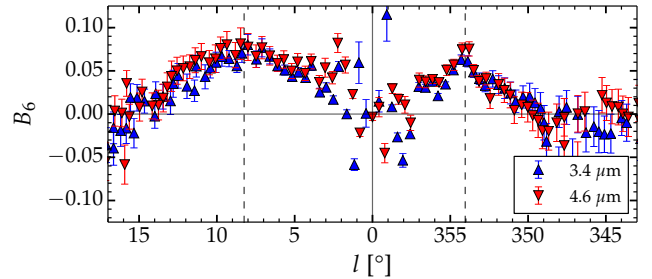

Figure 5. The B_6 harmonic amplitude as a function of Galactic longitude l. The E and W profiles peak at different projected angular distances (β and γ in Figure 2) from the Galactic Centre due to our perspective of the Milky Way's bar/peanut structure. The locations of the two peaks, indicated by vertical dashed lines, allow for the computation of the length and viewing angle of the X/P structure and, by proxy, of the bar.

and use the B_6 profile peak as the most reliable scale of the X/P structure. Nevertheless, the full range of the B_6 profile is still of interest, as it provides the width (W_Π) and 'shape' of the profile, which are additional quantitative and, respectively, qualitative measures of peanut structure. Also apparent from Figure 5 is that the X/P structure is slightly more prominent in the redder $4.6\,\mu$m band than at $3.4\,\mu$m.

4 RESULTS

4.1 The (X/P Structure + Bar) Geometry

In §3 we have measured the apparent (projected) extent of the Milky Way's X/P structure, E and W of the Galactic Centre, which we shall now use to obtain the intrinsic radius of the peanut ($R_{\Pi,\text{int}}$) as well as its orientation angle α with respect to our line-of-sight to the centre of the Galaxy. We have determined the radial location of the B_6 profile peak in the two directions (Figure 5) to be $\beta = 8°.25 \pm 0°.45$ and

$\gamma = 5°.96 \pm 0°.44$. These yield an intrinsic radius of the X/P structure of $R_{\Pi,\text{int}} = 1.67 \pm 0.27$ kpc from Equation 2, and an orientation angle of $\alpha = 37°{}^{+7°}_{-10°}$ from Equation 4. The uncertainties have been computed according to Appendix B, using Equations B10 (δR_{Π}) and B23 ($\delta^{+,-}\alpha$). The outer bounds (east and west) where the B_6 profile declines to zero (see Figure 5) could, in principle, also be used to constrain α. Estimating these points to occur at $\approx 16°.5\,W, -10°.5\,E$ yields a value for the orientation angle of $44°{}^{+10°}_{-13°}$. However, as explained in §3.3, the greater statistical and systematic uncertainties, as well as possible biasing from disc light, associated with these outer radial locations make this measurement less reliable than using the B_6 peak, which we do throughout the analysis.

Multiple studies, based on stellar populations and numerical simulations, have shown evidence that the Milky Way's central 'bulge' is not (primarily) the remnant of past merger events, i.e., a 'classical' bulge, but rather it was built predominantly from disc stars through the buckling and secular evolution of the Galactic bar, the latter itself originating from the disc (Shen et al. 2010, Ness et al. 2012, 2013; Di Matteo et al. 2014; Di Matteo 2016; Abbott et al. 2017; Debattista et al. 2017; see also Fragkoudi et al. 2017). This result is consistent with the X/P morphology and indicates that the X/P 'bulge' and bar are aligned, since one has formed from, and is still the thick central part of, the other (see also Martinez-Valpuesta & Gerhard 2011, Romero-Gómez et al. 2011 and Wegg, Gerhard & Portail 2015). There may be a small merger-built component to the Galactic bulge, with half light radius $R_e \approx 0.5$ kpc, assuming $h = 2.54 \pm 0.16$ kpc (see §A2 in Appendix A, where we model the Milky Way's radial light profile) and $R_e/h \approx 0.2$ (Courteau, de Jong & Broeils 1996, Graham & Worley 2008). However, we exclude the data in the inner 500 pc in §A2 and do not address the issue of a classical bulge in this paper, nor a nuclear bar, nor a nuclear disc (Alard 2001, Launhardt, Zylka & Mezger 2002, Nishiyama et al. 2005, Gerhard & Martinez-Valpuesta 2012). Here we assume that strictly the X/P structure is aligned with the long bar and use it as a proxy for its orientation angle (α as above) as well as its extent.

From a sample of 88 galaxies with X–shaped bulges, Laurikainen & Salo (2017) measured a mean $R_{\Pi,\text{obs}}/R_{\text{bar}}$ ratio of ≈ 0.4, in good agreement with Lütticke, Dettmar & Pohlen (2000). The former authors, however, also found a subtle dichotomy in normalised (by bar length) sizes of X–shapes and those of barlenses, computing average ratios typically higher than $\gtrsim 0.5$ for barlenses. They concluded, based on the argument that X/P 'bulges' and barlenses are the same structures viewed at different angles, that the intrinsic ratio is likely ≈ 0.5 for both (see their Fig. 8). More recently, Erwin & Debattista (2017) place the mean of this ratio in the range $0.42 \leqslant R_{\Pi,\text{obs}}/R_{\text{bar}} \leqslant 0.53$, where the lower and upper limits are determined by different definitions of bar length. With this in mind, based on the peak of the B_6 profile we estimate that the Milky Way bar has a radius of 4.2 ± 0.68 kpc if the $R_{\Pi,\text{int}}/R_{\text{bar}}$ ratio is 0.4, but may be as short as 3.2 kpc if $R_{\Pi,\text{int}}/R_{\text{bar}} = 0.5$.
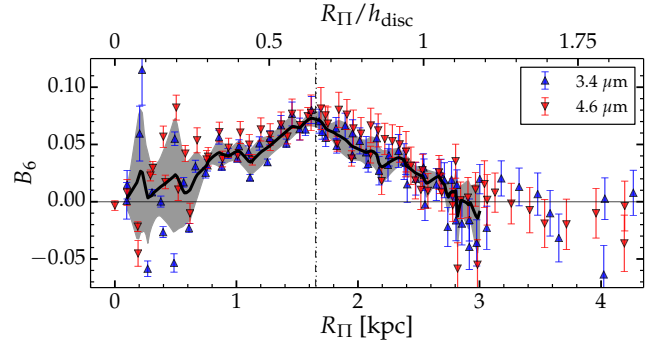
Figure 6. The radial B_6 profile of the Milky Way, as it would be viewed if the peanut were oriented side-on. The data points correspond to the extracted B_6 profiles in the E and W directions (Figure 5), corrected for the bar's/peanut's viewing angle α (adjusted to a 90° orientation, rather than as observed at 37°). The thick curve is the average over both directions and each wavelength, with the 1-σ scatter shown through the shaded region.

4.2 X/P Diagnostics and Scaling Relations

The viewing angle of the Milky Way's X/P structure enables us to deproject the four radial B_6 profiles (E, W, 3.4 μm and 4.6 μm, Figure 5), and thus compute the peanut's intrinsic metrics, such as length, height above the disc plane and integrated strength. The deprojected profiles (i.e., converted to a side-on view) are shown in Figure 6, along with an average profile (black curve) and its 1-σ scatter (grey shaded region). Following CG16, we classify this as a 'hump'–shaped profile which peaks at $R_{\Pi,\text{int}} = 1.67$ kpc and declines to zero by ≈ 3 kpc. From the average, deprojected B_6 profile we computed the peanut's quantitative diagnostics, which are listed in Table 1.

Specifically, we report the maximum amplitude of the 6th order harmonic (B_6), labelled as Π_{max}, the peanut intrinsic radius $R_{\Pi,\text{int}}$ and height above the disc plane $z_{\Pi,\text{int}}$, the integrated strength of the peanut instability (S_{Π}), the full width at half-maximum of the B_6 signature (W_{Π}), as well as the qualitative shape of the B_6 profile, as used in CG16. Table 1 additionally reports the orientation angle (α) of the (bar+X/P structure).

CG16 have shown that the X/P parameter space is not randomly populated but rather the X/P metrics give rise to several scaling relations. One such correlation involves the peanut radius, R_{Π}, and its vertical height above the disc, z_{Π}. This is shown in Figure 7, where the black and grey data points correspond to the twelve galaxies in the CG16 sample[4], and the red star corresponds to the Milky Way value as obtained here. This trend is relevant for constraining the age of X/P structures, in light of their 'radial drift' (see e.g., Quillen et al. 2014). As the peanut is believed to arise at the inner Lindblad resonance point, the bar's slowing down causes the resonance point to drift outward, elongating the peanut.

The Milky Way is consistent with the general trend in Figure 7, though appears to be marginally shifted towards

---

[4] The four grey data points correspond to two galaxies with nested X/P structures: hollow symbols for the inner and filled symbols for the outer.

Table 1. The Milky Way's X/P Diagnostics

$\Pi_{\max}^{(a)}$	$R_{\Pi,\mathrm{int}}^{(b)}$ [kpc, units of h]	$z_{\Pi,\mathrm{int}}^{(c)}$ [kpc, units of h]	$S_{\Pi}^{(d)}$ [kpc, units of h]	$W_{\Pi}^{(e)}$ [kpc, units of h]	$\alpha^{(f)}$ [°]	shape$^{(g)}$
0.073 ± 0.007	$1.67\pm0.27,\ 0.66\pm0.14$	$0.64\pm0.17,\ 0.25\pm0.07$	$5.67\pm2.00,\ 2.23\pm0.79$	$1.04\pm0.08,\ 0.41\pm0.04$	37^{+7}_{-10}	hump

(a)– maximum amplitude of B_6 harmonic; (b)– intrinsic radius of X/P structure; (c)– intrinsic vertical height of X/P structure; (d)– integrated strength of the B_6 profile; (e)– full width at half-maximum of the B_6 profile; (f)– peanut angle with Sun-(Galactic Centre) line-of-sight; (g)– qualitative shape of the B_6 profile (as defined in CG16).
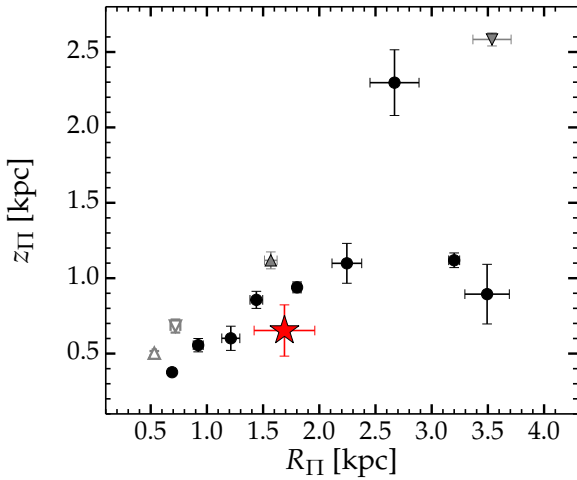
Figure 7. Trend between X/P length within, and height above, the disc plane. Black and grey data from CG16, where R_Π is projected and z_Π is intrinsic. The red star is the Milky Way data point computed in this work, for which both R_Π and z_Π are intrinsic.

a slightly higher R_Π value (or lower z_Π). However, in their analysis, CG16 were limited by the unknown viewing angles of the galactic bars in their galaxy sample, and hence their measured X/P radii were in fact projected quantities, i.e., their data are $R_\Pi \equiv R_{\Pi,\mathrm{obs}} \leqslant R_{\Pi,\mathrm{int}}$. For the Milky Way, our determination of the bar's viewing angle relieves this limitation and so our X/P radius is intrinsic, i.e. $R_\Pi \equiv R_{\Pi,\mathrm{int}}$. Note that CG16 obtained intrinsic z_Π values by using the inclinations of the galaxy discs to correct for projection effects in the vertical direction. Our z_Π value is also intrinsic, since we are viewing the Galaxy's disc almost perfectly edge-on (the disc's inclination is $i \lesssim 0°.2$).

Another set of correlations occur between the X/P size (length and height) and its integrated strength S_Π (Equation 1). These are shown in Figure 8, where, as before, the black and grey data corresponds to the CG16 sample. The line is their linear fit to the data and the red star corresponds to the Milky Way. Interestingly, these trends also hold when plotted in units of the disc's scale length (rather than in kpc), indicating that peanuts 'know' about their host disc. CG16 proposed to normalise, where applicable, the metrics of the peanut structures by h, since this provides quantities that are independent of the type or size of individual galaxies, or the uncertainties in their distance estimates. This also facilitates comparisons with numerical simulations. We

determined the scale length of the Milky Way by performing a photometric decomposition of the major axis surface brightness profile, separately in the E and W directions, and taking into account the Sun's placement within the disc as well as the Galaxy's spiral structure. The full analysis is presented in Appendix A. Our preferred models, shown in Figure 9, resulted in an average value over both bands and both directions, of $h = 2.54 \pm 0.16$ kpc, in good agreement with the literature (Licquia & Newman 2016, Bland-Hawthorn & Gerhard 2016).

Figure 8 shows how the Milky Way fits in with the ($z_\Pi - S_\Pi$) and ($R_\Pi - S_\Pi$) scaling relations. The Galaxy is consistent (within 2σ) with the trend seen in the CG16 sample, albeit with an X/P strength S_Π that is somewhat on the high side. The X/P strength, however, is also sensitive to the bar viewing angle α, since S_Π is an integral of the B_6 curve and α controls the deprojection ('stretching'), of the B_6 profile when adjusting to a side-on orientation of the peanut (Figure 6). As α was unknown for the CG16 galaxies, the scaling relations presented are between projected, and thus potentially underestimated in-plane quantities.

Finally, X/P structures are also known to correlate with their host galaxy's kinematics (Bureau & Freeman 1999, Debattista et al. 2005, Iannuzzi & Athanassoula 2015, Athanassoula, Rodionov & Prantzos 2017). CG16 have shown a (weak) trend between galaxy v_{rot}/σ (rotation velocity/velocity dispersion) ratio and the length and strength of the peanut structures, such that larger and stronger peanuts occur in more rotation-dominated systems. These correlations are shown in Figure 10, where the colour scheme is analogous to Figures 7 and 8. The data points framed in open squares have unreliable v_{rot}/σ ratios (see CG16 for details). As in Figure 8, these correlations also hold when the X/P parameters are normalised by the disc scale length h, once again indicating that the disc in which peanuts are embedded is important. For the Milky Way we adopted a v_{rot}/σ ratio of 2.27 ± 0.44 based on a disc rotation velocity of 238 ± 15 km s^{-1} (Bland-Hawthorn & Gerhard 2016; see also Schönrich 2012, Reid et al. 2014, Reid & Dame 2016) and a central velocity dispersion of 105 ± 20 km s^{-1} (Merritt & Ferrarese 2001, Gültekin et al. 2009).

5   DISCUSSION

5.1   The Milky Way's X/P Parameters in Context

The spatial parameters (length, height above the disc) of the Milky Way's X/P structure measured in this paper agree well with those of other nearby galaxies, making our Galaxy typical in this respect. The integrated strength of the X/P
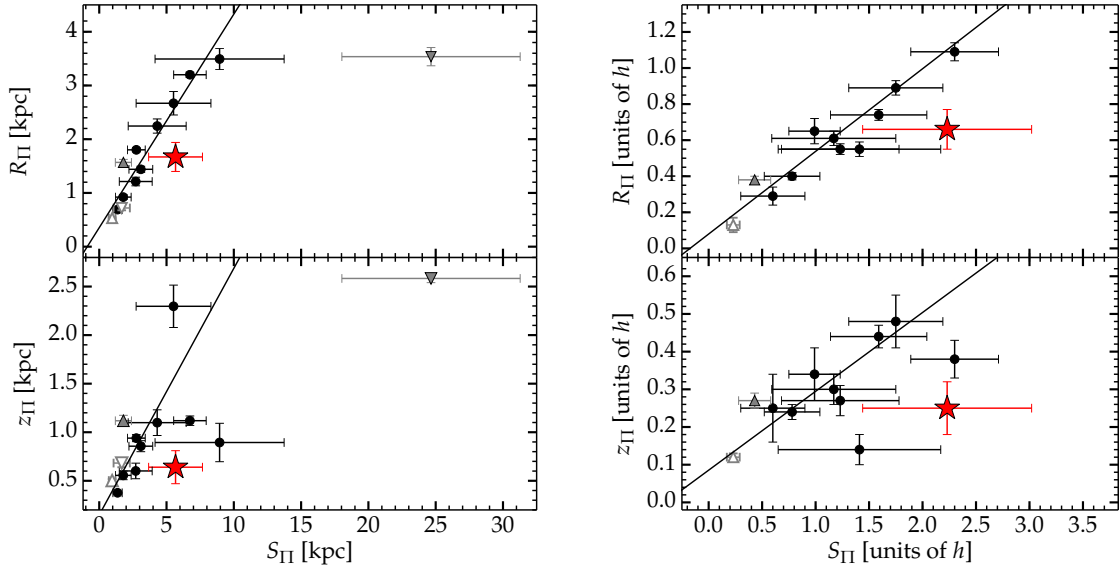
Figure 8. CG16 scaling relations showing X/P radius (top) and height (bottom) as a function of integrated strength. The colour scheme is analogous to Figure 7 and the lines represent linear fits from CG16. The correlations are shown in kpc (left) and in units of disc scale length h (right). The outer peanut of NGC 128 is an outlier from the trends (outside the plotting area in the right-hand panels), possibly having its X/P strength enhanced through interactions with its satellite.
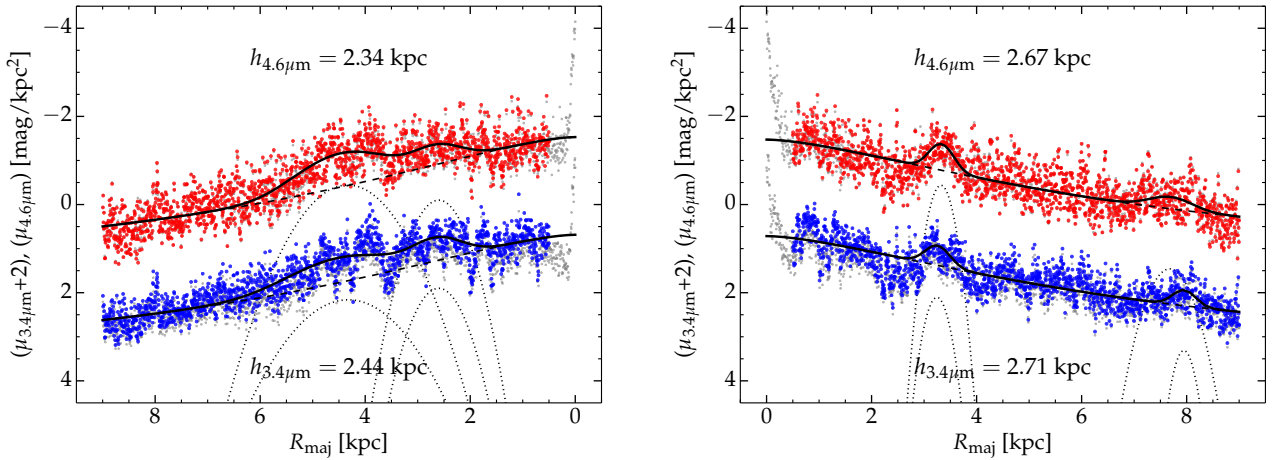

Figure 9. 1D cuts in the plane of the disc to the *East* of the Galactic Centre (left-hand side) and to the *West* (right-hand side). Grey symbols represent raw cuts from processed images (as in Figure 3) while blue and red data are corrected for dust extinction and glow and correspond to the $3.4\,\mu m$ and $4.6\,\mu m$ data, respectively. Black curves represent the best-fitting model (exponential+2 Gaussians), corrected for our vantage point within the disc and assuming Sun's Galactocentric distance of 8.2 kpc. Insets indicate the best-fit disc scale length h for each panel. The $3.4\,\mu m$ profiles are offset by 2 magnitudes, for display clarity, and the inner 500 pc were excluded from the fits, since the light in that radial range is dominated by a small scale but bright component.

structure appears, however, to be moderately larger than the general trend, which may be due to projection effects, as explained in §4.2. Specifically, the peanut strength, S_Π, is sensitive to the orientation angle (α) at which the bar, and X/P structure, are viewed. In a more end-on orientation, the observed (in projection) B_6 profile is more 'contracted' compared to a side-on view, and as the integral over this profile, S_Π has a maximal value in side-on orientation and decreases with decreasing α. While in this work our knowledge of α allowed us to deproject the Milky Way's B_6 profile

to side-on orientation, the galaxies in CG16 had unknown bar/peanut viewing angles, and hence possibly underestimated S_Π values. Note that an unknown α would also imply potentially underestimated R_Π values, but would not bias the peanut height (z_Π) measurements, which in CG16 are intrinsic values. Therefore, projection effects may only explain the moderate offset of the Milky Way in the $z_\Pi - S_\Pi$ trends (bottom panels in Figure 8).

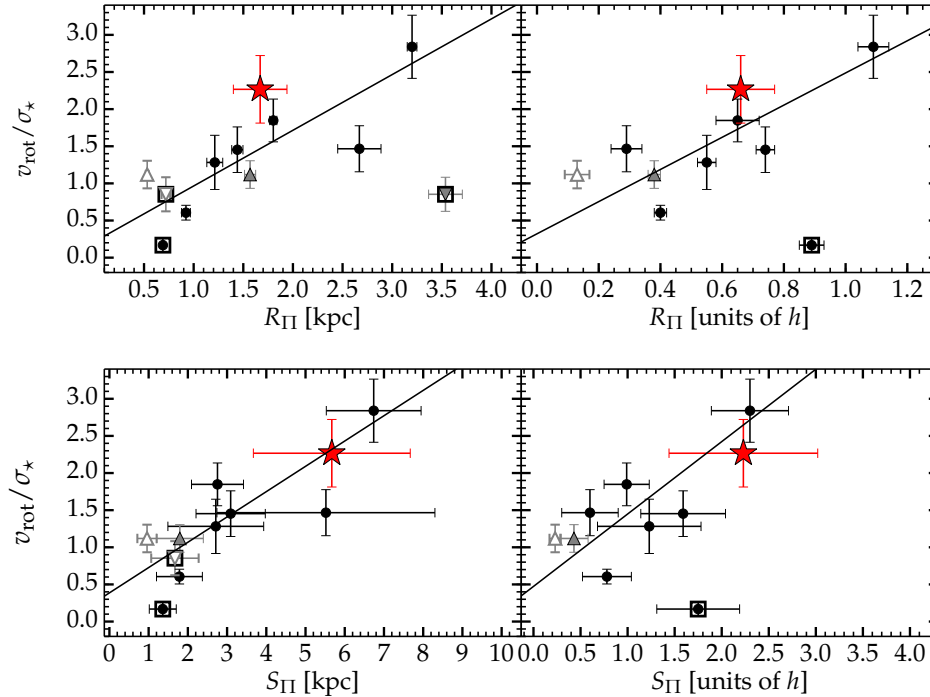An alternative, and intriguing, explanation for this is that the Milky Way may have had its X/P strength en-

Figure 10. CG16 scaling relations between galaxy $v_{\rm rot}/\sigma$ and the peanut properties: radius (top) and strength (bottom). The colour scheme is analogous to Figure 8, and data points framed in squares were excluded from the fit in CG16 (see §4.2). The correlations hold when the X/P parameters are both in kpc (left) and in units of disc scale length h (right).

hanced through tidal interactions with its infalling satellites, such as the *Small* and *Large Magellanic Cloud*, or the disrupted *Sagittarius* dwarf (Jiang & Binney 2000). Attempting to explain how boxy/peanut/X–shaped structures form, Binney & Petrou (1985) and Rowley (1988) argued that interactions with small satellite galaxies (disruption and accretion of material) can give rise to orbit families that lead to rectangular, boxy isophotes and cylindrical rotation in their larger companions. While this scenario was ruled unlikely to be the primary formation mechanism of X/P structures (see Bureau & Freeman 1999, their Sec. 2.1), satellite interactions may still serve to enhance the strength of the peanut. For example, NGC 128, one of the most prominent X/P galaxies, clearly shows material exchange with its smaller companion NGC 127, as shown in Fig. 3 in CG16. By contrast, the rest of the CG16 sample of X/P galaxies did not show any clear evidence of satellites. As such, the datum corresponding to NGC 128[5], plotted as the filled grey downward triangle in Figure 8, is a significant outlier of the trend. Note that accretion of the intergalactic medium (López-Corredoira, Betancort-Rijo & Beckman 2002) may also play a role in this respect.

Interestingly, the Milky Way's isophotes in the X/P region show an apparent, though weak, $North - South$ asymmetry, such that the northern two 'arms' of the X shape appear to have a wider opening angle than the southern two arms, in both filters. This is reminiscent of bars in the buck-

ling phase seen in simulations (e.g., Martinez-Valpuesta, Shlosman & Heller 2006) as well as observations (e.g., Erwin & Debattista 2016), which is the primary instability mechanism that leads to X/P structures. We may be observing the remaining signature of the Milky Way's past bar buckling event. The asymmetry, however, is only apparent on the eastern (closer) limb of the peanut structure (Figure 4, panels *a* and *c*), which warrants a more in-depth study of differences between positive and negative latitudes. This is, however, beyond the scope of this paper.

5.2 The Long Bar Parameters: Implications

5.2.1 *Comparison with Literature*

In Figure 11 we compare our bar parameters (orientation angle and radius) with other results from the literature. Our preferred parameters of $\alpha = 37^{\circ +7^{\circ}}_{-10^{\circ}}$ and $R_{\rm bar} = 4.16 \pm 0.68$ kpc agree well with Zasowski (2012), who measured $\alpha = 38^{\circ} \pm 6^{\circ}$ from GLIMPSE (Benjamin et al. 2005, Churchwell et al. 2009) data, and the recent study of Monari et al. (2017), who show evidence for a relatively short and fast bar with a co-rotation radius of ~ 4 kpc. We plot our preferred parameters, which assume a $R_{\Pi,\rm int}/R_{\rm bar}$ ratio of 0.4, in Figure 11 as the red star symbol. Additionally, our lower estimate for the bar length, which assumes $R_{\Pi,\rm int}/R_{\rm bar} = 0.5$, is shown by the black star symbol. The literature results were taken from Picaud (2004) (P04; $\alpha = 45^{\circ} \pm 9^{\circ}$, $R_{\rm bar} = 3.9 \pm 0.4$ kpc), Benjamin et al. (2005) (B05; $\alpha = 44^{\circ} \pm 10^{\circ}$, $R_{\rm bar} = 4.4 \pm 0.5$ kpc), from the combined works of the group Hammersley et al. (2000), López-Corredoira et al. (2001, 2007) and Cabrera-Lavers et al.

---

[5] More precisely, to the *outer* peanut of NGC 128. The inner peanut (empty grey downward triangle in Figure 8) appears to fit the trend quite well.
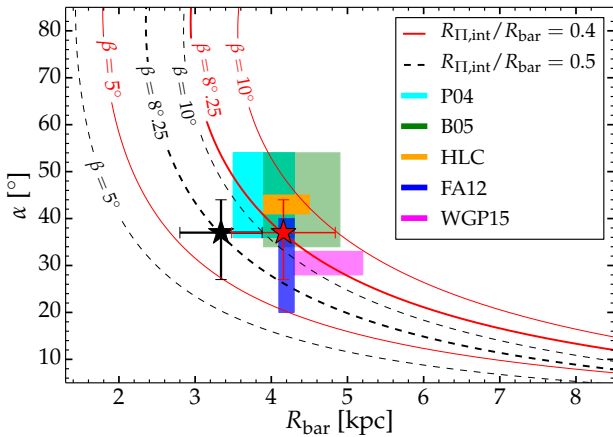
Figure 11. Bar radius vs. orientation angle α. Curves illustrate the coupling of the two parameters given our β (angular size of the peanut eastward of the Galactic Centre) measurement (thick) and taking reasonable upper and lower limits of it (thin). Red solid and black dashed curves assume different $R_{\Pi,\mathrm{int}}/R_{\mathrm{bar}}$ ratios (see legend). Boxes indicate literature results and their uncertainties, while the stars are the results of this work, assuming $R_{\Pi,\mathrm{int}}/R_{\mathrm{bar}}$=0.4 (red) and 0.5 (black).

(2007, 2008) (HLC; $\alpha = 43°\pm \sim 2°$, $R_{\mathrm{bar}} = 3.9 - 4.5$ kpc), from Francis & Anderson (2012) (FA12; $\alpha = 30° \pm 10°$, $R_{\mathrm{bar}} = 4.2 \pm 0.1$ kpc) and from Wegg, Gerhard & Portail (2015) (WGP15; $\alpha = 28° - 33°$, $R_{\mathrm{bar}} = 4.6 \pm 0.3 - 5.0 \pm 0.2$ kpc). Our preferred data point, without considering the error bars for the moment, is consistent (within the errors) with P04, B05 and FA12, but appears to show tension with WGP15 and HLC, i.e., lying roughly between their respective ranges but outside their uncertainty intervals, which are comparatively smaller than the other studies and, notably, exclude each other. The latter two groups advocate competing interpretations of the Milky Way's central components. HLC posit the existence of a long thin bar and a shorter, thicker, triaxial bulge, the two misaligned with each other. WGP15 on the other hand advocate the notion that the long bar has a smaller orientation angle, and is thus aligned with the X/P structure, and that in fact the latter is essentially the central, vertically thickened part of the former.

Due to our substantial uncertainty intervals, our result does not rule out either of the above two scenarios. But were we to relax some of our assumptions or measurements, and explore the systematics and sources of uncertainty in our analysis, could we arrive at a better agreement with either of the two pictures? We explore this in the following sub-sections, by again looking at the ($\alpha - R_{\mathrm{bar}}$) parameter space.

5.2.2 Limitations and Systematics

Although our methodology for detecting X/P structures is both sensitive and accurate for external galaxies (capable of detecting 'nested' X/P structures, as shown in CG16), our vantage point of the Milky Way may introduce uncertainties in this analysis. Specifically, we are observing the X/P structure through intervening disc light, which may 'wash out' the faint extremities of the peanut, both in–plane and

in the vertical direction. A more accurate approach would involve the use of data that is not affected by disc light, e.g., (2D) maps of the distribution of RCG stars, which are commonly used as tracers of Galactic structure. In addition, our analysis only considered the radial (length) and vertical (height) directions of what is in fact a three-dimensional structure. Additional uncertainties in the true 'ends' of the peanut may arise from its in-plane 'thickness', and how this projects onto the plane of the sky (e.g., Fig. 6 in López-Corredoira et al. 2007; see also Buta & Crocker 1991, Buta 1995, Laurikainen et al. 2011 and Salo & Laurikainen 2017 for interesting examples of peanuts viewed face-on). To avoid most of the aforementioned issues, and keep consistency with CG16, we have used the peak in the B_6 profile, rather than the point where it declines to zero, as the indicator of the peanut's characteristic scale. At this point the peanut is most prominent, and hence using it additionally ensures consistency with other studies that have measured X/P structures, which relied on identification techniques (e.g., visual inspection, unsharp masking) that are sensitive to the point where the feature is most prominent.

Of particular interest for this paper are studies which report the typical value of R_{Π}/R_{bar}, since we have relied on this ratio to obtain the bar length. Recent studies place its mean value, in nearby X/P galaxies, between $\sim 0.4 - 0.5$ (Laurikainen & Salo 2017, Erwin & Debattista 2017), but all find scatter in it. Prima facie, our analysis shows that a value closer to 0.4 for the Milky Way is more consistent with the bar parameters in the literature, while a value of 0.5 appears to underestimate the bar length (Figure 11). However, in the following sub-section we investigate how the reliability of our measured X/P size, and how the applicability of the $R_{\Pi,\mathrm{int}}/R_{\mathrm{bar}}$ ratio to our measurements of the Milky Way, affects our results.

5.2.3 Exploring the ($\alpha - R_{\mathrm{bar}}$) Coupling

Considering that we observe the (bar+X/P structure) in projection, it is obvious that our derived intrinsic X/P radius $R_{\Pi,\mathrm{int}}$ (and, by extension, R_{bar}) and viewing angle, are correlated quantities: a given *projected* size (i.e., the measurement/observation) can correspond to a large intrinsic size if the viewing angle α is small, or to a smaller intrinsic size if the angle is larger (see Figure 2, which applies to both the peanut and the bar, and any elongated structure viewed at an angle). This (α – intrinsic size) coupling, is shown in Figure 11 through the red and black curves, for which the observed quantity (projected size) is β, i.e., the peanut's angular size in the eastern direction (see Figure 2). If we were to assume that our measured value of $\beta = 8°.25$ is the only information we have[6], then the data point must lie on the thick red curve, if $R_{\Pi,\mathrm{int}}/R_{\mathrm{bar}} = 0.4$ (our preferred scenario), or on the thick dashed curve if $R_{\Pi,\mathrm{int}}/R_{\mathrm{bar}} = 0.5$. If we assume that the true value of α is smaller than 37° (i.e., if we assume that our measurement of γ was biased, since β and γ together constrain α), and is more in the region of

---

[6] We chose β because it corresponds to the nearer limb of the peanut, which in principle should be easier to measure. However, we repeated the exercise with γ – the projected angular size on the *West* (far) side – and obtained similar results.

$\sim 30°$, then travelling down the thick red curve brings us in good agreement with WGP15. On the other hand, a higher value of α ($\sim 43°$) improves the agreement with HLC. If we further assume that our measurement of β was biased as well, and the true end of the peanut occurs beyond $8°.25$ (we show $10°$ in Figure 11, a typical upper limit for the bulge–bar transition), then the opposite occurs. A lower value of β increases the discrepancy with all the literature numbers. All of this however is for a fixed $R_{\Pi,\mathrm{int}}/R_{\mathrm{bar}}$, a ratio necessary to map the X/P size (β) onto a bar size. Varying this ratio translates the three red curves in the x–direction, as illustrated through the black dashed curves, which are equivalent to the red curves but for a higher $R_{\Pi,\mathrm{int}}/R_{\mathrm{bar}}$ value of 0.5.

Most studies report on a bar length $\gtrsim 4 - 4.5$ kpc, which, in conjunction with our work, suggest that for the Milky Way, $R_{\Pi,\mathrm{int}}/R_{\mathrm{bar}}$ is close to ≈ 0.4. However, the long bar may not be as long after all. In a recent paper, Monari et al. (2017) argue, based on *Gaia* DR1 (Gaia Collaboration et al. 2016) and LAMOST (Liu et al. 2014) data, that the position of the *Hercules* stream in velocity space favours a shorter bar, with a co-rotation radius of ~ 4 kpc (at odds with Portail et al. 2017, who report a longer, ~ 6 kpc radius of co-rotation). A shorter bar would also be more consistent with bar-to-disc sizes in other disc galaxies, as the Milky Way is usually invoked to be a typical barred spiral. Erwin (2005) found bar sizes to range between 1–10 kpc (with a mean of 3.3 kpc) or 0.5–$2.5\,h$ for early-type disc galaxies (S0–Sab). Later-type disc galaxies, such as the Milky Way, which is believed to be Sb or Sbc, by most sources (Hodge 1983, Kennicutt 2001), have comparatively shorter bars, ranging from 0.5–3.5 kpc, or $0.2h$–$1.5h$. Assuming our measured value of $h = 2.54$ kpc for the disc's exponential scale length, this maps the WGP15 range (4.6–5) kpc into $(1.8$–$2)\,h$, the HLC range (3.7–4.5) kpc into $(1.5$–$1.8)\,h$ and our estimated range of (3.3–4.2) kpc into $(1.3$–$1.7)\,h$. Naturally, these numbers carry quite large uncertainties not only due to intrinsic scatter but also due to different definitions of 'bar length' (see Athanassoula & Misiriotis 2002, their Sec. 8).

As previously mentioned, Laurikainen & Salo (2017) report a mean $R_{\Pi,\mathrm{obs}}/R_{\mathrm{bar}}$ ratio of ~ 0.4 for X/P structures while for barlenses their measurements exceed ~ 0.5. From the argument that X/P structures and barlenses are the same structures viewed at different inclinations (edge-on vs face-on) and by analysing simulated X/P galaxies at different projection angles, they conclude that the mean intrinsic ratio is ≈ 0.5 for both features (with some scatter). While most literature measurements of the length of the long bar, coupled with our $R_{\Pi,\mathrm{int}}$, favour an $R_{\Pi,\mathrm{int}}/R_{\Pi,\mathrm{bar}}$ ratio of ≈ 0.4 for the Milky Way, a value closer to 0.5 would imply a shorter bar, as seen in Figure 11 (black star symbol). A shorter bar is not necessarily in contradiction with the findings of many authors. As suggested by Monari et al. (2017), a flat stellar distribution extending further than 4 kpc could simply correspond to loosely wound spiral arms that originate from the bar's ends. In light of the above arguments, we choose to keep our shorter estimate of $R_{\mathrm{bar}} = 3.24 \pm 0.54$ kpc as a plausible value.

The scenario in which the Milky Way's 'bulge' is the inner, thickened, X/peanut-shaped region of its long bar, which has arisen through the buckling of the former (Martinez-Valpuesta & Gerhard 2011, Romero-Gómez et al. 2011, WGP15), is a natural interpretation of our Galaxy's central components. This scenario is supported by numerical simulations as well as observational evidence that most of the stars in the bulge originate from the disc (Shen et al. 2010; Ness et al. 2013, 2014; Di Matteo et al. 2014; Di Matteo 2016), implying that it formed predominantly from the buckling and secular evolution of the disc and bar. In support of this picture, WGP15 have argued that the angle of the long bar is smaller than previously thought, and is consistent with that of the elongated 'bulge'. While we agree with WGP15 that the two structures are likely aligned, we propose, and show evidence, that it is not the long bar which has a lower angle ($\sim 30°$) than most literature measurements but that the X/P 'bulge' instead has a larger angle ($\sim 37°$) than previously thought. If WGP15 increase their α value to our value of $\sim 37°$ (i.e., move up the red curve in Figure 11), then their result would agree with our work and produce a bar radius shorter than 5 kpc.

5.3   The End of the Bar

An accurate accounting of the long bar is crucial if we are to understand the inner dynamics of the galaxy and, in particular, the disc-bar-bulge transition in this region. This has been a long-standing problem in the widely used *Besançon* (Robin et al. 2003) and *Galaxia* (Sharma et al. 2011) models of the Galaxy, for example. At present, these inner structures are inserted artificially and do not conform to a dynamically self-consistent framework.

Wegg, Gerhard & Portail 2015 have revealed that there are two scale height components extending into the long bar region: the 'thin' component and the 'superthin' component. The 'thin' bar has a scale height of 180 pc, with a declining density with radius, and appears to be the barred counterpart of the old inner disc. The 'superthin' component has a remarkably small scale height of 45 pc, and the density appears to *increase* outwards. They argue that the thinness may reflect a young stellar population that is at least 500 Myr in age to account for the presence of RCGs. The coldness of the superthin component may reflect young stars trapped in resonances at the bar ends. Such morphological features, called 'ansae', are seen in external galaxies and simulations (Martinez-Valpuesta, Knapen & Buta 2008, Athanassoula et al. 2015, Athanassoula 2016). Complex structures like these may complicate the determination of the long bar length and, indeed, the projected properties here are not symmetric about the Galactic Centre, even accounting for the different distances (Wegg, Gerhard & Portail 2015). At the present time, it is not possible to determine a definitive stellar age for either component, which is clearly an important test. We may alternatively be observing the beginnings of loosely wound spiral arms emerging from the ends of the bar, which, as they twist into our line-of-sight, would account for an increasing density of young stars at both ends. The presence of a prominent star formation region at the receding end of the bar, and associated with the *Scutum* arm, has been previously reported (López-Corredoira et al. 1999).

6 CONCLUSION

In this paper we measured quantitative parameters of the Milky Way's (X/Peanut)–shaped structure from the Fourier $n = 6$ component (cosine term, B_6) of its isophotes, extracted from $3.4\,\mu$m and $4.6\,\mu$m WISE wide-field imaging. From the radial B_6 profile extracted with the *IRAF* task ISOFIT, we determined the X/P length, height above the disc plane, as well as its orientation angle with respect to our line-of-sight to the Galactic centre. Specifically, we determined an intrinsic peanut radius of $R_{\Pi,\text{int}} = 1.67\pm0.27$ kpc, a height $z_\Pi = 0.65 \pm 0.17$ kpc, and a viewing angle of $\alpha = 37^{\circ}{}^{+7^{\circ}}_{-10^{\circ}}$. Using the X/P structure as a proxy of the Milky Way's long bar, we conclude that the latter is oriented at the same angle α and has an expected radius of $\approx 4.16 \pm 0.68$ kpc, but could possibly be as short as 3.24 ± 0.54 kpc. Our results are based on the picture in which the long bar and the elongated X/P structure of the Milky Way are not distinct and misaligned components, but are different regions of the same structure. Tilted at $\approx 37^{\circ}$ from an end-on orientation, we find that this structure is viewed at a wider angle than conventionally thought for the triaxial 'bulge' region ($\sim 27^{\circ}$) and a narrower angle than conventionally thought for the long thin bar ($\sim 43^{\circ}$).

The Milky Way appears to be a typical X/P galaxy, consistent with the CG16 scaling relations between the various X/P diagnostics (length, height and integrated strength of the peanut instability), as well as the observed correlation of v/σ with peanut length and strength. The X/P strength parameter appears however to be marginally higher than the trend observed in nearby X/P galaxies, which is possibly a consequence of projection effects but may alternatively point to an enhancement in the Galaxy's X/P strength caused by accretion from its satellites. Additionally, we find tentative evidence of a $North-South$ asymmetry in the X/P feature, possibly reflecting the Galactic bar's past buckling phase that led to the formation of the peanut. We performed a photometric decomposition of the major axis surface brightness profile, in both WISE bands, modelling the data with an exponential profile for the disc and Gaussian functions for the various spiral arms. We performed this in both the eastward and westward directions (with respect to the Galactic North) and obtained an average scale length of the disc of $h = 2.54 \pm 0.16$ kpc, in good agreement with the literature. As with other nearby X/P galaxies, the Milky way obeys the CG16 scaling relations when the peanut metrics are rescaled by h, lending further support to the disc origin of the peanut (Shen et al. 2010; Ness et al. 2012, 2013; Di Matteo et al. 2014; Di Matteo 2016).

REFERENCES

Abbott C., Valluri M., Shen J., Debattista V. P., 2017, ArXiv e-prints

Alard C., 2001, A&A, 379, L44

Athanassoula E., 2016, Galactic Bulges, 418, 391

Athanassoula E., Laurikainen E., Salo H., Bosma A., 2015, MNRAS, 454, 3843

Athanassoula E., Misiriotis A., 2002, MNRAS, 330, 35

Athanassoula E., Rodionov S. A., Prantzos N., 2017, MN-RAS, 467, L46

Babusiaux C., Gilmore G., 2005, MNRAS, 358, 1309

Benjamin R. A. et al., 2005, ApJL, 630, L149

Binney J., Petrou M., 1985, MNRAS, 214, 449

Bland-Hawthorn J., Gerhard O., 2016, ARA&A, 54, 529

Bureau M., Freeman K. C., 1999, AJ, 118, 126

Buta R., 1995, ApJS, 96, 39

Buta R., Crocker D. A., 1991, AJ, 102, 1715

Cabrera-Lavers A., González-Fernández C., Garzón F., Hammersley P. L., López-Corredoira M., 2008, A&A, 491, 781

Cabrera-Lavers A., Hammersley P. L., González-Fernández C., López-Corredoira M., Garzón F., Mahoney T. J., 2007, A&A, 465, 825

Cao L., Mao S., Nataf D., Rattenbury N. J., Gould A., 2013, MNRAS, 434, 595

Churchwell E. et al., 2009, PASP, 121, 213

Ciambur B. C., 2015, ApJ, 810, 120

Ciambur B. C., Graham A. W., 2016, MNRAS, 459, 1276

Combes F., Debbasch F., Friedli D., Pfenniger D., 1990, AAP, 233, 82

Courteau S., de Jong R. S., Broeils A. H., 1996, ApJL, 457, L73

Debattista V. P., Carollo C. M., Mayer L., Moore B., 2005, ApJ, 628, 678

Debattista V. P., Ness M., Gonzalez O. A., Freeman K., Zoccali M., Minniti D., 2017, MNRAS, 469, 1587

Di Matteo P., 2016, PASA, 33, e027

Di Matteo P. et al., 2014, A&A, 567, A122

Dwek E. et al., 1995, ApJ, 445, 716

Erwin P., 2005, MNRAS, 364, 283

Erwin P., Debattista V. P., 2016, ApJL, 825, L30

Erwin P., Debattista V. P., 2017, MNRAS, 468, 2058

Fragkoudi F., Di Matteo P., Haywood M., Gómez A., Combes F., Katz D., Semelin B., 2017, ArXiv e-prints

Francis C., Anderson E., 2012, MNRAS, 422, 1283

Gaia Collaboration et al., 2016, A&A, 595, A2

Gerhard O., 2002, in Astronomical Society of the Pacific Conference Series, Vol. 273, The Dynamics, Structure & History of Galaxies: A Workshop in Honour of Professor Ken Freeman, Da Costa G. S., Sadler E. M., Jerjen H., eds., p. 73

Gerhard O., Martinez-Valpuesta I., 2012, ApJL, 744, L8

Graham A. W., Worley C. C., 2008, MNRAS, 388, 1708

Gran F. et al., 2016, A&A, 591, A145

Gültekin K. et al., 2009, ApJ, 698, 198

Hammersley P. L., Garzon F., Mahoney T., Calbet X., 1994, MNRAS, 269, 753

Hammersley P. L., Garzón F., Mahoney T. J., López-Corredoira M., Torres M. A. P., 2000, MNRAS, 317, L45

Hodge P. W., 1983, PASP, 95, 721

Iannuzzi F., Athanassoula E., 2015, MNRAS, 450, 2514

Jiang I.-G., Binney J., 2000, MNRAS, 314, 468

Joo S.-J., Lee Y.-W., Chung C., 2017, ApJ, 840, 98

Jurić M. et al., 2008, ApJ, 673, 864

Kennicutt, Jr. R. C., 2001, in Astronomical Society of the Pacific Conference Series, Vol. 231, Tetons 4: Galactic Structure, Stars and the Interstellar Medium, Woodward C. E., Bicay M. D., Shull J. M., eds., p. 2

Lang D., 2014, AJ, 147, 108

Launhardt R., Zylka R., Mezger P. G., 2002, A&A, 384, 112

Laurikainen E., Salo H., 2017, A&A, 598, A10

Laurikainen E., Salo H., Athanassoula E., Bosma A., Herrera-Endoqui M., 2014, MNRAS, 444, L80

Laurikainen E., Salo H., Buta R., Knapen J. H., 2011, Advances in Astronomy, 2011, 516739

Li A., Draine B. T., 2001, ApJ, 554, 778

Licquia T. C., Newman J. A., 2016, ApJ, 831, 71

Liu C. et al., 2014, ApJ, 790, 110

López-Corredoira M., 2016, A&A, 593, A66

López-Corredoira M., 2017, ApJ, 836, 218

López-Corredoira M., Betancort-Rijo J., Beckman J. E., 2002, A&A, 386, 169

López-Corredoira M., Cabrera-Lavers A., Gerhard O. E., 2005, A&A, 439, 107

López-Corredoira M., Cabrera-Lavers A., Mahoney T. J., Hammersley P. L., Garzón F., González-Fernández C., 2007, AJ, 133, 154

López-Corredoira M., Garzón F., Beckman J. E., Mahoney T. J., Hammersley P. L., Calbet X., 1999, AJ, 118, 381

López-Corredoira M., Hammersley P. L., Garzón F., Cabrera-Lavers A., Castro-Rodríguez N., Schultheis M., Mahoney T. J., 2001, A&A, 373, 139

Lütticke R., Dettmar R.-J., Pohlen M., 2000, A&AS, 145, 405

Mainzer A. et al., 2014, ApJ, 792, 30

Martinez-Valpuesta I., Gerhard O., 2011, ApJL, 734, L20

Martinez-Valpuesta I., Knapen J. H., Buta R., 2008, in Astronomical Society of the Pacific Conference Series, Vol. 390, Pathways Through an Eclectic Universe, Knapen J. H., Mahoney T. J., Vazdekis A., eds., p. 304

Martinez-Valpuesta I., Shlosman I., Heller C., 2006, ApJ, 637, 214

McWilliam A., Zoccali M., 2010, ApJ, 724, 1491

Meisner A. M., Lang D., Schlegel D. J., 2017, AJ, 153, 38

Merrifield M. R., 2004, in Astronomical Society of the Pacific Conference Series, Vol. 317, Milky Way Surveys: The Structure and Evolution of our Galaxy, Clemens D., Shah R., Brainerd T., eds., p. 289

Merritt D., Ferrarese L., 2001, ApJ, 547, 140

Monari G., Kawata D., Hunt J. A. S., Famaey B., 2017, MNRAS, 466, L113

Ness M., Debattista V. P., Bensby T., Feltzing S., Roškar R., Cole D. R., Johnson J. A., Freeman K., 2014, ApJL, 787, L19

Ness M. et al., 2013, MNRAS, 430, 836

Ness M. et al., 2012, ApJ, 756, 22

Ness M., Lang D., 2016, AJ, 152, 14

Nishiyama S. et al., 2005, ApJL, 621, L105

Nozawa T., Fukugita M., 2013, ApJ, 770, 27

Pérez-Villegas A., Portail M., Gerhard O., 2017, MNRAS, 464, L80

Picaud S., 2004, in Astronomical Society of the Pacific Conference Series, Vol. 317, Milky Way Surveys: The Structure and Evolution of our Galaxy, Clemens D., Shah R., Brainerd T., eds., p. 142

Portail M., Gerhard O., Wegg C., Ness M., 2017, MNRAS, 465, 1621

Quillen A. C., Minchev I., Sharma S., Qin Y.-J., Di Matteo P., 2014, MNRAS, 437, 1284

Raha N., Sellwood J. A., James R. A., Kahn F. D., 1991, Nature, 352, 411

Reid M. J., Dame T. M., 2016, apj, 832, 159

Reid M. J. et al., 2014, apj, 783, 130

Robin A. C., Reylé C., Derrière S., Picaud S., 2003, A&A, 409, 523

Rojas-Arriagada A. et al., 2014, A&A, 569, A103

Romero-Gómez M., Athanassoula E., Antoja T., Figueras F., 2011, MNRAS, 418, 1176

Rowles J., Froebrich D., 2009, MNRAS, 395, 1640

Rowley G., 1988, ApJ, 331, 124

Salo H., Laurikainen E., 2017, ApJ, 835, 252

Schönrich R., 2012, MNRAS, 427, 274

Sevenster M., Saha P., Valls-Gabaud D., Fux R., 1999, mnras, 307, 584

Sharma S., Bland-Hawthorn J., Johnston K. V., Binney J., 2011, ApJ, 730, 3

Shen J., Rich R. M., Kormendy J., Howard C. D., De Propris R., Kunder A., 2010, ApJL, 720, L72

Stanek K. Z., Mateo M., Udalski A., Szymanski M., Kaluzny J., Kubiak M., 1994, ApJL, 429, L73

Vásquez S. et al., 2013, A&A, 555, A91

Wegg C., Gerhard O., 2013, MNRAS, 435, 1874

Wegg C., Gerhard O., Portail M., 2015, MNRAS, 450, 4050

Weiland J. L. et al., 1994, ApJL, 425, L81

Williams A. A. et al., 2016, ApJL, 824, L29

Wright E. L. et al., 2010, AJ, 140, 1868

Zasowski G., 2012, PhD thesis, University of Virginia

Zoccali M. et al., 2014, A&A, 562, A66

Zoccali M., Valenti E., 2016, PASA, 33, e025

7 ACKNOWLEDGEMENTS

APPENDIX A: MILKY WAY PHOTOMETRIC DECOMPOSITION

A1 Integrated Light Approach

CG16 have shown that the X/P parameters of external galaxies are not arbitrarily distributed, but define specific scaling relations. The X/P length and height are correlated with each other, and both further correlate with the strength of the structure. Additionally, X/P galaxies also show a weak trend between their v/σ ratio and the X/P length and strength. These trends hold when the various parameters are expressed either in kpc or in units of the host disc's scale length h.

To investigate how the Milky Way fits into this picture, we determined its disc scale length by fitting its major axis surface brightness profile, i.e. the surface brightness as a function of galactic longitude l, in the mid-plane (galactic latitude $b = 0$). This is similar to a typical galaxy decomposition, but it involves an extra step to correct for the fact that our vantage point is inside the galaxy being modelled. We first assume that the planar offset of the Sun is negligible, and that the disc (out to ~ 8 kpc) has an exponentially declining intensity profile given by:

$$I(r) = I_0 \exp(-r/h) \qquad (A1)$$

where I_0 is the intensity at the (Galactic) centre and h is the exponential scale length of the disc. The galactocentric radial co-ordinate r is expressed in heliocentric co-ordinates (R, l, b) as:

$$r(R, l; b=0) = \sqrt{R_0^2 + R^2 - 2RR_0 \cos(l)}. \qquad (A2)$$

As we assume the Sun to be embedded in the disc plane, the observed intensity in a particular direction along the mid-plane (given by l alone) is the integrated light from the position of the Sun to infinity:

$$I(l) = \int_0^\infty I(R', l; b=0)\mathrm{d}R'. \qquad (A3)$$

Assuming that the optical depth is also negligible (a reasonable assumption for our particular dataset), Equation A3 represents the model being fit to the observed mid-plane brightness profiles extracted from our wide-field imaging data, and corrected for dust absorption and IR glow (see §A2). In the case of a single-component exponential model, $I(R', l, b=0)$ is simply given by Equation A1, with r expressed as in Equation A2. However, any azimuthally symmetric radial profile can be used, and in fact we employ additional components to capture the various spiral arms we observe in the data.

A2 Disc Scale Length from *WISE* Data

We obtained the scale length (h) of the Milky Way's disc from the photometric decomposition of its major axis surface brightness profile (SBP), correcting for the fact that we are observing the disc from within, as detailed in §A2.

The surface brightness profiles were extracted by taking image "cuts" along the disc mid-plane. While discs are
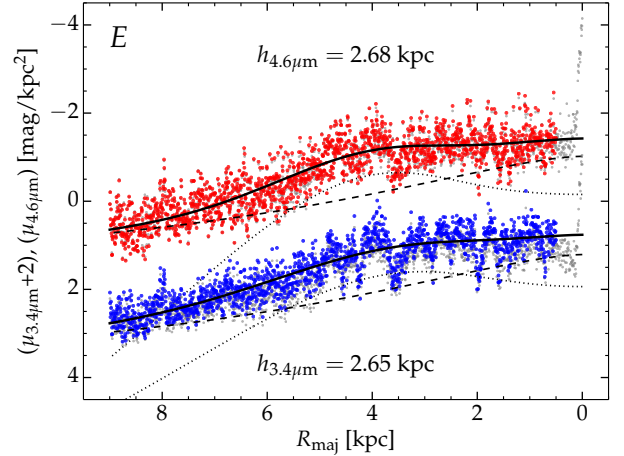
Figure A1. The eastward major axis surface brightness profile of the Milky Way at 3.4μm (blue data) and 4.6μm (red data). The models (black curves) consist of an exponential disc (dashed curves) and a Gaussian ring (dotted curves), the latter capturing the (*Scutum + far 3 kpc*) spiral arms as single, 'blended' features.

generally approximated to have exponentially declining light profiles, in practice they often display complicating features such as spiral arms, which induce "bumps" in the light profile. Because of the asymmetry induced by the Milky Way's various spiral arms, we again analysed the E and W sides separately.

The raw major axis light profiles are shown in Figures A1 and A2 through grey symbols. They were further corrected for the effects of dust, particularly dust glow and extinction. From Li & Draine (2001) (see their Fig. 10) we estimated dust glow to be $\approx 1/13$ of the stellar emission at 3.4μm and $\approx 1/8$ at 4.6μm. We further estimated the dust absorption at these wavelengths from extinction in the $V-$band. From Tab. 3 of Nozawa & Fukugita (2013) we used the ratios $A_{3.4\mu m}/A_V = 0.0346$ and $A_{4.6\mu m}/A_V = 0.0201$. The major axis A_V profile was extracted from the all-sky A_V extinction maps of Rowles & Froebrich (2009), and is shown in Figure A3. The dust-corrected surface brightness profiles are shown in Figures A1 and A2 as blue symbols (3.4μm) and red symbols (4.6μm). As dust is typically more centrally concentrated in disc galaxies, the net effect of these corrections was to slightly steepen the SBPs compared to raw cuts.

While it is tempting to model spiral arms in the usual manner, as Gaussian rings, one must be mindful of the fact that they have a logarithmic nature, increasing their distance from the centre as they wind around azimuthally. We see this exemplified by the *Scutum* arm, which peaks at different spatial scales in the two directions about the Galactic Centre, i.e. at ~ 4.5 kpc in the E and at ~ 8 kpc in the W. We did nevertheless first attempt to model the arms as Gaussian rings, employing the same technique of integrating the light along lines of sight (§A). Thus, a Gaussian ring appears to take the form shown in Figure A1 through the dotted curves. At the centre, the line-of-sight crosses perpendicular to the ring, so the SB value, given by twice the integral over the ring's thickness, is relatively low. By con-
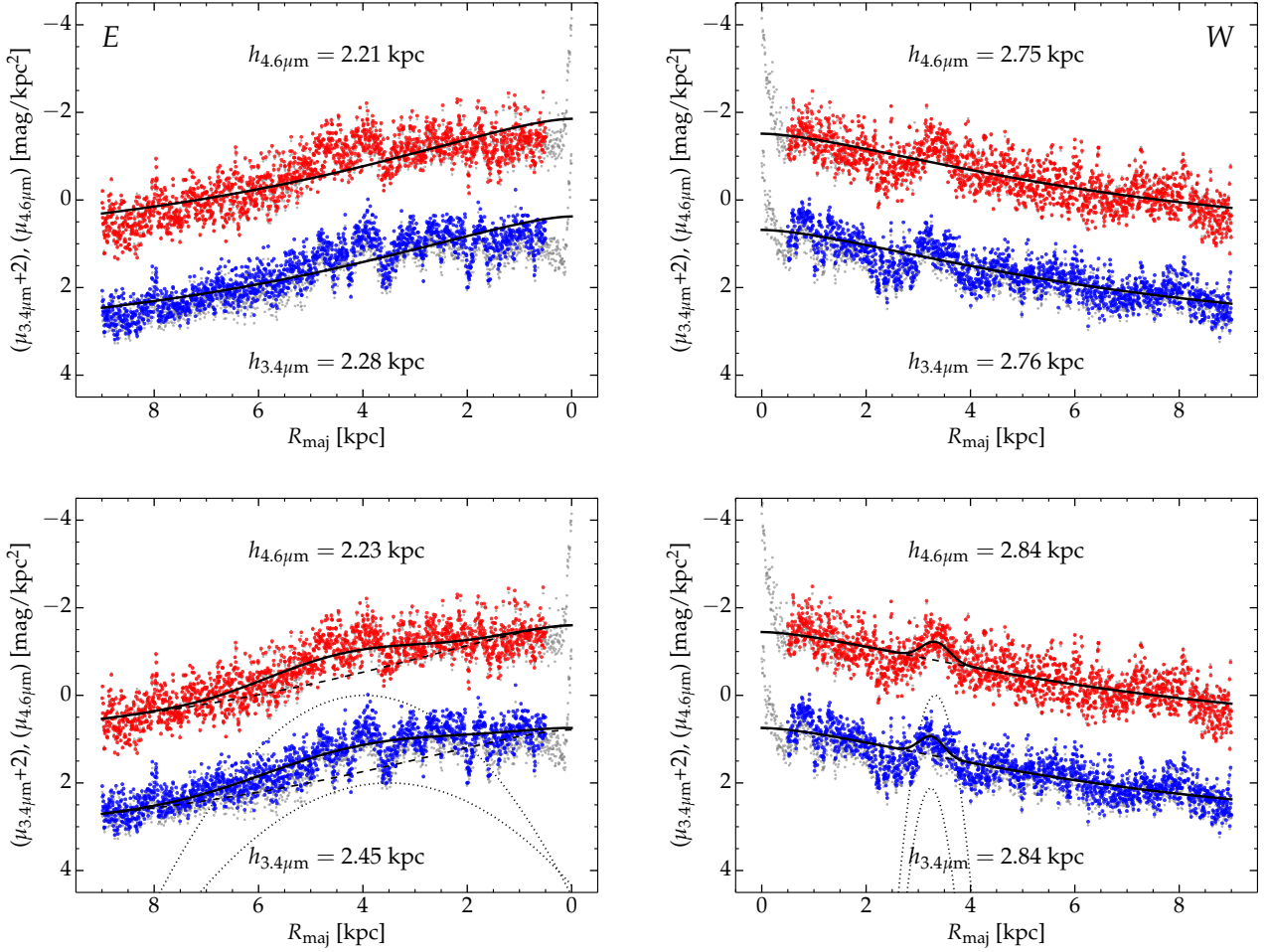
Figure A2. 1D cuts in the plane of the disc to the *East* of the Galactic Centre (left-hand side) and to the *West* (right-hand side). Blue and red data correspond to the 3.4μm and 4.6μm images, while black curves represent the best-fitting model, corrected for our vantage point within the disc and assuming Sun's Galactocentric distance of 8.2 kpc. Insets indicate the best-fit disc scale length *h* for each panel. **Top:** Single exponential models. **Bottom:** (exponential disc + 1 Gaussian spiral arm) models. **Bottom:** (exponential disc + 2 Gaussian spiral arms). See main text for a discussion on individual spiral arms and their modelling.
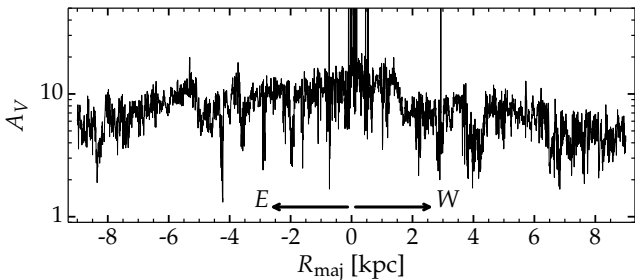
Figure A3. The *V*–band extinction profile along the major axis (disc mid-plane) extracted from the dust maps of Rowles & Froebrich 2009.

trast, at the ring's radius, the line-of-sight is tangential to the ring, running *along* it, so the integrated light reaches a maximum (bump) here, and gradually declines beyond this point. As noted above, a realistic spiral arm always has a lower curvature (or pitch angle) than a ring, which im-

plies that at its tangent point, a line of sight runs a longer distance along the spiral arm than it would along a more curved ring. Therefore, the SB profile of a spiral arm has a stronger Gaussian-like bump and a weaker flattening central tail than a ring. After experimenting with both functions we found the pure Gaussian to give more robust and consistent results, and so chose this form for modelling the spiral arms.

We modelled the data with increasing levels of sophistication. This is shown in Figure A2, where the left-hand panels correspond to the eastward SBP while the right-hand panels to the westward SBPs. On the eastward side the data shows the *Scutum* spiral arm as a rather prominent bump at ∼ 4.5 kpc, as well as the less prominent *far 3 kiloparsec arm* as a feature centred at ∼ 3 kpc. The dip occurring at ∼ 3.5 kpc is due to dust crossing the disc mid-plane, and is more pronounced (as expected) in the bluer filter. The westward SBPs show the *near 3 kiloparsec arm* at just beyond 3 kpc, and again the *Scutum* (or *Scutum-Centaurus*) arm, this time at ∼ 8 kpc. We began by modelling the data on both sides with just an exponential profile (Figure A2 top

panels). We further added a single spiral arm component (bottom panels) to the models, in each direction. Finally, we modelled both profiles with an exponential disc component and two spiral arm components, in each direction. We show these best-fit models in the main text of the paper, in Figure 9.

We adopt a 'global' value of the disc's scale length of h=2.54±0.16 kpc, the average of the best-fit (disc+2 spiral arms) models, in both filters and in the two directions. This result is in good agreement with the literature. For comparison, Licquia & Newman (2016) report an average scale length, in the infrared, of $2.51^{+0.15}_{-0.13}$ kpc, from a Bayesian averaging method of literature measurements. We also refer the reader to Bland-Hawthorn & Gerhard (2016) for a useful review on the Milky Way's structure. Finally, we note that a bar component, although faint, could also in principle be added to the models. We chose however not to include such a component since it is not well constrained by the data (which is additionally most affected by dust on the central spatial scales, where the bar is observed) and is thus degenerate with the spiral arm components.

APPENDIX B: DERIVATION OF THE X/P ABSOLUTE LENGTH AND VIEWING ANGLE

B1 Derivation Based on Stewart's Theorem

Equations 2 and 4 in the main text, which yield the X/P length (R_Π) and viewing angle (α), were derived by solving a system of two equations with the two quantities as the unknowns. The geometry of the problem is illustrated in Figure A1, which is analogous to Figure 2 but with different notation, to ensure clarity in this derivation.

The first equation relating R_Π and α came from considering the similar triangles $\triangle SAC$ and $\triangle SA'A''$. The fundamental theorem of similar triangles states that:

$$\frac{SA''}{SC} = \frac{A'A''}{AC} \tag{B1}$$

Analogously, from the similar triangles $\triangle SBC$ and $\triangle SB'B''$ it follows that:

$$\frac{SC}{SB''} = \frac{BC}{B'B''} \tag{B2}$$

As the two sides of the X/P structure are assumed to be equal ($A'C = B'C$), then $A'C\sin\alpha = B'C\sin\alpha = A'A'' = B'B''$, so, from B1 and B2, it follows that:

$$\frac{AC \cdot SA''}{SC} = \frac{BC \cdot SB''}{SC} \tag{B3}$$

Making the substitutions $SA'' = SC - A'C\cos\alpha$ and $SB'' = SC + B'C\cos\alpha$, and simplifying the denominators, B3 becomes:

$$AC(SC - A'C\cos\alpha) = BC(SC + B'C\cos\alpha) \tag{B4}$$

Rearranging and using the notation of Figure 2, we obtain the first equation which relates R_Π and α, namely:
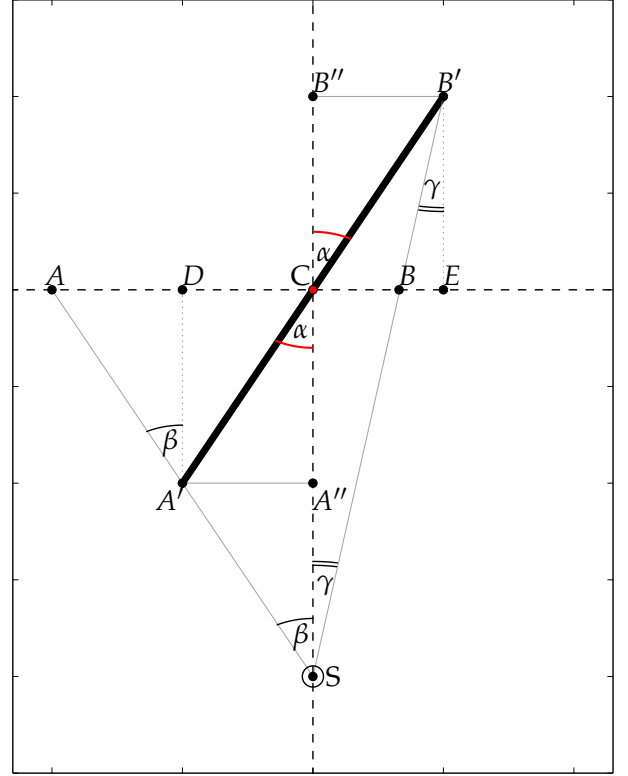
Figure A1. Schematic of the (Sun+peanut) configuration, analogous to Figure 2 but with different notation used throughout the derivations in the Appendix. S corresponds to the Sun, C to the Galactic Centre and the thick line represents the X/P structure, orientated at a viewing angle α.

$$\cos\alpha = \frac{R_0}{R_\Pi}\frac{R_\beta - R_\gamma}{R_\beta + R_\gamma} \equiv \eta\frac{R_0}{R_\Pi} \tag{B5}$$

The second equation relating R_Π and α is obtained from Stewart's theorem. In particular, in $\triangle CAS$, with CA' as the cevian, Stewart's theorem yields:

$$AC^2 \cdot SA' + SC^2 \cdot A'A = SA(A'C^2 + SA' \cdot A'A) \tag{B6}$$

where $SA = SC/\cos\beta \equiv R_0/\cos\beta$, and SA' and $A'A$ can be obtained from the similar triangles $\triangle SA'A''$ and $\triangle SAC$, as follows:

$$\frac{SA'}{SA} = \frac{SA''}{SC} \Leftrightarrow \frac{SA'\cos\beta}{R_0} = \frac{R_0 - R_\Pi\cos\alpha}{R_0} \Rightarrow$$
$$\Rightarrow SA' = \frac{R_0 - R_\Pi\cos\alpha}{\cos\beta} \tag{B7}$$

and

$$\begin{aligned} A'A &= SA - SA' \\ &= \frac{R_0}{\cos\beta} - \frac{R_0 - R_\Pi\cos\alpha}{\cos\beta} \\ &= \frac{R_\Pi\cos\alpha}{\cos\beta} \end{aligned} \tag{B8}$$

Noting that $AC = R_\beta$ and using the expressions in B5, B7 and B8, equation B6 becomes:

$$\frac{R_\beta^2 R_0(1-\eta)}{\cos\beta} + \frac{R_0^3\eta}{\cos\beta} =$$
$$\frac{R_0}{\cos\beta}\left[R_\Pi^2 + \frac{R_0\eta(R_0 - R_0\eta)}{\cos^2\beta}\right]. \tag{B9}$$

Having substituted all $(\cos\alpha)$ terms through B5, the only unknown in B9 is R_Π, and re-arranging for it yields the required Equation 2. The uncertainty in R_Π is propagated from β, η and R_β and is given by:

$$\delta R_\Pi = \frac{R_\Pi}{2}\left\{[2R_\beta(1-\eta)\delta R_\beta]^2 + \left[R_0^2\left(1 + \frac{2\eta - 1}{\cos^2\beta - R_\beta^2}\right)\delta\eta\right]^2\right.$$
$$\left. + \left(\frac{2\eta R_0^2\sin\beta\delta\beta}{\cos^3\beta}\right)^2\right\}^{1/2}, \tag{B10}$$

where $\delta\beta$ is the uncertainty in β, and δR_β is obtained from $\delta R_\beta = \sqrt{(R_0\delta\beta)^2 + (\beta\delta R_0)^2}$, which assumes the small angle approximation $\tan\beta \approx \beta$ and an uncertainty in R_0 of δR_0. In B10, $\delta\eta$ is the uncertainty in η, given by:

$$\delta\eta = \frac{2}{(\tan\beta + \tan\gamma)^2}\sqrt{[\tan\gamma\,\delta(\tan\beta)]^2 + [\tan\beta\,\delta(\tan\gamma)]^2}, \tag{B11}$$

which reduces, in the small angle approximation, to:

$$\delta\eta = \frac{2}{(\beta + \gamma)^2}\sqrt{(\gamma\,\delta\beta)^2 + (\beta\,\delta\gamma)^2}. \tag{B12}$$

B2   Viewing Angle and Uncertainties

One can also first derive an expression for α, and then recover R_Π, through B5. To do this we again start by defining two equations with the same two unknowns (R_Π and α). First, we see from Figure A1 that:

$$AC = DC + AD = A'C\,\sin\alpha + A'D\,\tan\beta. \tag{B13}$$

Since $AC \equiv R_\beta$, $A'C \equiv R_\Pi$, and $A'D = A''C = R_\Pi\cos\alpha$, B13 can be re-written as:

$$R_\beta = R_\Pi\sin\alpha + R_\Pi\cos\alpha\tan\beta. \tag{B14}$$

Also from Figure A1, we see that:

$$BC = EC - EB = B'B'' - EB'\tan\gamma$$
$$= B'C\,\sin\alpha - EB'\tan\gamma. \tag{B15}$$

But $BC \equiv R_\gamma$, $B'C \equiv R_\Pi$ and $B'E = B''C = R_\Pi\cos\alpha$, which, when substituted into B15, yields:

$$R_\gamma = R_\Pi\sin\alpha - R_\Pi\cos\alpha\tan\gamma. \tag{B16}$$

Dividing B14 and B16 by a factor of $(\cos\alpha)$ yields the equations:

$$\frac{R_\beta}{\cos\alpha} = R_\Pi(\tan\alpha + \tan\beta), \tag{B17}$$

and

$$\frac{R_\gamma}{\cos\alpha} = R_\Pi(\tan\alpha - \tan\gamma). \tag{B18}$$

Further dividing B17 by B18, and making the substitutions $R_\beta = R_0\tan\beta$ and $R_\gamma = R_0\tan\gamma$, results in:

$$\frac{R_0\tan\beta}{R_0\tan\gamma} = \frac{R_\Pi(\tan\alpha + \tan\beta)}{R_\Pi(\tan\alpha - \tan\gamma)}, \tag{B19}$$

where R_0 and R_Π simplify, and the equation rearranges into an expression for α as a function of only the two (measurable) angles β and γ, which is:

$$\frac{2}{\tan\alpha} = \frac{1}{\tan\gamma} - \frac{1}{\tan\beta}. \tag{B20}$$

Having thus obtained the angle α, one can the use it to calculate R_Π through B5. The uncertainty in α can be computed by propagating the uncertainties in β and γ. Since both angles are smaller than $\sim 10°$, one can approximate $\tan\beta \approx \beta$ and $\tan\gamma \approx \gamma$. Equation B20 is re-written as:

$$\tan\alpha \approx \frac{2\beta\gamma}{\beta - \gamma} \equiv T. \tag{B21}$$

The uncertainty in T is therefore:

$$\delta T = \frac{2}{(\beta - \gamma)^2}\sqrt{\gamma^4\delta\beta^2 + \beta^4\delta\gamma^2}, \tag{B22}$$

which yields the upper and lower uncertainties in α, namely $\delta^+\alpha$ and $\delta^-\alpha$ as follows:

$$\delta^+\alpha = \tan^{-1}(T + \delta T) - \tan^{-1}(T)$$
$$= \tan^{-1}(T + \delta T) - \alpha$$
$$\delta^-\alpha = \tan^{-1}(T) - \tan^{-1}(T - \delta T)$$
$$= \alpha - \tan^{-1}(T - \delta T). \tag{B23}$$

5

Galaxy Decomposition

Having developed, in Chapter 2, a method which extends isophotal structure analysis techniques from relatively simple, elliptical galaxies to complex, multi–component systems – such as disc galaxies, with bulge, bar, X/P, or barlens components – the present Chapter now turns to the analytical modelling of their radial surface brightness profiles (SBP), through the technique of galaxy decomposition.

Several versatile image-fitting programs have been recently developed and made available to the community (e.g., GALFIT – Peng et al. 2002, 2010; IMFIT – Erwin 2015; see §1.1.4), which has more or less homogenised two-dimensional decompositions in the literature during the past few decades. Nevertheless, despite its powerful impact, the 2D method suffers from several drawbacks, and can often be less stable and insightful than the 1D approach, as explained in §1.1.4, and detailed further in this Chapter. This has led some authors to exploit both techniques, for a particularly thorough treatment of the data (e.g., Laurikainen et al. 2005, 2010; Savorgnan & Graham 2016c). Although there is a long history of one-dimensional (1D) SBP modelling (see Graham 2013 for a review), most authors have either coded, or inherited private versions of, the fitting software. This lack of a robust, multi-purpose, publicly available platform for 1D SBP decompositions has motivated the development, and release into the public domain, of PROFILER, a new program designed for this purpose, which is presented in this Chapter.

PROFILER is designed to model multi-component systems, and is particularly tailored for (but not limited to) disc galaxies. As such, it can model classical exponential discs (Equation 1.2), truncated discs (Pohlen et al. 2004; Erwin et al. 2005; Pohlen & Trujillo 2006) via a broken exponential model, and edge-on discs, either with a Sérsic (1963) function (Pastrav et al. 2013) or with two special cases of the edge–on disc model (van der

Kruit & Searle 1981), namely along the major and minor axis, respectively. In addition to discs, PROFILER can model spheroids with a Sérsic (Caon et al. 1993) or core-Sérsic (Graham et al. 2003) model, bars with a Sérsic or Ferrers (1877) model, rings and spiral arms with a Gaussian model, and both resolved and point–like nuclear sources, with a variety of the above functions.

This code is extensively used throughout Chapters 3 and 6, to model the (non-exponential) edge-on discs, in the discy elliptical NGC 1271 (Graham et al. 2016a), and in a sample of X/P galaxies (Ciambur & Graham 2016), as well as to quantify the bulges of intermediate-mass black hole hosts (Graham et al. 2016b; Webb et al. 2017; Koliopanos et al. 2017). More recently, PROFILER was employed to model an embedded face-on disc in the dwarf early-type galaxy CG 611 (Graham et al. 2017).

Unless a galaxy is perfectly circular at all radii, its radial surface brightness profile (typically plotted along the major axis of the isophotes) is insufficient to reconstruct the 2D surface brightness distribution. To do this, the geometric parameters of the isophotes are required (ellipticity, position angle, and higher–order harmonic terms). PROFILER is designed to read isophote tables (such as the output of ELLIPSE or ISOFIT, see previous Chapter), and use their additional information to generate, and model, the "equivalent" axis (R_{eq}) profile. The latter is obtained by mapping each (quasi-elliptical) isophote onto an equivalent circle such that it conserves its enclosed surface area. The circularly symmetric R_{eq} profile thus easily allows one to compute the total flux of each component analytically (see Graham & Driver 2005 for the Sérsic model), from the best–fit parameters of the equivalent axis solution.

PROFILER is written in PYTHON and designed for flexibility, computational speed and interactive use through a graphics user interface (GUI). The user can in principle add any number, and combination, of components, chosen from the available functions, to build a model. The solution is reached through a least-squares minimisation, performed with the Levenberg-Marquardt algorithm (Marquardt 1963), via an external PYTHON library (LMFIT[1]). Particular care is taken when performing the convolution of the model SBP with the instrumental point spread function (PSF). This operation is required in order to reproduce the blurring present in astronomical images, caused by each telescope's resolution limit and, for ground–based instruments, by observing conditions (i.e., atmospheric

---

[1] `https://pypi.python.org/pypi/lmfit`

turbulence, or "seeing"). Since this process is inherently two–dimensional, the convolution operation in PROFILER is performed in 2D, and allows for ellipticity in the model (as shown to be important in Trujillo et al. 2001a,b), as well three different choices for PSF.

The remainder of this Chapter consists of the article "PROFILER– *A Fast and Versatile New Program for Decomposing Galaxy Light Profiles*", by B. C. Ciambur, as it appears in Publications of the Astronomical Society of Australia, Vol. 33, Ed. 62 (2016), reproduced with permission.

PROFILER – A Fast and Versatile New Program for Decomposing Galaxy Light Profiles

Bogdan C. Ciambur[1,2]

[1]Centre for Astrophysics and Supercomputing, Swinburne University of Technology, Hawthorn, VIC 3122, Australia
[2]Email: bciambur@swin.edu.au

Abstract

I introduce PROFILER, a user-friendly program designed to analyse the radial surface brightness profiles of galaxies. With an intuitive graphical user interface, PROFILER can accurately model galaxies of a broad range of morphological types, with various parametric functions routinely employed in the field (Sérsic, core-Sérsic, exponential, Gaussian, Moffat, and Ferrers). In addition to these, PROFILER can employ the broken exponential model for disc truncations or anti–truncations, and two special cases of the edge-on disc model: along the disc's major or minor axis. The convolution of (circular or elliptical) models with the point spread function is performed in 2D, and offers a choice between Gaussian, Moffat or a user-provided profile for the point spread function. PROFILER is optimised to work with galaxy light profiles obtained from isophotal measurements, which allow for radial gradients in the geometric parameters of the isophotes, and are thus often better at capturing the total light than 2D image-fitting programs. Additionally, the 1D approach is generally less computationally expensive and more stable. I demonstrate PROFILER's features by decomposing three case-study galaxies: the cored elliptical galaxy NGC 3348, the nucleated dwarf Seyfert I galaxy Pox 52, and NGC 2549, a double-barred galaxy with an edge-on, truncated disc.

PROFILER is freely available at https://github.com/BogdanCiambur/PROFILER.

Keywords: galaxies: fundamental parameters – galaxies: individual (NGC 2549, NGC 3348, Pox 52) – galaxies: structure – methods: data analysis

1 INTRODUCTION

Galaxies are complex structures assembled through a variety of physical processes which act at different stages of their life, such as gas accretion; star formation; disc formation, growth, and buckling; bar formation and buckling etc.; as well as mergers and interactions with neighbouring galaxies. The result is a rich variety of galactic components in the observed galaxy population. Classifying galaxies based on these structures, in the optical and/or near-infrared bands has been and still is now common practise (e.g., Jeans 1919, Hubble 1926, de Vaucouleurs 1959, Sandage 1975, de Vaucouleurs et al. 1991, Abraham, van den Bergh, & Nair 2003, Buta et al. 2015, etc.).

A quantitative structural classification requires a reliable method to separate out each structural component from the others that make up the galaxy. Moreover, individually analysing each constituent probes, the specific physical or dynamical processes associated with it and thus provides insight into galaxy evolution. The common practise is to model one of the fundamental diagnostics of a galaxy's structure, namely its radial light (or surface brightness) profile (SBP), by decomposing it into a sum of analytical functions, with each function representing a single component (e.g., Prieto et al. 2001, Balcells et al. 2003, Blanton et al. 2003, Naab & Trujillo 2006, Graham & Worley 2008). See Graham 2013 for a comprehensive review of modelling the light profile of galaxies.

One of the best methods to extract an SBP from a galaxy image is by fitting quasi-elliptical isophotes as a function of increasing distance from the photometric centre of the galaxy. In such schemes, the isophotes are free to change their axis ratio, or ellipticity, position angle (PA), and shape (quantified through Fourier harmonics) with radius, which ensures that the models capture the galaxy light very well. A popular tool for this is the IRAF task ELLIPSE (Jedrzejewski 1987), which works well for galaxies whose isophotes display low-level deviations from pure ellipses, such as elliptical galaxies or disc galaxies viewed relatively face-on. For more complex isophotal structures however, such as edge-on disc galaxies,

1

X/peanut-shaped bulges, bars, and barlenses, Ellipse has been shown to fail and the newer IRAF task Isofit[1] (Ciambur 2015) is more appropriate.

A somewhat different approach in performing galaxy decomposition is to directly fit the galaxy's projected light distribution, i.e. the galaxy image, in two dimensions (2D). Recent years have seen the advent and development of a number of programs dedicated to this purpose, notably GIM2D (Simard et al. 2002), Budda (de Souza, Gadotti, & dos Anjos 2004), Galfit (Peng et al. 2010), and Imfit (Erwin 2015).

In support for the 2D method, Erwin (2015) has invoked several drawbacks of one-dimensional (1D) profile modelling, namely that it is unclear which azimuthal direction to model (major axis, minor axis, or other), that most of the data from the image is discarded, and that non-axisymmetric components (such as bars) can be misinterpreted as axisymmetric components, and their properties cannot be extracted from a 1D light profile. While these issues certainly apply when one extracts the SBP by taking a 1D cut from a galaxy image, all of these issues are resolved if the SBP is obtained from an isophotal analysis. In particular, fitting isophotes makes use of the entire image (so no data is discarded) and apart from the SBP itself, this process additionally provides information about the isophotes' ellipticities, PAs, and deviations from ellipticity (in the form of Fourier modes). All of this information is sufficient to completely reconstruct the galaxy image for even highly complex and non-axisymmetric isophote shapes (see Ciambur 2015 and Section 5 of this paper). Having these extra isophote parameters allows one to obtain the SBP along any azimuthal direction, and identify and quantitatively study non-axisymmetric components such as bars or even peanut/X-shaped bulges (Ciambur & Graham 2016). It is therefore recommended to always use isophote tables rather than image cuts in 1D decompositions.

Overall, both 1D and 2D decomposition techniques present benefits as well as disadvantages. The 2D image-modelling technique has the advantage that every pixel (except those deliberately masked out due to contaminating sources) in the image contributes directly to the fitting process, whereas in an isophotal (1D) analysis, pixels contribute in an azimuthal-average sense. Multicomponent systems with different photometric centres can also pose a problem for 1D SBPs, which assume a single centre for all components at $R = 0$[2], but can however be easily modelled in 2D. On the other hand, 2D codes suffer from the fact that each component has a single, fixed value for the ellipticity, PA, and Fourier moments (such as boxyness or discyness, and also higher orders), which can in some cases limit the method considerably. Triaxial ellipsoids viewed in projection can have radial gradients in their ellipticities and PAs (Binney 1978, Mihalas & Binney 1981), an effect captured in a 1D isophotal analysis (where both quantities can change with radius) but not in a 2D decomposition[3].

There are notable examples in the literature where the 1D method has been preferred over the 2D technique. One such case is the decomposition of the Atlas[3D] (Cappellari et al. 2011) sample[4] of early-type galaxies, in Krajnović et al. (2013). I point the reader to Section 2 and Appendix A of their paper, where they discuss both methods and test the performance of their preferred 1D method against a 2D analysis (with Galfit). Another illuminating example is in Savorgnan & Graham (2016). They performed both 1D (with private code) and 2D (with Imfit) decompositions of 72 galaxies, out of which 41 did not converge or did not give meaningful solutions in 2D, whereas only nine could not be modelled in 1D. Section 4.1 in their paper also provides an insightful and practical comparison between 1D and 2D galaxy modelling techniques.

The past few decades have seen a flurry of 2D image-fitting codes, whereas publicly available tools that focus on 1D decompositions are scarce. In this paper, I present Profiler, a freely available code written in Python, designed to provide a fast, flexible, user-friendly, and accurate platform for performing structural decompositions of galaxy SBP.

The remainder of the paper is structured as follows. In Section 2, I describe the input data and information required by Profiler prior to the decomposition process. Section 3 is a concise review of typical galaxy components and the analytical functions employed to model them. Section 4 then details the fitting process, and Section 5 provides three example applications, each illustrating different features of Profiler. Finally, I summarise and conclude with Section 6.

2 THE INPUT DATA

With a view to streamline the decomposition process, Profiler has a built-in Graphical User Interface (GUI) coded in the standard Python package Tkinter. This ensures that the decomposition process is entirely interactive, with all settings, options, and input information readily changeable through buttons, text-box, and **check-box** widgets in the main GUI. Thus, the need to perpetually change a separate configuration file each time one wishes to modify settings is eliminated, and the user can employ the visualisation tools (which will be discussed in Section 5) and the GUI to make any required tweaks, until the solution is reached. Figure 1 presents the GUI, with most widgets active for illustration purposes. Note that the user must specify all this galaxy-specific information on a case-by-case basis, as is detailed below.

---

[1] https://github.com/BogdanCiambur/ISOFIT

[2] This applies also to ring components, which have their brightest point at $R > 0$ along the 1D profile. This radial parameter represents the radius of the ring, while its centre is still assumed to be at $R = 0$.

[3] Note, however, that the 2D code Imfit can generate 2D images from line-of-sight integration of 3D luminosity density.

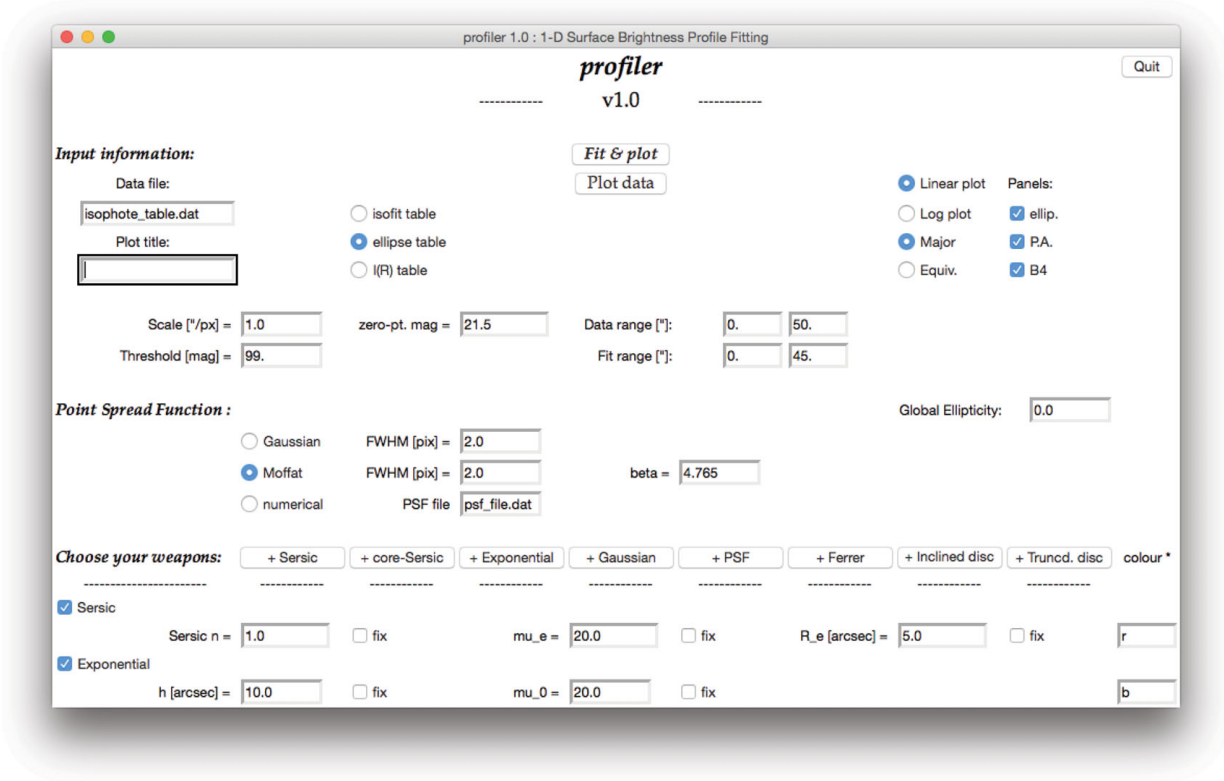[4] http://www-astro.physics.ox.ac.uk/atlas3d/

Figure 1. The PROFILER GUI, with two active components (Sérsic and exponential) for illustration purposes. All the text-boxes and check-boxes are set to default values, and must be changed by the user to the specifics of the data (see text for details). The component parameters too must be set to initial guess-values, from which the code obtains the best-fitting solution.

2.1. The surface brightness profile

PROFILER was designed to work with isophote tables generated by either ELLIPSE or ISOFIT. Apart from the galaxy light profile itself, the two programs provide useful ancillary information such as the isophotes' ellipticities, PAs, departures from pure ellipses, etc. Alternatively, the user can provide a simple table consisting of two columns, namely radius R and intensity $I(R)$.

Instrument-specific details are additionally required, in particular the CCD angular size of a pixel, in arcsec, and the zero-point magnitude. The isophote intensity I is then converted into surface brightness μ (in magnitudes arcsec^{-2}) through

$$\mu(R) = m_0 - 2.5\log_{10}\left[\frac{I(R)}{ps^2}\right], \qquad (1)$$

where m_0 is the zero-point magnitude and ps is the pixel angular size. In Equation (1), R generally corresponds to the isophote's semi-major axis (R_{maj}). Often the major axis profile is mapped onto the 'equivalent', or geometric mean axis, R_{eq}, through

$$R_{\mathrm{eq}} = R_{\mathrm{maj}}\sqrt{1 - \epsilon(R_{\mathrm{maj}})}, \qquad (2)$$

where $\epsilon(R_{\mathrm{maj}})$ is the isophote ellipticity, defined as 1 minus the axis ratio. This mapping converts the isophote into the equivalent circle that conserves the original surface area of the isophote (see the Appendix of Ciambur 2015 for a derivation). The equivalent axis profile is thus circularly symmetric, and decomposing it allows for an analytical computation of the total magnitude of components directly from their parameters (e.g., Graham & Driver 2005 for Sérsic parameters).

The user has a choice between modelling the profile along R_{maj} (the default) or R_{eq}. For the latter option, provided that the input data contains ellipticity information, PROFILER generates the equivalent axis profile internally and outputs the total magnitudes of components after the decomposition. If the input data is a two-column table, it is assumed that the R column is already the axis chosen by the user. Whenever the sampling step ΔR between successive isophotes is not constant, PROFILER linearly interpolates the SBP internally on a uniformly spaced radial axis before performing the PSF convolution.

2.2. The point spread function

The ability of telescopes to resolve a point-source is dictated by a number of factors, including their diffraction limit (due to the fact that they have a finite aperture), the detector spatial resolution (pixel size) and, for ground-based instruments, the distortion of wavefronts caused by turbulent mixing in the atmosphere, an effect known as 'seeing'. All of these effects blur astronomical images, spreading the light at every point in a way characteristic to each instrument. In an ideal image, a point source's profile is a delta function. In a real image, however, the functional form is called the instrumental *point*
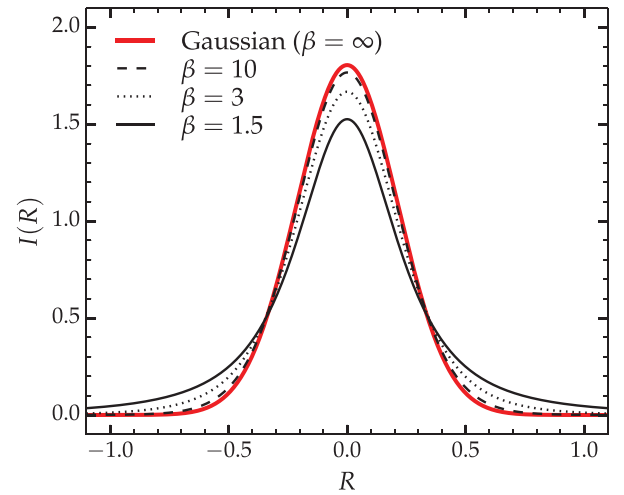

Figure 2. Different point spread functions represented as intensity vs. radius, in arbitrary units. The Moffat function (black curves) accounts for seeing effects (e.g., Airy rings) by transferring flux from the peak of the PSF into its wings. This is controlled by the β parameter and, for large values of β the Moffat approaches a Gaussian (red curve). All curves plotted here have an FWHM of 0.5.

spread function (PSF). In order to reconstruct the true distribution of light in an image, it is essential to know the PSF at every point across the focal plane.

The most basic aproximation of a PSF is a Gaussian functional form with the single parameter FWHM (or dispersion σ, the two being related by FWHM $= 2\sigma\sqrt{2\ln2}$). This form, however, underestimates the flux in the 'wings' of the PSF, which can bias decomposition parameters (Trujillo et al. 2001b found the effect to range between 10–30% for Sérsic parameters).

A more realistic approximation which *is* capable of modelling PSF wings is the Moffat profile (Moffat 1969), given by

$$I(R) = I_0\left[1 + \left(\frac{R}{\alpha}\right)^2\right]^{-\beta}, \qquad (3)$$

where α is a characteristic width related to the FWHM by the identity FWHM $= 2\alpha\sqrt{2^{1/\beta} - 1}$, and β controls the amount of light in the 'wings' of the profile compared to the centre (redistributing the light of the central peak into wings mimics the effect of spreading light in Airy rings). Figure 2 shows Moffat functions of the same FWHM but different values of β, as well as the limiting case where $\beta \rightarrow \infty$, which corresponds to a Gaussian (Trujillo et al. 2001b).

In practise, when characterising the PSF the usual norm is to fit either a Gaussian or a Moffat profile on bright, unsaturated stars in the image with e.g., the IRAF task IMEXAMINE. This task directly provides the FWHM for the former and (FWHM; β) for the latter case.

In PROFILER, the user has a choice of either Gaussian, Moffat, or data vector PSF. The first two require the parameters specific to each function, from which PROFILER

Table 1. An index of the functions available in PROFILER.

Function	Parameters	Used for
Sérsic	3	Ellipticals, bulges, bars, edge-on discs
Core-Sérsic	6	Cored ellipticals
Exponential	2	Discs
Broken exponential	4	(Anti-)truncated discs
Edge-on disc model	2	Edge-on discs
Ferrers	4	Bars
Gaussian	3 (1/0)	Rings, spiral arms, (point source/PSF)
Moffat	1/0	Point source/PSF
Data vector PSF	1/0	Point source/PSF

generates the PSF internally when needed. The third option requires a table of values, R and $I(R)$, in the form of a text file provided by the user[5]. The radial extent of the data vector PSF is required by PROFILER to at least match or exceed that of the galaxy profile. As I will show in Section 5.3, this feature is very useful when the analytical functions above do not provide a sufficiently exact description of the PSF.

3 THE MODEL

PROFILER can employ several analytical functions to model the radial light profiles of a galaxy's constituent components. The user is free to add an indefinite number of components to the model, and each component (function) can have its parameters freely varying or fixed to given values during the fit.

In the remainder, I provide a description of each function available in PROFILER in the context of the photometric component(s) which it is intended to model. A summary of all the functions, with their typical uses and number of parameters, is provided in Table 1 at the end of this section.

3.1. Ellipticals and galaxy bulges

3.1.1. The Sérsic model

There have been many attempts in the past to analytically describe the SBPs of elliptical galaxies, including deVaucouleurs' $R^{1/4}$ 'law' (de Vaucouleurs 1948, 1953), the King profile (King 1962, 1966), etc. See Graham (2013) for a review of these past efforts. At present, it is generally agreed that the most robust function for this purpose is given by the Sérsic (1963) $R^{1/n}$ model (Caon, Capaccioli, & D'Onofrio 1993, D'Onofrio, Capaccioli, & Caon 1994).

While the Sérsic function in itself does not contain any physical meaning, it is remarkably flexible and can accurately capture the light profiles of a broad range of spheroid components, from the small bulges of late-type spiral galaxies to the highly concentrated light profiles of bright elliptical
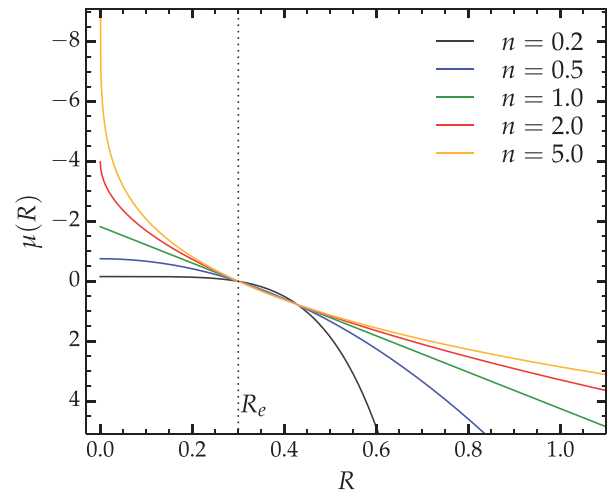

Figure 3. The Sérsic profile for five values of the Sérsic index n. The curves represent surface brightness as a function of radius, in arbitrary units, and all profiles have the same values of μ_e and R_e. The half-light radius, R_e, is indicated by the vertical dotted line.

galaxies. Additionally (as will be discussed in the following sections), the Sérsic profile can model discs and bars.

The Sérsic profile is parameterised by three quantities: the radius enclosing half of the light, R_e, the intensity at this radius, $I_e = I(R_e)$, and the concentration, or Sérsic index, n. It takes the form

$$I(R) = I_e \exp\left\{-b_n\left[\left(\frac{R}{R_e}\right)^{\frac{1}{n}} - 1\right]\right\}, \tag{4}$$

where b_n depends on n and is obtained by solving

$$\Gamma(2n) = 2\gamma(2n, b_n), \tag{5}$$

where Γ is the (complete) gamma function and γ the incomplete gamma function, given by the integral

$$\gamma(2n, x) = \int_0^x e^{-t} t^{2n-1} dt. \tag{6}$$

Figure 3 shows the Sérsic profile for a range of concentration parameters (n). The reader will also find a review of the Sérsic model, useful equations pertaining to it, as well as early references, in Graham & Driver (2005).

---

[5] One way to obtain this would be to extract the light profile of a bright star in the image.
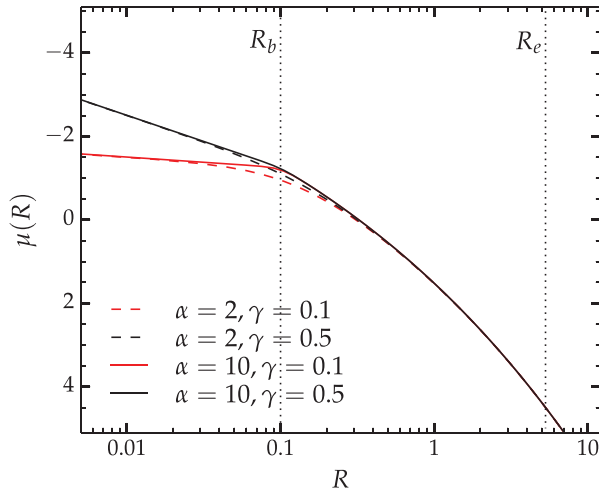
Figure 4. The core-Sérsic profile. The curves represent surface brightness as a function of radius, in arbitrary units. Red curves illustrate the effect of varying the inner slope γ, while black curves illustrate changing the break sharpness α. The break radius and effective radius are indicated through the vertical dotted lines, and are marked as R_b and R_e, respectively.

Figure 5. The three types of exponential disc models represented as surface brightness vs. radius, in arbitrary units. The black curve is a single exponential (Type I) profile. The broken exponential profile takes two forms: the Type II, or truncated, profile ($h2 < h1$, blue), and the Type III, or anti-truncated profile ($h2 > h1$, red).

3.1.2. The core-Sérsic model

The most luminous early-type galaxies display 'cored' central profiles, thought to be the result of black hole binary systems kicking out stars through 3-body interactions (Begelman, Blandford, & Rees 1980), thus causing a deficit of light in the centre (King 1978, Dullo & Graham 2012, 2014 and references therein). An ideal functional form which describes these types of objects is the 6-parameter core-Sérsic model (Graham et al. 2003), given by

$$I(R) = I' \left[1 + \left(\frac{R_b}{R} \right)^{\alpha} \right]^{\frac{\gamma}{\alpha}} \exp \left\{ -b_n \left[\frac{R^{\alpha} + R_b^{\alpha}}{R_e^{\alpha}} \right]^{\frac{1}{\alpha n}} \right\}. \quad (7)$$

The core-Sérsic function takes the form of a power law in the core region, which then transitions into a Sérsic form outside the core region (Figure 4). It is parameterised by the break (transition) radius R_b and half-light radius R_e, the inner profile slope γ, the smoothness of the transition, controlled by α, the Sérsic index n and a normalisation, or scale intensity I', which is related to the intensity at the break radius through Equation (6) in Graham et al. (2003), that is

$$I' = I_b \, 2^{-\gamma/\alpha} \exp \left[b_n \left(\frac{2^{1/\alpha} R_b}{R_e} \right)^{1/n} \right]. \quad (8)$$

The core-Sérsic model has also been recently implemented in 2D fitting codes, specifically in the GALFIT add-on code GALFIT-CORSAIR (Bonfini 2014), and in IMFIT (Erwin 2015).

3.2. Discs

3.2.1. The exponential model

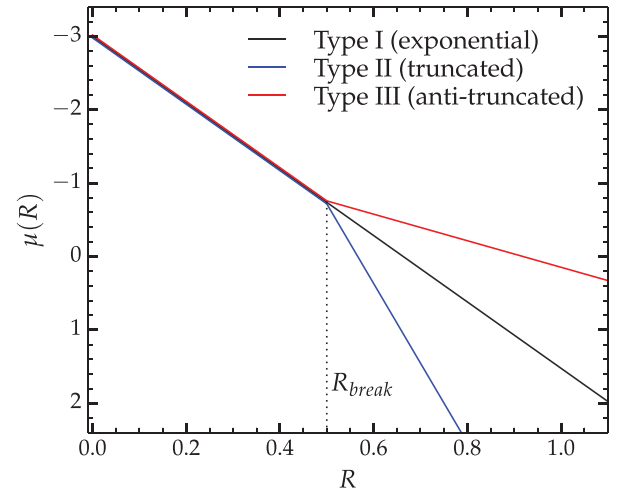The radial decline of light in flat galaxy discs has long been known to be approximately exponential (Patterson 1940,

de Vaucouleurs 1957, Freeman 1970). For disc components, PROFILER can employ the two-parameter exponential model:

$$I(R) = I_0 \exp \left(-\frac{R}{h} \right), \quad (9)$$

where I_0 is the intensity at $R = 0$ and h is the exponential scale length, which corresponds to the length in which the light diminishes by a factor of e, i.e., $I(h) = I_0/e$.

3.2.2. The broken exponential model

While the light profiles of galaxy discs are commonly assumed to be characterised by a single exponential for their whole extent (galaxies for which this is true are said to have 'Type I' profiles in the classification of Erwin, Pohlen, & Beckman 2008), as many as 90% (Pohlen & Trujillo 2006) of disc galaxies display a 'break' in their light profiles, **typically** at a few scale lengths from the photocentre (van der Kruit 1987, Pohlen et al. 2004). More specifically, this is an abrupt change in their exponential scale length (Figure 5). This phenomenon is referred to as a *truncation*, or 'Type II' profile, if the scale length decreases (the light fall-off becomes steeper) and an *anti-truncation*, or 'Type III' profile (Erwin, Beckman, & Pohlen 2005), if the scale-length becomes longer (the fall-off becomes shallower). PROFILER provides a broken exponential function to fit these types of profiles [Equation (10)], characterised by four free parameters: The central flux I_0, the break radius R_b, and the inner and outer scale lengths, h_1 and h_2, respectively.

$$I(R) = \begin{cases} I_0 \exp \left(-R/h_1 \right), & R \leqslant R_b \\ I_b \exp \left[-(R - R_b)/h_2 \right], & R > R_b, \end{cases} \quad (10)$$

where I_b is the brightness at the break radius, and is not a free parameter since $I_b = I(R_b)$.
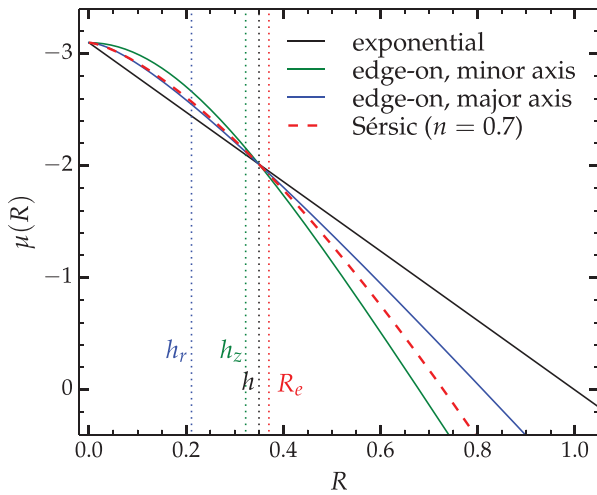
Figure 6. Various disc models: exponential (black, solid), edge-on disc along major-axis [Equation (12); blue, solid], edge-on disc along the minor-axis (Equation (13); green, solid), and Sérsic ($n = 0.7$; red, dashed). The profiles are represented as surface brightness vs. radius, in arbitrary units. They all have the same central surface brightness (μ_0) and the same *e*-folding radius, equal to h, the exponential scale length. The vertical dotted lines mark each profile's characteristic scale length (keeping the colour scheme).

3.2.3. The Edge-on disc model

When disc galaxies are viewed in close to edge-on orientation, the disc SBP exhibits a gradually shallower slope towards the centre (van der Kruit & Searle 1981; Pastrav et al. 2013). In this regime, PROFILER can use two special cases of the inclined disc profile of van der Kruit & Searle (1981), which is defined in 2D as a function of major axis R and minor axis Z, as

$$I(R, Z) = I_0 \left(\frac{R}{h_r}\right) K_1 \left(\frac{R}{h_r}\right) \operatorname{sech}^2 \left(\frac{Z}{h_z}\right), \quad (11)$$

where I_0 is the central intensity, h_r is the scale length in the plane of the disc (major axis), h_z is the scale length in the vertical (minor axis) direction ($\perp$ to the disc plane), and K_1 is the modified Bessel function of the second kind.

In the limiting case of $Z = 0$, Equation (11) reduces to the major axis form

$$I(R_{\mathrm{maj}}) = I_0 \left(\frac{R_{\mathrm{maj}}}{h_r}\right) K_1 \left(\frac{R_{\mathrm{maj}}}{h_r}\right). \quad (12)$$

Similarly, along the minor axis ($R = 0$), Equation (11) reduces to

$$I(R_{\mathrm{min}}) = I_0 \operatorname{sech}^2 \left(\frac{R_{\mathrm{min}}}{h_z}\right). \quad (13)$$

PROFILER can employ Equations (12) and (13) to fit edge-on discs along the major and minor axes, respectively. Note that neither h_r nor h_z are equal to the *exponential* scale length h. Their corresponding profiles do not decrease in intensity by a factor of e at every h_r or h_z (see van der Kruit & Searle 1981 for more details on the definition of these two scale parameters). One can readily discern this visually in Figure 6

(blue and green curves): The curvature of these profiles towards $R \to 0$ implies that they cannot be characterised by a single value for the *e*-folding radius, as exponential profiles are. Rather, the *e*-folding starts off large towards the centre (where the slopes are shallower) and gradually decreases with increasing R. At high radii, the *e*-foldings asymptote to constant values and therefore both profiles approach exponential forms. The major-axis profile has an *e*-folding length (from $R = 0$) equal to $1.658h_r$, whereas the minor-axis profile has an *e*-folding length equal to $1.085h_z$[6]. This is illustrated in Figure 6.

3.2.4. The Sérsic model for discs

The Sérsic function can also successfully model discs. The $n = 1$ Sérsic function is identical to an exponential and can be used to model Type I profiles, while inclined (edge-on) discs, or those with dusty centres, may be fitted with $n < 1$ Sérsic functions (typically in the range $n \sim 0.7 - 0.9$; see Figure 6). In this case, one can still recover its *e*-folding length h_S and central surface brightness μ_0 from

$$h_S = \frac{R_e}{(b_n)^n}, \quad (14)$$

and

$$\mu_0 = \mu_e - \frac{2.5}{\ln(10)} b_n. \quad (15)$$

As before, if $n \neq 1$, the *e*-folding radius is not unique along the whole profile and is again highest towards the centre and lower at high-R. When $n = 1$, Equations (14) and (15) reduce to $h_S = R_e/1.67835$ and $\mu_0 = \mu_e - 1.82224$, respectively. Unlike the edge-on disc model, the $n < 1$ Sérsic function does not asymptote to an exponential, but has an ever steeper slope with increasing R (see Figure 3).

3.3. Bars

Bars are common in disc galaxies (the fraction is $\sim 2/3$ in the near-infrared; Eskridge et al. 2000, Menéndez-Delmestre et al. 2007, Laurikainen et al. 2009, Nair & Abraham 2010) and display a characteristic flat profile which ends with a relatively sharp drop-off. This shows up in SBPs as a 'shelf'-like or 'shoulder'-like feature, usually (but not necessarily) between the inner spheroid component and the outer disc. Bars are often modelled with the four-parameter Ferrers profile (Ferrers 1877), expressed as

$$I(R) = I_0 \left[1 - \left(\frac{R}{R_{\mathrm{end}}}\right)^{2-\beta} \right]^{\alpha}, \quad (16)$$

where I_0 is the central brightness, R_{end} is the cut-off radius, and α and β control the inner slope and break sharpness (see Figure 7). Note that $\beta > 0$ causes a cusp in the central parts

---

[6] This factor is given by $1.085 = \operatorname{arccosh}(\sqrt{e})$, not to be confused with the factor $1.086 = 2.5/\ln(10)$ in Equation (17) from Graham & Driver (2005), which relates the central surface brightness of an *exponential* to the value at $R = h$ by $\mu_0 = \mu(h) - 1.086$.
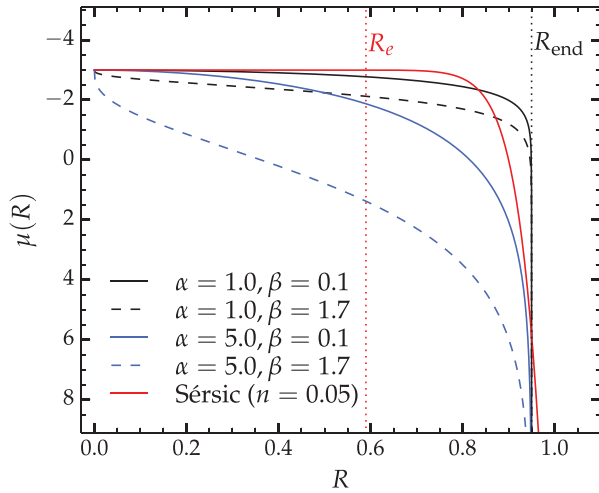
Figure 7. Possible bar components: the black and blue curves are all Ferrers profiles [Equation (16)] with the same central surface brightness (μ_0) and end radius (R_{end}), but different permutations of the α and β parameters, such that curves of the same colour illustrate the effect of changing β, while curves of the same style (i.e., solid vs. dashed) illustrate the effect of changing α. All profiles are represented as surface brightness vs. radius, in arbitrary units.

of the profile. As there is no observational evidence that the profiles of bars display such a cusp, it is recommended that β be set to 0.

Another function which can be used to model bars is a low-n Sérsic function (typically in the range $n \lesssim 0.1$–0.5, the drop-off being sharper the lower n is; see Figure 7, red curve).

3.4. Rings and spiral arms

The presence of spiral arms in a disc can cause deviations from an exponential profile in the form of 'bumps' (Erwin et al. 2005). A stellar ring also causes a 'bump' in the profile. These features are modelled in PROFILER via the three-component Gaussian profile, given by

$$I(R) = I(R_r) \exp\left[-\frac{(R - R_r)^2}{2\sigma^2}\right], \qquad (17)$$

where R_r is the radius of the bump, $I(R_r)$ is its peak intensity, and σ its width (dispersion).

4 FITTING THE DATA

Once the required input information is provided, the user must make a choice of components that are to make up the model. Before this (or at any point after having provided the input information), they can visualise the galaxy light profile and, if it is based on isophote fits with ELLIPSE or ISOFIT, the ellipticity ϵ, PA or B_4 (fourth cosine harmonic amplitude) profiles can be displayed. This helps the user decide which components to use and make an educated guess for the initial values of their parameters. The default setting is that all model

parameters are free, but the user has a choice to hold one or more of the parameters fixed to specific values during the fitting process.

The user must provide a value for a 'global' ellipticity of the central profile (ϵ_c), i.e. the part dominated by the PSF. ϵ_c is important for the convolution process because models with different ellipticities yield slightly different convolved SBPs, as will become clear in Section 4.1. As the galaxy being modelled often consists of a superposition of different components, each with its own ellipticity, a single value for ϵ does not apply to the entire model. However, ϵ_c is only relevant for the part of the model affected by the PSF, and should roughly correspond to the ellipticity of that component which dominates the light in the central few PSF FWHM.

The user can estimate ϵ_c as a luminosity-weighted average of the galaxy's ellipticity profile at a radius of $\sim$2–3 PSF FWHM. The values interior to this should be avoided because here the isophotes are circularised by the PSF, and do not reflect the component's ellipticity. If ϵ_c is not provided, the default value is set to zero, which corresponds to a circularly symmetric model.

When all the desired components are included, PROFILER can begin the search for the best-fitting solution through an iterative minimisation process, which begins with the parameter guess-values set by the user. Each iteration, corresponding to a specific location in the parameter space, consists of building a model, convolving it with the PSF, and comparing the result with the data.

4.1. PSF convolution

The convolution of the model with the PSF is performed in 2D due to two important aspects.

First, the axis ratio (or ellipticity) of a component affects the way its light distribution is blurred by seeing effects (see Trujillo et al. 2001a, 2001b). For a circularly symmetric PSF, if the component too is circularly symmetric then the light from a point located at a distance R from the centre is scattered the same way as any other point at the same radius R. However, if the component is elliptical, then the light at fixed distance from the centre is scattered more efficiently by points lying on the major axis than by the points in other azimuthal directions. In this case, the convolved major axis profile is systematically lower than in the circular case. This effect is illustrated in Figure 8, for three Sérsic profiles, each with three different axis ratios.

Second, the PSF convolution should not be performed in 1D, i.e., by convolving the SBP curve with the PSF profile. This is because each data point in the SBP represents a (local) *surface* brightness at a particular distance from the centre (R) and along a particular direction (θ), i.e., $I \equiv I(R, \theta)$. The SBP itself represents the radial distribution of light *for a particular choice of* θ (e.g., major axis: $\theta = 0$) and is analogous to, but more accurate than, a 1D cut from the image provided that the isophote PAs are constant with radius. As such, the area
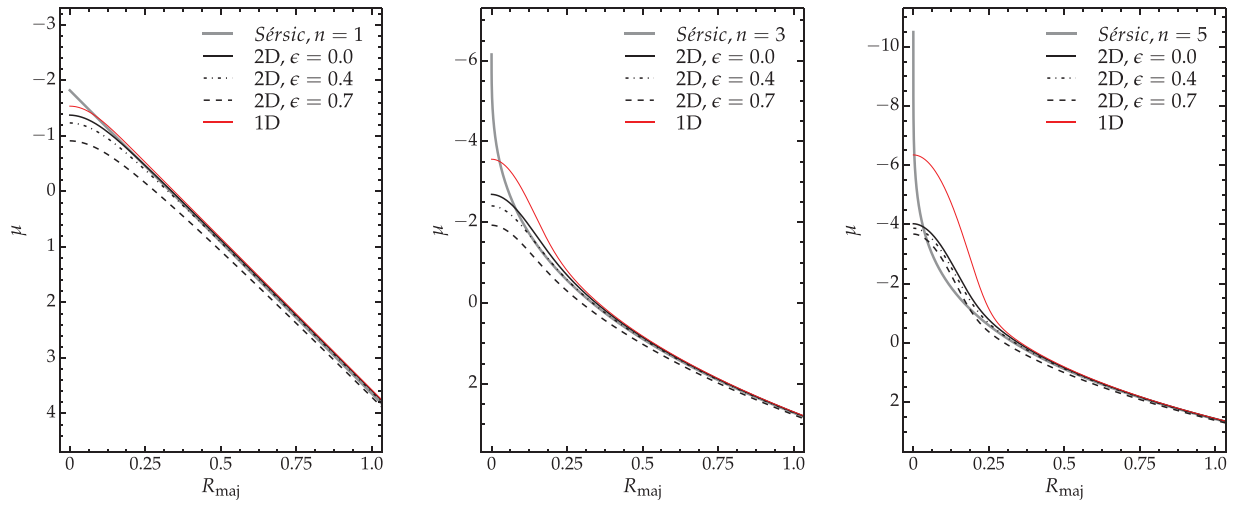
Figure 8. The effect of a component's ellipticity on the PSF convolution, for three different Sérsic functions with the same μ_e and R_e but different n. All profiles represent surface brightness as a function of radius, in arbitrary units. In each panel, the thick grey curve represents the unconvolved Sérsic profile, the thick black lines (solid, dot-dashed, and dashed) represent the profile convolved in 2D with a circular Gaussian PSF, assuming different ellipticities (ϵ) for the Sérsic model, while the thin red curve represents the profile (incorrectly) convolved in 1D with the same PSF profile. Convolving the grey curve in 1D is inappropriate because, while it does conserve the area under grey curve [Equation (18)], it does not conserve the total flux [Equation (19)], and therefore does not model the effect of seeing. The Gaussian FWHM was chosen to be large ($0.167 = 0.5R_e$, in the arbitrary units of the *x*-axis), for clarity.

under the curve,

$$\int_0^\infty I(R, \theta)\mathrm{d}R, \tag{18}$$

does not correspond to the total flux in the image, which requires an additional integration in the azimuthal direction:

$$\int_0^{2\pi} \int_0^\infty R\,I(R, \theta)\,\mathrm{d}R\,\mathrm{d}\theta. \tag{19}$$

A 1D convolution conserves the area under the SBP curve [Equation (18)] but not the total flux in the image [Equation (19)], and is therefore inappropriate to reproduce seeing effects in images, which conserve total flux. The difference between the two types of convolution (1D vs. 2D) is also illustrated in Figure 8.

The convolution is performed in several steps. If the fitting axis is the major axis, then an elliptical 2D light distribution is generated, with a global ellipticity provided by the user and the same profile along the major axis as that of the model SBP. If the fitting is performed along the equivalent axis, the convolution is performed as above except that ϵ_c is set to 0, since the equivalent axis is circularly symmetric by construction.

In the next step, a circularly symmetric 2D PSF is generated, on the same array as the model. This can be based on either the parameters of Gaussian or Moffat forms, or the user-provided data vector PSF. The model array and PSF array are then convolved using the FFT (Fast Fourier Transform) method, and finally, the resulting distribution's major axis profile is obtained, which represents the desired convolved model SBP. This quantity is compared with the data at each iteration.

4.2. Minimisation and solution

While most 2D decomposition codes perform signal-to-noise (S/N)-weighted minimisations in intensity units, PRO-FILER uses an unweighted least-squares method in units of surface brightness. Because noise in galaxy images is dominated by Poisson noise, galaxies have the highest S/N at the centre, where they are usually brightest. However, the central regions can often be affected by dust, active galactic nuclei, nuclear discs, or PSF uncertainty, the latter being particularly important for highly concentrated galaxies. Therefore, placing most of the weight on the central data points can substantially bias the fit for the entire radial range if all of these issues are not dealt with (see similar arguments in Graham et al. 2016). In an unweighted scheme, all data points along the SBP contribute equally to constraining the model and thus, even when the central data is biased, the model is still well constrained by the outer data points. The caveat, however, is that one must ensure that the image sky background is accurately measured and subtracted, otherwise the outer data points introduce a bias in the model. For example, if the outer data corresponds to an exponential disc, inaccurate background subtraction would lead to the wrong scale length, which affects the entire radial range because a disc component runs all the way to the centre.

The minimisation is performed with the PYTHON package LMFIT[7], and the method is a least-squares Levenberg–Marquardt algorithm (Marquardt 1963). The quantity being

---

[7] https://pypi.python.org/pypi/lmfit/

minimised is

$$\Delta_{\rm rms} = \sqrt{\sum_i (\mu_{{\rm data},i} - \mu_{{\rm model},i})}, \qquad (20)$$

where i is the radial bin, $\mu_{\rm data}$ is the data SBP, and $\mu_{\rm model}$ is the model at one iteration.

When the solution is reached, the result is displayed and a logfile is generated. The logfile contains a time-stamp of the fit, all the input information and settings, and a raw fit report with all parameters and their correlations. A more in-depth report follows, which lists each component's best-fit parameter values and, if the decomposition was performed on the equivalent axis, their total magnitude.

The quantity $\Delta_{\rm rms}$ quantifies the global quality of the fit, but a more reliable proxy of the solution's accuracy, in detail, is the residual profile: $\Delta\mu(R) = \mu_{\rm data}(R) - \mu_{\rm model}(R)$. A good fit is characterised by a flat $\Delta\mu$ profile which scatters about the zero value with a level of scatter of the order of the noise level in the data profile. Systematic features such as curvature usually signal the need for additional components, or modelling with inadequate functions, or biased data (caused by e.g., unmasked dust). While the addition of more components will invariably improve the fit, it must nevertheless remain physically motivated, i.e., the user should seek evidence for the presence of extra components, either in the image, ellipticity, PA, or B_4 profile. As noted in Section 3.4 of Dullo & Graham (2014), one should not blindly add Sérsic components.

The user can choose the radial range of data to be considered throughout the fit, by entering start and stop values (in arcsec). While excluding any data is not generally desirable (unless there are biasing factors in a particular range), particularly in the central regions, where most of the signal is, varying the radial extent of the data can provide an idea of the stability of the chosen model, and the uncertainties in its parameters.

5 EXAMPLE DECOMPOSITIONS

5.1. NGC 3348 – a cored elliptical galaxy

In the first example, I consider the galaxy NGC 3348, a massive elliptical galaxy with a cored inner SBP (Rest et al. 2001, Graham et al. 2003). Archival *HST* data taken with the *ACS/WFC* camera (*F814W* filter) was retrieved from the *Hubble Legacy Archive*[8] (Figure 9, panel *a*). The sky background was measured with IMEXAMINE close to the chip edges, and subtracted from the image. The galaxy light profile was extracted from the resulting image with ISOFIT and the PSF was characterised from the image by fitting a Moffat profile to bright stars, with IMEXAMINE.

The galaxy was modelled with a single core-Sérsic component, in the range 0–50 arcsec (roughly the distance from the photocentre to three out of four chip edges of the *ACS/WFC*

---

[8] http://hla.stsci.edu

chip), and the best-fitting solution is displayed in Figure 10. A 2D reconstruction of the image, with the *IRAF* task CMODEL, was further generated based on the isophote parameters, i.e., their surface brightness, ellipticity, and Fourier harmonics along the major axis. This reconstructed image was then subtracted from the original image, which resulted in the residual map shown in Figure 9, panel *b*. Panel *c* of the same figure shows the residual map obtained from the same isophote table but with the surface brightness column (red symbols in Figure 10) replaced with the modelled SBP (black curve in Figure 10).

The single-component fit yielded a core radius of $R_b = 0.43$ arcsec, break sharpness $\alpha = 1.86$, core slope $\gamma = 0.09$, half-light radius $R_e = 27.63$ arcsec, and Sérsic index $n = 4.91$. These results are generally in good agreement with Graham et al. (2003), though the outer Sérsic parameters, R_e and n, are both $\sim 21\%$ higher in this analysis. The break radius agrees well with their reported value of $R_b = 0.45$ arcsec, whereas the inner profile slope is shallower in this work than their reported value of $\gamma = 0.18$.

When interpreting these differences it must be taken into consideration that this analysis was performed on different imaging than the *WFPC2/F555W* data used in Graham et al. (2003). The *ACS/WFC/F814W* image was preferred in this instance due to its better spatial resolution and lower sensitivity to dust. Both aspects are important when probing small-scale structures like depleted cores. Additionally, and perhaps more importantly, Graham et al. (2003) performed the decomposition on deconvolved data from Rest et al. (2001), whereas PROFILER accounts for seeing effects by convolving the model instead. As Ferrarese et al. (2006) point out, deconvolving (noisy) data can lead to unstable results, as it is sensitive to noise and contamination from bright sources or dust. This can have a significant impact on small-scale features such as core regions. On the other hand, the convolution of a noiseless model is mathematically a more well-defined process, and hence is more robust. PROFILER's convolution scheme was tested with Sérsic and core-Sérsic models and Gaussian seeing, by modelling synthetic 2D images with known light profiles, that were generated and convolved with independent software (the IRAF tasks BMODEL and GAUSS).

The core-Sérsic model was tested with PROFILER on four additional cored galaxies (namely NGC 1016, NGC 3842, NGC 5982, and NGC 7619) and compared with results from Dullo & Graham (2012) and Dullo & Graham (2014). These works, like Graham et al. 2003, have used deconvolved profiles, but taken from Lauer et al. (2005). The core slopes obtained with PROFILER were systematically shallower ($\Delta\gamma \sim 0.05$–0.25) than the literature values computed from deconvolved data[9]. If this is indeed a systematic discrepancy and not simply a chance occurrence in the five galaxies considered

---

[9] Note, however, that these past studies performed the decomposition with α held fixed, whereas PROFILER allows this parameter to remain free. This aspect may influence the core profile slope γ.
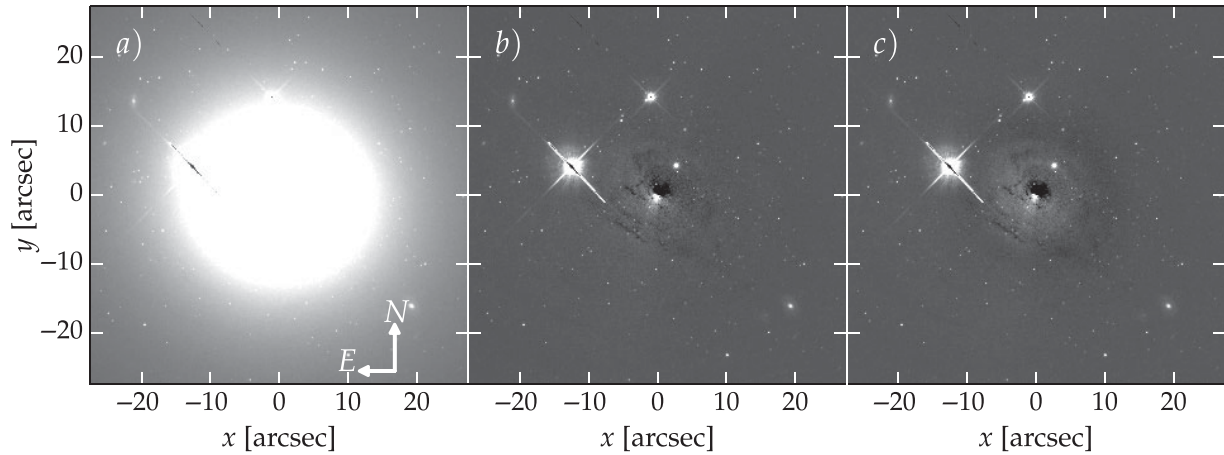
Figure 9. *Panel (a):* HST (F814W) image of the cored early-type galaxy NGC 3348. *Panel (b):* Image in (a) minus a 2D reconstruction generated with CMODEL (see Ciambur 2015), based on isophote fitting with ISOFIT. *Panel (c):* Image in (a) minus a reconstruction based on the same isophote tables but with the data surface brightness column (red circles in Figure 10, top panel) replaced by the decomposition model obtained with PROFILER (black curve in Figure 10, top panel). The image stretch was adjusted to reveal low small-level systematics (<0.05 mag arcsec^{-2}) causing the appearence of ripples (and correspond to the curvature in the residual profile $\Delta\mu(R)$, also shown in Figure 10, second panel from the top). The central systematic indicates that the core region is offset from the photometric centre of the external isophotes.
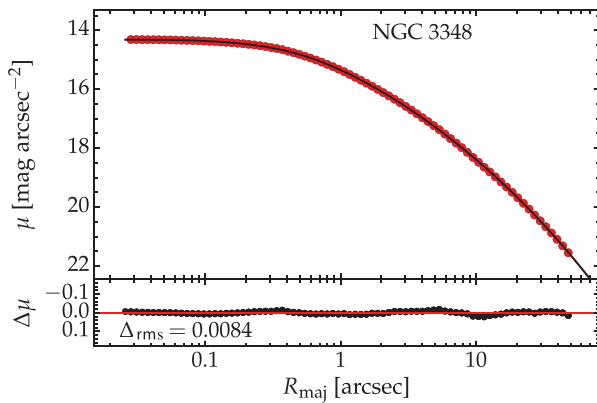
Figure 10. Major axis surface brightness profile (red circles) of the cored elliptical galaxy NGC 3842, obtained from the HST, F814W filter. The model is a core-Sérsic profile [black curve; Equation (7)], with break radius $R_b = 0.43$ arcsec, inner slope $\gamma = 0.09$, and break sharpness $\alpha = 1.86$. The profile beyond R_b has a Sérsic index of $n = 4.91$ and half-light radius of $R_e = 27.63$ arcsec. The bottom panel shows the residual profile ($\Delta\mu$).

here, this issue would imply that literature measurements of the cores' light deficit are biased-low, if the PROFILER result is indeed the correct one. This is probably the case, considering that (*i*) PROFILER accounts for seeing by convolving the model—a more robust approach than fitting deconvolved, noisy data; (*ii*) the convolution scheme was tested with independent software; and (*iii*) many literature results are based on deconvolved data and fits where the α parameter is not allowed to vary. In order to confirm this discrepancy and identify its causes, a more comprehensive study on a larger sample of cored galaxies would be necessary, which is however beyond the scope of this paper.

5.2. Pox 52—using the data vector PSF option

The second example is intended to illustrate how, when diffraction effects are significant, even the Moffat approximation of the true PSF is inadequate and can lead to wrong results. This can be avoided with PROFILER through the use of the data vector PSF feature.

The data chosen for demonstrating this feature was an HST image of the nucleated dwarf Seyfert 1 galaxy Pox 52 (Kunth, Sargent, & Bothun 1987, Barth et al. 2004, Thornton et al. 2008), observed with the ACS/HRC camera in the I−band (F814W filter).

The bright point-source (AGN) at the centre is 'spread' onto the detector into a distinct Airy pattern (see Figure 11), which is also obvious in the SBP (Figure 12). For this galaxy, the PSF was characterised from a bright, nearby star (inset of Figure 11), in two ways: (*a*) by fitting a Moffat profile with IMEXAMINE and (*b*) by fitting the star's light profile (extracted with ELLIPSE) with four Gaussians (for the Airy disc and first three rings)[10]. The galaxy's SBP was then fit with PROFILER with two components, namely a nuclear point source and a Sérsic component. This was done for both PSF choices, and the results are displayed in Figure 12.

The best-fitting Moffat profile from IMEXAMINE had an FWHM of 3.04 pixels and a β parameter of 7.41. The high value of β indicates that IMEXAMINE fit essentially a Gaussian on just the Airy disc (first peak of the PSF) and ignored the wings (Airy rings)[11].

---

[10] Note that a raw profile obtained with ELLIPSE (or ISOFIT) can be used as well, but this can be noisy at large distances from the star's centroid, so in this work this was modelled with four Gaussians, for a smooth result.

[11] This is most likely caused by IMEXAMINE's weighting scheme for pixels outside the half-maximum radius, which reduces the contribution of wings to the profile.
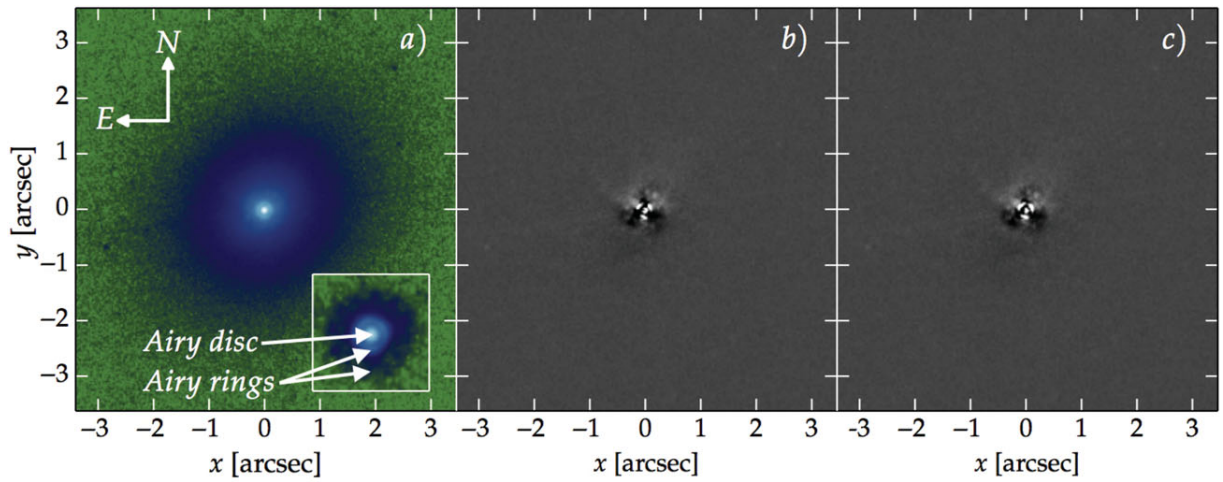
Figure 11. *I*-band image of Pox 52, taken with the *ACS/HRC* camera (*F*814*W* filter) onboard the *HST*. The three panels are analogous to Figure 4, except panel (*a*) is plotted on a logarithmic scale and false-colour scheme, for clarity. With a pixel size of 0.025 arcsec, the PSF is well sampled: The central point source displays a clear first Airy ring and a faint second. The Airy rings are also obvious in the surface brightness profile (Figure 12). The inset is a nearby bright star in the same data, to the SW of Pox 52. For clarity, it is zoomed-in by a ratio of 2:1 compared to the Pox 52 image.
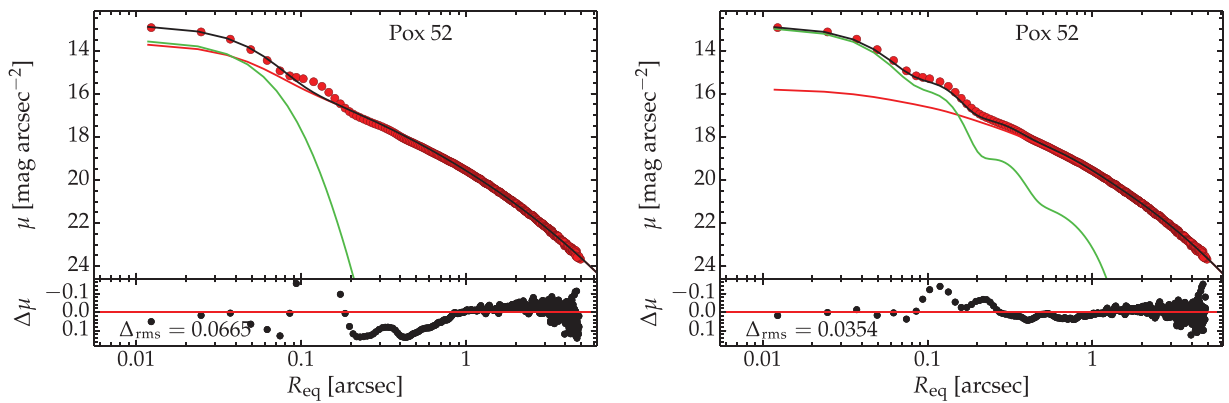
Figure 12. Equivalent axis surface brightness profile of Pox 52 (red circles) modelled with two choices of PSF: a Moffat PSF (left-hand panel) and a data vector PSF (right-hand panel). The models (black curves) are each built from a point-source (green) and a Sérsic component (red). The data vector PSF better captures the Airy rings (see Figure 11) and thus provides a superior model.

The decomposition solution with the Moffat PSF is a two-component model: a point source of central surface brightness $\mu_0 = 13.51$ and a Sérsic component characterised by $\mu_e = 19.62$, $R_e = 1.03$ arcsec, and $n = 4.19$. This solution is displayed in the left-hand panel of Figure 11. During the decomposition process, PROFILER tried to compensate for the unaccounted-for flux in the PSF wings (between 0.1–0.3 arcsec) by making the Sérsic component more concentrated than it should be. This illustrates a case when things went wrong, not because of PROFILER but because of the input PSF.

When performing the decomposition with a data vector PSF, the flux in the wings of the PSF is accounted for much more accurately, and the overall solution is better. Quantitatively, it was also a two-component model, with the point source $\mu_0 = 12.92$ and the Sérsic component $\mu_e = 20.11$, $R_e = 1.27$ arcsec, and $n = 3.12$. The Sérsic component is now less concentrated and its total magnitude $m = 16.33$ mag (in the Vega magnitude system) is ∼50% fainter than in the previous case, but in good agreement with the value of 16.2 reported by Thornton et al. (2008). Additionally, the residual profile displays considerably reduced curvature beyond 0.1 arcsec (Δ_{rms} is reduced by a factor of 2), though there is still systematic curvature at the scale of the first two Airy rings, which is due to the still imperfect PSF estimation.

5.3. NGC 2549 – one spheroid, two bars, and a truncated disc

The third example involves the complex edge-on galaxy NGC 2549. Apart from a spheroid and a disc component, this object shows the signatures of two nested bars, and was shown to host nested X/peanut-shaped structures associated with the two bars (Ciambur & Graham 2016).
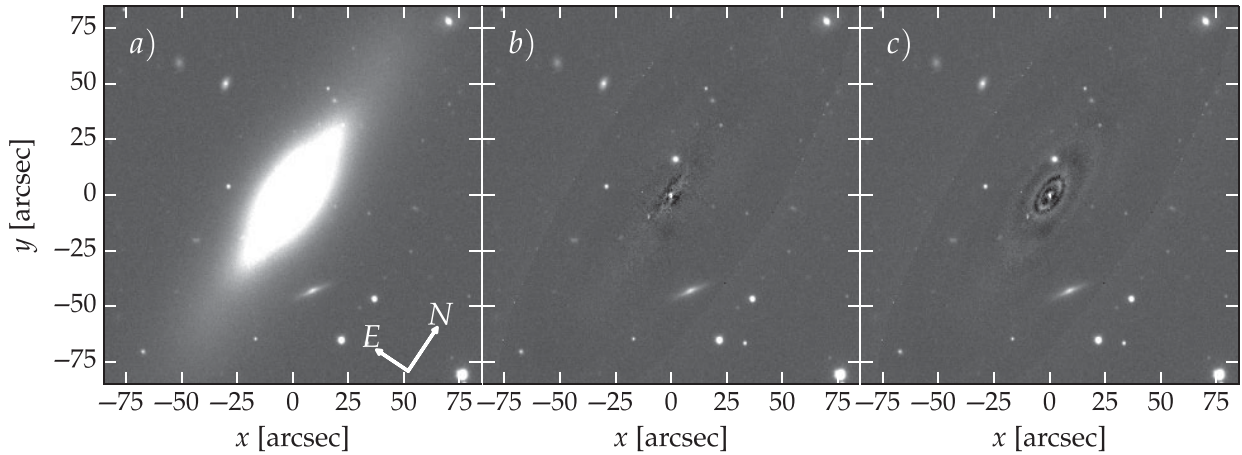
Figure 13. *Panel (a):* SDSS $r-$band image of NGC 2549. *Panel (b):* Image in (*a*) minus a 2D reconstruction generated with CMODEL (see Ciambur 2015), based on isophote fitting with ISOFIT. *Panel (c):* Image in (*a*) minus a 2D reconstruction with CMODEL, based on the same isophote tables but with the data surface brightness column (red circles in Figure 14, top panel) replaced by decomposition model obtained with PROFILER (black curve in Figure 14, top panel). The image stretch was adjusted to reveal low-level systematics, which cause the appearance of ripples (and correspond to the curvature in the residual profile $\Delta\mu(R)$, also shown in Figure 14, second panel from the top). However, the nested peanut structures are well captured (there are no X-shaped systematics).

SDSS r-band data from DR9 (Figure 13, panel *a*) was analysed as before, and the best-fitting model consisted of a Sérsic shperoid, two nested bars, also modelled with Sérsic functions, and a truncated (Type II) exponential disc, with a break radius of 86.2 arcsec, inner scale length $h1 = 42.7$ arcsec and outer $h2 = 27.2$. The solution is displayed in Figure 14, which also shows the ellipticity and B_4 harmonic profiles. Displaying these ancillary profiles is an option available to the user (as check-boxes in the GUI, see Figure 1) and, in conjunction with the residual profile, they are often useful to signal the presence of additional components—in this case, both $\epsilon(R_{\mathrm{maj}})$ and $B_4(R_{\mathrm{maj}})$ strongly indicate the presence of the inner bar component, and also display faint 'bumps' corresponding to the outer bar, which is however more obvious in the SBP. The detection of the nested bars is particularly important given that this galaxy is viewed edge-on, i.e., the most difficult orientation for finding bars.

As before, a 2D reconstruction of the galaxy image was performed with CMODEL, based on the best-fitting SBP and the isophote parameters computed by ISOFIT. This was subtracted from the original galaxy image, resulting in a residual image displayed in Figure 13, panel (*c*). The appearance of waves in-a-pond reflects the curvature in the residual profile $\Delta\mu$ (Figure 14). Note, however, that there are no X-shaped systematics, which indicates that the peanut bulges were well captured by the isophotal analysis.

6 CONCLUSIONS

I have introduced PROFILER, a flexible and user-friendly programme coded in PYTHON, designed to model radial SBP of galaxies.

With an intuitive GUI, PROFILER can model a wide range of galaxy components, such as elliptical galaxies or the bulges
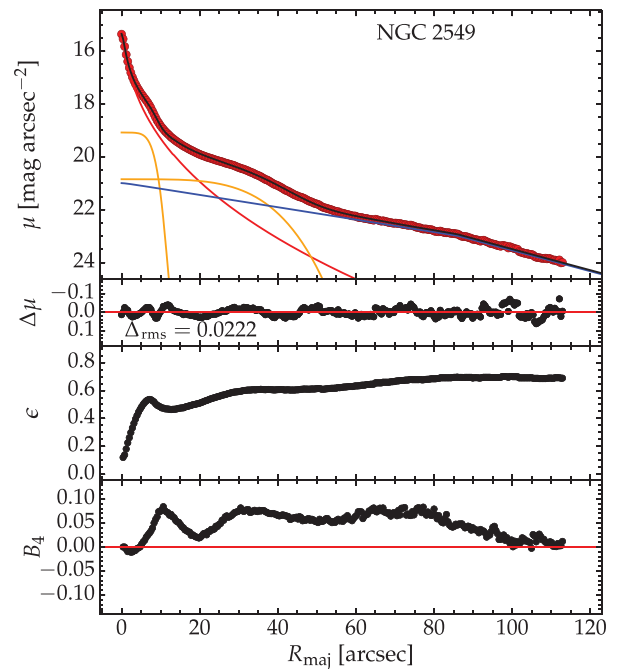

Figure 14. Top panel shows the major axis surface brightness profile decomposition of the edge-on, double-bar (nested peanut) galaxy NGC 2549, based on SDSS r-band data. The model is made up of a Sérsic spheroid (red), two nested, Sérsic bars (orange; $n = 0.15$ for the inner, $n = 0.23$ for the outer) and a truncated disc (blue) with a truncation radius of $R_b = 86$ arcsec. Directly underneath is he residual profile, followed by the ellipticity (ϵ) and B_4 (boxyness/discyness) profiles.

of spiral or lenticular galaxies, face-on, inclined, edge-on, and (anti-)truncated discs, resolved or unresolved nuclear point-sources, bars, rings, or spiral arms, with an arsenal of analytical functions routinely used in the field. These include

the Sérsic and core-Sérsic functions, the edge-on disc model, the exponential, Gaussian, Moffat, and Ferrers' functions. In addition, PROFILER can employ a broken exponential model (relevant for disc truncations or anti-truncations) and two 1D special cases of the 2D edge-on disc model, namely along the major axis and along the minor axis.

PROFILER is optimised to analyse isophote tables generated by the IRAF tasks ELLIPSE and ISOFIT but can also analyse two-column tables of radius and surface brightness. After reaching the best-fitting solution, the corresponding model parameters are returned. The major and equivalent axis profiles can both be analysed, and for the latter profile, each component's total magnitude is additionally returned.

The model convolution with the PSF is performed in 2D, with a FFT-based scheme. This allows for elliptical models, and additionally ensures that the convolution conserves the model's total flux (as a 1D convolution of the model profile with the PSF profile does not). Further, PROFILER allows for a choice between Gaussian, Moffat, or a user-provided data vector for the PSF (a table of R and $I(R)$ values). All of the possible PSF choices can also be used as point-source components in the model.

PROFILER is freely available from the following URL: https://github.com/BogdanCiambur/PROFILER.

ACKNOWLEDGEMENTS

REFERENCES

Abraham, R. G., van den Bergh, S., & Nair, P. 2003, ApJ, 588, 218
Balcells, M., Graham, A. W., Domínguez-Palmero, L., & Peletier, R. F. 2003, ApJL, 582, L79
Barth, A. J., Ho, L. C., Rutledge, R. E., & Sargent, W. L. W. 2004, ApJ, 607, 90
Begelman, M. C., Blandford, R. D., & Rees, M. J. 1980, Nature, 287, 307
Binney, J. 1978, ComAp, 8, 27
Blanton, M. R., et al. 2003, ApJ, 594, 186
Bonfini, P. 2014, PASP, 126, 935
Buta, R. J., et al. 2015, ApJS, 217, 32
Caon, N., Capaccioli, M., & D'Onofrio, M. 1993, MNRAS, 265, 1013
Cappellari, M. et al. 2011, MNRAS, 413, 813
Ciambur, B. C. 2015, ApJ, 810, 120
Ciambur, B. C., & Graham, A. W. 2016, MNRAS, 459, 1276

de Souza, R. E., Gadotti, D. A., & dos Anjos, S. 2004, ApJS, 153, 411
de Vaucouleurs, G. 1948, AnAp, 11, 247
de Vaucouleurs, G. 1953, MNRAS, 113, 134
de Vaucouleurs, G. 1957, AJ, 62, 69
de Vaucouleurs, G. 1959, HDP, 53, 275
de Vaucouleurs, G., de Vaucouleurs, A., Corwin, Jr. H. G., Buta, R. J., Paturel, G., & Fouqué, P. 1991, Vols. I–III (New York: Springer).
D'Onofrio, M., Capaccioli, M., & Caon, N. 1994, MNRAS, 271, 523
Dullo, B. T., & Graham, A. W. 2012, ApJ, 755, 163
Dullo, B. T., & Graham, A. W. 2014, MNRAS, 444, 2700
Erwin, P. 2015, ApJ, 799, 226
Erwin, P., Beckman, J. E., & Pohlen, M. 2005, ApJL, 626, L81
Erwin, P., Pohlen, M., & Beckman, J. E. 2008, AJ, 135, 20
Eskridge, P. B., et al. 2000, AJ, 119, 536
Ferrarese, L., Cote, P., Blakeslee, J. P., Mei, S., Merritt, D., & West, M. J. 2006, arXiv: astro-ph/0612139
Ferrers, N. M. 1877, QJPAM, 14, 1
Freeman, K. C. 1970, ApJ, 160, 811
Graham, A. W. 2013, in Elliptical and Disk Galaxy Structure and Modern Scaling Laws, eds. T. D. Oswalt & W. C. Keel (Dordrecht: Springer), 91
Graham, A. W., & Driver, S. P. 2005, PASA, 22, 118
Graham, A. W., Durré, M., Savorgnan, G. A. D., Medling, A. M., Batcheldor, D., Scott, N., Watson, B., & Marconi, A. 2016, ApJ, 819, 43
Graham, A. W., Erwin, P., Trujillo, I., & Asensio Ramos, A. 2003, AJ, 125, 2951
Graham, A. W., & Worley, C. C. 2008, MNRAS, 388, 1708
Hubble, E. P. 1926, ApJ, 64, 321
Jeans, J. H. 1919, Problems of Cosmogony and Stellar Dynamics (Cambridge: Cambridge University Press)
Jedrzejewski, R. I. 1987, MNRAS, 226, 747
King, I. 1962, AJ, 67, 471
King, I. R. 1966, AJ, 71, 64
King, I. R. 1978, ApJ, 222, 1
Krajnović, D., et al. 2013, MNRAS, 432, 1768
Kunth, D., Sargent, W. L. W., & Bothun, G. D. 1987, AJ, 93, 29
Lauer, T. R., et al. 2005, AJ, 129, 2138
Laurikainen, E., Salo, H., Buta, R., & Knapen, J. H. 2009, ApJL, 692, L34
Marquardt, W. D. 1963, JSIAM, 11, 431
Menéndez-Delmestre, K., Sheth, K., Schinnerer, E., Jarrett, T. H., & Scoville, N. Z. 2007, ApJ, 657, 790
Mihalas, D., & Binney, J. 1981, Galactic Astronomy: Structure and Kinematics (2nd edn.; San Francisco: W. H. Freeman and Co.)
Moffat, A. F. J. 1969, A&A, 3, 455
Naab, T., & Trujillo, I. 2006, MNRAS, 369, 625
Nair, P. B., & Abraham, R. G. 2010, ApJL, 714, L260
Pastrav, B. A., Popescu, C. C., Tuffs, R. J., & Sansom, A. E. 2013, A&A, 557, A137
Patterson, F. S. 1940, BHarO, 914, 9
Peng, C. Y., Ho, L. C., Impey, C. D., & Rix, H.-W. 2010, AJ, 139, 2097
Pohlen, M., Beckman, J. E., Hüttemeister, S., Knapen, J. H., Erwin, P., & Dettmar, R.-J. 2004, in Astrophysics and Space Science Library, Vol. 319, Penetrating Bars Through Masks of Cosmic Dust, eds. D. L. Block, I. Puerari, K. C. Freeman, R. Groess,

& E. K. Block (Dordrecht: Kluwer Academic Publishers), 713

Pohlen, M., & Trujillo, I. 2006, A&A, 454, 759

Prieto, M., Aguerri, J. A. L., Varela, A. M., & Muñoz-Tuñón, C. 2001, A&A, 367, 405

Rest, A., van den Bosch, F. C., Jaffe, W., Tran, H., Tsvetanov, Z., Ford, H. C., Davies, J., & Schafer, J. 2001, AJ, 121, 2431

Sandage, A. 1975, in Classification and Stellar Content of Galaxies Obtained from Direct Photography, eds. A. Sandage, M. Sandage, & J. Kristian (Chicago: The University of Chicago Press), 1

Savorgnan, G. A. D. and Graham, A. W. 2016, ApJS, 222, 10

Sérsic, J. L. 1963, BAAA, 6, 41

Simard, L., et al. 2002, ApJS, 142, 1

Thornton, C. E., Barth, A. J., Ho, L. C., Rutledge, R. E., & Greene, J. E. 2008, ApJ, 686, 892

Trujillo, I., Aguerri, J. A. L., Cepa, J., & Gutiérrez, C. M. 2001a, MNRAS, 321, 269

Trujillo, I., Aguerri, J. A. L., Cepa, J., & Gutiérrez, C. M. 2001b, MNRAS, 328, 977

van der Kruit, P. C. 1987, A&A, 173, 59

van der Kruit, P. C., & Searle, L. 1981, A&A, 95, 105

6

Galaxy Structure and Black Holes

Supermassive black holes are observed to correlate with a remarkable number of structural and dynamical properties of their host galaxies (§1.2.3). Such "scaling relations" between black hole mass ($M_\bullet$) and large scale galaxy properties, orders of magnitude beyond the black hole's gravitational sphere of influence, have been firmly established over the past decades (as reviewed in Graham 2016). Among these are $M_\bullet$ correlations with the host spheroid component's stellar and dynamical mass ($M_{\star,\mathrm{sph}}$, $M_{\mathrm{dyn,sph}}$), velocity dispersion (σ), luminosity (L_{sph}) and concentration (n_{sph}), as well as with the pitch angle (ϕ_{spir}) – or degree of winding – of the spiral arms in late-type galaxies. These scaling relations, calibrated with galaxies in the nearby Universe, where one has access to direct measurements of $M_\bullet$, provide a key constraint for both observational and theoretical studies of galaxy evolution, and reveal the principal physical processes which drive the co-evolution of black holes and their hosts.

The analysis tools developed and presented in the previous Chapters are brought into play here, to study the extrema of modern black hole scaling relations. The Chapter first addresses challenges to the high-mass end of the (black hole – host spheroid) scaling relations, in the form of apparently significant outliers termed "over–massive" black holes. In §6.1 one such alleged outlier, the discy elliptical (ES) galaxy NGC 1271, is studied. The remaining Sections of this Chapter focus on intermediate-mass black holes (IMBH), objects which are hypothesised to provide the link in the distinctly bi-modal black hole mass distribution currently observed, between stellar-mass ($< 10^2 M_\odot$), and supermassive ($> 10^5 M_\odot$), black holes. This intermediate-mass class is currently of considerable interest in the context of galaxy (and central black hole) evolution, as IMBHs may explain the formation of supermassive black holes, a topic still actively investigated (Volonteri & Bellovary 2012). However, IMBHs are beyond the capacity of current instruments to

resolve their sphere of influence, and thus obtain direct measurements of $M_\bullet$ (Miller & Colbert 2004; Mezcua 2017). As such, most IMBH candidates in the literature only have *predicted* masses via indirect methods, such as the above scaling relations. In §6.2, the host galaxy structure of an off-centre IMBH candidate, ESO 243-49 HLX-1, is investigated. §6.3 is dedicated to the late-type galaxy LEDA 87300, recently reported to host a *central* IMBH candidate. Finally, in §6.4, we apply multiple independent methods to predict the black hole mass of six other spiral galaxies with central IMBH candidates.

This Chapter cumulates research contributed to four articles, namely Graham et al. (2016a) (§6.1), Webb et al. (2017) (§6.2), Graham et al. (2016b) (§6.3) and Koliopanos et al. (2017) (§6.4). My contribution to Graham et al. (2016a) was to acquire and process the archival HST imaging data, and model the galaxy's surface photometry with ISOFIT. Further, I modelled the 1D major and equivalent axis light profiles, with PROFILER, and obtained the parameters of the galaxy's constituent components (listed in Table 1 in the paper). Of principal interest in this work were the spheroid component's major axis Sérsic index and total luminosity, which I obtained from the 1D fits. I generated Figures 2 and 3 in this paper, and provided text describing my contribution. My contribution to Webb et al. (2017) was to acquire and process the archival HST imaging data, and model the galaxy (ESO 243-49) surface photometry with ISOFIT (as in Chapter 2, for the same dataset), extracting its 1D radial light profile. I modelled the 1D major and equivalent axis light profiles, with PROFILER, revealing the barred nature of the galaxy and obtaining the best-fit parameters of its constituent photometric components. I provided two estimates for the mass of the central black hole in this galaxy, based on the spheroid parameters I obtained from the 1D models and the black hole scaling relations reported in Savorgnan et al. (2016) and Savorgnan (2016). Finally, I processed and modelled proprietary MUSE imaging of ESO 243-49 with ISOFIT, and subtracted the galaxy model to reveal the location, and constrain the astrometry, of HLX-1s optical counterpart. I generated Figure 3 in this paper, and provided text describing my contribution. My contribution to Graham et al. (2016b) was to acquire and process archival SDSS imaging of the galaxy in question, and model its surface photometry with ISOFIT. Resulting from this, I modelled its 1D light profile in two filters and obtained the best-fit parameters of its constituent components, which are listed in Table 1 of the paper. Of particular interest were the Sérsic index, magnitude and colour of the bulge component, which I obtained from the 1D fits. I generated Figures 2, 3, 4, 5 and 6 in the paper. My contribution to Koliopanos et al. (2017) was to acquire and process archival HST and *Spitzer* data, and model the surface

photometry of the galaxies in the sample with ISOFIT, extracting their 1D light profiles. I decomposed the latter, with PROFILER, obtaining the major axis Sérsic indices, and total luminosities, of their bulge components. I provided two predictions for the black hole mass in each galaxy, using the two bulge parameters and the black hole scaling relations reported in Savorgnan et al. (2016) and Savorgnan (2016), listed in Table 2 of the paper. I also computed the stellar mass of the bulge components, and generated Figures 2 and 4 in the paper.

NGC 1271 – an ES Galaxy with a $10^9 M_\odot$ Black Hole

Some recent studies of a few discy elliptical (ES) galaxies (see §1.1.1) have claimed that these objects harbour so-called "over-massive" black holes at their cores, i.e., significant outliers from the (high-mass end of) black hole scaling relations (see Savorgnan & Graham 2016a, and references therein). Graham et al. (2016a) addresses this alleged issue and analyses one such object, namely NGC 1271, a compact massive galaxy with an embedded disc, situated in the Abell 426 (*Perseus*) cluster (Brunzendorf & Meusinger 1999). Based on dynamical Schwarzschild models (Schwarzschild 1979; van den Bosch et al. 2008) constrained by spatially-resolved stellar kinematics, Walsh et al. (2015) estimated the mass of the central black hole in NGC 1271 to be $M_\bullet \sim 3 \times 10^9 M_\odot$. From their derived bulge stellar mass ($M_{\star,\mathrm{sph}}$), Walsh et al. (2015) concluded that NGC 1271 harbours an "over-massive" black hole, $\sim$ one order of magnitude higher than predicted by the ($M_\bullet - M_{\star,\mathrm{sph}}$) scaling relation of Kormendy & Ho (2013). Here we present an alternative structural analysis of this galaxy than that of Walsh et al. (2015), in which the spheroid component is extended and concentrated, and hosts an embedded, intermediate-scale disc. This naturally recovers agreement with the latest ($M_\bullet - M_{\star,\mathrm{sph}}$) scaling relations, for this galaxy (see other examples in Savorgnan & Graham 2016a).

We retrieved archival H–band imaging of NGC 1271, observed in the near-infrared $F160W$ filter, with the Wide Field Camera 3 ($WFC3$) on board the *Hubble* Space Telescope (HST) (Figure 6.1, panel a). After a careful examination of the sky background level, contaminating sources (such as star clusters, fore- and background stars, background galaxies) were masked and the galaxy isophotes were modelled with ISOFIT (Ciambur 2015; Chapter 2), which generated their surface brightness, ellipticity, position angle, and Fourier harmonics profiles. The reconstructed 2D surface brightness distribution (built with CMODEL, a sub-task associated with ISOFIT) resulting from these isophote parame-

ters, is shown in Figure 6.1, panel *b*. Panel *c* of the same figure displays the residual map resulting from the subtraction of the 2D model from the original image. Unlike its predecessor (Ellipse), Isofit correctly captured the isophote shape (particularly the discyness resulting from the embedded disc, and the rather boxy isophotes towards the outskirts), showing a "clean" residual map.
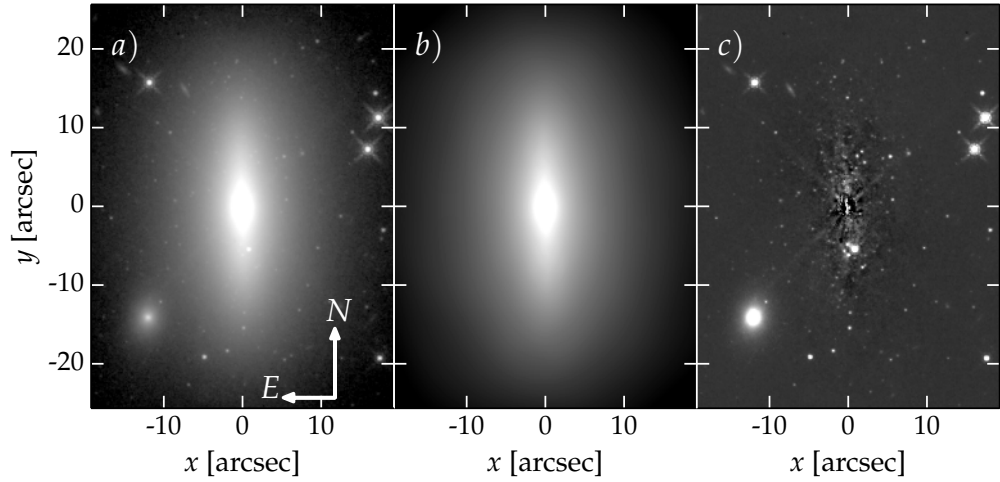

Figure 6.1 – Modelling the surface photometry of the ES galaxy NGC 1271. **Panel a)**: The HST image of the galaxy, observed with the Wide Field Camera 3 instrument, in the near-infrared H–band (F160W filter). The embedded, nearly edge-on, disc is quite apparent. **Panel b)**: The 2D model of the galaxy, constructed with Isofit and its associated task Cmodel (Ciambur 2015). **Panel c)**: The residual image (*a* minus *b*), with a re-adjusted instensity scale to enhance any faint remaining substructure, as well as embedded, foreground and background features.

In contrast to Walsh et al. (2015), who modelled this galaxy with three components, we opted for an alternative interpretation of NGC 1271, as an extended, concentrated shperoid with an intermediate-scale disc embedded within, and observed in nearly edge-on projection. Our preferred best-fit model is shown in the top panel of Figure 6.2 as the black curve over-plotted on the data (red and empty circles). This solution was obtained with Profiler (Ciambur 2016; Chapter 5), and consists of a Sérsic spheroid (red curve) with concentration $n_{\rm sph} = 4.26$, and a disc (blue curve) modelled with the 1D (major axis) special case of the "edge-on disc model" (van der Kruit & Searle 1981), which takes the form:
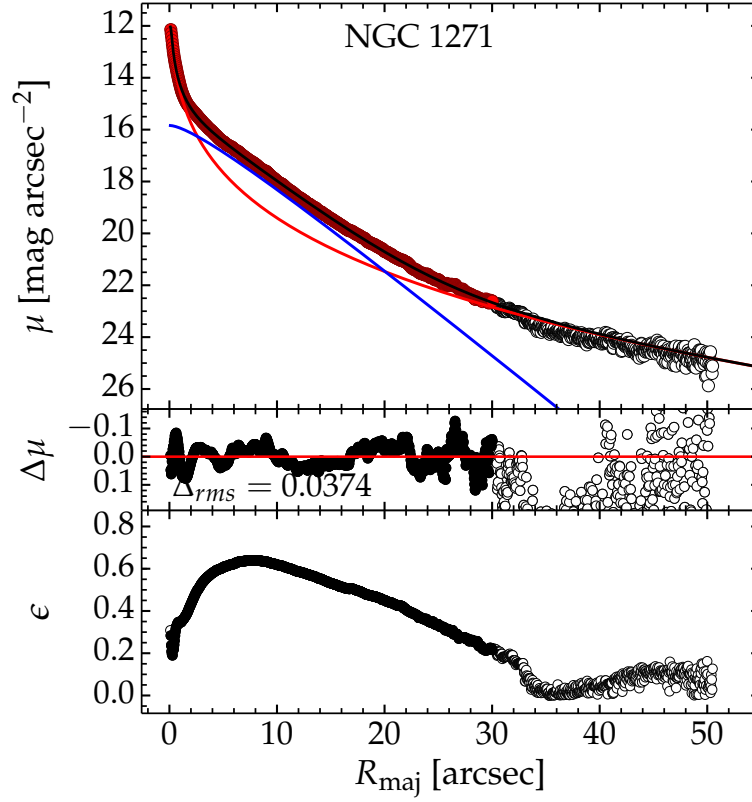
Figure 6.2 – Modelling the light profile of NGC 1271 with PROFILER (Ciambur 2016). **Top**: The major axis surface brightness profile (circles) and best-fit two-component model (black curve), made up of an embedded edge-on disc (blue curve) and a Sérsic spheroid component of concentration $n \approx 4$ (red curve). **Middle**: The residual profile (data minus model). **Bottom**: The ellipticity profile along the major axis, rising steadily as the light becomes dominated by the edge-on disc (up to $\sim 9''$), then declining as the spheroid light takes over at large scales. In all panels, empty circles correspond to data excluded from the fit.

$$I(R_{\mathrm{maj}}) = I_0 \left(\frac{R_{\mathrm{maj}}}{h_r} \right) K_1 \left(\frac{R_{\mathrm{maj}}}{h_r} \right), \tag{6.1}$$

where I_0 is the central brightness, h_r is a scale radius (different to the exponential scale length h) and K_1 the modified Bessel function of the second kind (see Chapter 5 for further details). This functional form was found superior to the routinely used exponential model, but did not significantly affect the derived spheroid parameters, which were of interest in this work. The model constructed in this way was convolved with the PSF,

which was measured from several bright, un-saturated stars in the image, and modelled with a Gaussian profile with a FWHM $= 0''.24$. Figure 6.2 additionally shows the residual profile ($\Delta\mu =$ data minus model) in the middle panel, as well as the ellipticity (ϵ) profile of the isophotes in the bottom panel. The "bump" in $\epsilon(R_{\mathrm{maj}})$, peaking at $\sim 9''$, is additional evidence of the embedded disc, and is typical in ES galaxies (Savorgnan & Graham 2016b).

In addition to the major axis, the surface brightness profile was mapped onto the equivalent axis, through the operation $R_{\mathrm{eq}} = R_{\mathrm{maj}}\sqrt{1-\epsilon}$. This mapping circularises each isophote such that its enclosed surface area is conserved, and generates a circularly-symmetric radial profile which allows one to compute the total flux of each model component analytically, from the best-fit parameters (e.g., Graham & Driver 2005 for Sérsic parameters). Thus, we obtained an apparent H–band magnitude of the spheroid of $m_{H,\mathrm{sph}} = 10.96 \pm 0.15$ mag (Vega). Factoring in the distance modulus of NHC 1271, galactic extinction and redshift dimming provided by the NASA Extragalactic Database (NED[1]), and the H–band stellar mass-to-light ratio reported by Walsh et al. (2015), resulted in a spheroid stellar mass of $M_{\star,\mathrm{sph}} \approx 9 \times 10^{10} M_\odot$. Taking this spheroid stellar mass in conjunction with the measured supermassive black hole mass (Walsh et al. 2015) brings NGC 1271 back in agreement with the ($M_\bullet - M_{\star,\mathrm{sph}}$) scaling relations (Scott et al. 2013; Savorgnan & Graham 2016c), undermining the claim of a "over-massive" black hole in this galaxy. NGC 1271 has provided support to the notion that many such ES galaxies have been erroneously labelled as hosting over-massive black holes due to the problematic modelling of their embedded discs (Savorgnan & Graham 2015, 2016b; Graham et al. 2016c).

ESO 243-49 – an Edge–on Disc Galaxy With an Off–centre IMBH Candidate

Having explored the high–mass end of the black hole distribution, we now turn our attention to intermediate-mass black holes (IMBHs), elusive objects defined to lie in the mass range $[2 \leqslant log_{10}(M_\bullet/M_\odot) \leqslant 5]$. In Webb et al. (2017), we investigated one of the few strong IMBH candidates observed to date, located off-centre in the edge-on disc galaxy ESO 243-49, a member of the cluster Abell 2877 (Santiago & Vale 2008). At a projected separation of $\sim 8''$ from the galaxy's photocentre, just above the plane of its stellar disc,

---

[1]`https://ned.ipac.caltech.edu`

the hyperluminous X–ray source HLX-1 was serendipitously detected by Farrell et al. (2009), and subsequently shown to be physically associated with ESO 243-49 (Soria et al. 2010) through the spectral properties of HLX-1's optical (V and R bands) counterpart. Given its X-ray and radio luminosities, HLX-1 was shown to be consistent with an accreting black hole with mass $M_\bullet \sim 10^4 M_\odot$ (Webb et al. 2012; Straub et al. (2014)), with a lower limit of $M_\bullet > 500 M_\odot$ (Farrell et al. 2009), making it a strong IMBH candidate. However, it is unclear how HLX-1 came to have its observed location in its host galaxy. An emerging hypothesis is that it originates from a past merger between ESO 243-49 and a dwarf galaxy with a central IMBH, which was subsequently stripped of its material in all but the dense nucleus, now observed as HLX-1's optical counterpart (Webb et al. 2010; Farrell et al. 2012). Alternatively, it may reside in a globular cluster, as some IMBHs are believed to do (Miller & Colbert 2004; Gill et al. 2008; Mezcua 2017). In order to study the merger scenario through numerical simulations (e.g., Mapelli et al. 2012), and elucidate the formation of HLX-1, a thorough understanding is required of its host galaxy. This paper was devoted to measure the structure, kinematics and *central* supermassive black hole mass of ESO 243-49.

In Chapter 2 (Ciambur 2015), high-resolution HST imaging of ESO 243-49, in the H–band (Farrell et al. 2012), was modelled as a case-study for Isofit's performance in reproducing the 2D surface brightness distribution of an edge-on galaxy. The correct extraction of its major axis surface brightness profile was demonstrated, which shows a curved radial fall-off of light (on a logarithmic, magnitude scale) at scales where the disc component dominates[2]. For comparison, Ellipse systematically underestimated the disc light, by up to roughly a factor of 2 (in flux) in places. Obviously one requires the correct shape of the surface brightness profile in order to accurately model each photometric component: an incorrect disc model, extrapolated to the centre, where other components usually dominate the light (e.g., bulges, bars, etc), would compromise those components as well. The correct H–band light profile, extracted with Isofit, was used here to decompose ESO 243-49 into its structural constituents.

The decomposition of ESO 243-49 is shown in Figure 6.3. The galaxy was modelled with a Sérsic bulge component (red dashed curve), with the best-fit parameters displayed in the inset in Figure 6.3. The disc was also modelled with a Sérsic function (dash-dot blue curve) as shown to be occasionally necessary in edge-on systems by Pastrav et al.

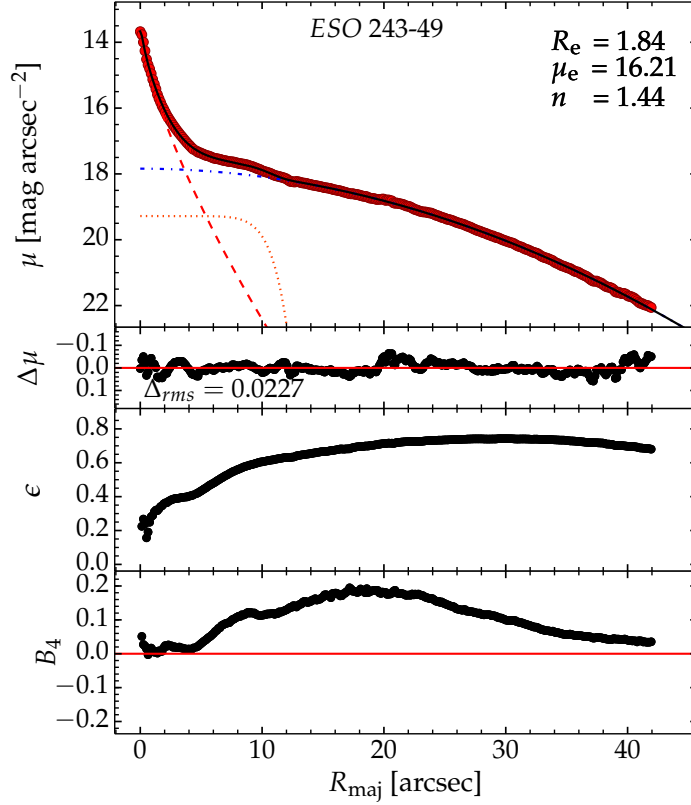[2]This behaviour has been noted and explained by Pastrav et al. (2013) for edge-on discs.

Figure 6.3 – Photometric decomposition of ESO 243-49, based on the H–band HST data from Chapter 2. Top three panels are analogous to Figure 6.2, while bottom panel shows the radial profile of the isophotes' B_4 harmonic amplitude. This galaxy was modelled with 3 components: a central Sérsic spheroid (red dashed curve; parameters inset in the top panel), a Sérsic edge-on disc (blue dot-dashed curve) and a Sérsic bar (dotted orange curve).

(2013). Finally, the signature of a bar component was detected, both as a slight excess in surface brightness above the (bulge+disc) model roughly between $5'' \lesssim R_{\mathrm{maj}} \lesssim 12''$ (Figure 6.3, top panel), and as a "bump" in the B_4 harmonic profile (Figure 6.3, bottom panel), peaking at $\sim 9''$. The bar too was modelled with a low–n Sérsic function, which provided a superior description, for this galaxy, than the Ferrers (1877) model (which is another function routinely used to fit bars, see Chapter 5). The PSF in this image was characterised, as before (§6.1), from bright stars in the image, and modelled with a Moffat profile, of average FWHM $= 2''$ and $\beta = 4.895$. The apparently short extent of the bar, coupled with a small, positive B_6 harmonic amplitude, indicates that it is probably viewed in close to end-on orientation. As in §6.1, the equivalent axis was constructed and modelled, yielding the integrated magnitude of each component. The resulting bulge-to-total

flux ratio of $(B/T)_H = 0.25 \pm 0.06$ indicates that ESO 243-49 is a barred S0 – S0/a galaxy (Graham & Worley 2008).

The bulge parameters, namely major axis Sérsic index and spheroid luminosity, were used to estimate the black hole mass of ESO 243-49 via the $(M_\bullet - n_{\rm sph})$ (Savorgnan 2016) and $(M_\bullet - L_{\rm sph})$ (Savorgnan et al. 2016) scaling relations. Thus we obtained a black hole mass of $\log(M_\bullet/M_\odot) = 6.69 \pm 0.57$ based on $n_{\rm sph} = 1.44 \pm 0.08$, and $\log(M_\bullet/M_\odot) = 6.85 \pm 0.27$, based on the spheroid absolute magnitude of $M_{\rm sph,H} = -22.08 \pm 0.18$ mag (additionally converted into an equivalent 3.6 μm magnitude as in Savorgnan & Graham 2016c).
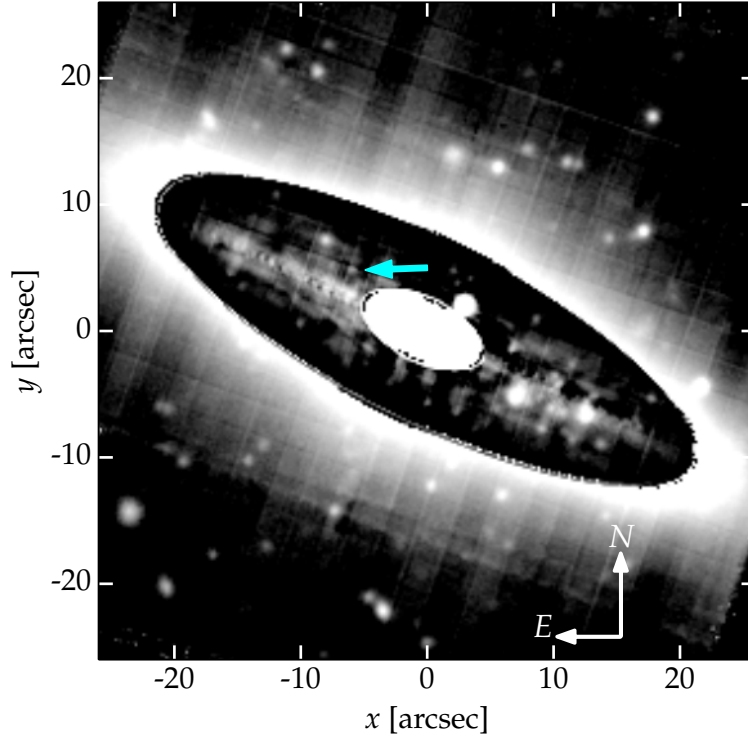

Figure 6.4 – The optical imaging (V–band) "face" of the MUSE data cube acquired for ESO 243-49 (Webb et al. 2017), with a subtracted partial model of the galaxy (dark elliptical annulus) constructed with ISOFIT/CMODEL. Among the left-over substructure is the optical counterpart of HLX-1, indicated by the blue arrow.

In addition to the structure of ESO 243-49, this article also investigated the kinematics of this galaxy and the spectral properties of HLX-1, through spatially resolved IFU spectroscopy obtained with the MUSE instrument (Bacon et al. 2010), in the wavelength

range 4750 – 9300 Å. Here, the sensitivity of IsoFit was required to model and subtract the diffuse galaxy light in the MUSE imaging, so as to accurately measure the astrometric position of HLX-1 and thus extract its associated spectrum from the data cube. Due to the $\sim 1''$ seeing (FWHM) in the imaging, most of the faint, resolved sources within the galaxy, including HLX-1, were highly blended with the diffuse galaxy light, making their astrometric identification impossible with any other technique than a careful modelling, and subtraction, of the host galaxy light distribution. This is shown in Figure 6.4, where HLX-1 is revealed in the residual map (dark elliptical annulus), as indicated with the blue arrow. Its astrometry thus constrained, the associated spectrum of HLX-1 was extracted in a region 3 pixels in radius around its position, from the MUSE data cube. This allowed for the computation of HLX-1's $V-$ and $R-$band magnitudes, as well as the investigation of the prominent Balmer H_α emission line (the feature previously used by Soria et al. 2010 to measure the distance to HLX-1) and its physical, environmental origin (i.e., from potential accretion disc, host star cluster or surrounding gas).

By investigating the environment of HLX-1, and the structure, morphology and supermassive black hole mass of its host galaxy, ESO 243-49, we have advanced our understanding of this interesting system, and brought strong constraints for future $N-$body/hydrodynamical simulations aiming to study its formation, testing in particular the merger scenario (Webb et al. 2010; Mapelli et al. 2012). This in turn can help understand where IMBHs form, and if/how they come to grow into the supermassive black holes that we observe in many galaxy cores.

LEDA 87300 – a Barred Disc Galaxy With a Central IMBH Candidate

Apart from off-centre hyperluminous X-ray sources (as discussed above), and possibly globular clusters (Gill et al. 2008; Lützgendorf et al. 2013), IMBHs are also believed to inhabit the nuclei of dwarf galaxies (Barth et al. 2004; Reines et al. 2013) or of late-type spirals with small bulges (Graham & Scott 2013). Such objects are particularly interesting to study, as they have the potential to explain the formation process of supermassive black holes (§1.2.3). In a recent study, Baldassare et al. (2015) reported the discovery of such an IMBH ($M_\bullet \sim 5 \times 10^4 M_\odot$) in the centre of the barred late-type (Sm) dwarf LEDA 87300 (which they designated "RGG 118" from its position the catalogue compiled by Reines

et al. 2013). This section presents my scientific contribution to the article Graham et al. (2016b), where we investigate how this galaxy fits in with the near-quadratic scaling between black hole mass and spheroid stellar mass. Specifically, there is mounting evidence that the log-linear ($M_\bullet - M_{\star,\rm sph}$) relation observed for bright elliptical galaxies (see §1.2.3) is broken, becoming steeper (near-quadratic) at low masses, i.e., for the Sérsic bulges of disc galaxies (Graham 2012; Graham & Scott 2013, 2015; Scott et al. 2013; Savorgnan et al. 2016). This has important consequences for our theory of (black hole – host galaxy) co-evolution. While at the high-mass end, the growth – in tandem – of both black hole and bulge is thought to be largely driven by (dry) mergers, additional gas-rich processes are required to steepen the relation at the low-mass end, resulting in a faster growth of the black hole (Graham & Scott 2013) relative to the spheroid. Baldassare et al. (2015) have attempted to quantify the bulge of this galaxy, but have not included the bar component in their analysis, which forced their bulge model to account for this excess flux, and led to an uncharacteristically high B/T ratio of ~ 0.3, given this galaxy's "late" morphological type (Sm). Obviously, to study correlations between black holes and galaxy bulges, a correct measure of both components is required. In this article, Graham et al. (2016b), we examine the location of LEDA 87300 on the ($M_\bullet - M_{\star,\rm sph}$) diagram, from the stand-point of a re-visited structural model for the galaxy, which takes the bar into account. The implications of this work are discussed in the context of how current supermassive black hole scaling relations extend into the IMBH regime, a crucial test of the rapid, "quadratic" black hole growth scenario, and thus of early black hole evolution.

We retrieved SDSS imaging of LEDA 87300 in the g' and r' bands. Two fields containing this galaxy were available from the ninth data release (DR9 – Ahn et al. 2012). In each filter, the two data sets were adjusted to the same level of seeing[3] and then stacked, to improve the signal-to-noise (panel a of Figure 6.5 shows the r'–band image resulting from this process). Further, the surface brightness profiles, and isophote geometric parameters, were extracted, in both bands, with Isofit. The PSF was modelled by fitting Gaussian profiles to several stars in the combined images, for each filter.

Despite the discernable presence of the bar (Figure 6.5, panel a), we first attempted to fit a 3-component model to the galaxy similar to that of Baldassare et al. (2015), namely an AGN point-source (shaped like the PSF), a (bulge+bar) Sérsic component (which we termed a "barge", to differentiate from the bulge in our later model) and an exponential

---

[3]This was necessary because, for a given filter, the atmospheric seeing conditions were different between the two exposures.
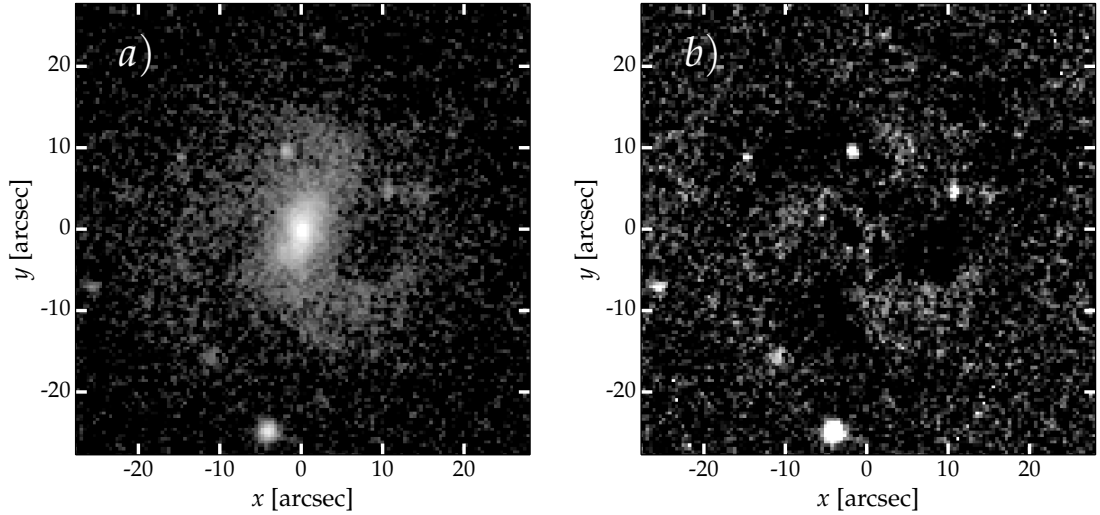
Figure 6.5 – The dwarf late-type galaxy LEDA 87300. **Panel a)**: Combined r'–band SDSS exposures (from two fields) revealing the bar and spiral pattern of this galaxy. **Panel b)**: The residual map obtained by subtracting the galaxy model, generated with ISOFIT, from the image in panel a. The intensity scale was re-adjusted to enhance the residuals, which reveal a tentative three-arm spiral pattern in the disc.

disc. Note that the disc presents a truncation (down-turn) in its light profile at $R_{\mathrm{maj}} \approx 16''$, beyond which its scale length becomes shorter. This spatial range was not modelled, however, as it did not affect the inner components of interest. This first model of the galaxy's light profile is shown in Figure 6.6 (left panel), and results in a barge-to-total flux ratio of ~ 0.1 in the r' band, still somewhat larger than the typical few % value for Scd/Sm galaxies (Graham & Worley 2008). Our preferred model consisted of a small Sérsic bulge, a Ferrers bar, and an exponential disc. This is shown, again for the r'–band (for comparison), in the right panel of Figure 6.6. Both the r' and the g' band data were modelled this way, along the major and the equivalent axis. We obtained an r' band $n_{\mathrm{sph}} = 1.08 \pm 0.06$ and absolute magnitude of $M_{\mathrm{sph},r'} = -15.2 \pm 0.4$ AB mag (corrected for extinction and gravitational redshift dimming, using NED as before). Adding the g' band results, we obtained a bulge colour of $(g' - r')_{\mathrm{sph}} = 0.5 \pm 0.2$ and a somewhat bluer bar colour of $(g' - r')_{\mathrm{bar}} = 0.2 \pm 0.2$. Following Baldassare et al. (2015), we computed the r'–band stellar mass-to-light ratio of the bulge from its $(g' - r')$ colour (Bell et al. 2003), obtaining a bulge stellar mass of $M_{\star,\mathrm{sph}} = 0.9 \times 10^8 M_{\odot}$, and a bulge-to-disc mass ratio of 0.04, consistent with other galaxies of its morphological type.

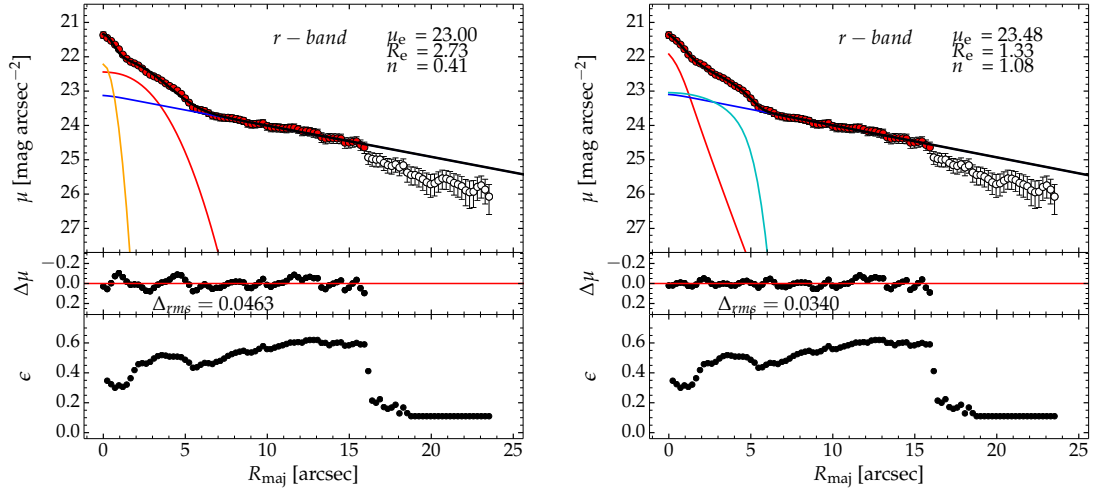The analysis continued with a revision of the measured stellar velocity dispersion, and

Figure 6.6 – Modelling the r'–band light profile of LEDA 87300.   **Left**:   A 3–component model consisting of an AGN point-source component (orange), a Sérsic "barge" (bulge+bar) component (red curve) and an exponential disc (blue curve).   **Right**: The preferred model, consisting of a Sérsic bulge (red curve), a Ferrers bar (cyan curve) and an exponential disc (blue curve). In both panels, the disc is modelled up to its truncation radius ($\sim 16''$), and the data beyond is excluded from the fit. The inset parameters correspond, in both panels, to the Sérsic component.

of the black hole mass. Specifically, the latter was reduced by a factor of ~ 1.74 from the virial black hole mass[4] estimate reported in Baldassare et al. (2015). This correction was warranted by the need for a reduced virial scaling factor f (see footnote 4) shown to be more appropriate for barred galaxies by Graham et al. (2011) (also Shankar et al. 2016). Having thus measured and refined both bulge parameters and black hole mass, LEDA 87300 was placed on the $(M_\bullet - M_{\star,\mathrm{sph}})$, $(M_\bullet - n_{\mathrm{sph}})$ and $(M_\bullet - \sigma_\star)$ diagrams.

This article has shown that LEDA 87300 is consistent with the near-quadratic $(M_\bullet - M_{\star,\mathrm{sph}})$ relation, observed to be obeyed by spiral galaxies (Graham 2013; Savorgnan et al. 2016). This is an important starting point to understand the evolutionary continuity between black holes and their host galaxies, as it extends into low-mass systems and the (as yet) largely unprobed intermediate-mass black hole regime. This work further showed consistency of this galaxy with the established $(M_\bullet - n_{\mathrm{sph}})$ and $(M_\bullet - \sigma_\star)$ relations, further

---

[4]With the virial (or "reverberation mapping") method, the black hole mass can be estimated from the spectral properties of emission lines originating from the 'broad line region" (BLR), which is assumed to be in virial equilibrium. Thus, $M_\bullet = f\, r_{\mathrm{BLR}}\, \sigma^2/G$, where r_{BLR} is the radius of the broad line region (usually quantified by the luminosity in a given emission line, e.g., H_α – Greene & Ho 2005), σ is the width of the line, f is a geometric scaling factor and G is the gravitational constant (see Kaspi et al. 2000; Peterson et al. 2004; Bentz et al. 2010).

strengthening our conclusions. Finally, the importance of properly accounting for every structural component in galaxy models, particularly bars (as demonstrated by Laurikainen et al. 2005) was re-enforced. In this particular case, the galactic bar entered in every aspect of the analysis, from the photometric decomposition to the black hole mass estimate.

The (Black Hole – Bulge) Correlation of Six (plus One) IMBH Candidates

The previous Section has shown how one dwarf late-type galaxy with an IMBH candidate at its core fits in with the low-mass extrapolation of black hole scaling relations established for supermassive black holes. Here (Koliopanos et al. 2017) we studied seven additional galaxies believed to host IMBHs. The galaxies were drawn from the more extended catalogue of Graham & Scott (2013), which contained 45 galaxies predicted to host IMBHs based on the K_s–band bulge luminosities reported in Dong & De Robertis (2006) and corrected for dust extinction in Graham & Scott (2013). The aim of this work was to refine the black hole mass predictions for these seven galaxies, possibly confirming their intermediate-masses, by jointly using multiple independent black hole scaling relations. Our galaxy sample was determined by the availability of archival radio and X-ray data required in part of the analysis, as explained below. We used multi-wavelength observations, in the radio, near-infrared, optical, ultraviolet, and X-ray, to estimate the black hole masses from the latest scaling relations between black hole mass and host bulge luminosity and concentration (Savorgnan et al. 2016; Savorgnan 2016), between black hole mass and the pitch angle of the host galaxy's spiral arms (Davis et al. 2017), and between black hole mass and its associated radio and X-ray emission (Plotkin et al. 2012).

For the photometric analysis, near-infrared archival data was acquired from two sources. High-resolution HST images in the I–band ($F814W$ filter) were acquired from the *Hubble* Legacy Archive[5], for the galaxies NGC 628, NGC 3185 and NGC 3486. The remaining four objects, NGC 3198, NGC 3507, NGC 4314 and NGC 4470, either displayed significant dust obscuration (often crossing the bulge region, which for our purposes required accurate modelling) or had not been observed with the HST. For these objects we therefore opted for redder *Spitzer* observations, with the IRAC 1 instrument (at 3.6 μm), where dust effects were reduced, albeit at the cost of spatial resolution. These were retrieved from the

---

[5]`http://hla.stsci.edu`

S^{4}G archive[6], and benefited from the fact that the ($M_\bullet - L_{\text{sph}}$) relation used to predict their black holes (Savorgnan et al. 2016), was calibrated in the same bandpass, in which light is an excellent tracer of stellar mass (Savorgnan & Graham 2016c).

Contaminating sources (star clusters, dust lanes, fore/background objects) were masked out in all images. For each galaxy, the PSF was characterised by fitting Moffat profiles to bright stars, with the IRAF task IMEXAMINE. The major axis radial surface brightness profiles were then extracted by fitting each galaxy's isophotes with ISOFIT, which additionally provided the ellipticity, position angle and Fourier harmonics of the isophotes. All this information was used to perform multi-component decompositions, with PROFILER, of the major axis light profile, which provided the bulge major axis Sérsic index (n_{sph}), and the equivalent axis light profile, which provided the bulge apparent magnitudes (m_{sph}). All galaxies apart from NGC 628 were found to be barred, and consistent with their previously reported morphological classification, with the exception of NGC 4470, which we reported to be bulge-less but barred. All bulge magnitudes were further corrected for galactic foreground extinction (from NED, as before) and intrinsic extinction (for the I–band data – Driver et al. 2008). Finally, distance moduli listed in the NED database were used to compute the absolute bulge magnitudes for all six galaxies with bulges out of the seven in the sample. An average colour of ($F814W - 3.6\ \mu$m) = 3.53 ± 0.03 mag was measured for NGC 4314, which was observed in both filters. This was assumed to be representative for the entire sample, and was used to convert the bulge luminosities of the three galaxies observed with HST from the I–band ($F814W$ filter) to 3.6 μm. The major axis Sérsic indices of the galaxy bulges, and their 3.6 μm absolute magnitudes, were used to predict the mass of the central black holes in these galaxies, according to the ($M_\bullet - n_{\text{sph}}$) relation (Savorgnan 2016) and ($M_\bullet - M_{\text{sph},3.6\mu\text{m}}$) relation (Savorgnan et al. 2016). The derived bulge parameters and predicted black hole masses are listed in Table 6.1.

In addition to the above two (black hole – bulge) scaling relations, two additional, independent methods were used to estimate the black hole masses in these galaxies. The first relied on the observed correlation between the mass of an accreting black hole and its associated radio and X-ray emission, known as the "fundamental plane of black hole activity" (FP-BH – Merloni et al. 2003). X-ray data from archival *Chandra* and *XMM Newton* observations, and proprietary radio data observed with the *Karl G. Jansky* Very Large Array (VLA), were used to predict the black hole masses, from the updated FP-BH re-

---

[6]http://irsa.ipac.caltech.edu/data/SPITZER/S4G/

Table 6.1 – Bulge parameters and black hole mass predictions from the near-infrared image analysis. (*a*) bulge major axis Sérsic index; (*b*) bulge absolute magnitude at 3.6 μm; (*c*) predicted black hole mass from the ($M_\bullet - n_{\rm sph}$) relation (Savorgnan 2016); (*d*) predicted black hole mass from the ($M_\bullet - M_{\rm sph,3.6\mu m}$) relation (Savorgnan et al. 2016).

Source	$n_{\rm sph}^{(a)}$	$M_{\rm sph,3.6\mu m}^{(b)}$ [mag]	$\log(M_\bullet/M_\odot)^{(c)}$	$\log(M_\bullet/M_\odot)^{(d)}$
NGC 628	1.16±0.20	-21.25±0.21	6.7±0.4	6.6±0.7
NGC 3185	1.77±0.25	-21.15±0.41	7.3±0.3	6.6±0.8
NGC 3198	1.08±0.35	-20.06±0.32	6.6±0.5	6.0±0.8
NGC 3486	2.43±0.40	-22.00±0.50	7.7±0.3	7.0±0.6
NGC 3507	1.74±0.35	-20.29±0.41	7.3±0.3	6.1±0.8
NGC 4314	1.20±0.28	-20.89±0.43	6.8±0.5	6.4±0.7
NGC 4470	–	–	–	–

lation of Plotkin et al. (2012). Three galaxies in the sample (NGC 628, NGC 4314 and NGC 4470) lacked coincident radio sources, and upper limits for $M_\bullet$ were computed based on radio fluxes corresponding to the 3σ level of the observed root-mean-squared noise. Finally, we predicted black hole masses, for each galaxy, exploiting the observed correlation between $M_\bullet$ and the degree of winding, or pitch angle ($\phi_{\rm spir}$), of the spiral arms (Seigar et al. 2008; Berrier et al. 2013; Davis et al. 2017). Optical imaging (better than near-infrared for detecting spiral structure) from various sources was used to measure the pitch angles with the method described in Davis et al. (2012), while the updated ($M_\bullet - \phi_{\rm spir}$) relation of Davis et al. (2017) yielded black hole mass estimates.

Having applied a battery of independent methods to update their black hole mass predictions, we then studied these galaxies in the context of the near-quadratic ($M_\bullet - M_{\star,\rm sph}$) scaling relation, as before for LEDA 87300 (§6.3). The bulge stellar mass ($M_{\star,\rm sph}$) was calculated for each galaxy using a stellar mass-to-light ratio of $\Gamma_{3.6\mu m} = 0.65$ (Savorgnan et al. 2016) for the spheroid magnitudes derived from (*Spitzer*) 3.6 μm data, and $\Gamma_I = 2.7$ (Yoshino & Ichikawa 2008) for the spheroid magnitudes obtained from (HST) *I*–band data. The resulting ($M_\bullet - M_{\star,\rm sph}$) diagram is presented in Figure 6.7, which plots the predicted black hole masses, based on major axis Sérsic index (red stars), spiral arm pitch angle (blue squares) and the fundamental plane of black hole activity (green circles), as a function of their spheroid stellar mass, for all but the bulge-less galaxy NGC 4470. Over-plotted in this diagram are linear scaling relations derived by Savorgnan et al. (2016) for
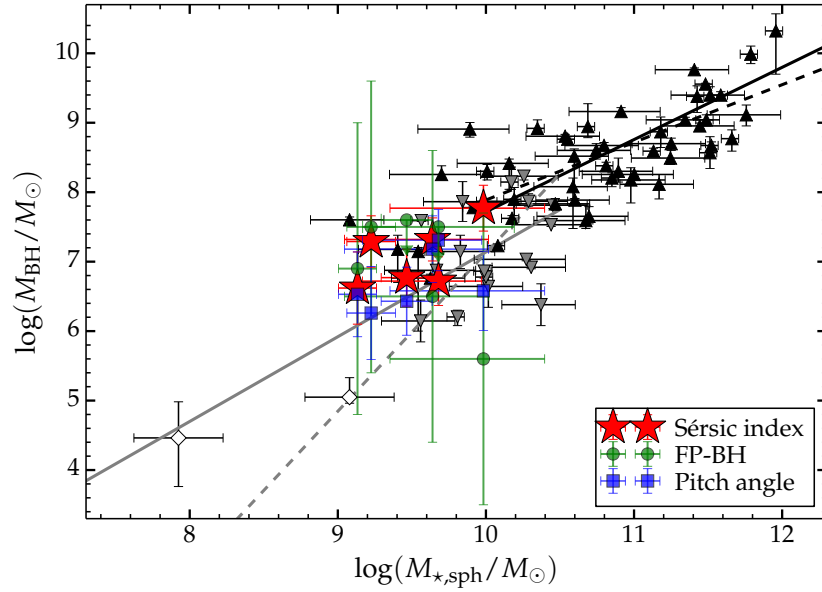
Figure 6.7 – The placement of the six IMBH candidates in the $(M_\bullet - M_{\star,\mathrm{sph}})$ diagram. The red stars correspond to the $M_\bullet$ predictions based on bulge major axis Sérsic index (n_{sph}), while the blue squares and green circles correspond to $(M_\bullet - \phi_{\mathrm{spir}})$ and fundamental plane of black hole activity (FP-BH) predictions, respectively. Overplotted is the "broken" relation of Savorgnan et al. (2016), which has a shallower slope for early-type galaxies (black lines and upward triangles) than for late-type galaxies (grey lines and downward triangles). The fourth prediction for $M_\bullet$ is not explicitly plotted, to avoid crowding, but would lie roughly on the solid grey line, for the corresponding $M_{\star,\mathrm{sph}}$ of each of the six galaxies in the sample. The open diamonds correspond to the IMBH mass and spheroid stellar mass of LEDA 87300 (§6.3) and those of Pox 52 (Barth et al. 2004; Thornton et al. 2008; Ciambur 2016).

early-type galaxies (black) and late-type spirals (grey), together with the corresponding data from which they were derived (black and grey triangles, respectively). The solid lines correspond to Y-on-X regressions, while the dashed lines are symmetric (bisector) regressions, performed in Savorgnan et al. (2016). Since the bulge stellar mass is related to its luminosity via the mass-to-light ratio, our black hole mass predictions from the $(M_\bullet - M_{\mathrm{sph},3.6\mu\mathrm{m}})$ relation would lie roughly[7] on the solid grey line, and so were not explicitly plotted here, to avoid crowding. Finally, the open diamonds represent two other galaxies with central IMBH candidates, namely LEDA 87300 (discussed in §6.3 above), and the dwarf Seyfert 1 galaxy Pox 52 (Barth et al. 2004; Thornton et al. 2008; Ciambur 2016).

---

[7]The predicted $M_\bullet$ for the three galaxies observed at 3.6 μm would lie exactly on the solid grey line, which has been derived by Savorgnan et al. (2016) based on 3.6 μm data. The other three galaxies would lie close to the solid grey line, subject to the accuracy of the assumed ($F814W$ - 3.6 μm) colour.

Figure 6.7 shows that our new multi-method black hole mass predictions are above the IMBH range for all six galaxies considered. The bulge-less nature of NGC 4470 restricted our $M_\bullet$ estimates to two methods, namely the FP-BH and ($M_\bullet - \phi_{\mathrm{spir}}$) relation, both yielding a black hole mass of $\log(M_\bullet/M_\odot) \sim 7.5$, again well above the IMBH range. This is consistent with their morphological classification, ranging from Sa to Sc, which suggested that they may host bigger bulges (and thus more massive black holes) than those associated with IMBHs. Nevertheless, this work has shown general consistency among the predictions of four independent black hole scaling relations, albeit with large error bars. The approach is thus a promising start to probe the extension of existing black hole scaling relations into the unknown IMBH regime, which can be achieved with an extended galaxy sample (e.g., Graham & Scott 2013), and may also benefit from the addition of the ($M_\bullet - \sigma$) relation (Ferrarese & Merritt 2000; Gültekin et al. 2009; Graham & Scott 2013) to the array of methods.

7

Concluding Remarks & Outlook

This thesis has brought scientific contributions to the field of galaxy structure and quantitative morphology, with the main focus on structural properties and scaling relations in barred disc galaxies. (X/peanut)–shaped structures in nearby galaxies, and in the Milky Way, were modelled and quantified with new principles and unprecedented accuracy, leading to the discovery of nested peanut structures, X/P structural scaling relations (size, strength), and to new constraints for the size and orientation of the Milky Way's bar and X–shaped "bulge". In addition, the high- and low-mass ends of modern black hole scaling relations were studied, specifically an alleged "over-massive" outlier of the relations in an ES early-type galaxy, as well as central, and off-centre, intermediate-mass black hole candidates in disc galaxies.

In Chapter 2, a new formalism was developed for modelling galaxy isophotes, where their deviations from pure ellipticity are expressed as a function of an ellipse-specific azimuthal co-ordinate: the eccentric anomaly. This scheme was implemented in the IRAF software package IsoFIT, and its performance was demonstrated on different scientific case-study galaxies with complex isophotal structure, with a particular focus on disc galaxies viewed in edge-on projection. IsoFIT was shown to produce high-accuracy models of galaxy surface brightness, extracting unbiased radial light profiles, and completely removing the cross-shaped, (purely artificial) residual sub-structure frequently affecting its predecessor algorithm, ELLIPSE. Galaxies with strong, or complicated, deviations from ellipticity can now be modelled, opening the way for new science.

The accurate construction of a galaxy model, and subsequent subtraction from the original image, can greatly facilitate the study of underlying sources in the galaxy. In this precise respect, IsoFIT has contributed to the understanding of the intermediate-mass

black hole candidate HLX-1, the hyperluminous X–ray source embedded off–centre in the edge-on disc galaxy ESO 243-49 (Farrell et al. 2009). Specifically, in Ciambur (2015) a model of the host galaxy was constructed, which allowed for the identification and quantification of the optical counterpart of HLX-1 in H–band HST imaging, a wavelength range where this was not previously possible with other techniques (such as, e.g., Soria et al. 2010, for the R–band), but nevertheless important to constrain the source's spectral energy distribution. The same technique was applied to MUSE data in Webb et al. (2017) (see Chapter 6), particularly on the imaging "face" of the data cube, in order to determine the astrometry of HLX-1, and thus identify the relevant spectrum associated with it. This same technique is generally applicable to the study of over-lapping X–ray, or radio, sources in galaxies, and the identification of possible optical counterparts. Additionally, this technique can be applied to study the spatial distribution of globular clusters around galaxies, (and, e.g., constrain the density profile of the host galaxy and halo), or indeed any sub-structure which differentiates itself from the diffuse galaxy light.

Isofit has also brought important contributions to the study of edge-on galaxy discs, particularly when measuring their precise shape, or even their detection, is non-trivial. One example is provided by the embedded edge-on disc in the ES galaxy NGC 1271, where disc light dominates that of the concentrated spheroid only over an intermediate radial scale (Graham et al. 2016a; see Chapter 6). Another example constitutes edge-on discs with outer breaks in their profiles, towards the faint outskirts of galaxies where the sky background and the PSF become important effects relative to the disc flux (Borlaff et al. 2017). In both cases, Isofit has enabled accurate modelling of the galaxy surface photometry, and has provided superior galaxy models compared to the results obtained with the 2D code Galfit.

Finally, in the mathematical formulation in Isofit, the deviations from pure ellipticity, expressed as Fourier harmonics of different orders, can be used to trace and quantify galaxy structure beyond boxyness or discyness. This has been applied in Chapters 3 and 4 of this thesis, where the 6th order term was used to quantitatively characterise X/Peanut–shaped structures in a sample of twelve nearby galaxies (Ciambur & Graham 2016), as well as in the Milky Way (Ciambur et al. 2017).

In Chapter 3, a new framework was introduced to accurately and quantitatively measure X/P structures in edge-on disc galaxies, based on the characteristic signature they

leave in the host galaxy's isophotal structure, as measured with IsoFit. This work demonstrates that the amplitude of the 6th order harmonic, B_6, traces the X/P structure remarkably well, and the radial B_6 profile provides a means to measure peanuts metrics (radial and vertical extent) as well as the integrated "strength" of the X/P instability. This framework was applied to the archetypal X/P galaxy NGC 128, the first galaxy of this class to be noted (by Burbidge & Burbidge 1959), and to eleven other systems previously known in the literature to host peanut structures. Near-infrared imaging of these galaxies, observed with HST, *Spitzer* (S^4G), and SDSS (data release 9), was analysed with IsoFit to extract their isophote parameters. It was found that the peanut length, height, and strength, define specific scaling relations, which hold in physical units (kpc) but also when normalised by the exponential scale length (h) of their host discs, indicating an underlying connection between the two components. This provides a concrete observational constraint for X/P formation and secular evolution theory, which has been predominantly explored in the past through N–body simulations (e.g., Combes & Sanders 1981; Athanassoula 2005; Martinez-Valpuesta et al. 2006; Quillen et al. 2014) which, however, have seldom been compared against observations in a more than qualitative way (see, however, Laurikainen & Salo 2017). Secondly, two galaxies in the sample (NGC 128 and NGC 2549) were found to harbor previously unknown double (or nested) peanut structures. The photometric decomposition of their host galaxies revealed that they are double-barred (as in Erwin 2011), which confirms the X/P–bar association. It is worth noting that Martinez-Valpuesta et al. (2006) have shown that bars may undergo multiple buckling phases (the vertical instability mechanism which leads to the formation of an X/P structure in the inner regions of the bar) as they grow and evolve, though the resulting peanuts do not actually co-exist temporally, as observed here. Therefore, the discovery of such nested X/P structures provides another concrete observational prediction for simulations to reproduce. Finally, it was noted that NGC 128 appears to host a particularly strong X/P structure when compared with the rest of the sample. Given the presence of a significant companion with which this galaxy visibly exchanges material (a situation not observed with the other eleven objects in the sample), it was suggested that this may be quantitative evidence for an enhancement of the X/P structure resulting from "galactic cannibalism", as discussed in Binney & Petrou (1985).

The framework presented in Chapter 3 allows in principle for direct comparisons between observations (projected light distribution of galaxies) and simulations (projected density distributions). IsoFit therefore provides a common ground to compare the two,

constraining the models with observations and, conversely, interpreting the observations with numerical models. For example, X/P formation theory invokes a dynamical instability of bars (Raha et al. 1991), which themselves result from swing amplified dynamical instabilities in stellar discs (Toomre 1981). The observed scaling relations between X/P parameters, and their invariance to normalisation by the disc h, provide verifiable constraints for galaxy simulations, pertaining to the secular co-evolution between peanuts and the discs from which they originate. Additionally, the shape of the B_6 profile was found to vary across the galaxies in the sample considered in Chapter 3, indicating the presence of additional information encoded in the isophotes. This may allow in the future for the discrimination between different formation, or enhancement, mechanisms (e.g., inner Lindblad Resonance – Combes et al. 1990; accretion via cannibalism of satellites, etc.), or possibly constrain the orientation angle of bars in edge-on projection. These different possibilities can be tested by directly applying the technique developed here to numerical simulations, such as the models presented in Athanassoula (2016), Salo & Laurikainen (2017), or the $GalMer$[1] simulation suite (Chilingarian et al. 2010).

In Chapter 4, the framework elaborated in Ciambur & Graham (2016) was applied to the closest X/P structure to the Sun: that in our own Galaxy. In doing so, we have tackled, and brought an alternative perspective to, the long-standing debate regarding the nature, size and orientation of the Milky Way's bar and "bulge" (e.g., Hammersley et al. 1994; López-Corredoira et al. 2007; Wegg et al. 2015). For this analysis, near-infrared WISE imaging was used (Lang 2014), in two filters, namely at 3.4 μm and 4.6 μm, chosen to minimise as far as possible the biasing effects of dust (obscuration and glow). Our perspective of the Milky Way from within its stellar disc warranted a special treatment of the data. Specifically, the $East$ and $West$ directions (in Galactic co-ordinates) were modelled separately, to account for the asymmetry in the isophotes about the centre of the Galaxy, induced by the close-up perspective of the inclined bar and X/P structure. Taking this into account, we obtained the orientation angle and thus intrinsic size of the Milky Way's peanut, which we used to infer the geometry of the long bar. The emerging picture is that of a typical thin bar between 3 and 4 kpc in radius, with a vertically thickened inner $\sim$ half, where it assumes the characteristic peanut morphology, and which is oriented at $\sim 37°$ with respect to our line-of-sight to the centre of the Galaxy. The constraints obtained here could be refined further by applying this technique to maps of the "red clump" giants distribution, a (stellar) tracer population of Galactic structure in

---

[1]http://galmer.obspm.fr

the bar and X/P region (e.g., Wegg & Gerhard 2013).

The Milky Way's X/P structure is similar to those of nearby galaxies. Its spatial parameters – radius and vertical height above the disc – are consistent with the trends presented in Chapter 3 (Ciambur & Graham 2016), while the strength of the X/P instability appears somewhat higher (but within 2σ) than expected. This might be evidence for an enhancement of the Milky Way's peanut caused by interaction with its satellite companions such as *Sagittarius*, or the Magellanic Clouds (§1.2.2). Alternatively, this could suggest a relatively recent X/P formation through a bar buckling phase, as suggested by a slight ($North - South$) asymmetry in the peanut isophotes (akin to galaxies in the process of buckling – Erwin & Debattista 2016). Both possibilities would benefit from follow-up studies, but can in principle be probed via $N-$body simulations of (Milky Way)-like galaxies (Shen et al. 2010; Athanassoula et al. 2017), with or without companions, as they form and evolve their bars and X/P feature. Adding such theoretical input, and directly comparing with observations, constitutes an effective avenue to better understand our Galaxy's past evolution and large-scale morphology, and thus provide a stronger foundation to use the Milky Way as a benchmark system for other galaxies.

Chapter 5 has focussed on the parametric modelling of galaxy radial light profiles, and PROFILER, the software program developed for this purpose, was introduced, described and demonstrated. PROFILER was designed to model multi-component systems, and devotes particular attention to galactic discs, for which it can employ five different models. In addition to discs, the program can model spheroids (with and without cores), bar components, rings, spiral arms, and point-like or resolved nuclear sources. An especially careful treatment is given to the PSF convolution operation, which is performed in 2D between the PSF (which has three possible choices) and circularly-symmetric or elliptical models. Both the major, and geometric mean (or "equivalent"), axis profiles can be modelled, and in the latter case, the total flux of each component is provided, in addition to the parameters of the best-fit solution. PROFILER has been extensively used throughout this thesis, to study the structural composition of X/P galaxies (Chapter 3), spiral galaxies hosting intermediate-mass black hole (Chapter 6), and ES, and dwarf early-type, galaxies (Graham et al. 2016a; Graham et al. 2017).

PROFILER was released into the public domain, and is intended to provide a robust galaxy decomposition platform for extragalactic structural studies, *alternative* (or com-

plementary) to the recent, publicly available 2D image-fitting programs, such as GALFIT (Peng et al. 2010), or IMFIT (Erwin 2015). By analysing the 1D surface brightness profiles of galaxies and using the associated (radially-varying profiles of) different isophote parameters, such as ellipticity, position angle, and higher-order harmonic terms, this approach can overcome some of the biases and limitations of the 2D method. PROFILER's intuitive design and extended arsenal of analytical functions available to model various components, makes it easily applicable to a broad range of galaxy morphological types, and with broad use, offers the potential to homogenise 1D decompositions in the literature, as the aforementioned image-fitting tools have accomplished with the 2D approach.

Chapter 6 has presented contributed research to four articles, and focuses on challenges to, and unexplored regimes in, the numerous existing scaling relations between central black holes and their host galaxy structure (i.e., spheroid luminosity, stellar mass, concentration, velocity dispersion, etc.). First, an investigation was performed into an alleged "over-massive" black hole, at the core of the discy elliptical galaxy NGC 1271 (Walsh et al. 2015). A careful modelling of the host galaxy, however, revealed consistency with the high-mass end of the (black hole – host spheroid) scaling relations (Graham et al. 2016a). Second, the focus shifted to the un-probed low-mass end of these relations, occupied by rare, "intermediate-mass" black holes (IMBH). This elusive class of black holes, defined to lie within the mass range $[2 \leqslant \log_{10}(M_\bullet/M_\odot) \leqslant 5]$, is believed to constitute the seeds of supermassive black holes, though, as yet, little observational evidence for such objects has been gathered, due primarily to the limits of current instrumentation (Mezcua 2017). In Webb et al. (2017), we studied the environment of HLX-1, a promising IMBH candidate (Farrell et al. 2009) located off-centre in the disc galaxy ESO 243-49. Using high-resolution HST imaging in the H–band, we modelled the radial light profile of ESO 243-49, revealing (despite the edge-on disc orientation) the presence of a bar component. We further measured the spheroid Sérsic index and luminosity, which provided – via the scaling relations in Savorgnan et al. (2016) and Savorgnan (2016) – two estimates for the *central*, supermassive, black hole mass of this galaxy ($M_\bullet \sim 10^7 M_\odot$). These are important constraints for future N-body simulations aiming to test the merger-scenario of HLX-1 with its host galaxy, which require a thorough understanding of the structure and and supermassive black hole mass, of ESO 243-49, as was measured here. Further, in Graham et al. (2016b), we studied the spiral galaxy LEDA 87300, reported to host an IMBH at its core (Baldassare et al. 2015). We revealed the barred nature of this galaxy, which had previously not been accounted for, thus biasing the (bulge+disc) only decompo-

sition of Baldassare et al. (2015). We interpreted this galaxy in the context of the broken $(M_\bullet - M_{\star,\mathrm{sph}})$ relation, and its possible extension into the unprobed intermediate-mass regime. This work has powerful implications for our understanding of the formation of supermassive black holes. In Koliopanos et al. (2017) we employed four independent black hole scaling relations to jointly constrain the masses of six IMBH candidates. Specifically, we used the fundamental plane of black hole activity (relating the mass of an accreting black hole with its associated X-ray and radio emission – Merloni et al. 2003), the correlations between black hole mass and the luminosity and concentration of the host spheroid (Savorgnan et al. 2016; Savorgnan 2016), and the scaling relation between black hole mass and the spiral arm pitch angle (Berrier et al. 2013). This analysis can be extended in the future to a broader sample of galaxies with IMBH candidates (such as the 45 candidates in Graham & Scott 2013), thus probing the galaxy – black hole co-evolution into the IMBH regime.

Finally, all the elements presented above have the potential to shed new light upon the effect of bar-related secular processes on black hole growth. Numerous studies have shown that non-axisymmetric structures like bars or peanuts can regulate the inflow of gas towards the centre of a galaxy (see Fragkoudi et al. 2016 and references therein), possibly providing a gas reservoir from which black holes can accrete, become active and grow. The photometric technique for identifying and quantifying X/P structures, presented in Chapter 2, can be used in conjunction with kinematic diagnostics (Debattista et al. 2005) to gauge their prevalence of X/P structures in the galaxy population, in all orientations. Further, via structural decomposition with the method presented in Chapter 5, black hole scaling relations can be constructed for this galaxy class, which may show evidence of gas-driven "quadratic growth" (Graham & Scott 2013) believed to operate in late-type galaxies, at the low-mass end. Such investigations will serve to refine our understanding of how supermassive black holes grow and evolve within their host galaxies.

Additional Publications

In addition to the articles presented in this thesis, I have contributed to the following articles:

- "*Implications for the Origin of Early-type Dwarf Galaxies: A Detailed Look at the Isolated Rotating Early-type Dwarf Galaxy LEDA 2108986 (CG 611), Ramifications for the Fundamental Planes S_K^2 Kinematic Scaling, and the SpinEllipticity Diagram*", by A. W. Graham, J. Janz, S. J. Penny, I. V. Chilingarian, **B. C. Ciambur**, D. A. Forbes & R. L. Davies, ApJ, Vol. 840, ID. 68 (2017)

- "*Evolution of the Anti-truncated Stellar Profiles of S0 Galaxies Since $z = 0.6$ in the SHARDS Survey: I - Sample and Methods*", by A. Borlaff, C. M. Eliche-Moral, J. E. Beckman, **B. C. Ciambur**, P. G. Pérez-González, G. Barro, A. Cava, N. Cardiel, A&A, in press (2017)

Bibliography

Abraham, R. G., van den Bergh, S., & Nair, P. 2003, ApJ, 588, 218

Aguerri, J. A. L., Beckman, J. E., & Prieto, M. 1998, AJ, 116, 2136

Ahn, C. P., Alexandroff, R., Allende Prieto, C., et al. 2012, ApJS, 203, 21

Andredakis, Y. C., Peletier, R. F., & Balcells, M. 1995, MNRAS, 275, 874

Arnold, J. A., Romanowsky, A. J., Brodie, J. P., et al. 2014, ApJ, 791, 80

Aronica, G., Athanassoula, E., Bureau, M., et al. 2003, Ap&SS, 284, 753

Athanassoula, E. 1992, MNRAS, 259, 345

Athanassoula, E. 2005, MNRAS, 358, 1477

Athanassoula, E. 2016, Galactic Bulges, 418, 391

Athanassoula, E., & Bosma, A. 1985, ARA&A, 23, 147

Athanassoula, E., Laurikainen, E., Salo, H., & Bosma, A. 2015, MNRAS, 454, 3843

Athanassoula, E., & Misiriotis, A. 2002, MNRAS, 330, 35

Athanassoula, E., Morin, S., Wozniak, H., et al. 1990, MNRAS, 245, 130

Athanassoula, E., Rodionov, S. A., & Prantzos, N. 2017, MNRAS, 467, L46

Bacon, R., Copin, Y., Monnet, G., et al. 2001, MNRAS, 326, 23

Bacon, R., Accardo, M., Adjali, L., et al. 2010, in SPIE, Vol. 7735, Ground-based and
    Airborne Instrumentation for Astronomy III, 773508

Balcells, M., Graham, A. W., Domínguez-Palmero, L., & Peletier, R. F. 2003, ApJL, 582,
    L79

Baldassare, V. F., Reines, A. E., Gallo, E., & Greene, J. E. 2015, ApJ, 809, L14

Barazza, F. D., Jogee, S., & Marinova, I. 2008, ApJ, 675, 1194

Barth, A. J., Ho, L. C., Rutledge, R. E., & Sargent, W. L. W. 2004, ApJ, 607, 90

Barton, I. J., & Thompson, L. A. 1997, AJ, 114, 655

Bell, E. F., McIntosh, D. H., Katz, N., & Weinberg, M. D. 2003, ApJS, 149, 289

Bender, R. 1988a, A&A, 202, L5

Bender, R. 1988b, A&A, 193, L7

Bender, R., & Moellenhoff, C. 1987, A&A, 177, 71

Bender, R., & Nieto, J.-L. 1990, A&A, 239, 97

Bensby, T. 2014, in IAU Symposium, Vol. 298, Setting the scene for Gaia and LAMOST, ed. S. Feltzing, G. Zhao, N. A. Walton, & P. Whitelock, 17–27

Bentz, M. C., Walsh, J. L., Barth, A. J., et al. 2010, ApJ, 716, 993

Berentzen, I., Athanassoula, E., Heller, C. H., & Fricke, K. J. 2004, MNRAS, 347, 220

Bernardi, M., Hyde, J. B., Sheth, R. K., Miller, C. J., & Nichol, R. C. 2007, AJ, 133, 1741

Berrier, J. C., Davis, B. L., Kennefick, D., et al. 2013, ApJ, 769, 132

Bertola, F., & Capaccioli, M. 1978, ApJL, 219, L95

Binney, J., & Petrou, M. 1985, MNRAS, 214, 449

Bland-Hawthorn, J., & Gerhard, O. 2016, ARA&A, 54, 529

Bland-Hawthorn, J., Vlajić, M., Freeman, K. C., & Draine, B. T. 2005, ApJ, 629, 239

Blanton, M. R., & Moustakas, J. 2009, ARA&A, 47, 159

Borlaff, A., Eliche-Moral, M. C., Beckman, J. E., et al. 2017, ArXiv e-prints

Bosma, A. 1978, PhD thesis, PhD Thesis, Groningen Univ., (1978)

Bournaud, F., & Combes, F. 2002, A&A, 392, 83

Brunzendorf, J., & Meusinger, H. 1999, A&AS, 139, 141

Bundy, K., Fukugita, M., Ellis, R. S., et al. 2009, ApJ, 697, 1369

Bundy, K., Bershady, M. A., Law, D. R., et al. 2015, ApJ, 798, 7

Burbidge, E. M., & Burbidge, G. R. 1959, ApJ, 130, 20

Bureau, M., & Freeman, K. C. 1999, AJ, 118, 126

Buta, R. 1996, in Astronomical Society of the Pacific Conference Series, Vol. 91, IAU Colloq. 157: Barred Galaxies, ed. R. Buta, D. A. Crocker, & B. G. Elmegreen, 11

Buta, R., & Block, D. L. 2001, ApJ, 550, 243

Buta, R. J., Knapen, J. H., Elmegreen, B. G., et al. 2009, AJ, 137, 4487

Buta, R. J., Sheth, K., Athanassoula, E., et al. 2015, ApJS, 217, 32

Cabrera-Lavers, A., González-Fernández, C., Garzón, F., Hammersley, P. L., & López-Corredoira, M. 2008, A&A, 491, 781

Cabrera-Lavers, A., Hammersley, P. L., González-Fernández, C., et al. 2007, A&A, 465, 825

Caldwell, N., Rose, J. A., Sharples, R. M., Ellis, R. S., & Bower, R. G. 1993, AJ, 106, 473

Caon, N., Capaccioli, M., & D'Onofrio, M. 1993, MNRAS, 265, 1013

Cappellari, M., Emsellem, E., Krajnović, D., et al. 2011, MNRAS, 416, 1680

Carter, D. 1978, MNRAS, 182, 797

Carter, D. 1987, ApJ, 312, 514

Chemin, L., Balkowski, C., Cayatte, V., et al. 2006, MNRAS, 366, 812

Chilingarian, I. V., Di Matteo, P., Combes, F., Melchior, A.-L., & Semelin, B. 2010, A&A, 518, A61

Christlein, D., & Zaritsky, D. 2008, ApJ, 680, 1053

Ciambur, B. C. 2015, ApJ, 810, 120

Ciambur, B. C. 2016, PASA, 33, e062

Ciambur, B. C., & Graham, A. W. 2016, MNRAS, 459, 1276

Ciambur, B. C., Graham, A. W., & Bland-Hawthorn, J. 2017, MNRAS, submitted

Combes, F., Debbasch, F., Friedli, D., & Pfenniger, D. 1990, A&A, 233, 82

Combes, F., & Sanders, R. H. 1981, A&A, 96, 164

Comerón, S., Elmegreen, B. G., Salo, H., et al. 2012, ApJ, 759, 98

Conselice, C. J. 2003, ApJS, 147, 1

Conselice, C. J. 2014, ARA&A, 52, 291

Conselice, C. J., Bershady, M. A., & Jangren, A. 2000, ApJ, 529, 886

Courteau, S., Dutton, A. A., van den Bosch, F. C., et al. 2007, ApJ, 671, 203

Cox, T. J., Jonsson, P., Primack, J. R., & Somerville, R. S. 2006, MNRAS, 373, 1013

Croom, S. M., Lawrence, J. S., Bland-Hawthorn, J., et al. 2012, MNRAS, 421, 872

Croton, D. J., Springel, V., White, S. D. M., et al. 2006, MNRAS, 365, 11

Curtis, H. D. 1918, Publications of Lick Observatory, 13, 9

Davies, R. L., Efstathiou, G., Fall, S. M., Illingworth, G., & Schechter, P. L. 1983, ApJ, 266, 41

Davis, B. L., Berrier, J. C., Shields, D. W., et al. 2012, ApJS, 199, 33

Davis, B. L., Graham, A. W., & Seigar, M. S. 2017, ApJ

Davis, B. L., Kennefick, D., Kennefick, J., et al. 2015, ApJL, 802, L13

de Sitter, W. 1917, MNRAS, 78, 3

de Souza, R. E., Gadotti, D. A., & dos Anjos, S. 2004, ApJS, 153, 411

de Vaucouleurs, G. 1957, AJ, 62, 69

de Vaucouleurs, G. 1959, Handbuch der Physik, 53, 275

de Vaucouleurs, G. 1963, ApJS, 8, 31

de Vaucouleurs, G., de Vaucouleurs, A., Corwin, Jr., H. G., et al. 1991, Third Reference Catalogue of Bright Galaxies. Volume I: Explanations and references. Volume II: Data for galaxies between 0^h and 12^h. Volume III: Data for galaxies between 12^h and 24^h.

Debattista, V. P., Carollo, C. M., Mayer, L., & Moore, B. 2005, ApJ, 628, 678

Del Burgo, C., Carter, D., & Sikkema, G. 2008, A&A, 477, 105

Di Matteo, P. 2016, PASA, 33, e027

Djorgovski, S., & Davis, M. 1987, ApJ, 313, 59

Dong, X. Y., & De Robertis, M. M. 2006, AJ, 131, 1236

D'Onofrio, M., Capaccioli, M., & Caon, N. 1994, MNRAS, 271, 523

Draine, B. T. 2003, ARA&A, 41, 241

Dressler, A., Lynden-Bell, D., Burstein, D., et al. 1987, ApJ, 313, 42

Dreyer, J. L. E. 1888, Mem R Astron Soc, 49, 1

Dreyer, J. L. E. 1895, Mem R Astron Soc, 51, 185

Dreyer, J. L. E. 1910, Mem R Astron Soc, 59, 105

Driver, S. P., Popescu, C. C., Tuffs, R. J., et al. 2008, ApJ, 678, L101

Dwek, E., Arendt, R. G., Hauser, M. G., et al. 1995, ApJ, 445, 716

Eckart, A., & Genzel, R. 1997, MNRAS, 284, 576

Efstathiou, G., Ellis, R. S., & Carter, D. 1982, MNRAS, 201, 975

Elmegreen, B. G., & Elmegreen, D. M. 1985, ApJ, 288, 438

Emsellem, E., Cappellari, M., Krajnović, D., et al. 2007, MNRAS, 379, 401

Erwin, P. 2005, MNRAS, 364, 283

Erwin, P. 2011, Memorie della Societa Astronomica Italiana Supplementi, 18, 145

Erwin, P. 2015, ApJ, 799, 226

Erwin, P., Beckman, J. E., & Pohlen, M. 2005, ApJL, 626, L81

Erwin, P., & Debattista, V. P. 2013, MNRAS, 431, 3060

Erwin, P., & Debattista, V. P. 2016, ApJL, 825, L30

Erwin, P., & Debattista, V. P. 2017, MNRAS, 468, 2058

Erwin, P., & Sparke, L. S. 2003, ApJS, 146, 299

Eskridge, P. B., Frogel, J. A., Pogge, R. W., et al. 2000, AJ, 119, 536

Faber, S. M., Dressler, A., Davies, R. L., Burstein, D., & Lynden-Bell, D. 1987, in Nearly Normal Galaxies. From the Planck Time to the Present, ed. S. M. Faber, 175–183

Faber, S. M., & Jackson, R. E. 1976, ApJ, 204, 668

Farrell, S. A., Webb, N. A., Barret, D., Godet, O., & Rodrigues, J. M. 2009, Nature, 460, 73

Farrell, S. A., Servillat, M., Pforr, J., et al. 2012, ApJ, 747, L13

Ferrarese, L., & Merritt, D. 2000, ApJL, 539, L9

Ferrarese, L., Côté, P., Jordán, A., et al. 2006, ApJS, 164, 334

Ferrers, N. M. 1877, Quart. J. Pure Appl. Math., 14

Forbes, D. A., Proctor, R., Strader, J., & Brodie, J. P. 2007, ApJ, 659, 188

Fragkoudi, F., Athanassoula, E., & Bosma, A. 2016, MNRAS, 462, L41

Franx, M., Illingworth, G., & Heckman, T. 1989, ApJ, 344, 613

Franx, M., & Illingworth, G. D. 1988, ApJ, 327, L55

Freeman, K. C. 1970, ApJ, 160, 811

Friedli, D., Wozniak, H., Rieke, M., Martinet, L., & Bratschi, P. 1996, A&AS, 118, 461

Friedmann, A. 1922, Zeitschrift fur Physik, 10, 377

Gadotti, D. A. 2009, MNRAS, 393, 1531

Gadotti, D. A., Athanassoula, E., Carrasco, L., et al. 2007, MNRAS, 381, 943

Galilei, G. 1610, Sidereus Nuncius

Ganda, K., Falcón-Barroso, J., Peletier, R. F., et al. 2006, MNRAS, 367, 46

Gerhard, O. 2002, in Astronomical Society of the Pacific Conference Series, Vol. 273, The Dynamics, Structure & History of Galaxies: A Workshop in Honour of Professor Ken Freeman, ed. G. S. Da Costa, E. M. Sadler, & H. Jerjen, 73

Gerhard, O., & Martinez-Valpuesta, I. 2012, ApJL, 744, L8

Gerhard, O. E., & Binney, J. J. 1996, MNRAS, 279, 993

Ghez, A. M., Klein, B. L., Morris, M., & Becklin, E. E. 1998, ApJ, 509, 678

Ghez, A. M., Salim, S., Weinberg, N. N., et al. 2008, ApJ, 689, 1044

Gil de Paz, A., Madore, B. F., Boissier, S., et al. 2005, ApJL, 627, L29

Gill, M., Trenti, M., Miller, M. C., et al. 2008, ApJ, 686, 303

Gillessen, S., Eisenhauer, F., Trippe, S., et al. 2009, ApJ, 692, 1075

Gilmore, G., & Reid, N. 1983, MNRAS, 202, 1025

Gnedin, O. Y., Goodman, J., & Frei, Z. 1995, AJ, 110, 1105

Graham, A. W. 2001, AJ, 121, 820

Graham, A. W. 2012, ApJ, 746, 113

Graham, A. W. 2013, Elliptical and Disk Galaxy Structure and Modern Scaling Laws, ed. T. D. Oswalt & W. C. Keel, 91

Graham, A. W. 2016, Galactic Bulges, 418, 263

Graham, A. W., Ciambur, B. C., & Savorgnan, G. A. D. 2016a, ApJ, 831, 132

Graham, A. W., Ciambur, B. C., & Soria, R. 2016b, ApJ, 818, 172

Graham, A. W., Colless, M. M., Busarello, G., Zaggia, S., & Longo, G. 1998, A&AS, 133, 325

Graham, A. W., & Driver, S. P. 2005, PASA, 22, 118

Graham, A. W., & Driver, S. P. 2007, ApJ, 655, 77

Graham, A. W., Durré, M., Savorgnan, G. A. D., et al. 2016c, ApJ, 819, 43

Graham, A. W., Erwin, P., Caon, N., & Trujillo, I. 2001, ApJ, 563, L11

Graham, A. W., Erwin, P., Trujillo, I., & Asensio Ramos, A. 2003, AJ, 125, 2951

Graham, A. W., & Guzmán, R. 2003, AJ, 125, 2936

Graham, A. W., Janz, J., Penny, S. J., et al. 2017, ApJ, 840, 68

Graham, A. W., Onken, C. A., Athanassoula, E., & Combes, F. 2011, MNRAS, 412, 2211

Graham, A. W., & Scott, N. 2013, ApJ, 764, 151

Graham, A. W., & Scott, N. 2015, ApJ, 798, 54

Graham, A. W., & Worley, C. C. 2008, MNRAS, 388, 1708

Greene, J. E., & Ho, L. C. 2005, ApJ, 630, 122

Greenhill, L. J., Booth, R. S., Ellingsen, S. P., et al. 2003, ApJ, 590, 162

Grosbøl, P., Patsis, P. A., & Pompei, E. 2004, A&A, 423, 849

Gültekin, K., Richstone, D. O., Gebhardt, K., et al. 2009, ApJ, 698, 198

Hammersley, P. L., Garzon, F., Mahoney, T., & Calbet, X. 1994, MNRAS, 269, 753

Hammersley, P. L., Garzón, F., Mahoney, T. J., López-Corredoira, M., & Torres, M. A. P. 2000, MNRAS, 317, L45

Häring, N., & Rix, H.-W. 2004, ApJ, 604, L89

Hawkins, K., Jofré, P., Masseron, T., & Gilmore, G. 2015, MNRAS, 453, 758

Herschel, J. F. W. 1864, Phil. Trans. R. Soc. Lond. Ser. I, 154, 1

Herschel, W. F. 1786, Phil. Trans. R. Soc. Lond. Ser. I, 76, 457

—. 1802, Phil. Trans. R. Soc. Lond. Ser. I, 92, 477

Hevelius, J., & von Schmieden, J. E. 1690, Prodromus Astronomiae

Hodge, P. W. 1983, PASP, 95, 721

Hodierna, G. B. 1654, De Systemate Orbis Cometici Deque Admirandis Coeli Characteribus

Hohl, F. 1971, ApJ, 168, 343

Hubble, E. 1929, Proceedings of the National Academy of Science, 15, 168

Hubble, E. P. 1925, Popular Astronomy, 33

Hubble, E. P. 1926, ApJ, 64

Hubble, E. P. 1936, Realm of the Nebulae

Jarvis, B. J. 1986, AJ, 91, 65

Jeans, J. H. 1919, Problems of cosmogony and stellar dynamics

Jeans, J. H. 1929, The universe around us

Jedrzejewski, R. I. 1987a, MNRAS, 226, 747

—. 1987b, MNRAS, 226, 747

Jurić, M., Ivezić, Ž., Brooks, A., et al. 2008, ApJ, 673, 864

Kalberla, P. M. W., & Dedes, L. 2008, A&A, 487, 951

Kannappan, S. J., Fabricant, D. G., & Franx, M. 2002, AJ, 123, 2358

Kant, I. 1755, Allgemeine Naturgeschichte und Theorie des Himmels

Kapteyn, J. C. 1922, ApJ, 55, 302

Kapteyn, J. C., & van Rhijn, P. J. 1920, ApJ, 52, 23

Kaspi, S., Smith, P. S., Netzer, H., et al. 2000, ApJ, 533, 631

Kautsch, S. J. 2009, PASP, 121, 1297

Kennicutt, Jr., R. C. 2001, in Astronomical Society of the Pacific Conference Series, Vol. 231, Tetons 4: Galactic Structure, Stars and the Interstellar Medium, ed. C. E. Woodward, M. D. Bicay, & J. M. Shull, 2

Knapen, J. H. 2010, in Galaxies and their Masks, ed. D. L. Block, K. C. Freeman, & I. Puerari, 201

Knapp, G. R., Turner, E. L., & Cunniffe, P. E. 1985, AJ, 90, 454

Koliopanos, F., Ciambur, B. C., Graham, A. W., et al. 2017, A&A, 601, A20

Kormendy, J. 2013, Secular Evolution in Disk Galaxies, ed. J. Falcón-Barroso & J. H. Knapen, 1

Kormendy, J., & Bender, R. 1996, ApJL, 464, L119

Kormendy, J., & Ho, L. C. 2013, ARA&A, 51, 511

Kormendy, J., & Illingworth, G. 1982, ApJ, 256, 460

Kormendy, J., & Kennicutt, Jr., R. C. 2004, ARA&A, 42, 603

Kormendy, J., & Richstone, D. 1995, ARA&A, 33, 581

Krajnović, D., Cappellari, M., de Zeeuw, P. T., & Copin, Y. 2006, MNRAS, 366, 787

Krajnović, D., Emsellem, E., Cappellari, M., et al. 2011, MNRAS, 414, 2923

Krajnović, D., Alatalo, K., Blitz, L., et al. 2013, MNRAS, 432, 1768

Kuijken, K., & Merrifield, M. R. 1995, ApJL, 443, L13

Lacy, J. H., Townes, C. H., Geballe, T. R., & Hollenbach, D. J. 1980, ApJ, 241, 132

Lang, D. 2014, AJ, 147, 108

Lauer, T. R. 1985, MNRAS, 216, 429

Launhardt, R., Zylka, R., & Mezger, P. G. 2002, A&A, 384, 112

Laurikainen, E., & Salo, H. 2002, MNRAS, 337, 1118

Laurikainen, E., & Salo, H. 2017, A&A, 598, A10

Laurikainen, E., Salo, H., Athanassoula, E., Bosma, A., & Herrera-Endoqui, M. 2014, MNRAS, 444, L80

Laurikainen, E., Salo, H., & Buta, R. 2005, MNRAS, 362, 1319

Laurikainen, E., Salo, H., Buta, R., & Knapen, J. H. 2011, MNRAS, 418, 1452

Laurikainen, E., Salo, H., Buta, R., Knapen, J. H., & Comerón, S. 2010, MNRAS, 405, 1089

Leavitt, H. S. 1908, Annals of Harvard College Observatory, 60, 87

Lemaître, G. 1927, Annales de la Société Scientifique de Bruxelles, 47, 49

Lemons, S. M., Reines, A. E., Plotkin, R. M., Gallo, E., & Greene, J. E. 2015, ApJ, 805, 12

Licquia, T. C., & Newman, J. A. 2016, ApJ, 831, 71

Liller, M. H. 1966, ApJ, 146, 28

Lin, C. C., & Shu, F. H. 1964, ApJ, 140, 646

Lin, C. C., & Shu, F. H. 1966, Proceedings of the National Academy of Science, 55, 229

López-Corredoira, M., Cabrera-Lavers, A., Mahoney, T. J., et al. 2007, AJ, 133, 154

López-Corredoira, M., Hammersley, P. L., Garzón, F., et al. 2001, A&A, 373, 139

Lotz, J. M., Primack, J., & Madau, P. 2004, AJ, 128, 163

Lotz, J. M., Davis, M., Faber, S. M., et al. 2008, ApJ, 672, 177

Lundmark, K. 1924, MNRAS, 84, 747

Lütticke, R., Dettmar, R.-J., & Pohlen, M. 2000, A&A, 362, 435

Lützgendorf, N., Baumgardt, H., & Kruijssen, J. M. D. 2013, A&A, 558, A117

Lynden-Bell, D. 1967, MNRAS, 136, 101

Madau, P., & Rees, M. J. 2001, ApJL, 551, L27

Magorrian, J., Tremaine, S., Richstone, D., et al. 1998, AJ, 115, 2285

Malin, D. F., & Carter, D. 1983, ApJ, 274, 534

Malin, D. F., Quinn, P. J., & Graham, J. A. 1983, ApJ, 272, L5

Malin, D. F., & Zealey, W. J. 1979, S&T, 57, 354

Malumuth, E. M., & Kirshner, R. P. 1981, ApJ, 251, 508

Mapelli, M., Zampieri, L., & Mayer, L. 2012, MNRAS, 423, 1309

Marconi, A., & Hunt, L. K. 2003, ApJ, 589, L21

Marius, S. 1614, Mundus Jovialis

Marquardt, W. D. 1963, JSIAM, 11

Martin, P. 1995, AJ, 109, 2428

Martinez-Valpuesta, I., & Shlosman, I. 2004, ApJ, 613, L29

Martinez-Valpuesta, I., Shlosman, I., & Heller, C. 2006, ApJ, 637, 214

Masters, K. L., Springob, C. M., Haynes, M. P., & Giovanelli, R. 2006, ApJ, 653, 861

Masters, K. L., Nichol, R. C., Hoyle, B., et al. 2011, MNRAS, 411, 2026

McWilliam, A., & Zoccali, M. 2010, ApJ, 724, 1491

Merloni, A., Heinz, S., & di Matteo, T. 2003, MNRAS, 345, 1057

Merrifield, M. R. 2004, in Astronomical Society of the Pacific Conference Series, Vol. 317, Milky Way Surveys: The Structure and Evolution of our Galaxy, ed. D. Clemens, R. Shah, & T. Brainerd, 289

Merritt, D., & Sellwood, J. A. 1994, ApJ, 425, 551

Messier, C. 1784, Connoissance des Temps, 227

Mezcua, M. 2017, ArXiv e-prints

Mihalas, D., & Binney, J. 1981, Galactic astronomy: Structure and kinematics /2nd edition/

Mihos, J. C., Richstone, D. O., & Bothun, G. D. 1992, ApJ, 400, 153

Miller, M. C., & Colbert, E. J. M. 2004, International Journal of Modern Physics D, 13, 1

Miller, M. C., & Hamilton, D. P. 2002, MNRAS, 330, 232

Miyoshi, M., Moran, J., Herrnstein, J., et al. 1995, Nature, 373, 127

Moriondo, G., Giovanardi, C., & Hunt, L. K. 1998, A&AS, 130, 81

Ness, M., & Lang, D. 2016, AJ, 152, 14

Ness, M., Freeman, K., Athanassoula, E., et al. 2012, ApJ, 756, 22

Nieto, J.-L., Bender, R., & Surma, P. 1991, A&A, 244, L37

Nieto, J.-L., Capaccioli, M., & Held, E. V. 1988, A&A, 195, L1

Nishiyama, S., Yasui, K., Nagata, T., et al. 2013, ApJ, 769, L28

Norman, C. A., Sellwood, J. A., & Hasan, H. 1996, ApJ, 462, 114

Obrić, M., Ivezić, Ž., Best, P. N., et al. 2006, MNRAS, 370, 1677

Ostriker, J. P., & Peebles, P. J. E. 1973, ApJ, 186, 467

Pastrav, B. A., Popescu, C. C., Tuffs, R. J., & Sansom, A. E. 2013, A&A, 557, A137

Patsis, P. A., Athanassoula, E., Grosbøl, P., & Skokos, C. 2002, MNRAS, 335, 1049

Patterson, F. S. 1940, Harvard College Observatory Bulletin, 914, 9

Peebles, P. J. E. 1972, ApJ, 178, 371

Peletier, R. F., Davies, R. L., Illingworth, G. D., Davis, L. E., & Cawson, M. 1990, AJ, 100, 1091

Peng, C. Y., Ho, L. C., Impey, C. D., & Rix, H.-W. 2002, AJ, 124, 266

Peng, C. Y., Ho, L. C., Impey, C. D., & Rix, H.-W. 2010, AJ, 139, 2097

Peterson, B. M., Ferrarese, L., Gilbert, K. M., et al. 2004, ApJ, 613, 682

Pfenniger, D., & Friedli, D. 1991, A&A, 252, 75

Plotkin, R. M., Markoff, S., Kelly, B. C., Körding, E., & Anderson, S. F. 2012, MNRAS, 419, 267

Pohlen, M., Beckman, J. E., Hüttemeister, S., et al. 2004, in Astrophysics and Space Science Library, Vol. 319, Penetrating Bars Through Masks of Cosmic Dust, ed. D. L. Block, I. Puerari, K. C. Freeman, R. Groess, & E. K. Block, 713

Pohlen, M., & Trujillo, I. 2006, A&A, 454, 759

Prieto, M., Aguerri, J. A. L., Varela, A. M., & Muñoz-Tuñón, C. 2001, A&A, 367, 405

Prugniel, P., & Simien, F. 1997, A&A, 321, 111

Quillen, A. C., Minchev, I., Sharma, S., Qin, Y.-J., & Di Matteo, P. 2014, MNRAS, 437, 1284

Quinlan, G. D., & Shapiro, S. L. 1990, ApJ, 356, 483

Raha, N., Sellwood, J. A., James, R. A., & Kahn, F. D. 1991, Nature, 352, 411

Rees, M. J. 1984, ARA&A, 22, 471

Reines, A. E., Greene, J. E., & Geha, M. 2013, ApJ, 775, 116

Rix, H.-W., & White, S. D. M. 1990, ApJ, 362, 52

Rix, H.-W., & Zaritsky, D. 1995, ApJ, 447, 82

Robertson, H. P. 1929, Proceedings of the National Academy of Science, 15, 822

Romanowsky, A. J., & Fall, S. M. 2012, ApJS, 203, 17

Rubin, V. C., Ford, Jr., W. K., & Thonnard, N. 1980, ApJ, 238, 471

Ryu, T., Tanaka, T. L., Perna, R., & Haiman, Z. 2016, ArXiv e-prints

Salo, H., & Laurikainen, E. 2017, in AAS/Division of Dynamical Astronomy Meeting, Vol. 48, AAS/Division of Dynamical Astronomy Meeting, 303.02

Sánchez, S. F., Kennicutt, R. C., Gil de Paz, A., et al. 2012, A&A, 538, A8

Sandage, A. 1961, The Hubble atlas of galaxies

Sandage, A., & Bedke, J. 1994, The Carnegie Atlas of Galaxies. Volumes I, II.

Sanders, D. B., & Mirabel, I. F. 1996, ARA&A, 34, 749

Santiago, B. X., & Vale, T. B. 2008, A&A, 485, 21

Savorgnan, G. A. D. 2016, ApJ, 821, 88

Savorgnan, G. A. D., & Graham, A. W. 2015, MNRAS, 446, 2330

Savorgnan, G. A. D., & Graham, A. W. 2016a, MNRAS, 457, 320

—. 2016b, MNRAS, 457, 320

Savorgnan, G. A. D., & Graham, A. W. 2016c, ApJS, 222, 10

Savorgnan, G. A. D., Graham, A. W., Marconi, A., & Sani, E. 2016, ApJ, 817, 21

Schechter, P. L. 1980, AJ, 85, 801

Schjellerup, H. C. F. C. 1874, Description des Étoiles Fixes: Composeés au Milieu du Dixième Siècle de Notre Ére par l'Astronome Persan Abd-al-Rahman al-Šūfī

Schödel, R., Feldmeier, A., Kunneriath, D., et al. 2014, A&A, 566, A47

Schönrich, R. 2012, MNRAS, 427, 274

Schwarzschild, M. 1979, ApJ, 232, 236

Schweizer, F. 1976, ApJS, 31, 313

Scott, N., Graham, A. W., & Schombert, J. 2013, ApJ, 768, 76

Seidel, M. K., Cacho, R., Ruiz-Lara, T., et al. 2015, MNRAS, 446, 2837

Seigar, M. S., Kennefick, D., Kennefick, J., & Lacy, C. H. S. 2008, ApJ, 678, L93

Sellwood, J. A. 2011, MNRAS, 410, 1637

Sellwood, J. A. 2014, Reviews of Modern Physics, 86, 1

Sellwood, J. A., & Wilkinson, A. 1993, Reports on Progress in Physics, 56, 173

Sérsic, J. L. 1963, Boletin de la Asociacion Argentina de Astronomia La Plata Argentina, 6, 41

Shankar, F., Bernardi, M., Sheth, R. K., et al. 2016, MNRAS, 460, 3119

Shapley, H. 1914, ApJ, 40, 448

Shapley, H. 1928, Nature, 122, 482

Shapley, H., & Swope, H. H. 1924, Studies of the Galactic Center.

Shaw, M. A. 1987, MNRAS, 229, 691

Shen, J., Rich, R. M., Kormendy, J., et al. 2010, ApJL, 720, L72

Sheth, K., Regan, M., Hinz, J. L., et al. 2010, PASP, 122, 1397

Shetty, R., Vogel, S. N., Ostriker, E. C., & Teuben, P. J. 2007, ApJ, 665, 1138

Simard, L., Willmer, C. N. A., Vogt, N. P., et al. 2002, ApJS, 142, 1

Simien, F., & Michard, R. 1990, A&A, 227, 11

Skrutskie, M. F., Cutri, R. M., Stiening, R., et al. 2006, AJ, 131, 1163

Slipher, V. M. 1913, Lowell Observatory Bulletin, 2, 56

Slipher, V. M. 1917, Proceedings of the American Philosophical Society, 56, 403

Soltan, A. 1982, MNRAS, 200, 115

Soria, R., Hau, G. K. T., Graham, A. W., et al. 2010, MNRAS, 405, 870

Sparke, L. S., & Sellwood, J. A. 1987, MNRAS, 225, 653

Straub, O., Godet, O., Webb, N., Servillat, M., & Barret, D. 2014, A&A, 569, A116

Strauss, M. A., & Willick, J. A. 1995, Phys. Rep., 261, 271

Swaters, R. A., van Albada, T. S., van der Hulst, J. M., & Sancisi, R. 2002, A&A, 390, 829

Tanaka, Y., Nandra, K., Fabian, A. C., et al. 1995, Nature, 375, 659

Thilker, D. A., Bianchi, L., Meurer, G., et al. 2007, ApJS, 173, 538

Thornton, C. E., Barth, A. J., Ho, L. C., Rutledge, R. E., & Greene, J. E. 2008, ApJ, 686, 892

Toomre, A. 1981, in Structure and Evolution of Normal Galaxies, ed. S. M. Fall & D. Lynden-Bell, 111–136

Trujillo, I., Aguerri, J. A. L., Cepa, J., & Gutiérrez, C. M. 2001a, MNRAS, 321, 269

Trujillo, I., Aguerri, J. A. L., Cepa, J., & Gutiérrez, C. M. 2001b, MNRAS, 328, 977

Tully, R. B., & Fisher, J. R. 1977, A&A, 54, 661

van Albada, T. S. 1982, MNRAS, 201, 939

van den Bosch, R. C. E., van de Ven, G., Verolme, E. K., Cappellari, M., & de Zeeuw, P. T. 2008, MNRAS, 385, 647

van der Kruit, P. C. 1987, A&A, 173, 59

van der Kruit, P. C. 2001, in Astronomical Society of the Pacific Conference Series, Vol. 230, Galaxy Disks and Disk Galaxies, ed. J. G. Funes & E. M. Corsini, 119–126

van der Kruit, P. C., & Searle, L. 1981, A&A, 95, 105

Verheijen, M. A. W. 2001, ApJ, 563, 694

Visser, H. C. D. 1980, A&A, 88, 149

Volonteri, M., & Bellovary, J. 2012, Reports on Progress in Physics, 75, 124901

von Humboldt, A. 1850, Kosmos, Vol. 3, 187

Walsh, J. L., van den Bosch, R. C. E., Gebhardt, K., et al. 2015, ApJ, 808, 183

Webb, N., Cseh, D., Lenc, E., et al. 2012, Science, 337, 554

Webb, N. A., Barret, D., Godet, O., et al. 2010, ApJ, 712, L107

Webb, N. A., Guérou, A., Ciambur, B., et al. 2017, ArXiv e-prints

Wegg, C., & Gerhard, O. 2013, MNRAS, 435, 1874

Wegg, C., Gerhard, O., & Portail, M. 2015, MNRAS, 450, 4050

Weiland, J. L., Arendt, R. G., Berriman, G. B., et al. 1994, ApJL, 425, L81

Weiner, B. J., Williams, T. B., van Gorkom, J. H., & Sellwood, J. A. 2001, ApJ, 546, 916

Whyte, L. F., Abraham, R. G., Merrifield, M. R., et al. 2002, MNRAS, 336, 1281

Wolf, M. 1908, Publikationen des Astrophysikalischen Instituts Koenigstuhl-Heidelberg, 3, 109

Wright, E. L., Eisenhardt, P. R. M., Mainzer, A. K., et al. 2010, AJ, 140, 1868

Wright, T. 1750, An Original Theory or New Hypothesis of the Universe

Yoachim, P., & Dalcanton, J. J. 2006, AJ, 131, 226

Yoshino, A., & Ichikawa, T. 2008, PASJ, 60, 493

Young, C. K., & Currie, M. J. 1994, MNRAS, 268, L11

Zibetti, S., Charlot, S., & Rix, H.-W. 2009, MNRAS, 400, 1181

A

Authorship Indication Forms

Swinburne Research

Authorship Indication Form
For PhD (including associated papers) candidates

DECLARATION

We hereby declare our contribution to the publication of the 'paper' entitled:

Beyond ELLIPSE(s): Accurately Modeling the Isophotal Structure of Galaxies with ISOFIT and CMODEL

First Author

Name: ____Constantin Bogdan Ciambur____   Signature: _~Ciambur B~_

Percentage of contribution: 100 %   Date: 13 / 06 / 2017

Brief description of contribution to the 'paper' and your central responsibilities/role on project:
Software development, data collection, analysis and interpretation of results writing of the manuscript.

Second Author

Name: _____   Signature: _____

Percentage of contribution: ____ %   Date: _ _ / _ _ / _ _ _ _

Brief description of your contribution to the 'paper':

Third Author

Name: _____   Signature: _____

Percentage of contribution: ____ %   Date: _ _ / _ _ / _ _ _ _

Brief description of your contribution to the 'paper':

Fourth Author

Name: _____   Signature: _____

Percentage of contribution: ____ %   Date: _ _ / _ _ / _ _ _ _

Brief description of your contribution to the 'paper':

Principal Coordinating Supervisor: Name:____Alister W. Graham____ Signature: _~Alister Graham~_

Date: 13 / 06/ 2017

In the case of more than four authors please attach another sheet with the names, signatures and contribution of the authors.

Swinburne Research

Authorship Indication Form
For PhD (including associated papers) candidates

DECLARATION

We hereby declare our contribution to the publication of the 'paper' entitled:

Quantifying the (X/Peanut)-shaped Structure in Edge-on Disc Galaxies: Length, Strength, and Nested Peanuts

First Author

Name: _____ Constantin Bogdan Ciambur _____   Signature: _____

Percentage of contribution: _80_ %   Date: 13 / 06 / 2017

Brief description of contribution to the 'paper' and your central responsibilities/role on project:
Data collection and analysis, interpretation of results, writing of the manuscript.

Second Author

Name: _____ Alister W. Graham _____   Signature: _____

Percentage of contribution: _20_ %   Date: 13 / 06 / 2017

Brief description of your contribution to the 'paper':
Scientific ideas, extensive editing of paper, literature review

Third Author

Name: _____   Signature: _____

Percentage of contribution: ____%   Date: _ _ / _ _ / _ _ _ _

Brief description of your contribution to the 'paper':

Fourth Author

Name: _____   Signature: _____

Percentage of contribution: ____%   Date: _ _ / _ _ / _ _ _ _

Brief description of your contribution to the 'paper':

Principal Coordinating Supervisor: Name: _____ Alister W. Graham _____   Signature: _____

Date: 13 / 06 / 2017

In the case of more than four authors please attach another sheet with the names, signatures and contribution of the authors.

Swinburne Research

Authorship Indication Form
For PhD (including associated papers) candidates

DECLARATION

We hereby declare our contribution to the publication of the 'paper' entitled:

Quantifying the (X/Peanut)-shaped Structure of the Milky Way - New Constraints on the Bar Geometry

First Author

Name: Constantin Bogdan Ciambur   Signature: _____

Percentage of contribution: 70 %   Date: 13 / 06 / 2017

Brief description of contribution to the 'paper' and your central responsibilities/role on project:
Data acquisition and analysis, interpretation of results, writing of the manuscript.

Second Author

Name: Alister W. Graham   Signature: _____

Percentage of contribution: 25 %   Date: 13 / 06 / 2017

Brief description of your contribution to the 'paper':
Scientific ideas, editing of text, contributed to mathematical analysis, literature review

Third Author

Name: Joss Bland-Hawthorn   Signature: _____

Percentage of contribution: 5 %   Date: 14 / 7 / 17

Brief description of your contribution to the 'paper':
Suggested some improvement to work and text.

Fourth Author

Name: _____   Signature: _____

Percentage of contribution: ____%   Date: __ / __ / ____

Brief description of your contribution to the 'paper':

Principal Coordinating Supervisor: Name: Alister W. Graham   Signature: _____

Date: 13 / 06 / 2017

In the case of more than four authors please attach another sheet with the names, signatures and contribution of the authors.

Authorship Indication Form
For PhD (including associated papers) candidates

NOTE

This Authorship Indication form is a statement detailing the percentage of the contribution of each author in each associated 'paper'. This form must be signed by each co-author and the Principal Coordinating Supervisor. This form must be added to the publication of your final thesis as an appendix. Please fill out a separate form for each associated paper to be included in your thesis.

DECLARATION

We hereby declare our contribution to the publication of the 'paper' entitled:

PROFILER - A Fast and Versatile New Program for Decomposing Galaxy Light Profiles

First Author

Name: _____Constantin Bogdan Ciambur_____   Signature: _____

Percentage of contribution: 100 %   Date: 13 / 06 / 2017

Brief description of contribution to the 'paper' and your central responsibilities/role on project:

Software development, data collection, analysis and interpretation of results, writing of the manuscript.

Second Author

Name: _____   Signature: _____

Percentage of contribution: ____ %   Date: _ _ / _ _ / _ _ _ _

Brief description of your contribution to the 'paper':

Third Author

Name: _____   Signature: _____

Percentage of contribution: ____ %   Date: _ _ / _ _ / _ _ _ _

Brief description of your contribution to the 'paper':

Fourth Author

Name: _____   Signature: _____

Percentage of contribution: ____ %   Date: _ _ / _ _ / _ _ _ _

Brief description of your contribution to the 'paper':

Principal Coordinating Supervisor: Name:_____Alister W. Graham_____ Signature: _____

Date: 13 / 06 / 2017

In the case of more than four authors please attach another sheet with the names, signatures and contribution of the authors.